

City Research Online

City, University of London Institutional Repository

Citation: Nwokoye, I. I. (2024). Novel Bioimpedance Instrumentation Architectures with Significant Performance Improvement for Accurate Skin Health Assessment. (Unpublished Doctoral thesis, City St. George's, University of London)

This is the accepted version of the paper.

This version of the publication may differ from the final published version.

Permanent repository link: https://openaccess.city.ac.uk/id/eprint/36247/

Link to published version:

Copyright: City Research Online aims to make research outputs of City, University of London available to a wider audience. Copyright and Moral Rights remain with the author(s) and/or copyright holders. URLs from City Research Online may be freely distributed and linked to.

Reuse: Copies of full items can be used for personal research or study, educational, or not-for-profit purposes without prior permission or charge. Provided that the authors, title and full bibliographic details are credited, a hyperlink and/or URL is given for the original metadata page and the content is not changed in any way.

City Research Online: http://openaccess.city.ac.uk/ publications@city.ac.uk/

Novel Bioimpedance Instrumentation Architectures with Significant Performance Improvement for Accurate Skin Health Assessment

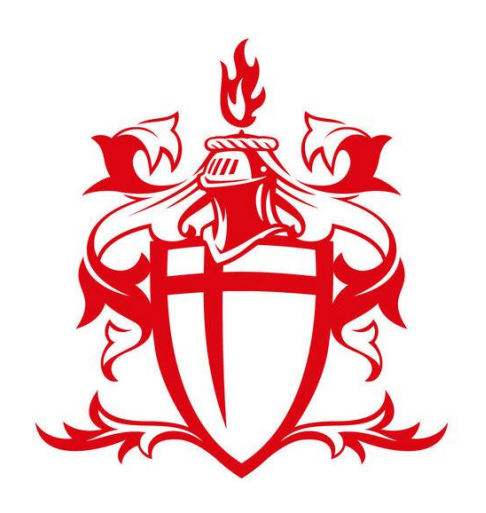
By

Ifeabunike Izunna Nwokoye.

1st Supervisor: Dr. Iasonas. Triantis

2nd Supervisor: Prof. P.A. Kyriacou

PhD Thesis in Biomedical Engineering



Research Centre for Biomedical Engineering
School of Science and Technology
City St. George's, University of London

This dissertation is submitted for the degree of Doctor of Philosophy

Decemeber 2024.

Declaration of own work.

I declare that the work presented in this thesis was conducted in compliance with the University's Regulations and Code of Practice for Research Degree Programmes and has not been submitted for any other academic award. Except where explicitly referenced, this work is entirely my own. All views expressed in this dissertation are solely those of the author.

Abstract

This thesis presents innovative advancements in bioimpedance technology, focusing on the development and validation of systems tailored for accurate, reliable, and portable skin health assessment and a broad range of biomedical applications. By identifying and addressing the limitations inherent in current bioimpedance methods such as limited bandwidth, reduced accuracies due to phase errors, operator dependencies, and limited portability, this research introduces novel architectures designed to minimize systematic errors, thereby enhancing the clinical applicability of bioimpedance technology.

The study begins by outlining the clinical and research motivations for advancing bioimpedance technology, particularly for skin health monitoring. A comprehensive examination of the electrical properties of biological tissues, with emphasis on skin, establishes a strong theoretical foundation. This groundwork supports the investigation into clinical diagnostic innovative circuit designs, skin hydration multimodal approaches, and error mitigation techniques. This research integrates bioimpedance with optical assessment techniques to develop a hybrid system for skin diagnostics, demonstrating the advantages of multimodal sensing in providing a more comprehensive evaluation of skin hydration and overall skin health.

Key contributions of this thesis include assessment of skin hydration using a multimodal approach, analytical comparison of bioimpedance systems, the development of a Phase Error Compensated Synchronous Demodulation (PECSD) system and an Adaptive Howland Current Source (AHCS) with Automatic Gain Control (AGC). Additionally, the thesis presents a method for assessing cell integrity under haemolytic conditions.

The experimental results indicate that the AHCS significantly improves measurement accuracy by addressing bandwidth limitations in conventional Mirrored Enhanced Howland Current Source (MEHCS), enhancing stability and accuracy across frequencies up to 3 MHz, and maintaining consistent current output even at lower current amplitudes of up to $100\mu A$. The PECSD system further enhances accuracy by reducing phase errors in the synchronous demodulation system from over 21% to below 5%. Experimental validations highlight these systems' effectiveness in applications such as skin health diagnostics including skin hydration monitoring, and cell integrity assessment in the case of skin cancer, underscoring their versatility and robustness for real-time clinical diagnostics.

In summary, this thesis advances bioimpedance technology, making it a more precise and adaptable tool for non-invasive diagnostics. The proposed innovations hold promising potential for broad clinical applications, particularly in dermatology and tissue viability assessment, positioning bioimpedance as a valuable technology of next-generation diagnostic tools.

Acknowledgements

First and foremost, I would like to express my gratitude to God Almighty for granting me the life, health, and strength to complete this PhD program. To Him alone be all praise, in Jesus' name. Amen.

I extend my deepest appreciation to my supervisor, Dr. Iasonas Triantis, for his invaluable guidance, support, contributions, and friendship throughout my research. I am truly grateful for all his efforts and encouragement.

My heartfelt thanks also go to my second supervisor, Prof. Kyriacou Panicos, for his assistance with essential lab resources. I am sincerely thankful for his support.

I owe a profound debt of gratitude to Dr. Panos loakim, who referred me to my supervisor and has supported and guided me throughout my PhD journey. I am deeply appreciative of his recommendation and continued encouragement.

I would also like to thank my close family, my parents, and siblings for their prayers, financial support, and moral encouragement. To my beloved wife, Neera, and my children, Ada and Amara, thank you for your patience and understanding, especially during the many long days when I juggled full-time work with PhD commitments. Your support has been invaluable, and I am forever grateful.

Contents

Declaration	n of own work	2
Abstract .		3
Acknowle	dgements	4
List of Fig	ures	8
List of Tab	les	12
Glossary o	f terms	13
Chapter 1		16
Introducti	on:	16
1.2	Skin health monitoring assessment methods	20
1.2.1	Corneometry	20
1.2.2	Fluorescent Confocal Microscopy:	20
1.2.3	Photodynamic Fluorescent Spectroscopy.	21
1.2.4	Multispectral Optoacoustic Tomography (MSOT)	22
1.2.5	Bioimpedance for skin cancer	22
1.3	Motives	23
1.4	Aims	24
1.5	Objectives	24
1.6	Novelty	24
1.6	Thesis Organisation	25
1.7	List of Publications.	27
Chapter 2		28
Tissue I	mpedance: Exploring the Characteristics of Biological Tissues	28
2.1	Electrical Equivalent circuit of Human Skin.	29
2.2	Frequency dependency of biological tissue electrical properties	30
2.2.1	Tissue Anisotropy.	31
2.3	Biological tissue impedance model and model equation	33
2.3	Impedance Measurements	34
2.4	Interface Impedance	34
2.5	Electrode configuration	36
2.5.1	Bipolar configurations	36
2.6	Electrode design	39
2.6.1	Interdigitated Electrodes	40
2.6.2	Spiral Shape Electrodes	41
2.6.3	Concentric Electrodes.	42
2.7	Electrode Placement	44

2.8	Current profiling of equivalent circuit model of skin Tissue.	44
2.10	Conclusion on Chapter 2.	47
Chapte	r 3	48
	odal Experimental Assessment of Skin Hydration using Bioimpedance and Optical sensi	_
3.1	Design and development of Bioimpedance measurement system	
3.2	Design and Development of the Optical Sensor.	
3.3	Ex_vivo measurements using Bioimpedance and Optics	
3.4	In-Vivo Experiment.	
3.5	Conclusion on Chapter 3.	
•	r 4	
	npedance instrumentation (Drive Circuit)	
4.:	` ,	
4.2		
4.3		
4.4		
4.5	,	
4.	, , ,	
4.8	•	
-	r 5	
	ts of the systematic sources of errors on the measurement accuracy of the bioimpedanc	
	surement system.	
5.:		
5.2		
5.4	,	
5.5	, , , , ,	
5.0	6 Magnitude and Phase detection system and analysis	103
5.	7 Systematic errors of Bioimpedance measurement system	105
5.8	•	
5.	7.1. Effects of IA phase errors on the MP measurements of the systems	106
5.7	7.2. Effects of IA dc offsets errors on the MP measurements of the systems	111
5.	7.3. Effects of inter-demodulation phase shift errors of SD system	115
5.7	7.4. Effects of Aperture delay error of the S/H circuit of SS system	118
5.8	Multifrequency Measurements with the three (SD, MP, SS) bioimpedance systems.	.122
5.9	9 Comparing the Systems response to input step change	126
5.	10 Discussion on the System Comparison	127

5.10	Conclusion on chapter 5	129
Chapter	5	130
Pha	se Optimisation for SD system	130
6.2	The reference sinusoidal signal (V _{in}) Generation	133
6.3	PECSD Circuit diagram and analysis.	136
6.4	Effects of sensing resistor (Rsense) on the accuracy of the signal	139
6.5	Effects of common mode offset voltage of IA on the accuracy of the PECSD	141
6.6	Phase detector lead and lag phase pulses (from the implemented hardware)	144
6.8	PECSD Experimental Results.	146
6.10	Analysing PECSD performance through simulations	154
6.11	Conclusion on Chapter 6	155
Chapter :	7	156
Adapt	ve Howland Current Source	156
7.1	Inaccuracies In Variants of Howland Current Source (HCS)	156
7.2	Higher bandwidth requirements in Bioimpedance measurements	157
7.3	Automatic gain control (AGC) architecture	157
7.4	Functional block diagram of the system Design	158
7.5	Circuit design.	160
7.7	ACHS Tracking Speed	171
7.8	Noise analysis of ACHS and MEHCS	172
7.9	Effects of AHCS feedback resistors Tolerance on circuit performance	175
7.11	Conclusion on chapter 7	178
Chapter 8	3	179
Assess	ment on the integrity of Blood cells using ACHS	179
8.1	Electrode Design.	180
8.2	Blood Sample	181
8.3	Experimental Procedure	181
8.4	Biological experimental result analysis	182
8.5	Conclusion on chapter 8	183
Chapter 9	9	185
Conclusio	on on thesis.	185
9.1 Fu	ıture Work	187
Referenc	es	188
<u>Appendi</u>	c:Circuit Simulation and PCB Schematics and Code	199
		100

List of Figures.

Figure 2. 1	Skin Anatomy, showing the various layers of the skin adapted from [44]	. 28
Figure 2. 2	A detailed electrical equivalent circuit of skin, adopted from [44], [48]	. 29
	Ideal slab of a biological tissue where A is tissue thickness, σ is the conductivity and εr	
the relative	permittivity[51]	. 30
Figure 2. 4	The Basic equivalent circuit of the slab of tissue represented with a resistor in parallel	to
-	or. (Image adapted from [3])	
Figure 2. 5	Dispersion in Tissues and relative pernittivity as a function of frequency adapted from	
	Diagram illustrating the biological cell model[55]	
•	Fricke model of biological tissue with equivalent resistances [56]	
J	Stern electrode/electrolyte interface impedance model adopted from[47]	
_	Equivalent circuit model of electrode/electrolyte interface[62]	
_	A bipolar electrode configuration set-up illustrating the electrode / electrolyte interface.	
_		
•	L A tetrapolar electrode configuration set-up illustrating the electrode / electrolyte	
_	npedance	. 38
	2 Interdigitated electrode configurations showing (a) electrode configuration and (b) the	
•	circuit[66]	
•	Spiral electrode configuration showing (a) electrode configuration and (b) the	
_	circuit model [66][62]	.41
•	Concentric electrodes.	
_	5 Square electrodes [69]	
_	5. Spice simulation of Current profiling of equivalent circuit model of skin Tissue	
_	7 Electrode Placement Configuration and Possible Electrode Shapes for a Bioimpedanc	
Application	ı[23] [66][72][74]	.46
Figure 3. 1	Bioimpedance Measuring system based on Magnitude detection[58]	. 49
Figure 3. 2k	The experimental set -up for multimodal experimental skin assessment [81]	.51
Figure 3. 3	Optical wearable sensor connected to the ZenPPG processing system	. 52
Figure 3. 4	Impedance magnitude vs. time for bipolar electrode configuration	.54
Figure 3. 5	Impedance magnitude vs. time for tetrapolar electrode configuration	.54
Figure 3. 6	Percentage increase in impedance magnitude for bipolar electrode configuration	. 55
Figure 3. 7	Percentage increase in impedance magnitude for tetrapolar electrode configuration	.55
Figure 3.8	Raw voltage output from optical sensor for selected LED wavelengths	.56
Figure 3. 9	Corneometer output readings for porcine skin sample (a) before and (b) after the ex v	ivo
desorption	experiment	.57
Figure 3. 10	Comparison of outputs from all techniques for in vivo experiment. Bioimpedance	
measureme	ent here is Tetrapolar	.58
Figure 4. 1	equivalent circuit model of VCCS [92]	.59
Figure 4. 2	Basic Howland current source (BHCS) [92].	.60
Figure 4. 3	Enhanced Howland current source (EHCS) [92]	62
_	Current output of BHCS for varying resistive Loads.	
	Current output of EHCS for varying resistive Loads	
-	Block diagram of VCCS with the parasitic capacitances C1, C2 and C3 C3 [1]	
Figure 4. 7	Buffered feedback topology for HCS [98]	.68

Figure 4. 8 EHCS with negative impedance converter [98]	69
Figure 4. 9 Mirrored Enhanced Howland Current Source (MEHCS) [97]	70
Figure 4. 10 EHCS with GIC for output impedance improvement [98]	71
Figure 4. 11 Output impedances of EHCS and the corresponding variants	72
Figure 4. 12 schematic diagram of instrumentation amplifier	73
Figure 4. 13 Schematic diagram of instrumentation amplifier with common mode inputs	74
Figure 4. 14 Effects of electrode impedance on common mode signals rejection of the IA	75
Figure 4. 15 Schematic diagram of instrumentation amplifier showing input and output parasition	С
capacitances	76
Figure 4. 16 System-level block diagram of the three designs: SD, MP and SS systems [58], [59]	77
Figure 4. 17 Synchronous demodulation system.	78
Figure 4. 18 Demodulation signals and V _{meas} as a function of Time.	80
Figure 4. 19 Multiplier and low pass filter outputs for 5V peak of Vmeas at no phase shift	81
Figure 4. 20 Synchronous Sampling system implemented in this work	82
Figure 4. 21. SS system graphs showing the peak detector pulse, the sampled Vmeas data and t	he
Vmeas for a purely resistive load of $5k\Omega$ for an injected current of 1mA	84
Figure 4. 22 Sampling pulses of synchronous sampling at 100kHz	85
Figure 4. 23 Magnitude and Phase Bioimpedance system implemented in this work	86
Figure 4. 24 Magnitude and phase measurement result measurement stages of measurements	at
1kHz	87
Figure 4. 25 Summarized systematic and topography related sources of errors in Bioimpedance	
measurement system[39], [43], [102]	88
Figure 4. 26 PCB photographs of the MECHS and SD, SS, and MP systems designed in and explain	ned
in this chapter	89
Figure 5. 1 Categories of bioimpedance applications in relation to the impedimetric system	
specifications required.	
Figure 5. 2 Simulink model developed for the comparative assessment of the three impedimetric	
topologies.	
Figure 5. 3 Showing the details of (5.3a) current injection, and (5.3b) load measurement stages of	
Bioimpedance system Simulink block	
Figure 5. 4 Details of (5.4a) the injected current and measured voltage and (5.4b) Magnitude and	
phase graph for $5K\Omega//50nF$ simulation graph of Simulink.	
Figure 5. 5 Synchronous detection system showing (5.5a) the system block diagram (5.5b) The r	
and Imaginary to Magnitude and phase block diagram	
Figure 5. 6 Illustrating the measurement stages for SD system showing (5.6a) the multiplier out	puts
and (5.6b) Real and imaginary measurements results and their converted magnitude and phase	
values	
Figure 5. 7 Synchronous Sampling system Simulink blocks showing (5.7a) SS system block diagram	
(5.7ai) The peak amplitude pulse generation block, (5.7aii) Zero crossing detection pulse and (5.7aii)	
Error injection block	
Figure 5. 8 Error values for SS system trigger pulses.	
Figure 5. 9 SS Peak sampling pulse derivation graphs.	
Figure 5. 10 SS Peak sampling pulse derivation graphs.	101
Figure 5. 11 SS systems showing the result of Real, Imaginary, Magnitude and Phase Impedance	
values for RC load of 5K Ω 50nF at 100Hz for an injected current of 1mA	
Figure 5. 12 MP system showing (5.12a) the system block diagram and (5.12ax) The polarity and	
phase detection block diagram	103

Figure 5. 13 Illustrates the measurement stages of the MP system showing (5.13a) Detected ph	ase
with MP system, (5.13b) Duty cycle and (5.13c) Magnitude and Phase measurement	104
Figure 5. 14 Error selection and injection block.	106
Figure 5. 15 Introduced phase errors at the output of sensing block	107
Figure 5. 16 Effects of IA phase errors on the Impedance magnitude results of all the system	107
Figure 5. 17 Effects of IA phase errors on the Impedance phase results of the all the system	108
Figure 5. 18 Relative percentage impedance magnitude errors of R and RC loads due to added I	Α
phase shifts errors.	108
Figure 5. 19 Relative and absolute impedance phase errors of R and RC loads due to added IA p	hase
shifts	109
Figure 5. 20 Introduced dc offsets of the sense circuits	112
Figure 5. 21 Effects of IA offset errors on the Impedance magnitude results of the all the system	n.113
Figure 5. 22 Effects of IA offset errors on the Impedance phase results of the all the system	113
Figure 5. 23 Relative percentage impedance magnitude errors of R and RC loads due to added IA	١.
offset errors.	114
Figure 5. 24 Relative and absolute impedance phase errors of R and RC loads due to added IA o	ffset
errors	114
Figure 5. 25 Effects of SD inter-demodulation phase errors on the Impedance magnitude results	of
SD system	
Figure 5. 26 Effects of SD inter-demodulation phase errors on the Impedance phase results of SI	D
system	116
Figure 5. 27 Relative percentage impedance magnitude errors of R and RC loads due to added S	D
inter-demodulation phase errors.	117
Figure 5. 28 Relative and absolute impedance phase errors of R and RC loads due to added SD i	nter-
demodulation phase errors.	117
Figure 5. 29 Introduced Aperture delays errors.	118
Figure 5. 30 Effects of SS aperture errors on the Impedance magnitude results of the all the syst	:em
	119
Figure 5. 31 Effects of SS aperture errors on the Impedance phase results of the all the system	119
Figure 5. 32 Relative percentage impedance magnitude errors of R and RC loads due to added S	SS
aperture errors	120
Figure 5. 33 Relative and absolute impedance phase errors of R and RC loads due to added SS	
aperture errors	120
Figure 5. 34 Relative percentage impedance magnitude errors for R and RC loads due to added	SS
aperture (zero crossing) errors.	121
Figure 5. 35 Relative and absolute impedance phase errors for R and RC loads due to added SS	
aperture (zero crossing) errors.	122
Figure 5. 36 Diagram of circuit used for multifrequency experiment.	123
Figure 5. 37 Summed signals at the output of the instrumentation amplifier	124
Figure 5. 38 Impedance magnitude of the three bioimpedance systems with a summed input	124
Figure 5. 39 Comparing the response of the systems in response to step change	127
Figure 6. 1 Block diagram of the automatic Phase Error Compensated Synchronous Demodulati	on
system (PECSD).	
Figure 6. 2 Frequency Synthesizer Circuit designed for this project	
Figure 6. 3 PCB photo of Frequency synthesizer	
Figure 6. 4 I&Q generated signals from the digital synthesizer circuit	

Figure 6. 12 Input and output of the Instrumentation amplifier with a common mode offset vo	_
of 12VDC.	142
Figure 6. 13 Output of the comparator with and without the common mode offset voltage of L	۹. 142
Figure 6. 14 CMRR of the measurement side IA.	143
Figure 6. 15 showing (a) phase pulses due to V_{in} leading V_{sense} and (b) phase pulses due to V_{in} leading V_{sense} and (c) phase pulses due to V_{in} leading V_{sense} and (d) phase pulses due to V_{in} leading V_{sense} and (e) phase pulses due to V_{in} leading V_{sense} and V_{in} leading V_{in} leadi	gging
sense by 50deg	144
Figure 6. 16 Set up for Experiment with PECSD	
Figure 6. 17 Output current MECHS for a resistive load of 1-5KΩ	146
Figure 6. 18 showing (a) phase shift Vsense and V _{in} before and (b) after phase compensation at	
300kHz	
Figure 6. 19 V{RE} of the low pass filter as a function of RC load for (a) 1kHz (b) 10kHz (c) 100kHz	
200kHz (e) 300kHz	
Figure 6. 20 V{IM} of the low pass filter as a function of RC load for (a) 1kHz (b) 10kHz (c) 100kl	
200kHz (e) 300kHz	149
Figure 6. 21 Impedance magnitude and phase for RC loads (1 k Ω ,244pF and 3 k Ω , 33.5 nF) as a	
function of frequency	
Figure 6. 22 showing (a) Impedance magnitude percentage phase error and (b) impedance phase	
percentage errors for RC loads.	
Figure 6. 23 (a) Impedance magnitude vs. frequency for resistive loads. (b) Impedance magnitude	
percentage error vs. frequency for resistive loads	152
Figure 6. 24 Impedance phase errors for compensated and uncompensated SD systems as a	
function of frequency for resistive loads.	
Figure 6. 25 System step response for SD system with (a) and without (b) compensation	
Figure 6. 26 Relative percentage errors (6.26a) and absolute phase errors (6.26) of the R and R	
load before and after compensation.	154
Figure 7.4. ACC maters for available stabilization [422]	457
Figure 7. 1 AGC system for amplitude stabilisation. [133]	
Figure 7. 2 Functional block diagram of the AHCS.	
Figure 7. 3 Circuit Diagram of AHCS	
Figure 7. 4 Photograph of the AHCS circuit board with the main stages labelled	
Figure 7. 5 Raw data: input and output voltages of the ACHS in open and closed loop for a 2 kg	
load	
Figure 7. 6 Output current vs. frequency for various loads for MEHCS and AHCS	
Figure 7. 7 (a) Percentage errors of 1 mA output current for MEHCS and AHCS for all loads at al	
frequencies and (b) scaled to 5% Figure 7. 8 Measured output voltage of MEHCS and AHCS compared to the ideal result as a	167
	160
function of load at frequencies from 1 kHz to 3 MHz for lout=1mA.	
Figure 7. 9 Output current of 100 μA as a function of frequencies for both MEHCS and AHCS	
Figure 7. 10 (a) Percentage errors of 100 μA output current for MEHCS and AHCS and (b) scaled low error values (up to 5%)	
, ,	169
Figure 7. 11 (a) Equivalent MEHCS output impedance circuit and (b) The Measurement	171
configuration	
Figure 7. 12 Output Impedance as a function of frequency for MEHCS and AHCS	
Figure 7. 13 AHCS settling time at its highest operating frequency of 3MHz	
Figure 7. 14 Noise Analysis of single-ended Howland current source	
Figure 7. 15 Simulation: Voltage noise across different loads for single-ended MEHCS	
Figure 7. 16 Effects on I_{out} for lowering R_{h1-4} from (a) &(c) 100 k Ω to (b)& (d) 5 k Ω in single-end MEHCS and AHCS.	
IVIERUS ANU ARUS	エノコ

-	rcentage errors of ACHS at extreme temperature variations (a) at -20° and (b) at 40°.
	nulation: AHCS output current vs. frequency for RC loads (applied $I_{out} = 1 \text{ mA}$) 176
Figure 8. 2 PCB Figure 8. 3 COM Figure 8. 4 Micr	ematic block diagram interrogation of blood cells using ACHS
List of Table	? S
Table 5. 1 Applie	d cancer incident in 36 countries [22]
Table 6. 2 Imped synchronous dete	register clock signals and the subsequent output of the dividing counter
Table 6. 3 Impe synchronous dete = 1, AV_meas =1.	dance output variables for both phase compensated and uncompensated ection system. R Load = $1k\Omega$, RC Load = $1k\Omega+244$ pF. Rsense = $1k\Omega$. IA gains: AVsense lout = 1 mA. Vin = 1 V
= 10, A _{V_meas} = 1. N Table 7. 2 Calcu variations	CS and AHCS measured peak outputs for Load = $2 \text{ K}\Omega$. R_{sense} = 100Ω . IA gains: $A_{\text{V_sense}}$ Nominal I_{out} = 1 mA . V_{in} = 1 V
TUDIC 7.3 IVIAIII	Teatures of Arres and comparison with other designs

Glossary of terms

SD Synchronous detection

MP Magnitude and Phase

SS Synchronous Sampling

VCCS Voltage controlled Current Source

IA Instrumentation Amplifier

PECSD Phase Error Correction for SD System

BHCS Basic Howland Current Source

EHCS Enhanced Howland Current Source

MEHCS Mirrored Enhanced Howland Current Source

S/H Sample and Hold

 E_{i1} + Injection electrode

*E*_{i2} - Injection electrode

 E_{m1} + Measurement electrode

 E_{m2} - Measurement electrode

Vdemod_0 Reference 0-degree demodulation signal

Phase-det-pulse Type II Phase detector pulse

NC No compensation

TCR Temperature Coefficient of Resistance

 R_{ref} This is the reference resistance, measured at a specific reference temperature T_{ref}

 T_{ref} Resistor reference temperature

 A_{vfb} The integrator DC output expressed as unitless gain

 I_{leak} Leakage current through the output impedance of the current source

 I_{out} Total output current by the VCCS

 V_{comp} Output of the comparator as part

 V_{track} Output of the Integrator

 G_{COR} AGC gain

 I_{outER} Erroneous output current of the current source.

AGC Automatic gain control

VGA Variable gain Amplifier

Z_L Load Impedance

C_m Membrane Capacitance

α Alpha dispersion

β Beta dispersion

γ Gamma dispersion

 Z_o Output Impedance

 σ_{sl} Electrolyte conductivity

K_{cell} Cell Constant

 Z_{Tb} Output Impedance of EHCS in a bipolar electrode configuration.

 Z_{Tt} Output Impedance of EHCS in a tetrapolar electrode configuration.

V{RE} Voltage output of the lock in amplifier of the Real Impedance for SD system

V{IM} Voltage output of the lock in amplifier of the Imaginary Impedance for SD system

 $Re\{Z\}$ Real Impedance of the synchronous detection system

 $IM\{Z\}$ Imaginary Impedance of the synchronous detection system

 $V\{RE\}_{cc}$ Sampled Voltage Output S/H circuit for Real Impedance in SS system

 $V\{IM\}_{SS}$ Sampled Voltage Output S/H circuit for Imaginary Impedance SS system

 $\{RE\}_{ss}$ Real Impedance of the SS system

 $\{IM\}_{ss}$ Imaginary Impedance of the SS system

 V_{ia} Voltage input of the all-pass filter

 V_{oa} Voltage output of the all-Pass filter

CMRR Common mode rejection ratio

 A_D Differential gain

ACM Common Mode Gain

ACHS Adaptive Howland current source

R_{sense} Sense resistor of the ACHS

Vsense Measured voltage of sensing resistor R_{sense}

Vmeas Measured output voltage of the of the load impedance for ACHS and MECHS

VGA Variable gain amplifier.

 V_{in} Reference sine wave signal for the VCCS

 $+V_{settle}$, Output of the comparator when $V_{sense} < V_{in}$

 $-V_{settle.}$ Output of the comparator when $V_{sense} > V_{in}$

 $V_{osc}(t)$ Output of the comparator when $V_{sense} = V_{in}$

V+ 15VDC

V- -15VDC

VDD +5VDC

VEE -5VDC

Chapter 1.

Introduction:

Bioelectrical impedance measurements (BIM) involve the application of low-intensity alternating current (AC) typically ≤ 0.5 mA for low frequency tissue applications (ideally below 5kHz) [1], and ≤ 1 mA for higher frequency tissue applications [2]. This current induces a potential difference across the tissue[3][4][5][6]. Consequently, bioelectrical impedance values offer crucial insights into the physiological and pathological conditions of biological cells and tissues [4][7][8][9]. This technique is widely adopted in biomedical applications such as Impedance myography, tomography, impedance for body composition and many other physiological assessment and tissue characterization [10][11][12].

Amongst many clinical applications, one prominent application of BIM is in the area of skin health monitoring. Monitoring skin health not only enhances quality of life and reduces healthcare costs, but it can also be life-saving [3] [4].

Among various skin health issues, skin hydration is one of the most common concerns[13]. Untreated dry skin can lead to conditions such as eczema and infections, and it may serve as a prognostic factor for more serious conditions, including diabetes, kidney problems, and, in extreme cases, cancer[14], [15], [16], [17].

According to statistics from the United Kingdom's National Eczema Society, 1 in 5 children and 1 in 10 adults in the UK suffer from eczema[18][19]. In the United States, an article by WebMD reports that around 9.6 million children under the age of 18 have eczema, with one-third experiencing moderate to severe forms of the condition[20].

At the more severe end of the spectrum, involving skin cancer, data from Cancer Research UK indicates approximately 17,537 new cases of melanoma skin cancer annually between 2017 and 2020, with around 2,341 deaths each year in the UK[21]. On a global scale, GLOBOCAN 2020 as shown in Table 1.1 estimated the incidence of skin cancer across 185 countries, reporting 173,844 cases of melanoma and 722,384 cases of non-melanoma skin cancer in 2020[22].

These statistics emphasize the critical importance of early and effective skin health monitoring to prevent severe conditions and improve health outcomes. To detect skin conditions, patients typically rely on visual inspection of the affected area and consult a dermatologist, who primarily examines the skin visually. The effectiveness of this approach depends heavily on the dermatologist's skill. In more severe cases, a biopsy may be taken, which is an invasive procedure that causes discomfort and is often performed only after the disease has already progressed.

The use of instruments allows for the detection of signs that may not be visible or recognizable through sensory perception alone. This is where a portable skin health monitor becomes highly valuable. Many diseases, including skin cancer, can have a preclinical phase

or enter periods of remission, making early detection and ongoing monitoring crucial for effective therapy and prevention[23]. The ability to recognize or track diseases in these early stages could significantly improve outcomes, especially in detecting precursors to conditions like melanoma[22], [23].

Home health monitoring devices provide numerous advantages. They enable early detection of health issues, allowing for timely interventions and prevention of complications. These devices also facilitate better communication between patients and healthcare providers, leading to more personalized care plans. Additionally, they can reduce healthcare costs by preventing unnecessary hospitalizations and emergency room visits. By offering convenience and flexibility, home monitoring devices empower individuals to take control of their health and improve their overall well-being.

Although non-invasive instruments for monitoring skin health exist, they are typically limited to specialized laboratories due to their complexity, need for trained operators, and constraints related to cost, functionality, or practicality. This highlights the need for a portable, user-friendly device that enables patients to monitor their skin health at home, minimizing operator dependency and requiring little to no specialized training.

While this Thesis will be focused on developing an accurate, portable and home instrument for skin health monitoring, Chapter 1 will review non-invasive methods for monitoring skin health, particularly focusing on skin hydration and the detection of extreme skin health conditions such as skin cancer

	INCIDENCE							MORTALITY					
	MALES			FEMALES			MALES	MALES			S		
Cancer Site	Cases	Age standard ized Rate (world)	Cumula tive Risk, Ages, 0- 74yrs, %	Cases	Age standar dized Rate (world)	Cumulat ive Risk, Ages, 0- 74yrs, %	Cases	Age standar dized Rate (world)	Cumulat ive Risk, Ages, 0- 74yrs, %	Cases	Age standardize d Rate (world)	Cumulative Risk, Ages, 0-74yrs, %	
Lip, oral Cavity	264,211	6	0.68	113,502	2.3	0.26	125,022	2.8	0.32	52,735	1	0.12	
Salivary glands	29,694	0.7	0.07	23,889	0.5	0.05	13,353	0.3	0.03	9425	0.2	0.02	
Oropharynx	79,045	1.8	0.22	19,367	0.4	0.05	39,590	0.9	0.9	8553	0.2	0.02	
Nasopharyn x	96,371	2.2	0.24	36,983	0.8	0.09	58,094	1.3	1.3	21,914	0.5	0.05	
Hypopharyn x	70,254	1.6	0.19	14,000	0.3	0.03	32,303	0.7	0.7	6296	0.1	0.01	
Esophagus	418,350	9.3	1.15	185,750	3.6	0.44	374,313	8.3	8.3	169,76 3	3.2	0.38	
Stomach	719,523	15.8	1.87	369,580	7	0.79	502,788	11	11	266,00 5	4.9	0.55	
Colon	600,896	13.1	1.49	547,619	10	1.12	302,117	6.4	6.4	274,74 1	4.6	0.45	
Rectum	443,358	9.8	1.18	288,852	5.6	0.65	204,104	4.4	4.4	134,91 8	2.4	0.26	
Anus	21,706	0.5	0.06	29,159	0.6	0.07	9,416	0.2	0.2	9,877	0.2	0.02	
Liver	632,320	14.1	1.65	275,357	5.2	0.6	577,522	12.9	12.9	252,65 8	4.8	0.55	
Gallbladder	41,062	0.9	0.1	74,887	1.4	0.16	30,265	0.7	0.7	54,430	1	0.11	
Pancreas	262,865	5.7	0.66	232,908	4.1	0.45	246,840	5.3	0.62	219,16 3	3.8	0.41	
Larynx	160,265	3.6	0.45	24,350	0.5	0.06	85,351	1.9	0.23	14,489	0.3	0.03	
Lung	1,435,94 3	31.5	3.78	770,828	14.6	1.77	1,188,6 79	25.9	3.08	607,46 5	11.2	1.34	

Table continued on page 19

Melanoma of skin	173,844	3.8	0.42	150,791	3	0.33	32,385	0.7	0.07	24,658	0.4	0.05
Nonmelano ma of Skin	22,348	15.1	1.4	475,725	7.9	0.75	37,596	0.8	0.07	26,135	0.4	0.04
Mesothelio ma	21,560	0.5	0.05	9,310	0.2	0.02	18,681	0.4	0.04	7,597	0.1	0.02
Kaposi Sarcoma	23,413	0.5	0.05	10,857	0.3	0.02	9,929	0.2	0.02	5,157	0.1	0.01
Breast				2,261,41 9	47.8	5.2				684,99 6	13.6	1.49
Vulva				45,240	0.9	0.09				17,427	0.3	0.03
Vagina				17,908	0.4	0.04				7,995	0.2	0.02
Cervix uteri				604,127	13.3	1.39				341,83 1	7.3	82
Corpus uteri				417,367	8.7	1.05				97,370	1.8	0.22
Ovary				313,959	6.6	0.73				207,25	4.2	0.49
Penis	36,068	0.8	0.09				13,211	0.3	0.03			
Prostrate	1,414,25 9	30.7	3.86				375,304	7.7	0.63			

Table 1. 1 World cancer incident in 36 countries [22].

1.2 Skin health monitoring assessment methods.

1.2.1 Corneometry

Corneometer is currently the gold standard for measuring skin hydration[24]. Corneometry measures variations of the capacitance of the stratum corneum by means of instruments that translate the biophysical data into units of skin hydration. The Corneometer operates based on the principle of capacitance measurement, which relates to the electrical properties of the skin. The skin's stratum corneum behaves like a dielectric material. Water, being a highly polar molecule, increases the capacitance of the skin. When the skin is hydrated, the water content in the stratum corneum causes a measurable change in capacitance which is directly proportional to the skin's moisture level[24], [25], [26]. The capacitance values measured by the device are converted into units that represent the level of skin hydration. These units provide a relative scale to assess how dry or hydrated the skin is. A higher capacitance indicates higher water content in the skin, while a lower capacitance indicates dry or dehydrated skin.

While skin hydration measurements with Corneometer is non-invasive and painless, it suffers from several limitations.

- a) **Sensitivity to pressure**: Since the electrodes are always spring loaded, results can be affected by how much pressure is applied when the probe is placed on the skin. Uneven or excessive pressure may cause inaccurate readings. As such, results may vary from one operator to another[27].
- b) *Lack of profiling*: Measurement result with the Corneometer is a hydration value for a constant depth of about 30µm[28]. Consequently, hydration changes at varying skin depths which could reveal critical clinical information and diagnostic features of skin conditions may not be captured by Corneometer measurements.

1.2.2 Fluorescent Confocal Microscopy:

Confocal microscopy, utilizing near-infrared lasers in the range of 800–850 nm, has been designed to enhance the visualization of skin structures up to a depth of 200–250 μ m. However, this maximum depth is restricted by light scattering at the surface of the stratum corneum and the limited penetration of ultraviolet light. To further improve contrast within skin tissue, the use of external fluorescent markers has been adopted [29].

As reported in [29], the clinical application of in vivo fluorescence confocal microscopy for the non-invasive diagnosis and therapeutic monitoring of non-melanoma skin cancer was explored. The researchers evaluated the clinical utility of a fluorescent confocal laser scanning microscope (FLSM), which used an argon-ion laser at a wavelength of 488 nm, for systematically assessing normal and diseased skin in vivo, correlating the findings with routine histology. The results revealed characteristic features of basal cell carcinoma, such as basal

cell nests, which were clearly visible under fluorescent confocal microscopy and were confirmed through histological analysis.

Despite the fact that this method shows promising capabilities and high sensitivity to cancer cell detection, there are also some limitations and some of which are:

- a) **Limited Penetration Depth**: The typical wavelength of around 800 nm provides good resolution but limits penetration depth. Resolution decreases at higher wavelengths, making this approach less suitable for detecting deeper tumours [14].
- Complex Instrumentation: The equipment required for this procedure is highly complex and necessitates specialized training for proper operation and interpretation of results.
- c) **Slightly Invasive**: To enhance the accuracy of distinguishing between cancerous and non-cancerous cells, an intraepidermal injection of fluorescein may be used. This can cause discomfort or pain for patients [29][14].
- d) **Operator-Dependent Errors**: The accuracy of this method is highly dependent on the skill and expertise of the operator, which can introduce variability in the results.

1.2.3 Photodynamic Fluorescent Spectroscopy.

Photodynamic fluorescent spectroscopy, involves the introduction of a photosensitive marker such as 5-aminolevulinic acid (ALA), which is metabolized into protoporphyrin IX (PpIX) through chemical reactions in the skin, followed by light exposure. PpIX is absorbed by healthy cells but accumulates in tumor cells. In basal cell carcinoma, the most common form of cancer worldwide, exposure to ultraviolet light causes the cancerous areas to exhibit a distinctive coral-red fluorescence, which can be easily differentiated from the lower fluorescence of surrounding normal tissue[30].

In addition to its diagnostic use, this method can also be employed to destroy cancer cells. Photosensitizers, which are inactive on their own, are activated when light of a specific wavelength is applied to the treated skin. Upon activation, the photosensitizer generates excited oxygen molecules within the damaged cells. These molecules selectively kill the abnormal cells, affecting only the skin areas exposed to the light source. This leads to localized inflammation, which typically heals after the treatment, restoring normal skin health[31]. Challenges with this method are:

a) **Post-Procedure Effects**: Photosensitizers like 5-ALA have a low penetration rate, necessitating the application of high concentrations. After treatment, photosensitization remains active for at least 32 hours. During this period, exposure to ambient light may lead to severe phototoxic reactions such as swelling, erythema,

- and scaling. Therefore, patients are advised to avoid bright light and sun exposure for 24–48 hours post-treatment [31].
- b) Inaccuracies and False-Negative Fluorescence: False-negative results may occur due to interference from factors such as the high fluorescence of surrounding hair, making this method unsuitable for examining skin lesions in densely hairy areas. Additionally, interference from dermal infections, viral warts, and inflammatory diseases may compromise the accuracy of the fluorescence [31].
- c) **Operator-Dependent Errors**: The accuracy of this method is highly dependent on the skill and technical expertise of the operator, which can lead to variability in results.

1.2.4 Multispectral Optoacoustic Tomography (MSOT).

An imaging technique that produces high-resolution optical images in scattering media, such as biological tissues. MSOT works by illuminating tissue with light pulses, typically lasting 1–100 nanoseconds[32], [33]. These light pulses are absorbed by the tissue, leading to thermo-elastic expansion caused by slight temperature changes, a process known as the optoacoustic or photoacoustic effect. The resulting temperature changes generate sound waves, which travel to the skin's surface. By detecting these sound waves at multiple locations, detailed images of the underlying tissues can be reconstructed [32], [33].

While MSOT has shown promising results in detecting skin cancer at depths greater than 2mm[34], several challenges still hinder its widespread clinical use for skin cancer detection. These challenges include technical complexities, limited availability, and the need for further refinement to improve accuracy and reliability. Some of the challenges are:

- a) Overestimation of Melanoma Thickness Due to Lymphocytic Infiltration: Lymphocytic infiltration, a benign accumulation of lymph cells in the skin commonly associated with basal cell carcinoma and malignant melanoma, can create hypoechoic extensions. This may lead to an overestimation of tumour thickness on ultrasound[17].
- b) **Cost**: High-resolution ultrasound equipment is expensive, which limits its accessibility for widespread clinical use.
- c) **Operator Dependency**: The accuracy of this method is highly dependent on the operator's skill and technical expertise, meaning that results can vary significantly based on the operator's proficiency [32], [33].

1.2.5 Bioimpedance for skin cancer

Bioimpedance technique has proven to be another important non-invasive method for the detection of skin cancer. Impaired tissue sites due to cancer characteristically lose the

integrity of the cell[35]. As a result, the phase shift caused by the cell membrane is compromised, with values significantly lower than those observed in normal reference non-impaired sites. Also, the altered cellular structure and increased vascularization associated with cancer result in distinctively lower impedance magnitude compared to a reference non-cancerous site[36], [37]. Studies have shown that malignant melanoma can be differentiated from benign nevi with approximately 75% specificity at 100% sensitivity [23].

While various methods for skin cancer detection, such as thermal imaging, exist, they come with their own set of challenges. Bioimpedance techniques offers unique advantages, It is user-friendly, as it does not require specialized training, thereby reducing operator dependency errors. Additionally, it is relatively affordable and can be adapted for point of care devices[23]. Depending on the instrumentation, bioimpedance demonstrates relatively high sensitivity in detecting skin cancers. However, the accuracy of bioimpedance systems can decline across different loads and frequencies due to systemic and instrumentation errors, limiting its broader clinical applicability[38]. Nevertheless, research suggests that advancements in instrumentation and technology could significantly enhance the diagnostic accuracy of bioimpedance systems for skin cancer detection[40], [41].

Overall, it can be claimed that there is a clear need for a portable instrument that will monitor skin health outside specialised settings and without the need for a trained operator. An instrument that will exhibit appropriate accuracy to inform the patient / user promptly about the onset of the change of their skin condition. Among the aforementioned technologies, bioimpedance emerges as the most promising candidate for non-invasive skin diagnosis, owing to the fact that it can be portably adapted for home, requires little or no special skills operate and can scan deeper tissues layers[17], [23], [25]. However conventional instrumentation cannot offer the desired performance, due to systematic errors in the architectures used in the most widely used designs[38][41].

1.3 Motives

There is a need for enhanced bioimpedance circuit architectures in skin health monitoring, driven by the need for more accurate, reliable, and comprehensive assessments. To achieve this, several key performance parameters must be optimized. One of the primary parameters is the bandwidth of the injection circuitry. This plays a crucial role in determining the depth of tissue penetration during scanning, thereby enabling a more thorough evaluation of skin layers and conditions[42]. It has been reported that higher bandwidth allows for more detailed tissue profiling and, as such would lead to better diagnostic capabilities[23].

Another critical parameter is the phase error on the injection side, which directly affects the accuracy of phase measurements in bioimpedance analysis. Eliminating this error is essential for enhancing the precision of tissue characterization and ensuring that the collected data

accurately reflects the physiological properties of the skin particularly in bioimpedance skin applications where phase difference between the injected current and measured voltage serves as a key diagnostic factor[43]. Optimizing these parameters will ultimately lead to bioimpedance systems that offer improved performance, facilitating better diagnostics and interventions in skin health assessment.

1.4 Aims

To design, analyse, and test novel bioimpedance circuits that address and overcome systematic sources of error, and thereby enhance diagnostic accuracy in skin health assessments.

1.5 Objectives

- To experimentally assess skin tissues using a non-optimized bioimpedance circuit, compare bioimpedance methods with optical techniques and standardized skin hydration measurements (using a Corneometer), and identify gaps for improving measurement accuracy.
- To analyse the sources of error in bioimpedance systems and mathematically quantify their impact on measurement accuracy.
- To conduct a system-level simulation of common bioimpedance topologies, introducing the sources of errors and illustrating how various sources of error affect the measurement accuracy in each system.
- To design and test a novel circuit for phase error correction in bioimpedance systems.
- To design and test a novel circuit aimed at achieving a wider bandwidth for improved system performance.
- To also experimentally investigate the performance of the improved system in assessing the integrity of cells by measuring the impedance of lysed and unlysed blood samples.

1.6 Novelty

The novelty of this project lies in its multi-faceted approach to optimising bioimpedance systems for skin health monitoring and cell integrity assessment which represents a key diagnostic marker in skin cancer evaluation, focusing on aspects that have not been fully explored or improved in existing systems. Specifically, the key innovative elements include:

- The author conducted a multimodal assessment of skin hydration using a standard magnitude-only impedance measurement circuit, comparing it with an optical approach against the Corneometer. This assessment identified complementarity in methods and highlighted areas for improving sensitivity and accuracy
- The author did a comprehensive Comparison of Bioimpedance Measurement Techniques: The project proposes a thorough mathematical analysis and simulationbased comparison of existing bioimpedance measurement systems, analysing their sources of error and accuracy in a detailed manner. While many studies focus on the performance of individual bioimpedance systems, this project's comparative approach offers a new perspective that will provide insights into which system is the most suitable for skin health monitoring, particularly for diagnostic applications such as skin cancer detection.
- The author also designed an Error Correction and System Optimization circuitry for synchronous demodulation system (PECSD): A significant novel aspect is the focus on correcting error sources in the selected bioimpedance system, particularly those that affect its phase accuracy, which is a crucial signature in the early detection of skin cancer. Existing bioimpedance systems often overlook phase measurement optimisation, making this project's emphasis on improving phase accuracy a key innovation that could lead to more reliable diagnostic results.
- The author further enhanced the bandwidth of the system injections side for better skin assessment: Another innovative part of this project is the introduction of an automatic gain control (AGC) circuit at the injection side current source, designed to improve the system's bandwidth. Unlike the traditional approach, which focuses on enhancing output impedance at a single frequency, the use of AGC enables broader, more accurate measurements. This addresses a key limitation of current systems, which are typically optimised for a narrow frequency range. The wider bandwidth facilitated by the AGC allows for a more detailed analysis of tissue properties, enabling the collection of comprehensive result about skin health and achieving greater scan depth across impaired tissue sites.
- The author also performed cell integrity measurements using lysed and unlysed blood samples, comparing the measurement accuracy of the optimised system with standard impedance laboratory instruments at relatively high frequencies. This validation demonstrates the efficacy of the optimized system over non-optimized systems in cell integrity assessment and biological sample analysis.

1.6 Thesis Organisation

• **Chapter Two**: This chapter provides an in-depth discussion of the skin and its properties. It includes an analysis of the equivalent circuit model of biological skin,

- with a focus on the electrode configurations used for skin measurements. The chapter also covers interface impedances, electrode design, geometry, and placement.
- **Chapter Three**: This chapter discusses the multimodal assessment of skin hydration, combining optical method and technology with bioimpedance. It examines the strengths and weaknesses of each technique and concludes by highlighting the complementarity of a hybrid approach.
- Chapter Four: This chapter explores the drive and sense circuits in bioimpedance systems. It provides a detailed mathematical analysis of the sources of error in both circuits and introduces three primary bioimpedance systems, which are then analysed mathematically.
- **Chapter Five**: This chapter offers a system-level comparison of the three bioimpedance systems using MATLAB SIMULINK. Systematic and topology-specific errors are identified, simulated, and their impact on measurement accuracy is evaluated and compared.
- **Chapter Six**: This chapter describes the phase error correction circuit developed for this thesis, titled "Phase Error Correction for Synchronous Demodulation System." It explains the design approach, including the underlying concepts and circuit design protocols. The results demonstrate the improvements in measurement accuracy achieved through the phase error correction.
- **Chapter Seven**: This chapter details the design and procedures used to achieve wider bandwidth at the injection side. It discusses bandwidth enhancement techniques, their limitations, and proposes an improved mechanism involving automatic gain control (AGC) feedback. This approach not only ensures wider bandwidth but also enhances the accuracy of the measurements.
- **Chapter Eight**: This chapter demonstrates the use of AHCS in blood cell integrity assessment. It detailed the measurement protocol employing ACHS and a standard Laboratory Impedance analyser, used to profile the integrity of blood cells during lysed and un-lysed conditions. Results showed a good performance and accuracy was over 95% match to the result of impedance analyser.
- Chapter Nine: This chapters concludes the work done and also suggest directions for future work.

1.7 List of Publications.

- I. M. Gidado, I. I. Nwokoye, I. F. Triantis, M. Qassem, and P. A. Kyriacou, "Multi-Modal Spectroscopic Assessment of Skin Hydration," *Sensors*, vol. 24, no. 5, p. 1419, Feb. 2024, doi: 10.3390/s24051419.
- I. I. Nwokoye and I. F. Triantis, "A 3 MHz Low-Error Adaptive Howland Current Source for High-Frequency Bioimpedance Applications," *Sensors*, vol. 24, no. 13, Jul. 2024, doi: 10.3390/s24134357.
- I. I. Nwokoye and I. F. Triantis, "A Phase Error Correction System for Bioimpedance Measurement Circuits," Applied Sciences (Switzerland), vol. 14, no. 12, Jun. 2024, doi: 10.3390/app14125202.
- M. Rabbani, I. Nwokoye, E. Rahman, M. B. Powner, and I. F. Triantis, "A High Frequency Bioimpedance System for Monitoring Haemolysis,".

Chapter 2.

Tissue Impedance: Exploring the Characteristics of Biological Tissues.

Understanding skin conductance requires knowledge of the skin's underlying structure. Figure 2.1 illustrates the skin's anatomy, comprising three main layers: the deepest layer, the hypodermis (subcutaneous tissue), followed by the dermis and the epidermis. These layers collectively shield the body from external elements. Beneath the surface, the skin harbours' blood vessels, nerves, sweat glands, and hair follicles. The outermost layer of the skin, the epidermis, contains the stratum corneum, a layer of dead cells that contributes significantly to its high impedance, which has been reported to exceed $100k\Omega$ for frequencies below 1kHz[44].

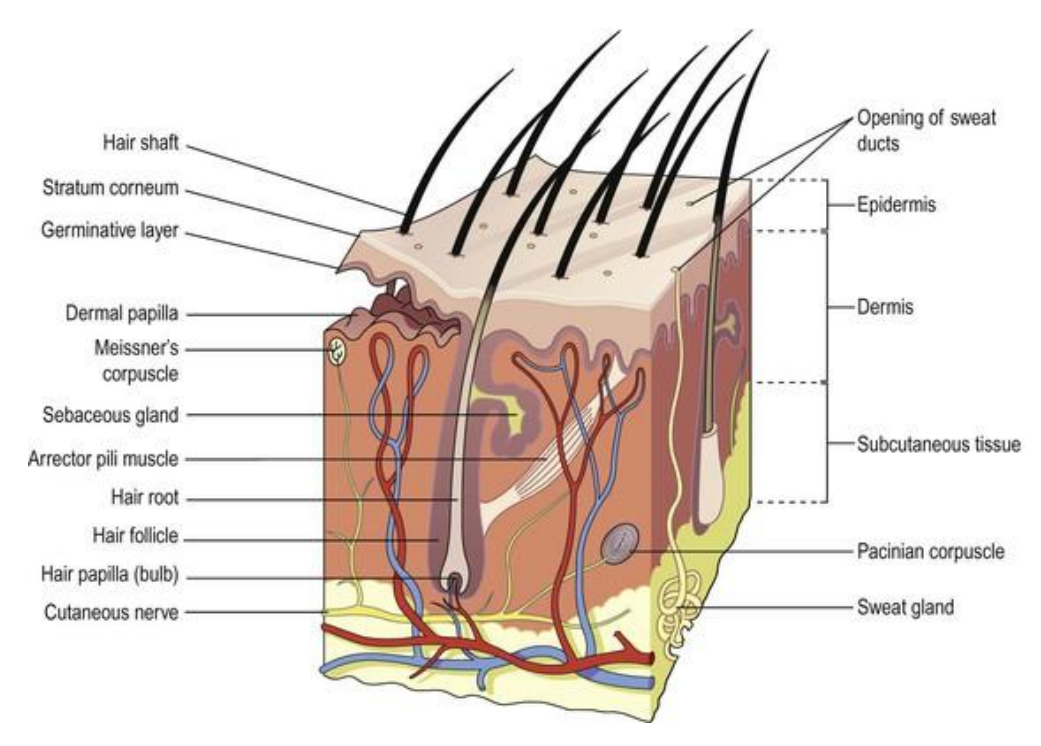


Figure 2. 1 Skin Anatomy, showing the various layers of the skin adapted from [44]

Every bioimpedance measurements on the skin begins with placement of electrodes. The skin layers can be modelled and represented as RC components connected both in series and parallel. Deeply analysing the equivalent circuit of the skin yields the diagram as shown in Figure 2.2. When electrodes are placed on the skin, electrode half-cell potential E_{hc} is developed due to the electrochemical reactions occurring at the electrode's surface, involving the transfer of electrons between the electrode and the ions in the solution[45], [46].

The electrical double layer, which behaves like a lossy capacitor (C_{dl}) due to limited charge mobility, and a resistor (R_{dl}) due to the presence of electrolytes, constitutes the skin interface impedance[47].

Furthermore, when an electrode is coupled to the skin, the skin surface itself behaves like a semi-permeable membrane, giving rise to a potential difference E_{se} across the skin. In addition, the resistance due to sweat on the skin surface is represented as R_s .

2.1 Electrical Equivalent circuit of Human Skin.

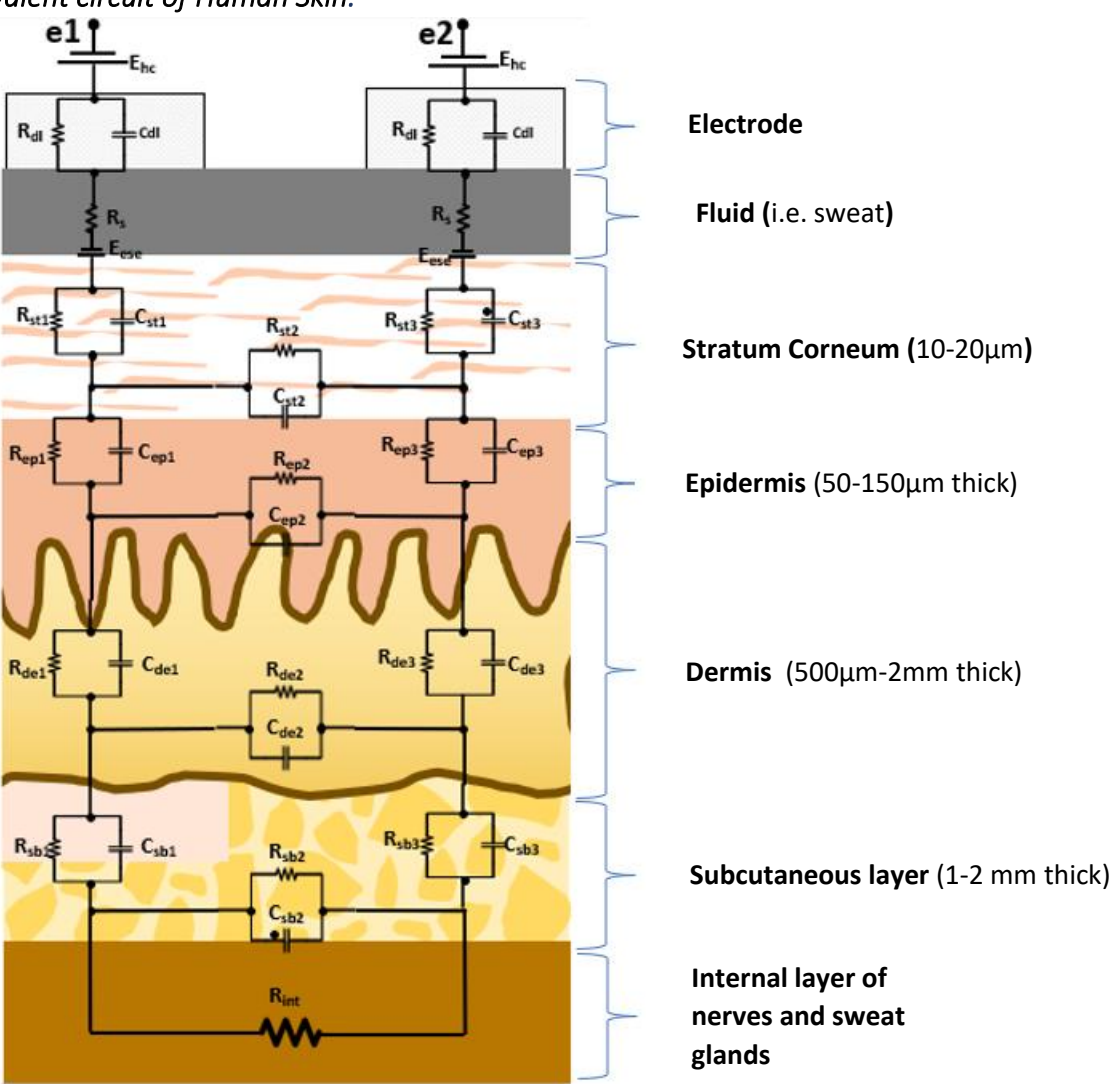


Figure 2. 2 A detailed electrical equivalent circuit of skin, adopted from [44], [48]

Although the stratum corneum is technically considered part of the epidermis, it has significantly higher impedance compared to the rest of the epidermis. The stratum corneum is composed of cell remnants known as corneocytes and fatty acids, interspersed with skin appendages such as sweat glands and hair follicles. Corneocytes, responsible for the water-absorbing properties of the stratum corneum, mainly contribute to its capacitive properties (C_{st1-3}) . Meanwhile, the skin appendages are primarily responsible for its resistive properties (R_{st1-3}) [46].

The epidermis layer lies directly beneath the stratum corneum and varies in thickness across different parts of the body. Its electrical properties are primarily influenced by ionic diffusion, represented as capacitive components (C_{ep1-3}), and ionic transport occurring mainly through skin appendages, represented as resistive components (R_{ep1-3}) [45], [49].

The electrical properties of the dermis layer, including its capacitive components (C_{de1-3}) and resistive components (R_{de1-3}), are significantly influenced by its primary constituents such as collagen, elastin fibres, blood vessels, lymph vessels, sweat ducts, and other skin appendages. The ion content in sweat notably impacts the dermis's conductivity, creating a parallel current path alongside the skin appendages. Furthermore, the presence of blood and lymph vessels facilitates the diffusion of ions, such as sodium (Na+), which further affect the electrical characteristics of the dermis. Notably, the dermis is thicker than the upper skin layers, typically ranging from 1 to 4 mm[45].

2.2 Frequency dependency of biological tissue electrical properties.

Tissues exhibits dual characteristics of both conductors and dielectrics, housing both free and bound (fixed) charges within their structure. Consequently, tissue impedance encompasses both conductive and dielectric elements. The conductivity σ facilitates the movement of free charges, directly correlating with the concentration of dissolved ions within the biological medium. As the ion concentration diminishes, electric resistance correspondingly increases.

On the other hand, the relative permittivity factor ε_r accounts for the movement of bound charges within the dielectric in response to an applied electrical field. At lower frequencies, variations in the applied electric field are slow enough to allow dipoles within the medium to align with the field and reach equilibrium before its polarity reverses. Beyond a certain frequency threshold, however, the medium's viscosity arising from the interactions between the molecules and the constraints they impose on each other's movement impedes dipole response to field variations, causing a time delay in medium reaction and subsequent energy dissipation in the form of heat[50].

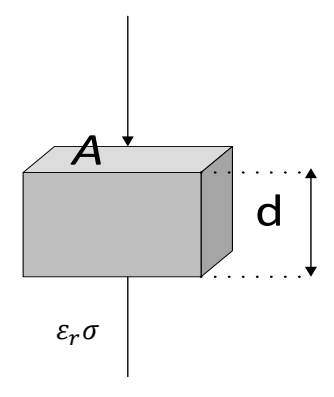


Figure 2. 3 Ideal slab of a biological tissue where A is tissue thickness, σ is the conductivity and ε_r the relative permittivity [51].

Figure.2.3 can also be represented in its basic parallel RC equivalent circuit model in Figure.2.4 from where frequency dependency properties can further be calculated.

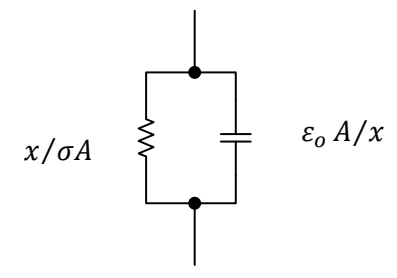


Figure 2. 4 The Basic equivalent circuit of the slab of tissue represented with a resistor in parallel to the capacitor. (Image adapted from [3]).

The frequency dependency of tissue is known as dispersion and this can mathematically be represented in relation to complex admittance Y^* and capacitance C^* .

$$Y^* = G + j\omega C = \frac{A}{x} \left(\sigma + j\omega \varepsilon_o \varepsilon_r \right) \tag{2.1}$$

Where G, ω and C are conductance, angular frequency, and capacitance respectively. As such, as the frequency increases $j\omega C\gg G$, permittivity becomes dominant while conductive component of admittance dominates at low frequencies.

2.2.1 Tissue Anisotropy.

The electrical properties of tissues, such as permittivity or conductivity, typically exhibit directional dependence. This phenomenon arises from the inherent morphological patterns within the tissue, such as the alignment of muscle fibres, tendons, nerve fibres, and blood vessels[51]. Skeletal muscle demonstrates anisotropic behaviour, meaning its conductivity differs significantly along the fibre axis (longitudinal) compared to perpendicular directions. As such, tissue impedance is contingent upon its specific structural arrangement and geometry[50], [51].

The frequency dependent behaviour of permittivity and conductivity in biological tissues is known as dispersion[51]. As shown in Figure 2.5, the frequency-dependent dielectric behaviour of biological tissues is typically grouped into three dispersion regions: alpha (α), beta (β), and gamma (γ).

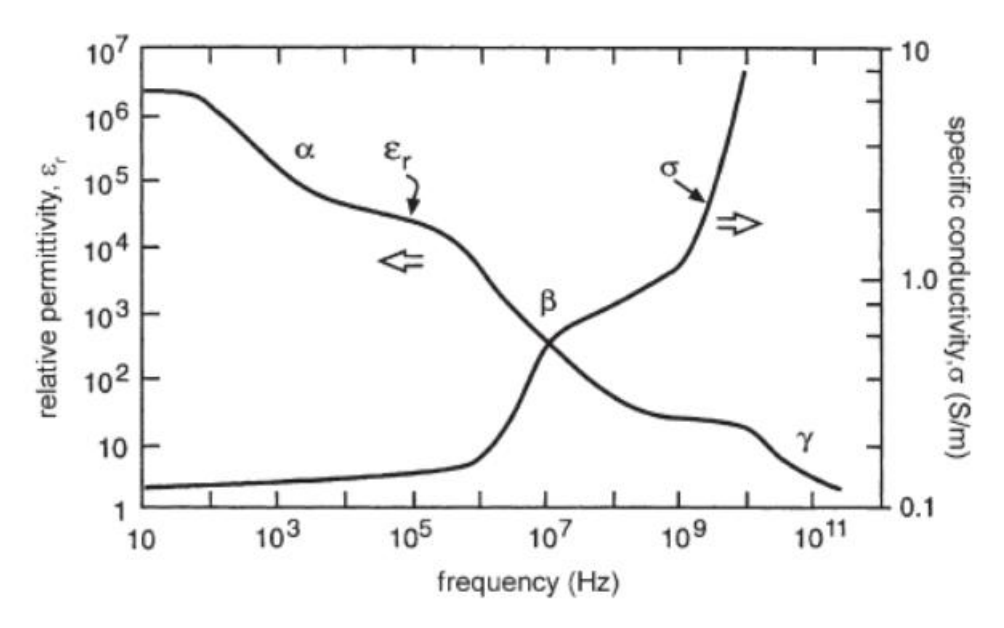


Figure 2. 5 Dispersion in Tissues and relative pernittivity as a function of frequency adapted from [52]

(i) α dispersion: Alpha dispersion is a characteristic low-frequency phenomenon observed between approximately 10 Hz and 10 kHz, as shown in the leftmost region of the graph where the relative permittivity reaches extremely high values (above 10^5) and then decreases steeply with increasing frequency[53]. This behaviour is primarily attributed to interfacial polarization mechanisms, including the slow diffusion and accumulation of ions near cellular membranes and at electrode interfaces (Maxwell Wagner effects), as well as the formation of capacitive double layers that dominate the dielectric response in this range[53], [50], [54].

(ii) β dispersion: Beta dispersion occurs in the intermediate frequency range between about 10 kHz and 100 MHz, as marked in the central region of the graph where the relative permittivity decreases further while the specific conductivity continues to rise. This dispersion mainly arises from the capacitive polarization of cell membranes, which act as dielectric barriers separating conductive intra and extracellular fluids. Under an applied alternating field, charges accumulate along the membrane surfaces, producing a pronounced dielectric response that resembles a distributed RC circuit. As frequency increases, membrane capacitive effects diminish because the field oscillates too rapidly for charge separation to persist, resulting in a further drop in permittivity and a continued increase in conductivity. β dispersion is particularly important in bioimpedance measurements for skin assessment because it reflects impedance changes arising from both intracellular and extracellular compartments, thereby offering a holistic representation of the tissue's composition and integrity [50], [54].

(iii) γ *dispersion*: Gamma dispersion occurs within the gigahertz frequency range and is primarily attributed to the polarization behaviour of water molecules [50], [54].

2.3 Biological tissue impedance model and model equation

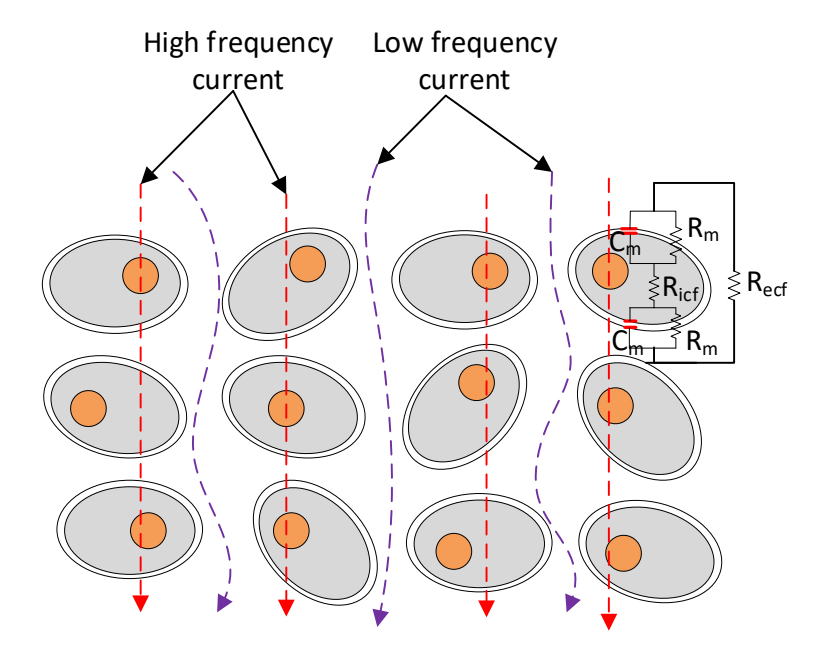


Figure 2. 6 Diagram illustrating the biological cell model[55]

Biological media are distinguished by the presence of cells, within which exist the intracellular medium, consisting of intracellular water (ICW), and the extracellular medium, composed of extracellular water (ECW) [61]. The resistance of intracellular electrolytes is represented by resistors R_{icf} , while extracellular resistance is modelled by R_{ecf} . ICW and ECW are separated by the cell membrane, acting as a dielectric, and represented by a capacitor C_m and with membrane resistance R_m . as shown in Figure 2.6.

While there have been several models describing the behaviour of biological tissues, the Fricke's model has been reported to have given good method for giving a simple description of biological model and its environments at microscopic level. In this model as shown in Figure 2.7, R_{ecf} and R_{icf} represent the resistances of ECF and ICF, respectively, while C_m is the cell membrane capacitance.

$$Z = R_{\infty} + \frac{(R_0 - R_{\infty})}{1 + (i\omega\tau)^{1-\alpha}}$$
 (2.2)

$$R_{\infty} = \frac{R_{icf} * R_{ecf}}{R_{icf} + R_{ecf}}, \quad R_0 = R_{ecf}, \quad \tau = (R_{icf} + R_{ecf})C_m$$
 (2.3)

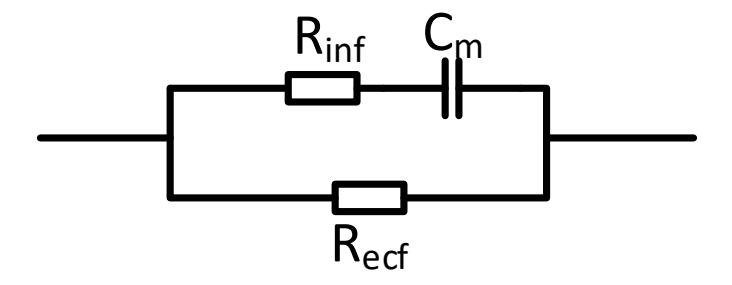


Figure 2. 7 Fricke model of biological tissue with equivalent resistances [56].

With $\omega=2\pi f$, R_0 , and R_∞ are the respective impedance at low and high frequencies. τ is the time constant. The value of α typically ranges between 0 and 1, with 0 representing a purely resistive behaviour and 1 being purely capacitive [51], [57].

2.3 Impedance Measurements.

Bioimpedance measurement involves the assessment of tissue electrical properties across a spectrum ranging from a few Hertz to several megahertz. The choice of frequencies depends on the specific application. Depending on whether dynamic or static properties are being assessed, bioimpedance can be measured either sequentially, at one frequency at a time, or concurrently across multiple frequencies. This technique, often referred to as bioimpedance spectroscopy, offers insights across a range of frequencies[26], [58], [59].

For bioimpedance measurement on the skin as considered in this Thesis, a known signal is applied to the tissue to excite its electrical properties in relation to the applied signal frequency. This signal must be precisely determined and is typically kept constant to facilitate impedance calculation using Ohm's law. In most instances, a constant AC current is injected to measure voltage, although voltage injection has also been explored; however, the former is more widely favoured due to safety considerations. Firstly, maintaining a constant current eliminates the need for additional circuitry to monitor the injected current. Secondly, constant current injection is generally considered safer, as the impedance of biological tissue can unexpectedly decrease due to physiological factors, which may otherwise lead to an increase in current and potentially pose a risk to the subject [58], [59].

2.4 Interface Impedance

When a metal electrode comes into contact with an electrolytic solution, charged ions are generated at the interface between the electrode and the solution. These ions migrate into the solution, creating a charged layer on the electrode's surface. Consequently, a double layer is formed immediately upon the wetting of the metal[60]. The first double layer model of electrode/electrolyte interface was proposed by Helmholtz in 1853[60]. Helmholtz assigned the double layer a molecular capacitor where one layer of the capacitor represents the charges in the electrode side and the other the ions, separated by the minimum distance of the electrolytes. The double layer capacitance as proposed by Helmholtz is further shown in eq.2.4

$$C_H = \frac{\varepsilon_0 \varepsilon_r}{l} \tag{2.4}$$

Where C_H is the Helmholtz capacitor, ε_0 and ε_r are the permittivity of free space and relative permittivity of the material, l is the distance between the double layer. However, in Helmholt model, the thickness of the double layer would increase in diluted solution, making the model only suitable for high concentration electrolyte[47]. Gouy-Chapman's model further

illustrated the influence of thermal motion in facilitating exchange of counterions between the double layer and the electrolytic solution. While Gouy-Chapman's model showed good result for low concentration of electrolytes, it was not suitable for highly charged surfaces [60].

Stern model which is the widely adopted model when modelling interface impedance was developed by Stern and taking into consideration the finite size of the counterions and their binding properties at the surface. Stern's interface impedance model is shown in Figure 2.8.

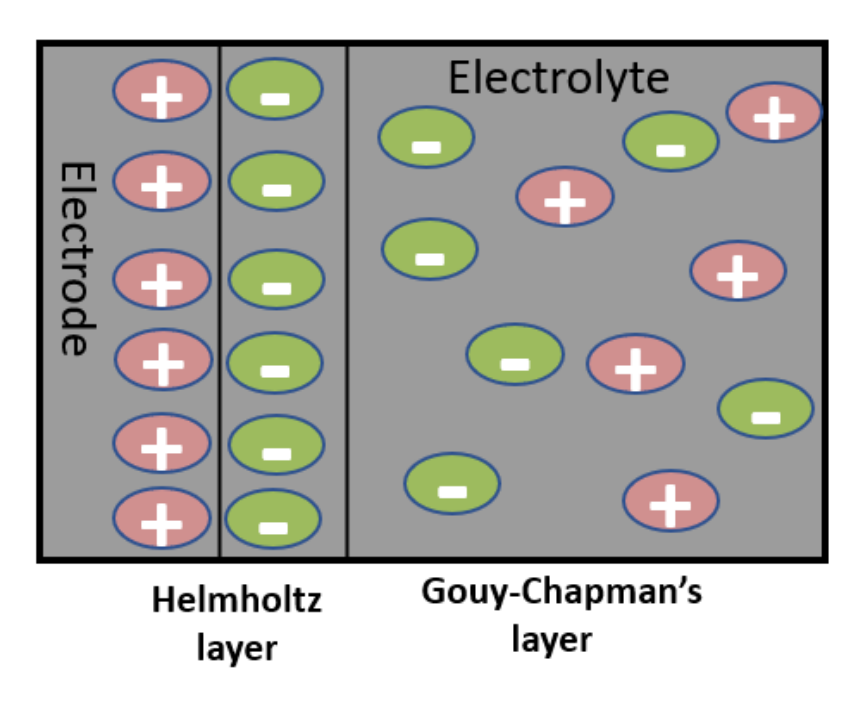


Figure 2. 8 Stern electrode/electrolyte interface impedance model adopted from [47].

The Stern model combines the Helmholtz layer (compact layer right at the surface) with the Gouy–Chapman diffuse layer further out, providing a more realistic description under these circumstance[61]. The double layer capacitance is mathematically represented by eq2. 5.

$$\frac{1}{C_S} = \frac{1}{C_H} + \frac{1}{C_{GC}} \tag{2.5}$$

Where C_s is the double layer capacitance, C_H is the capacitance of the Helmholtz outer layer and C_{GC} is the capacitance of the diffuse layer. It can be seen that the electrode/electrolyte interface impedance are from the charge transfer within the Stern/Helmholtz layer and the Gouy-chapman's layer. This can further be represented in the equivalent circuit model in Figure.2.9.

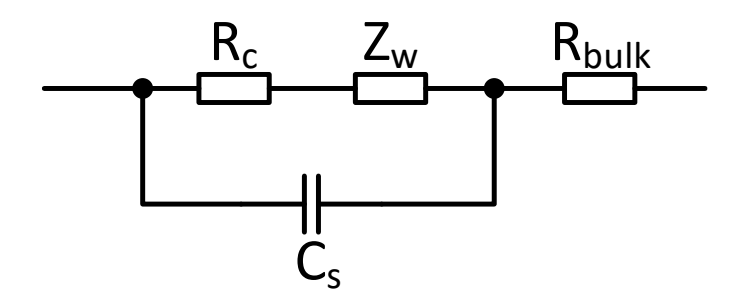


Figure 2. 9 Equivalent circuit model of electrode/electrolyte interface[62]

The equivalent circuit model of interface impedance represented in Figure 2.9 shows the Nest impedance controlled by change transfer resistor (R_C), the diffusion limitation impedance within Gouy-chapman's layer known as Warburg impedance (Z_w), the electrical double layer modelled as a lossy capacitor due to limited charge mobility and electrolyte resistance (R_{bulk}).

2.5 Electrode configuration.

There are several electrodes' configurations in bioimpedance measurements, however the two most popular ones namely bipolar and tetrapolar configurations have been considered in this work.

2.5.1 Bipolar configurations

In a bipolar electrode configuration, the same pair of electrodes is used for both current injection and voltage measurements[63]. While this setup is less complex and easier to implement, it presents significant challenges. One of the main issues is the sensitivity of the shared injection and measurement path, which can lead to erroneous measurements. This is primarily due to the substantial effects of the electrode/electrolyte interface, which can introduce inaccuracies in the measured voltage[63], [64]. These interface effects, such as impedance changes and polarization, can significantly and erroneously affect the measurements. Figure 2.10 illustrates a bipolar electrode configuration set-up.

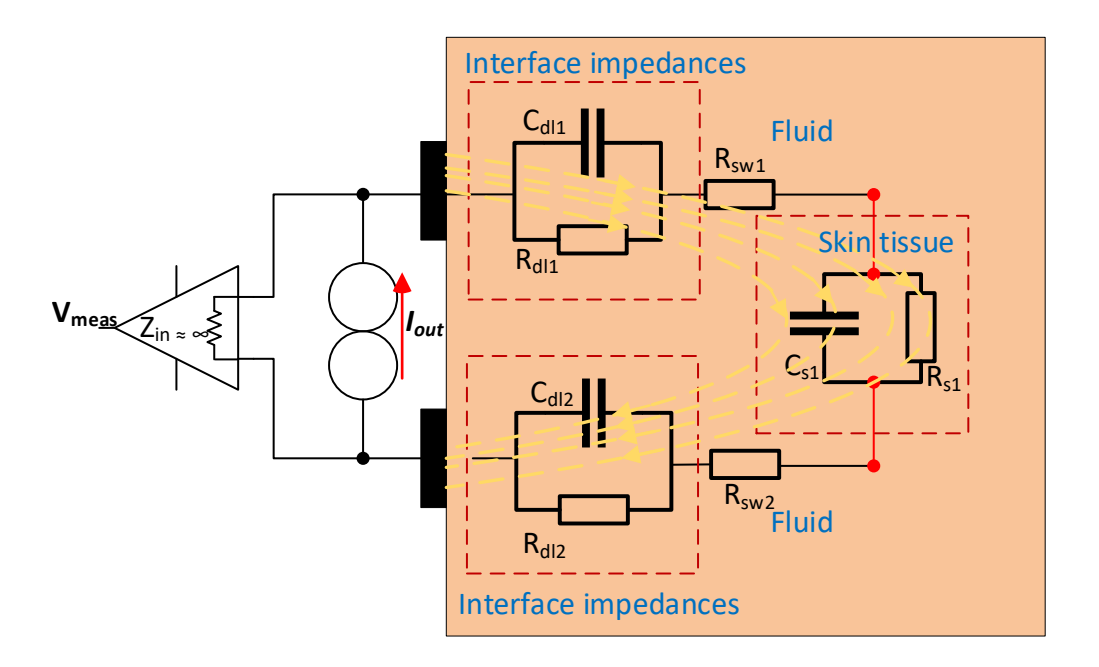


Figure 2. 10 A bipolar electrode configuration set-up illustrating the electrode / electrolyte interface impedance.

In Figure.2.10, the same electrode used for injection is used for measurement, as such the injected (I_{out}) current travels throughout interface impedances and the target skin impedances. The cumulative voltage drops of the interface impedances adds to the total voltage measured by the instrumentation amplifier.

Assuming that input impedance of the instrumentation amplifier is ideally infinite, then the total impedance (Z_T) seen by the current source is

$$Z_{Tb} = (XC_{dl1}//R_{dl1}) + R_{sw1} + (XC_{s1}//R_{s1}) + R_{sw2} + (XC_{dl2}//R_{dl2})$$
 (2.6)

$$Z_{Tb} = \frac{R_{dl1}}{1 + j\omega R_{dl1}C_{dl1}} + R_{sw1} + \frac{R_{s1}}{1 + j\omega R_{s1}C_{s1}} + R_{sw2} + \frac{R_{dl2}}{1 + j\omega R_{dl2}C_{dl2}}$$
(2.7)

Where $(C_{dl1}, R_{dl1}, C_{dl2}, R_{dl2})$ are the electrode / electrolyte interface impedances between the pairs of current injection and voltage measurement electrodes and the skin site it was placed on.

 R_{sw1} and R_{sw2} are the impedances due to fluid i.e sweat on the skin. C_{s1} , R_{s2} are the target skin site. As such correlating with Fig 2.9, $(C_{dl1} \text{ and } C_{dl2})$ represents C_s the double layer capacitance while $(R_{dl1} \text{ and } R_{dl2})$ represents R_C the charge transfer resistance and R_{sw1} and R_{sw2} represents the bulk resistance of the electrolyte (R_{bulk}). Warbug impedance Zw has been omitted for simplicity.

Hence the voltage measured by the instrumentation amplifier (V_{meas})

$$V_{measb} = I_{out} \left\{ \frac{R_{dl1}}{1 + j\omega R_{dl1} C_{dl1}} + R_{sw1} + \frac{R_{s1}}{1 + j\omega R_{s1} C_{s1}} + R_{sw2} + \frac{R_{dl2}}{1 + j\omega R_{dl2} C_{dl2}} \right\} (2.8)$$

$$V_{measb} = V_{dl1} + V_{sw1} + V_{s1} + V_{sw2} + V_{dl2}$$
 (2.9)

Therefore, assuming infinite output impedance of the current source and infinite input impedance of the measurement circuit and negligible parasitic electrode reactance and resistance, the total measured voltage in a bipolar electrode configuration becomes a summation of the electrode/electrolyte interface impedances and the target tissue impedance which resultantly would create errors in the accuracy of the measurements. "The summation of electrode interface impedance and target tissue impedance would lead to measurement inaccuracies.

2.5.2 Tetrapolar Electrode configurations.

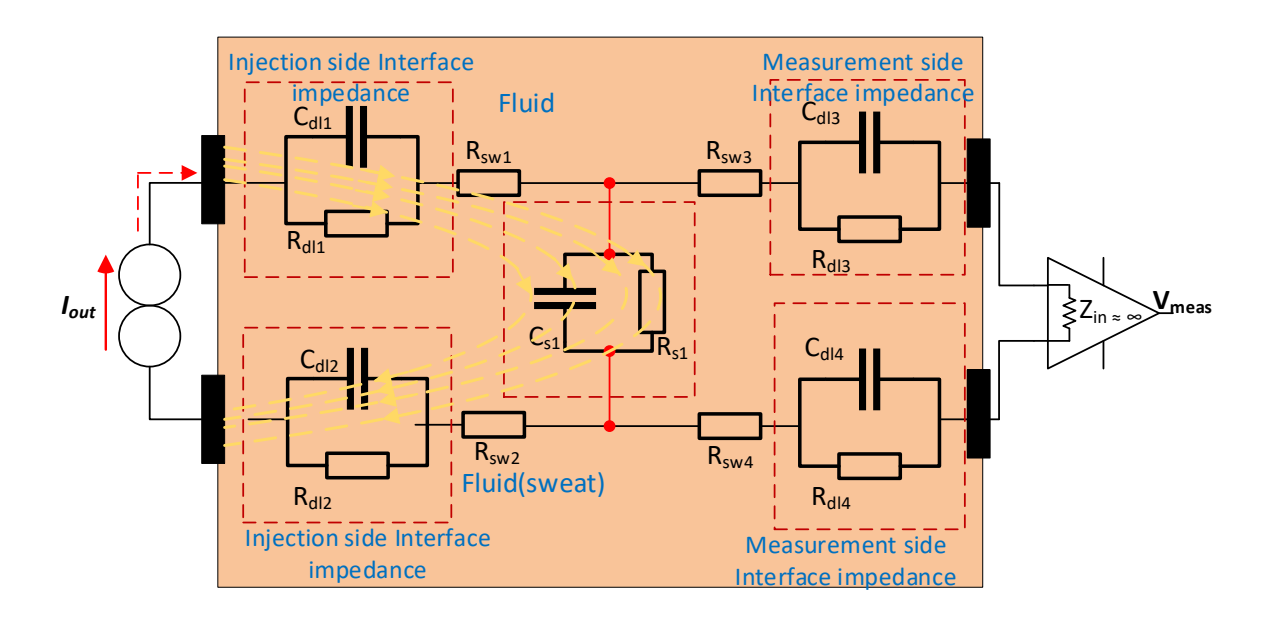


Figure 2. 11 A tetrapolar electrode configuration set-up illustrating the electrode / electrolyte interface impedance

In the tetrapolar electrode configuration, as illustrated in Figure. 2.11, a specific arrangement of four electrodes is employed to enhance measurement accuracy. Two pairs of electrodes are used, with the first pair designated for current injection and the second pair reserved for voltage measurement. This configuration helps to isolate the voltage measurement from the influence of the electrode/electrolyte interface impedance at the measurement electrodes.

When taking measurements, the current injection electrodes deliver a known current into the target tissue. This current flows through the tissue and through the electrode/electrolyte interface impedance at the injection site electrodes. The current then travels through the tissue, reaching the target site. Importantly, the input of the measurement instrumentation amplifier, connected to the voltage measurement electrodes has high very input impedance, so little or no current flows through. As a result, the current pathway is limited to the electrode/electrolyte interface impedance at the injection electrodes and the target tissue itself.

By isolating the voltage measurement from the interface impedance effects, the tetrapolar electrode configuration provides a more accurate and reliable representation of the target

tissue's electrical characteristics[63]. The transfer impedance (Z_{Tt}) contributing to measured voltage in the tetrapolar electrode configuration is

$$Z_{Tt} = (XC_{s1}//R_{s1}) (2.10)$$

$$Z_{Tt} = \frac{R_{s1}}{1 + j\omega R_{s1}C_{s1}} \tag{2.11}$$

$$V_{meast} = I_{out} \left\{ \frac{R_{s1}}{1 + j\omega R_{s1} C_{s1}} \right\}$$
 (2.12)

$$V_{meast} \approx V_{s1}$$
 (2.13)

Where V_{s1} = The impedance contribution mainly from the measurement across the target skin site.

2.6 Electrode design.

Bioimpedance measurement is influenced by various factors, not only including anthropometric parameters such as body size, shape, and composition but also the design characteristics of the electrodes themselves. Bioimpedance measurement electrodes for human skin measurements come in various types, each tailored to specific requirements based on the measurement mode, external conditions, placement method, and electrode location on the body. The measurement mode can be static, where impedance measurements are not dynamically varying due to volumetric blood changes, or dynamic, where impedance measurements are due to blood volumetric variations. External conditions, such as laboratory settings or different physical activities, also influence the choice of sensor type[62].

When selecting electrodes, it is crucial to consider the method of fixation and the location of the electrodes on the skin. Given that naturally skin is not a uniform structure and exhibits varying local properties, the design of the sensor must account for these variations. To obtain a reliable average local impedance, the geometry of the electrodes plays a significant role. The construction of the sensor should ensure adequate contact with the skin across different areas to accurately reflect the local impedance.

The electrodes' geometry is essential in achieving consistent and representative measurements. Various electrode shapes and configurations can be employed to maximize contact area and ensure uniform pressure distribution on the skin [65].

The following subsection delves into these electrode design factors in greater detail. It explores how different electrode shapes and interface models affect the measurement of electrical impedance, particularly in the assessment of the skin layer. By understanding these influences, we can better interpret impedance measurements and improve the accuracy of diagnostic procedures that rely on this technology.

2.6.1 Interdigitated Electrodes

The interdigitated or interdigital electrode (IDE) normally used in bipolar measurement is a finger-like shaped electrode used to measure the capacitance value of a device under test (DUT). The operation principle of an interdigitated sensor is based on the electrodynamics of two parallel plate capacitors. An AC current or voltage source is applied between the positive and negative terminals to generate an electric field between the electrodes. This electric field penetrates the DUT, altering the impedance of the sensor. Since the sensor behaves like a capacitor, its capacitive reactance is influenced by the DUT. When the measurand interacts with the sensing membrane (the dielectric material) of the interdigitated capacitor (IDC), the dielectric constant changes, thereby changing the sensor's capacitive reactance.

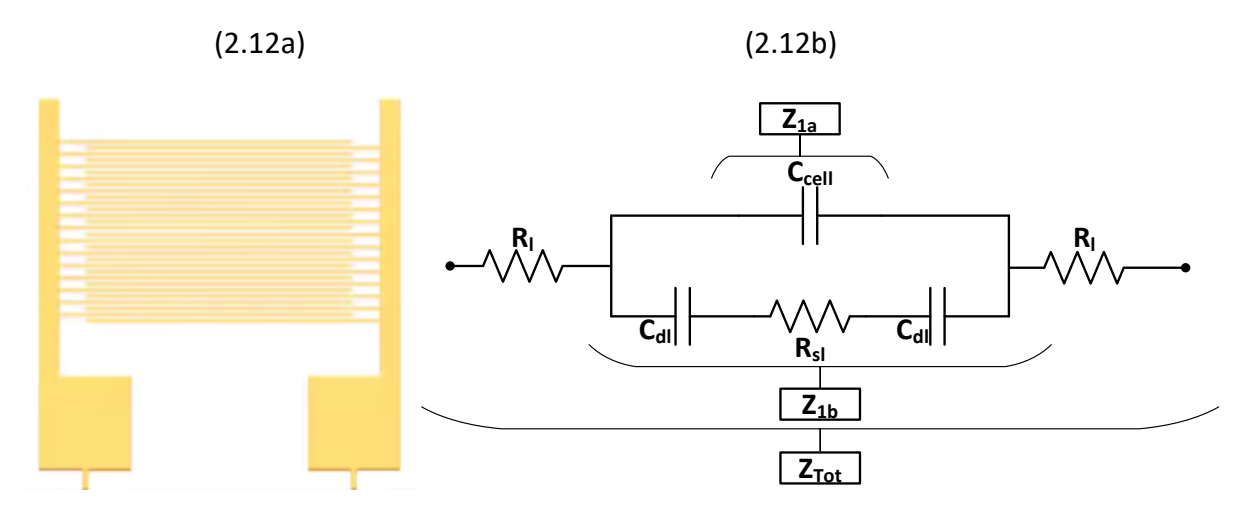


Figure 2. 12 Interdigitated electrode configurations showing (a) electrode configuration and (b) the equivalent circuit [66].

Figure 2.12 illustrates the diagrammatic representation of the interdigitated electrode, with it's equivalent circuit model in Figure.2.12b showing R_l , the lead resistances, C_{cell} , the double layer capacitances, R_{sl} , the resistance of the medium solution, C_{cell} , the direct capacitive coupling between the parts of the fingers.

 R_{sl} is a function of electrolyte conductivity σ_{sl} and the cell constant K_{cell} which serves as a geometrical scaling factor for the electrode configuration, as expressed in eq. (2.14).

$$R_{sl} = \frac{K_{cell}}{\sigma_{sl}} \tag{2.14}$$

The Cell constant K_{cell} can also be represented following eq. (2.15)

$$K_{cell} = \frac{2}{(N-1)L} \cdot \frac{K(k)}{K(\sqrt{1-k^2})}$$
 (2.15)

Where N and L are the number and length of fingers respectively, and K(k) is the integral of the modulus k, where k is defined in eq.(2.16).

$$k = \cos\left(\frac{\pi W}{\lambda}\right) \tag{2.16}$$

Where W and λ are the width of the electrode and wavelength representing the periodicity of the interdigitated electrode structure.

The direct coupling between the two electrodes C_{cell} is represented by

$$C_{cell} = \frac{\varepsilon_0 \varepsilon_{rsl}}{K_{cell}} \tag{2.17}$$

 $arepsilon_0$ and $arepsilon_{rsl}$ are respectively the absolute permittivity and the relative permittivity of the solution

2.6.1.1 Biomedical Applications requiring Interdigitated electrodes

One of the major advantages of the interdigitated electrode configurations is its high sensitivity[66], making it particularly well-suited for measuring capacitance values. This high sensitivity is advantageous for bioimpedance applications, including skin hydration assessment, a critical factor in detecting skin conditions such as eczema. In skin hydration assessment, the dielectric constant of the skin changes with its water content. Interdigitated electrodes can detect these changes with high precision due to their ability to measure minute variations in capacitance. Though not used in the skin hydration experiment in this project, they are a key component in most Corneometer and skin hydration sensors[67].

2.6.2 Spiral Shape Electrodes

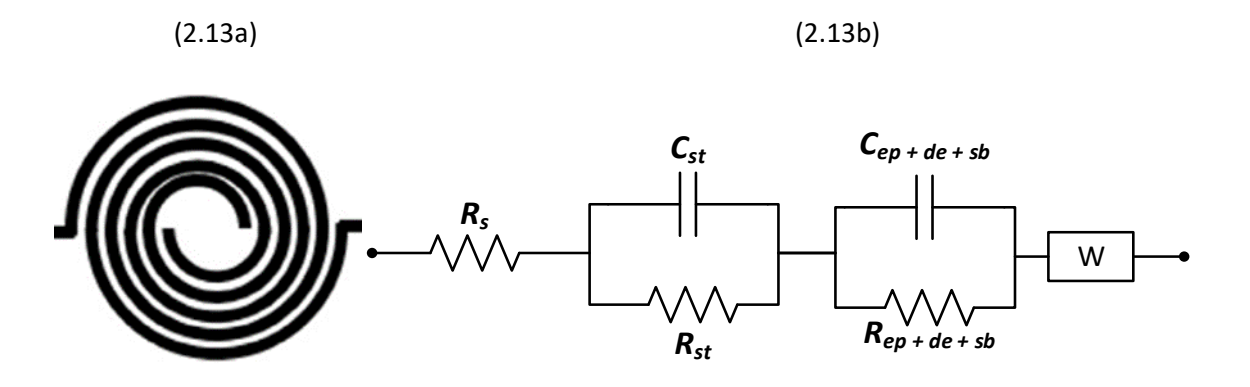


Figure 2. 13 Spiral electrode configuration showing (a) electrode configuration and (b) the equivalent circuit model [66][62].

Spiral electrodes are a type of bioimpedance electrode, typically used in a bipolar electrode configuration and designed to measure the average local impedance of human skin. These sensors are constructed in the form of two concentric spiral-shaped electrodes. The spiral geometry allows for the averaging of skin impedance measurements from a relatively large area of the skin. This design is particularly effective in accounting for the anisotropic

properties of the skin. This is mainly because it could be adapted to measure areas of high impedances i.e dry skin and low impedances (sweat skin area) by varying the distances between the spiral electrodes[45], [62].

Figure.2.13 (a) and (b) shows the spiral electrode design shape and its equivalent circuit respectively. These can be analysed using eq.2.27.

$$Z(f) = R_{s} + \frac{R_{st}}{1 + j2\pi f R_{st} C_{st}} + \frac{R_{ep+ed+st}}{1 + j2\pi f R_{ep+ed+st} C_{ep+ed+st}} + \frac{\alpha}{\sqrt{j\pi f}}$$
(2.18)

Following the eq.2.27. Z is the measured impedance at a specified frequency f. R_s is the coupling material resistance between the electrode and the skin. R_{st} and C_{st} are the resistance and the capacitance of the stratum corneum respectively, $R_{ep+ed+st}$ and $C_{ep+ed+st}$ are the resistance and the capacitance of underlying skin tissue represented as a series combination of epidermis, dermis, and subcutaneous layer. α is the Warburg coefficient where $0 < \alpha < 1$.

2.6.2.1 Bioimpedance Applications requiring Spiral electrode geometry.

The use of spiral electrode geometry has been employed in most measurements to eliminate the anisotropic properties of the skin and measure the impedance independently of the direction in which the sensing device is located. This geometry has found its applicability in skin sweat and stress level monitoring[50], [62].

2.6.3 Concentric Electrodes.



Figure 2. 14 Concentric electrodes.

The concentric shape of the electrodes as shown in Figure 2.14 consists of multiple rings centred at the same point, creating a highly organized and efficient design for impedance measurement. This is a tetrapolar configuration that includes a guard electrode positioned between the voltage sensing electrode and the current measurement electrode, effectively eliminating unwanted leakage currents at the skin surface. This design feature enhances the accuracy of the measurements by preventing external interferences[23].

The circular edge of the concentric electrode shape is specifically designed to minimize the fringing electric field, which can distort measurement accuracy. By reducing this field, the electrodes ensure a more uniform distribution of the electric field across the skin surface. Additionally, the increased electrode area contributes to a higher signal-to-noise ratio, resulting in clearer and more reliable data.

The penetration depth of the current, an important factor in measuring impedance, is influenced by the distance between the electrodes. A greater distance allows the current to penetrate deeper into the skin, enabling the measurement of impedance at various skin depths.

2.6.3.1 Bioimpedance Applications requiring Concentric electrode geometry.

The variability in penetration depth offered by concentric electrode designs makes them highly versatile for assessing different skin types and performing diverse measurement protocols[23], [68]. This adaptability allows researchers and clinicians to adapt the electrode configuration to target specific tissue layers or depths, improving measurement accuracy and sensitivity. Concentric electrode geometry is commonly employed in bioimpedance applications that involve detailed cellular investigations. For example, it has been used in the detection and monitoring of skin conditions such as skin cancer [23].

2.6.4 Square and circular array shape.

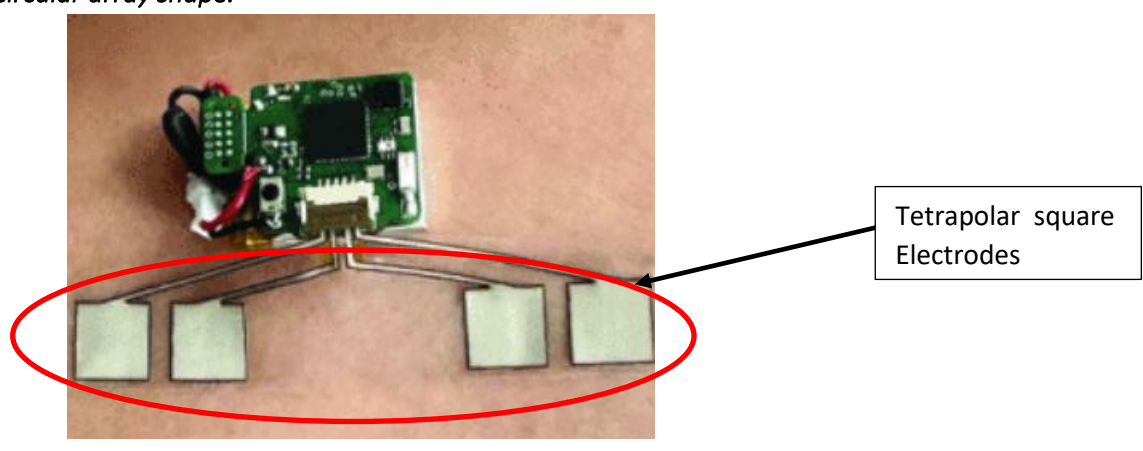


Figure 2. 15 Square electrodes [69]

Square and circular array electrodes are among the most common electrode configurations to implement. They are widely used in bioimpedance applications, such as ECG monitoring, plethysmography and tomography. Typically, these geometries consist of four electrodes, with one pair designated for current injection and the other pair for voltage measurement. This tetrapolar measurement approach effectively minimizes the impact of the electrode-electrolyte interface[45].

Despite their advantages, these configurations are known to suffer from fringing effects, particularly at the edges of the electrode. Fringing effects, caused by the non-uniform electric field distribution inherent to square electrode geometries, can introduce nonlinearity in impedance measurements. This makes it challenging to accurately estimate changes in the skin's electrophysiological parameters. [45].Impedance changes within the fringing electric field area exacerbate this issue, further complicating the measurement process[45][70].

2.7 Electrode Placement

The accuracy of bioimpedance measurements depends significantly on the precise placement of electrodes. Tissue conductivity varies based on the direction relative to the tissue structure, a property known as anisotropy. This means that in many biological tissues, the conductivity can differ when measured laterally (parallel to the tissue surface) versus perpendicularly (orthogonal to the surface). Such variations are often attributed to the structural organization of cells and the extracellular matrix[71].

For example, muscle tissue typically exhibits higher conductivity along the direction of the muscle fibres (lateral) compared to perpendicular to the fibres. This is due to the alignment of conductive pathways within the muscle, which facilitate easier flow of electrical currents along the lateral fibre direction.

Electrode placement for bioimpedance applications can be broadly categorized into two types: whole body electrode placement and localized electrode placement[71], [72], [73].

2.8 Current profiling of equivalent circuit model of skin Tissue.

Figure 2.16 illustrates a graphical representation of a basic equivalent model of skin tissue. The equivalent circuit model employed is a simple RC parallel circuit, as shown in Figure. 2.4, adopted for its simplicity. R fixed at $1k\Omega$ represents the intracellular fluid, and C represents the cell membrane, varying from 5nF to 30nF. The respective currents through the resistive, capacitive, and combined resistive-capacitive components were individually measured. As expected, at higher frequencies, the cell membrane impedance becomes very small, allowing most of the current to pass through. The circuit schematic and parameter used to generate graph of Figure 2.16 is shown in Appendix B.

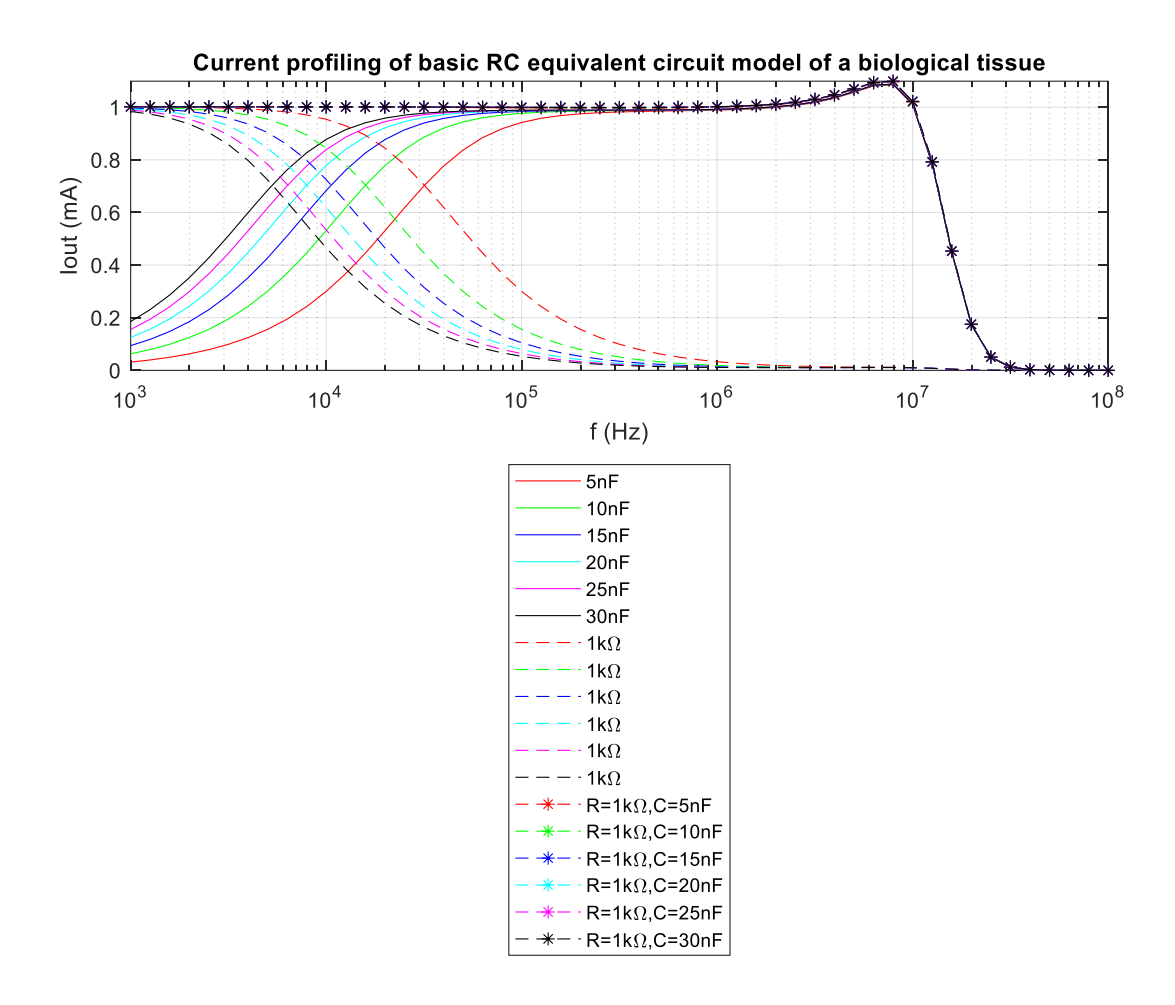


Figure 2. 16. Spice simulation of Current profiling of equivalent circuit model of skin Tissue.

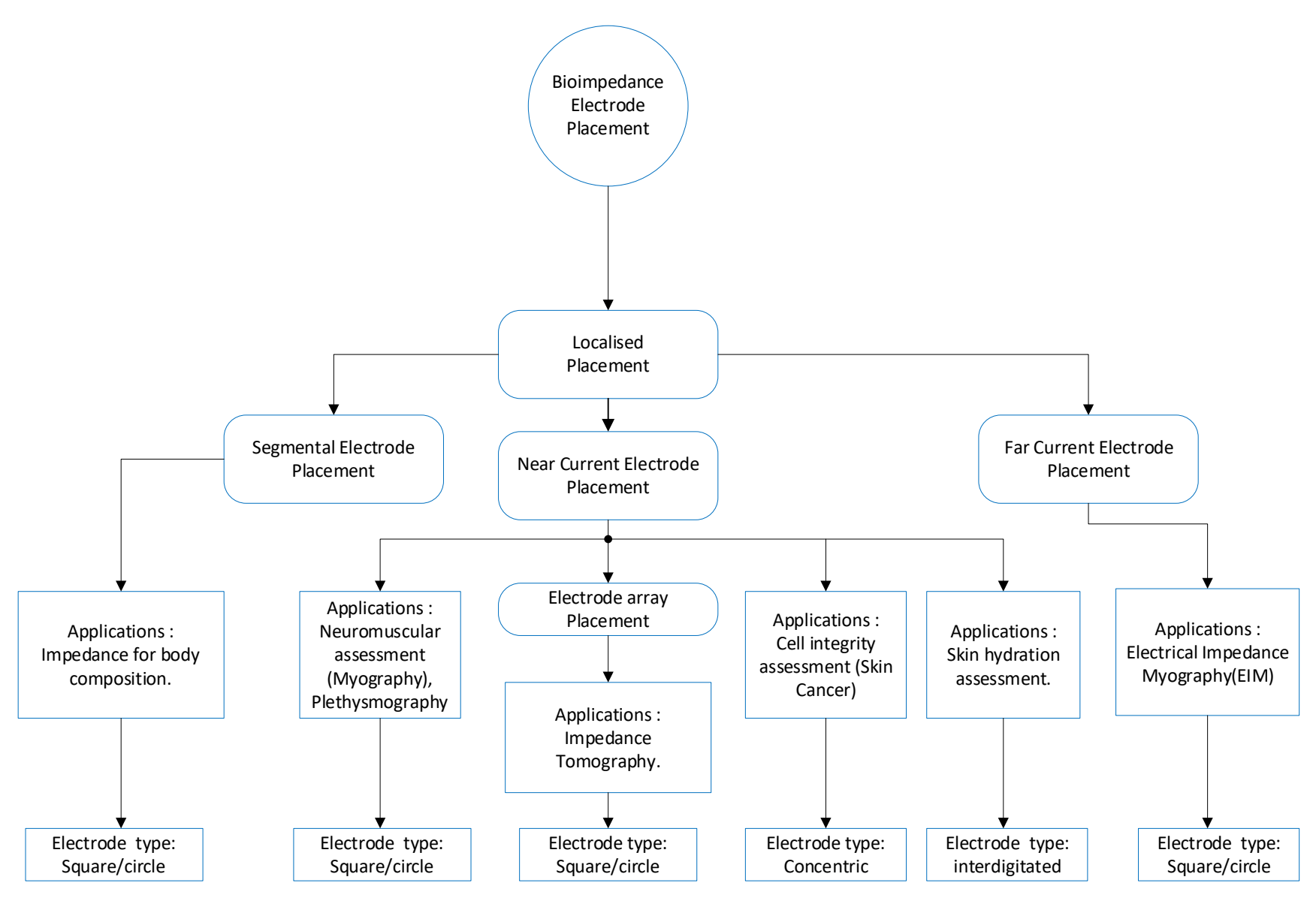


Figure 2. 17 Electrode Placement Configuration and Possible Electrode Shapes for a Bioimpedance Application [23] [66][72][74]

2.9 Summary of Bioimpedance application electrode configurations and placement.

Figure 2.17. illustrates the various configurations for electrode placements in a bioimpedance application. It also showcases the different electrodes shapes, demonstrating the versatility and adaptability of electrode design to specific bioimpedance measurement needs.

2.10 Conclusion on Chapter 2.

This chapter provided a detailed explanation of the skin, its layers, and associated structures, drawing connections to their equivalent circuit models. The presented equivalent circuit was analysed in depth. Additionally, various electrode configurations, placements, and their impact on geometry and interface impedances were discussed. The analysis from this chapter helped categorize different electrode shapes for specific bioimpedance applications.

A simulation of the skin's equivalent circuit model was conducted in LTspice to further illustrate how biological tissues are profiled by alternating current (AC). This simulation enhanced understanding by demonstrating the principles underlying tissue profiling through bioimpedance.

The next chapter, Chapter 3, will focus on a multimodal assessment of skin hydration, utilizing different techniques, with a particular emphasis on bioimpedance and optical methods.

Chapter 3

Multimodal Experimental Assessment of Skin Hydration using Bioimpedance and Optical sensing.

The typical techniques used in measuring the hydration of the skin and its barrier function are electrical-based sensors, with the gold standard device being the corneometer. However, although such devices are widely used and considered accurate, they may exhibit a range of errors that can introduce significant measurement discrepancies which have not been adequately addressed in commercial devices[24]. Corneometer errors can be grouped into two main categories: (i) errors that relate to the electrode—skin contact properties, and (ii) errors due to the nature of the measurand, given that the corneometer does not directly measure water content, and they lack detailed skin profiling [6–10].

Errors in category (i) include variability as a function of contact area and geometry, electrode material, and applied pressure [24]. These errors can be associated with the fact that such instruments feature a two-electrode (bipolar) configuration. The corneometer's principle of operation is described by the wider theory of bioimpedance measurements. Bioelectrical impedance (or bioimpedance) sensing is applied in a broad range of biomedical applications, including body composition estimation, cardiac output measurements, cell culture monitoring, and monitoring of skin hydration, to name a few [9]. The electrical properties of biological tissues are influenced by factors including their morphology, physiology, and pathological conditions[75][50].

The primary source of errors in bipolar bioimpedance systems, including typical corneometers, relates to the electrode–electrolyte double layer introducing a contact impedance that can significantly interfere with the measured value[76]. As measurements are taken across a range of frequencies the detrimental effect of the contact impedance varies significantly, especially when small electrodes and/or low frequencies are employed[77][78].

A commonly employed method for mitigating the impact of contact impedance on measurements involves utilizing four electrodes[78][54], [79], [80]. Referred to as tetrapolar electrical impedance measurement (TEIM), this technique effectively reduces the adverse effects of the double layer on the measurement. The appropriateness of the tetrapolar approach for measuring hydration has been demonstrated in the literature [16], [26]. It is, therefore, desirable to compare the effectiveness of tetrapolar versus bipolar hydration measurements to assess the significance of the double layer errors in electrical sensing methods.

Bioimpedance hydration sensing relates to the skin's electrical properties, like permittivity and conductivity, whose combined values vary with different water content levels. As the measurements reflect water content only indirectly, they are expressed in arbitrary values [26]. This reliance on electrical properties results in errors in category (ii), including decreased sensitivity at high hydration levels, susceptibility to environmental variations, and fluctuations

with electrolyte concentrations. These errors can be minimised by sensing water content directly, which can be made possible through optical sensing based on the capability to directly detect water-related bands present within the spectral response[26].

The ex vivo investigation involved employing the desorption of porcine skin over a 6h duration at room temperature, with measurements taken at fixed intervals. Furthermore, an in vivo indicative study was conducted to ascertain the sensors' accuracy when applied to human skin by examining their raw outputs, considering various affecting parameters. Analysis of both methodologies facilitated comprehensive insights into the efficacy and advantages of employing multi-modal approaches for skin hydration measurement with a focus on optimizing the bioimpedance system to potentially eliminate the aforementioned errors of corneometer.

3.1 Design and development of Bioimpedance measurement system.

The block diagram of the bioimpedance magnitude measurement system designed and used in this experiment is shown in Figure 3.1. It consists of an AC current generation stage connected to a pair of current-injecting electrodes and an impedance magnitude measurement stage connected to a separate pair of voltage-measuring electrodes. Both the current injection and voltage measurement electrodes are typically a conductivity sensor in a tetrapolar configuration shown in Fig3.2a. The current injection comprises a Howland current source (U1). The measurement stage consists of the blocks U2-U4, comprised of an instrumentation amplifier, an active full-wave precision rectifier, and an active second-order low-pass filter. Full details of the set-up is shown in Fig.3.3.

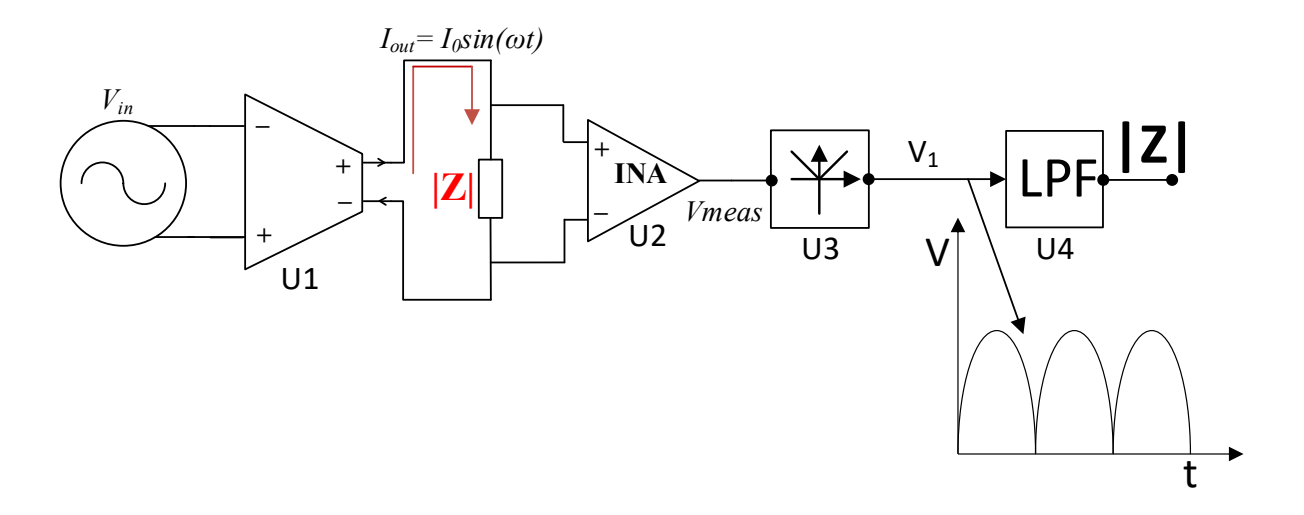


Figure 3. 1 Bioimpedance Measuring system based on Magnitude detection[58]

The component U1 is a mirrored-enhanced Howland current source (MEHCS), allowing for a fully floating load, this is further discussed in Chapter 4 in great detail. The output current flowing through the load impedance |Z| of the biological sample under test is

$$I_{out} = g_m V_{in} (3.1)$$

$$|Z| = \frac{V_1 * \pi}{2 * I_{out} * A_v} \tag{3.2}$$

Where A_v is the gain of the instrumentation amplifier, g_m is the transconductance of the current source. U2 is the instrumentation amplifier measuring the resulting voltage across the porcine skin.

The instrumentation was connected to a commercially available [81], tetrapolar conductivity sensor featuring electrodes shown in Figure 3.2a, specified for a frequency range of 100 Hz to 10 kHz.



Figure 3.2a. Measuring tetrapolar sensor used in the experiment[81]

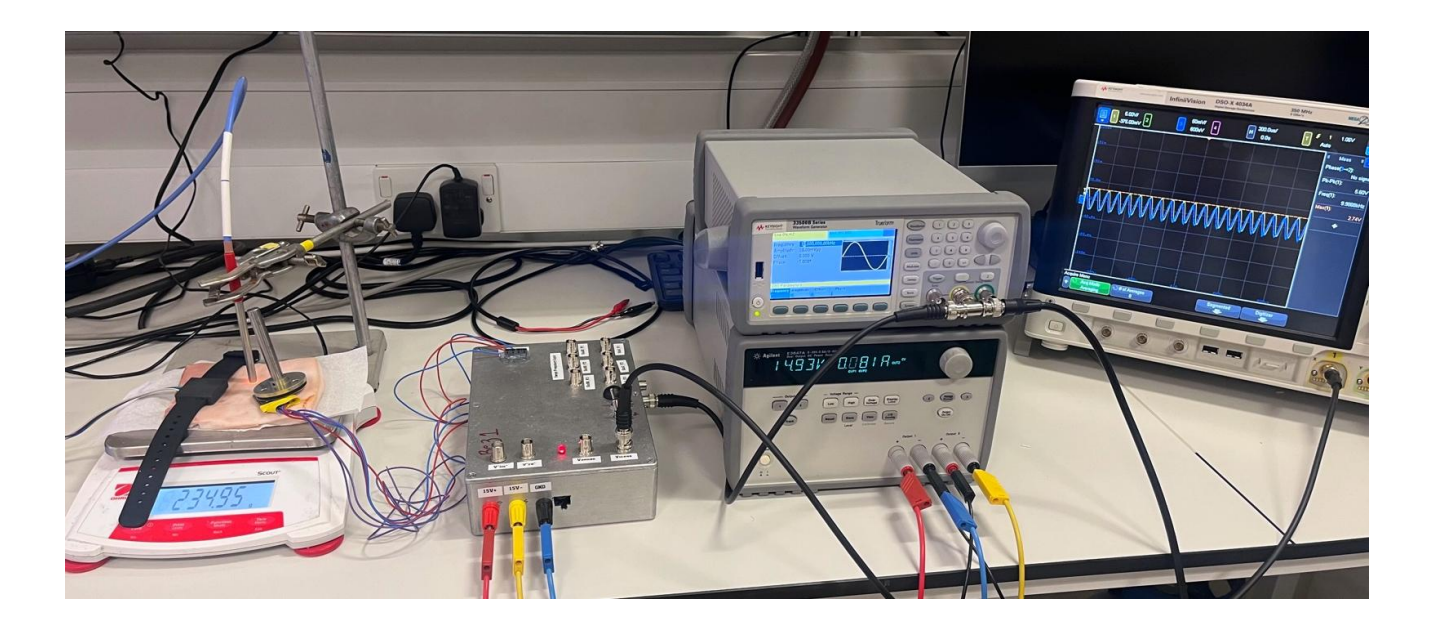


Figure 3. 2b The experimental set -up for multimodal experimental skin assessment [81].

The current injection electrodes ($E_{1,4}$) were spaced 3 mm apart, whereas the voltage measurement electrodes ($E_{2,3}$) were positioned with a 2 mm separation. Theoretically, the penetration depth is approximately equal to half the inter-electrode distance[23]; thus, the approximate sensing depth was 1.5 mm. Given that the average skin thickness is less than 6 mm [82], [83], [84], this sensor predominantly covered the top layers of the skin.

3.2 Design and Development of the Optical Sensor.

A multi-wavelength optical sensor was designed and developed, comprising 4 LED wavelengths and a single central photodiode. The photodiode employed in this experimental configuration was the LAPD-09-17-LCC, a photodetector with a large surface area based on InGaAs (indium gallium arsenide) semiconductor technology. InGaAs sensors are known to have high sensitivity and responsiveness within the wavelength range spanning 900 nm to 1700 nm, appropriate for the LEDs selected.

The selected light-emitting diodes (LEDs) were within the near-infrared wavelength range, i.e., 975 nm, 1050 nm, 1300 nm, and 1450 nm, each equipped with a dome lens. Among these, the 1050nm LED was characterized as the reference wavelength due to its minimal interference from water absorption bands at that specific wavelength [85].

A 3D-printed casing enclosure was created to surround the printed circuit board (PCB) comprising the optical sensor in order to provide a consistent spacing for an optical window whilst permitting minimization of the occlusion effects due to direct skin contact. The optical window utilized was a Raman-grade calcium fluoride (CaF2) window, permitting near-infrared wavelengths to pass through without significant absorption [86]. Watch straps were attached

to the PCB casing to allow the sensor to be used as a wearable device on the wrist. The final wearable optical sensor and the 3D-printed casing can be seen in Figure 3.3.



Figure 3. 3 Optical wearable sensor connected to the ZenPPG processing system.

The developed optical sensor was interfaced with a processing unit named ZenPPG[87]. This ZenPPG system encompasses essential components for producing the output signals, including a transimpedance amplifier circuit for converting the photodiode's output current into a corresponding voltage signal, current sources responsible for supplying power to the LEDs in a multiplexed manner, and a composite board structure housing a microcontroller, along with power distribution components. The output of the ZenPPG processing system was connected to a computer via a data acquisition card (DAQ) (NI USB-6212), facilitating data pre-processing and a graphical representation of the results using LabVIEW software.

3.3 Ex vivo measurements using Bioimpedance and Optics.

A sample of porcine skin was secured and cut to remove any extraneous adipose or connective tissue. The skin sample had a thickness of 3 mm, consisting of the skin layer and a thin layer of fat. In order to establish optimal hydration, the sample was placed in a humidity chamber set at a controlled relative humidity (RH) of 90%, with the temperature maintained at 25 °C over a duration of 12hrs. Porcine skin is a suitable model for testing skin hydration measurement devices due to its high similarity to human skin in terms of optical properties and tissue layer composition. It offers reproducibility and consistency, making it appropriate for use in controlled ex vivo experiments [88].

Once the sample had achieved its augmented hydration level, it was placed directly onto an analytical scale, where its initial gravimetric measurement was recorded. In the initial 120 min of the experiment, porcine skin bioimpedance measurements from bipolar and tetrapolar electrode configurations were taken, as shown in Figures 3.4 and 3.5, respectively, where

data recorded at 20 min intervals are indicated by the markers and a spline interpolant was used to generate the data trend traces. Measurements were carried out for frequencies of 1 kHz, 5 kHz, and 10 kHz. The selection of frequencies was influenced by the bandwidth constraints of the conductivity sensor and the impedance system and were lower than the typical maximum bandwidth of corneometers (about 0.9–1.2 MHz), but within range of the lower end of their reported bandwidth [89][90] making the chosen values relevant.

As anticipated, in all cases, impedance increased over time, reflecting transepidermal water loss from the surface of the porcine skin. The impedance values at 5 kHz and 10 kHz were lower, which was attributed to the decreased reactance of the tissue's reactive impedance component at higher frequencies. Notably, the bipolar configuration (denoted as B in the legend) exhibited higher impedance baseline values compared to the tetrapolar measurements (denoted as T), indicating the influence of electrode/electrolyte interface impedance. The impedance variation over the course of the experiments seemed more pronounced in the tetrapolar results.

The overall impedance variation in each case was better illustrated through the plotting of the percentage impedance magnitude increase, shown in Figure.3.6 and 3.7. for the bipolar and tetrapolar configurations, respectively. The percentage increase for each data set was calculated using the formula in Eq. (3.3):

Percentage Increase =
$$\frac{\text{Final Value-Starting Value}}{\text{Starting Value}} \times 100$$
 3.3

A percentage increase of >21% in impedance magnitude was observed in both cases of electrode configuration as can be seen in Figure.3.6 and Figure.3.7. However, the bipolar configuration exhibited a lower percentage increase in impedance at lower frequencies. This can be attributed to the domination of electrode to electrolyte effect of bipolar configuration which is more pronounced at lower frequencies[63].

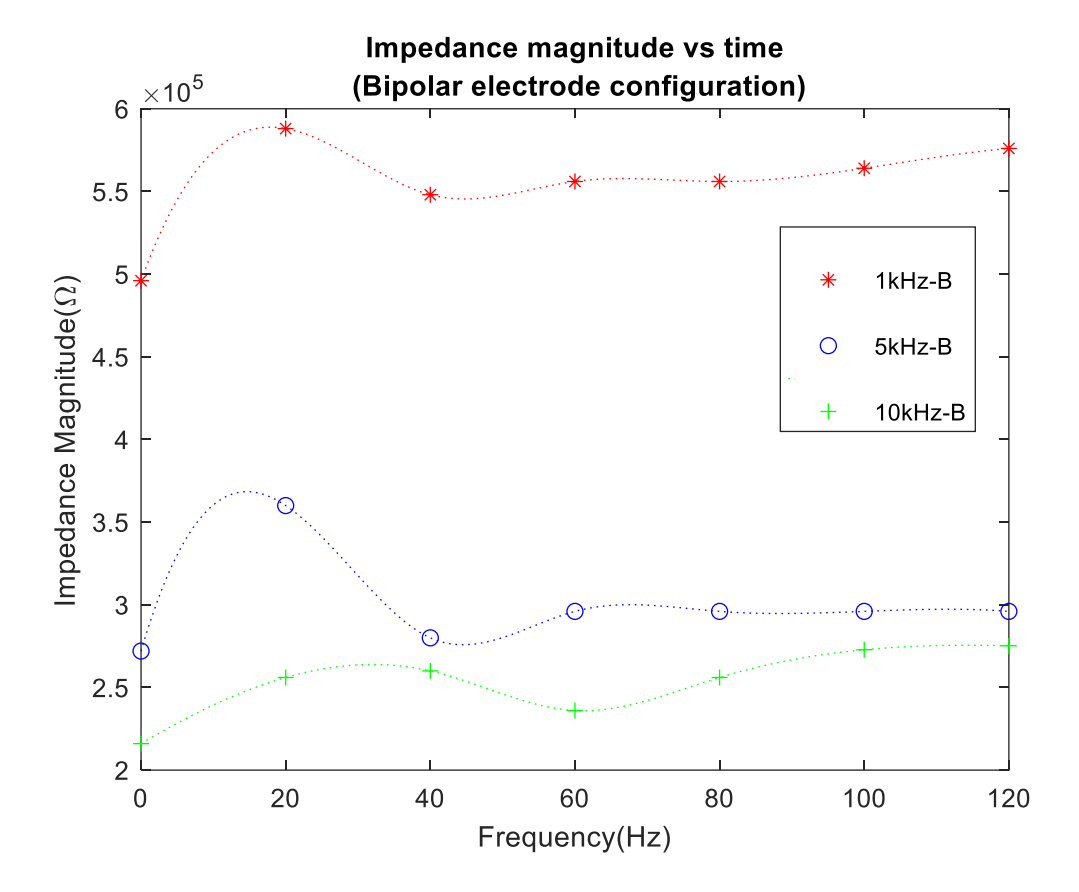


Figure 3. 4 Impedance magnitude vs. time for bipolar electrode configuration.

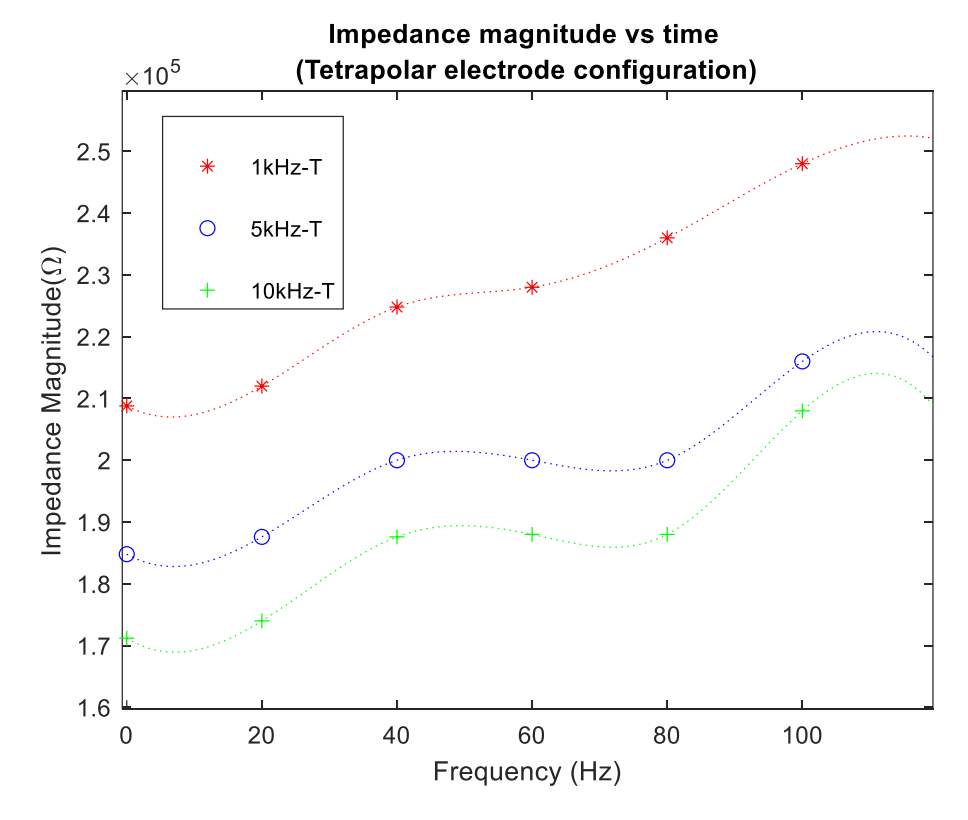


Figure 3. 5 Impedance magnitude vs. time for tetrapolar electrode configuration

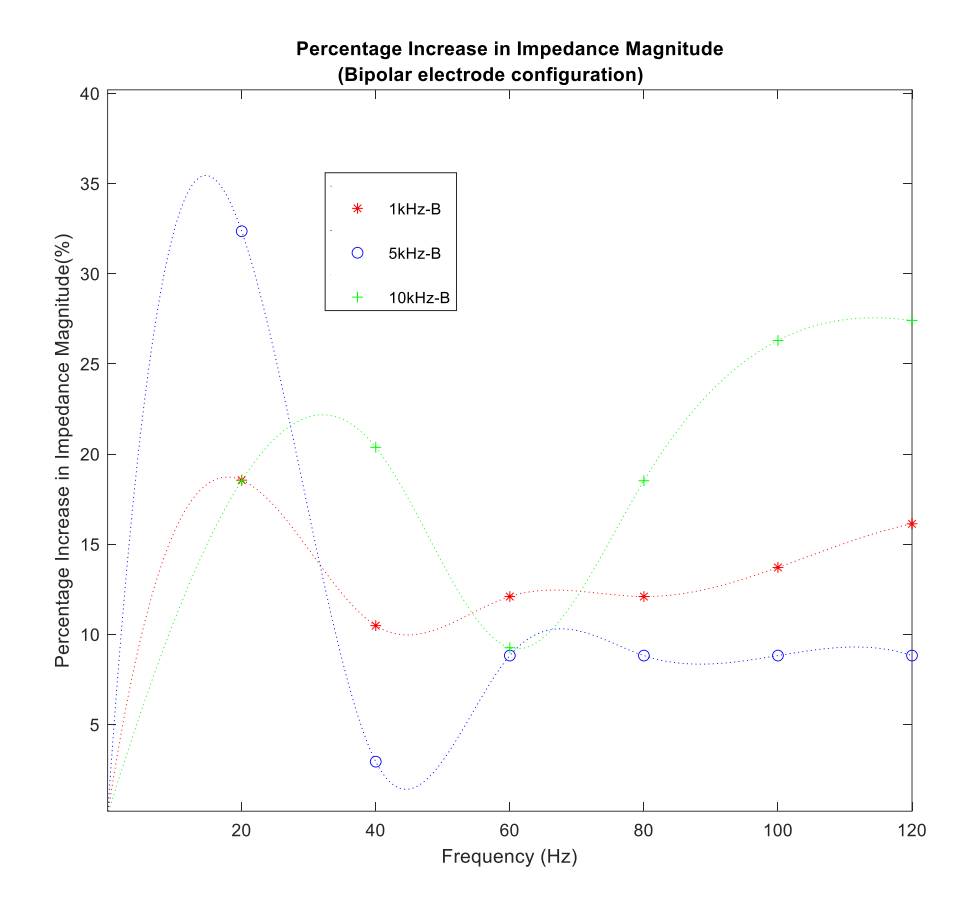


Figure 3. 6 Percentage increase in impedance magnitude for bipolar electrode configuration

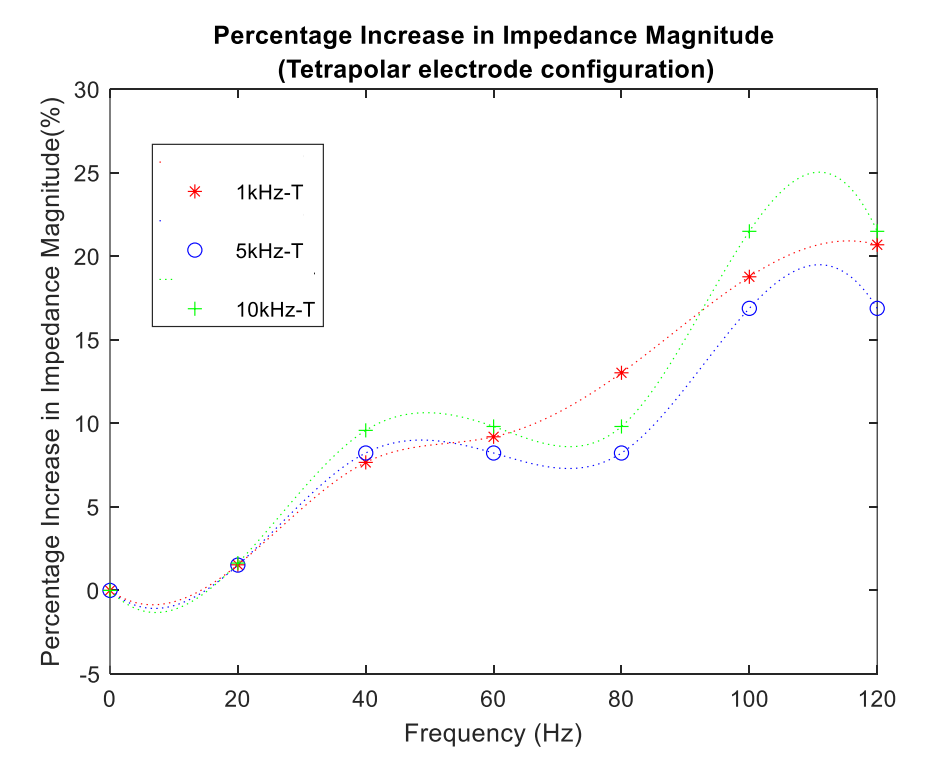


Figure 3. 7 Percentage increase in impedance magnitude for tetrapolar electrode configuration

At the same time, measurements were recorded with the optics sensor probe however for 6hrs. An upward-sloping correlation was evident in the voltage measurements over the total experimental duration. This was consistently observable across all four distinct wavelengths, with the least perceptible variation recorded at 1050 nm, indicating a 0.02 V increment, while the most significant alteration was at 1450 nm, reflecting a pronounced 0.15 V increase, and, thus, an increased rate of change. This is consistent with the established literature, which suggests the presence of a distinct and significant water absorption peak at 1450 nm[91]. This is illustrated in Figure 3.8.

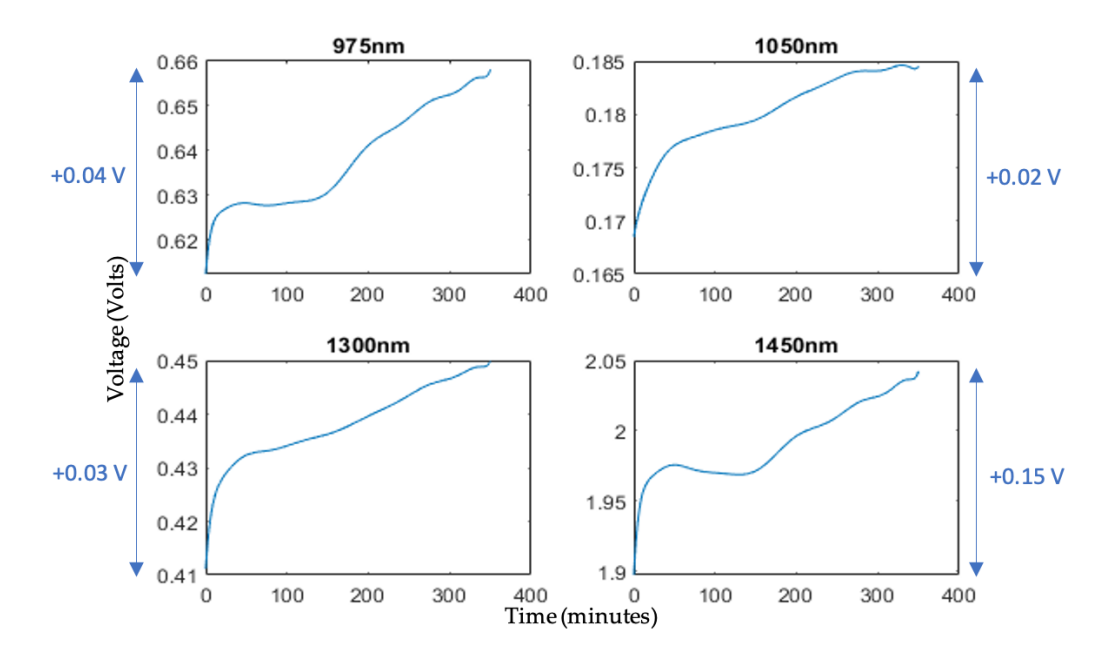


Figure 3. 8 Raw voltage output from optical sensor for selected LED wavelengths

Furthermore, the Corneometer was used to assess the hydration status of the porcine skin sample at the start and end of the experiment. Hydration results from Corneometer furthers validates the bioimpedance measurements with result shown in Figure 3.9. It can be observed from Figure 3.9 that average hydration index before the desorption test and ideally wet porcine skin was more than that observed after the desorption, further confirming the results obtained in the experiment.

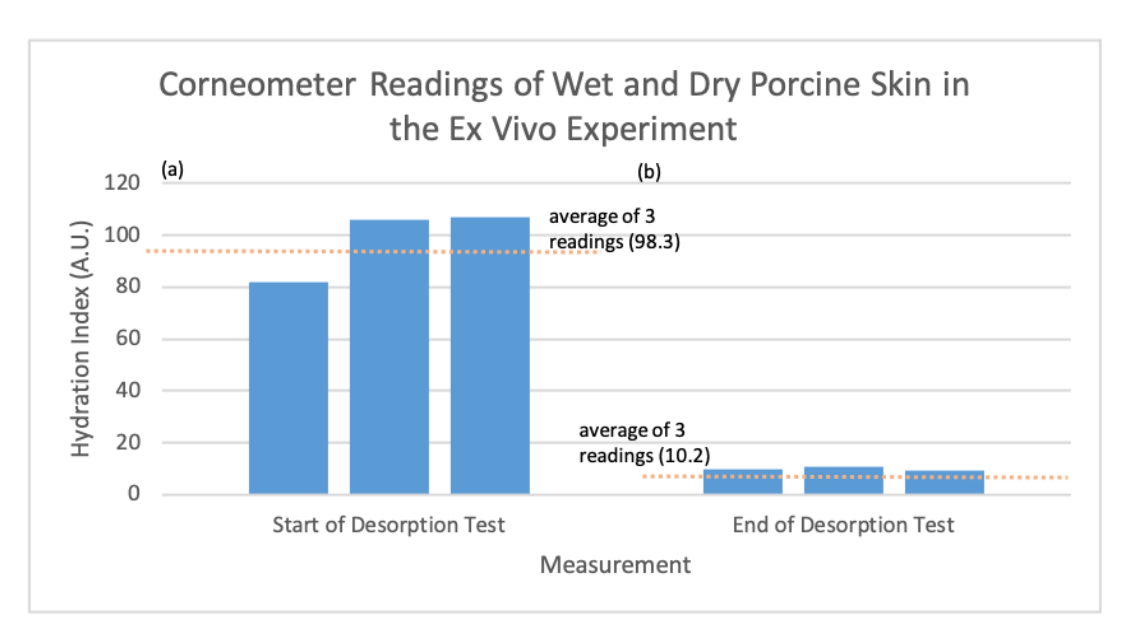


Figure 3. 9 Corneometer output readings for porcine skin sample (a) before and (b) after the ex vivo desorption experiment

3.4 In-Vivo Experiment.

The in vivo indicative case study was an investigation aimed at further validating the efficacy of the developed bioimpedance measurement system when applied to human skin. Two conditions were examined on the forearms of the participants: dry skin (baseline) and damp skin (simulating external influences and changes in water content). Bioimpedance measurements were performed at 1 kHz, while optical sensor measurements were also taken at the wavelength of 1450 nm.

The introduction of ionized water on the skin resulted in a reduction in the measured impedance magnitude. This can be attributed to the substantial influence of dissolved ions on the electrical conductivity of water, providing it with the capacity to conduct electricity. The anticipated decrease in impedance magnitude when ionized water is applied to the skin aligned with corneometer measurements, indicating an increase in hydration levels following water application. Trends observed from the optical sensor output presented a decline in measured voltage with increased hydration, analogous to the bioimpedance sensor.

Figure.3.10 presents a bar chart illustrating measurements from the three systems. Notably, under dry skin conditions, bioimpedance measurements was adopted here and it displayed a higher impedance value for dry skin than for damp skin, which was attributed to decreased ionic presence on the skin surface due to reduced water content. Corneometer values were higher for damp skin than dry skin, as anticipated due to increased capacitance resulting from elevated water levels on the skin surface. Optical measurements exhibited higher reflected voltage for dry skin compared to damp skin, indicating reduced light absorption.

In Vivo Results - Comparison of Techniques in Different Conditions

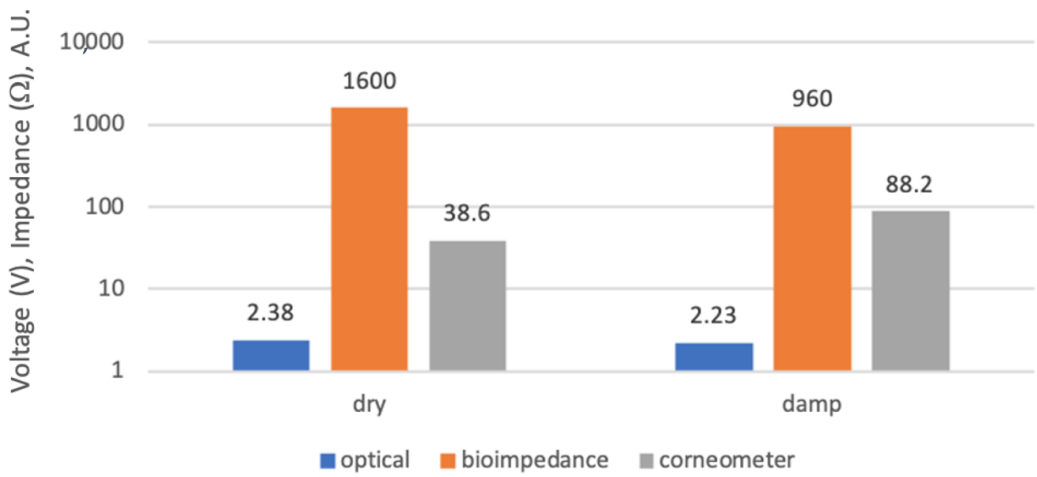


Figure 3. 10 Comparison of outputs from all techniques for in vivo experiment. Bioimpedance measurement here is Tetrapolar

3.5 Conclusion on Chapter 3.

This chapter presents an analysis of skin hydration measurements using bioimpedance, validated through experimental testing alongside an optical sensor. The results from both methods were compared with the Corneometer, the gold standard for hydration measurement. Findings indicate that bioimpedance demonstrates greater sensitivity to hydration changes and better dynamic range than the optical sensor.

A hybrid measurement approach, combining the strengths of both bioimpedance and optical sensors, holds promise for an improved hydration monitoring system. Increasing the scanning frequency of bioimpedance beyond the range of the Corneometer could enhance depth profiling and measurement accuracy. Furthermore, adopting a multifrequency bioimpedance approach would enable hydration assessment at various skin depths, creating a detailed hydration profile across skin layers.

Also, the bandwidth limitation of the bioimpedance circuit used for this experiment further restricts the ability to scan deeper layers of the skin. This highlights the need for a system capable of scanning at higher frequencies to achieve effective skin depth profiling while maintaining accuracy.

Chapter 4 will explore bioimpedance instrumentation in greater depth, providing a mathematical analysis to identify potential error sources and discussing strategies to optimize both measurement accuracy and bandwidth.

Chapter 4

Bioimpedance instrumentation (Drive Circuit).

Determining the transfer impedance of a biological material requires injecting a predetermined low-amplitude constant current. As previously noted, this is typically ≤ 0.5 mA for low-frequency tissue applications (ideally below 5 kHz)[1], and ≤ 1 mA for higher frequency tissue applications, above the aforementioned frequency [2]. The resulting voltage is then measured, and the impedance values are derived using Ohm's law. Voltage sources can also be used, however current sources are preferred due to being a safer procedure[59]. Most bioimpedance systems use a Voltage-Controlled Current Source (VCCS) that converts a sinusoidal voltage (V_{in}) into a current (I_{out}) with theoretically infinite output impedance (Z_{out}). This high impedance ensures that the current magnitude remains constant and is unaffected by variations in the load impedance. Figure 4.1 illustrates the ideal equivalent circuit model of VCCS, with injection electrodes Z_{e1} and Z_{e2} delivering constant current into a load Z_{L} .

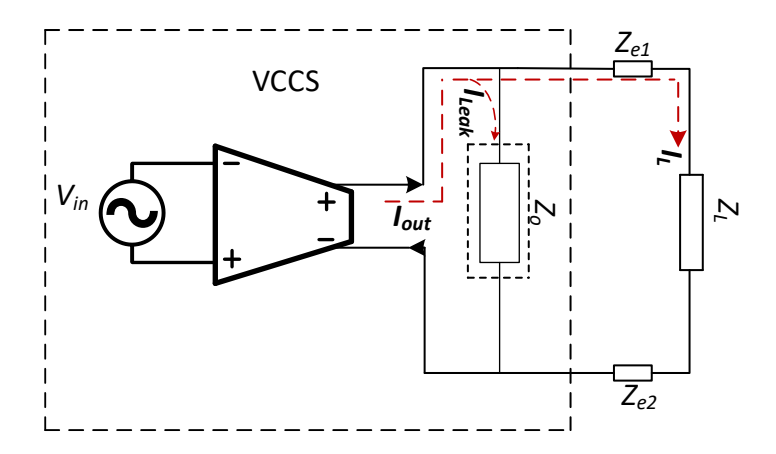


Figure 4. 1 equivalent circuit model of VCCS [92].

Further analysing the circuit in Figure 4.1, the total impedance Z_{total} is a parallel combination of output impedance and the series combination of the electrode impedances and the load impedance. I_{leak} is the leakage current through the output impedance of the current which ideally should be zero if Z_o is infinite.

$$\frac{1}{Z_{total}} = \frac{1}{Z_o} + \frac{1}{Z_{e1} + Z_L + Z_{e2}} \tag{4.1}$$

$$I_{leak} = I_{out} \frac{Z_{e1} + Z_L + Z_{e2}}{Z_o + (Z_{e1} + Z_L + Z_{e2})}$$
(4.2)

$$I_L = I_{out} \frac{Z_o}{Z_o + (Z_{e1} + Z_L + Z_{e2})}$$
 (4.3)

With Z_o approaching infinity

$$Z_o >> Z_{e1} + Z_L + Z_{e2}$$
 (4.4)

$$I_{leak} \approx I_{out} \frac{Z_{e1} + Z_L + Z_{e2}}{Z_o} \tag{4.5}$$

$$I_{leak} \approx 0 \tag{4.6}$$

$$I_L \approx I_{out} \frac{Z_o}{Z_o} = I_{out} \tag{4.7}$$

It can be seen from the analytical equation from eq.4.1 to eq.4.7 that the output current I_{out} equals the current flowing through the load with infinite Z_o .

4.1 Howland Current Source (HCS).

The Howland current source is widely used in designing current sources due to its bidirectional output, relatively high output impedance, and stability[93]. Figure 4.2 below shows the basic configuration of Howland current source.

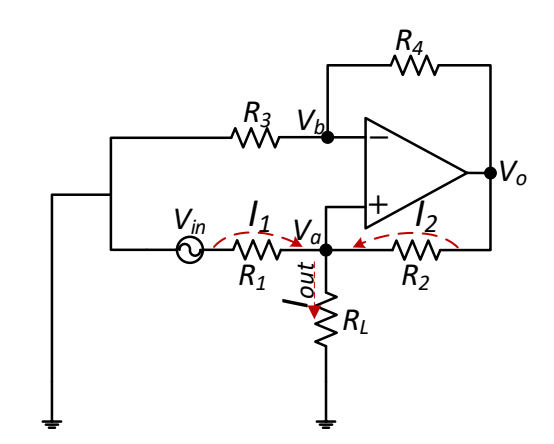


Figure 4. 2 Basic Howland current source (BHCS) [92].

Analysing, Figure 4.2

Assuming $V_a = V_b$

$$V_b = \frac{V_0 * R_3}{R_3 + R_4} \tag{4.8}$$

Assuming that the resistors are perfectly matched i.e $R_1=R_2=R_3=R_4$

$$V_a = V_b = \frac{V_o}{2} \tag{4.9}$$

$$I_1 = \frac{V_{in} - V_a}{R_1}$$
 4.10

$$I_2 = \frac{V_0 - V_a}{R_2} \tag{4.11}$$

$$I_{out} = \frac{V_{in} - V_a}{R_1} + \frac{V_o - V_a}{R_2}$$
 4.12

Substituting for V_a in eq.4.12

$$I_{out} = \frac{V_{in} - \frac{V_o}{2}}{R_1} + \frac{V_o - \frac{V_o}{2}}{R_2}$$
 4.13

Since $R_1 = R_2$, R_2 could be substituted for R_1

$$\frac{V_{in} - \frac{V_o}{2}}{R_1} + \frac{V_o - \frac{V_o}{2}}{R_1}$$
 4.14

Current through the load

$$I_{out=} \ \frac{V_{in}}{R_1} = I_L$$

4.15

Following the assumptions:

If
$$V_{in} = 1V$$

$$R_1 = R_2 = R_3 = R_4 = 50 \text{K}\Omega$$

$$R_L = 10 \text{K}\Omega$$

$$I_{out=} \frac{V_{in}}{R_3} = 20 \mu A$$

$$V_a = I_{out*} R_L = 1V \text{ for } R_L = 50 \text{K}\Omega.$$

Following eq.4.9, $2 * V_a = V_o$

$$V_o = 2V$$
.

One of the main drawbacks of basic Howland current source as shown in Figure 4.2 is inefficiency and especially when driving a high load. Voltage output of basic Howland current source is dependent on the load and, as such, as the load increases, the op amp output voltage increases and might have the op amp output saturated, more power is wasted unlike EHCS. Additionally, the Enhanced Howland current source is capable of driving more current into the load, as demonstrated in the analysis below.

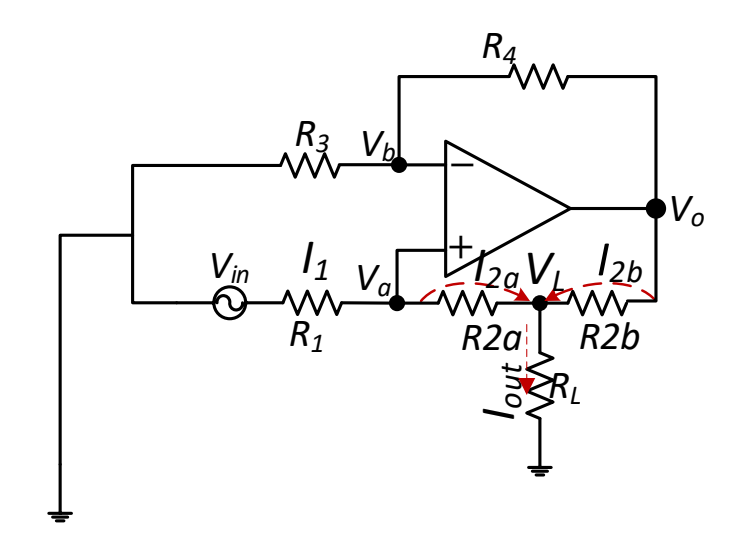


Figure 4. 3 Enhanced Howland current source (EHCS) [92].

In the Enhanced Howland current source as shown in Figure 4.3, it can be observed that the positive feedback resistor R2 was split into R2a and R2b and the transconductance determined by R2b. As such, the ratio of the feedback resistors becomes (R3/R4) = (R1/R2a+R2b) instead of (R3/R4) = (R1/R2) as in the case of BHCS. Op amp output voltage in EHCS is independent of the voltage across the load. This can further be exemplified below.

If the resistors are perfectly matched i.e

$$R_3 = R_4$$
, and $R_1 = R_{2a} + R_{2b}$ 4.16

Recall that in eq.4.9 $V_a = V_b = \frac{V_o}{2}$

Assuming that $\mathit{V}_a = \mathit{V}_b$ as specified in eq.4.9, current through R_1 and $\mathit{R}2_a$

$$I_1 = \frac{V_{in}}{R_1 + R_{2a}} \tag{4.17}$$

current through $R2_h$

$$I_2 = \frac{V_0}{R_{2b}}$$
 4.18

$$I_{out} = I_1 + I_2 = \frac{V_{in}}{R_1 + R_{2a}} + \frac{V_o}{R_{2b}}$$
 4.19

Recall that in eq.4.9 $V_o = 2V_a$

$$V_o = 2V_a = 2 * I_1 * R_{2a}$$
 ($I_1 \approx I_{2a}$ for a virtual grad reference now at V_L) 4.20

Substituting for I_1 in eq.4.20

$$V_o = \frac{2*V_{in}*R_{2a}}{R_1 + R_{2a}} \tag{4.21}$$

Substituting for V_o in eq. 4.18

$$I_2 = \frac{2*V_{in}*R_{2a}}{R_{2b}(R_1 + R_{2a})} \tag{4.22}$$

$$I_{out} = I_1 + I_2 = \frac{V_{in}}{R_1 + R_{2a}} + \frac{2*V_{in}*R_{2a}}{R_{2b}(R_1 + R_{2a})}$$
 4.23

$$I_{out} = \frac{(V_{in} * R_{2b}) + (2 * V_{in} * R_{2a})}{R_{2b}(R_1 + R_{2a})}$$

$$4.24$$

Substituting $R_1 - R_{2a} = R_{2b}$ of eq. 4.16 in the numerator of eq.4.24

$$I_{out} = \frac{V_{in}*(R_1 - R_{2a}) + (2*V_{in}*R_{2a})}{R_{2b}(R_1 + R_{2a})}$$

$$4.25$$

$$I_{out} = \frac{V_{in}*(R_1 + R_{2a})}{R_{2b}(R_1 + R_{2a})}$$

$$4.26$$

$$I_{out} = \frac{V_{in}}{R_{2b}}$$
 where the transconductance determined by $R2b$ 4.27

As such the transconductance gain

$$gm = \frac{I_{out}}{V_{in}} = \frac{1}{R_{2b}} * \frac{R_4}{R_3}$$
 4.28

gm also depends on the feedback the ratio eta_{fb} used and in this case

$$\beta_{fb} = \frac{R_3}{R_3 + R_4} \tag{4.29}$$

$$\frac{1 - \beta_{fb}}{\beta_{fb}} = \frac{R_4}{R_3}$$
 4.30

$$gm = \frac{I_{out}}{V_{in}} = \frac{1}{R_{2b}} * \frac{R_4}{R_3} = \frac{1}{R_{2b}} * \frac{1 - \beta_{fb}}{\beta_{fb}}$$

$$4.31$$

Hence for the same reference voltage V_{in} of 1V, $R_3=R_4$ = 50k Ω , R_1 = 50k Ω , R_{2a} = 49k Ω , R_{2b} = 1k Ω . Using eq.4.16-4.27

 $I_1 = 10.1 \, \mu A$.

 $V_a = 10.1 \,\mu A * 49 \text{k}\Omega = 0.494 \text{V}.$

 $V_0 = 0.989 \text{V}$

 $I_2 = 0.989 \text{mA}$

 $I_{out} = 1 \text{mA}$

It could be seen that with exactly same parameters, Enhanced Howland could drive more current into the load and also the operational amplifier output voltage V_o was half to that obtained in basic Howland current, as such this ensures the amplifier does not saturate and the current source remained within its power supply compliance limits.

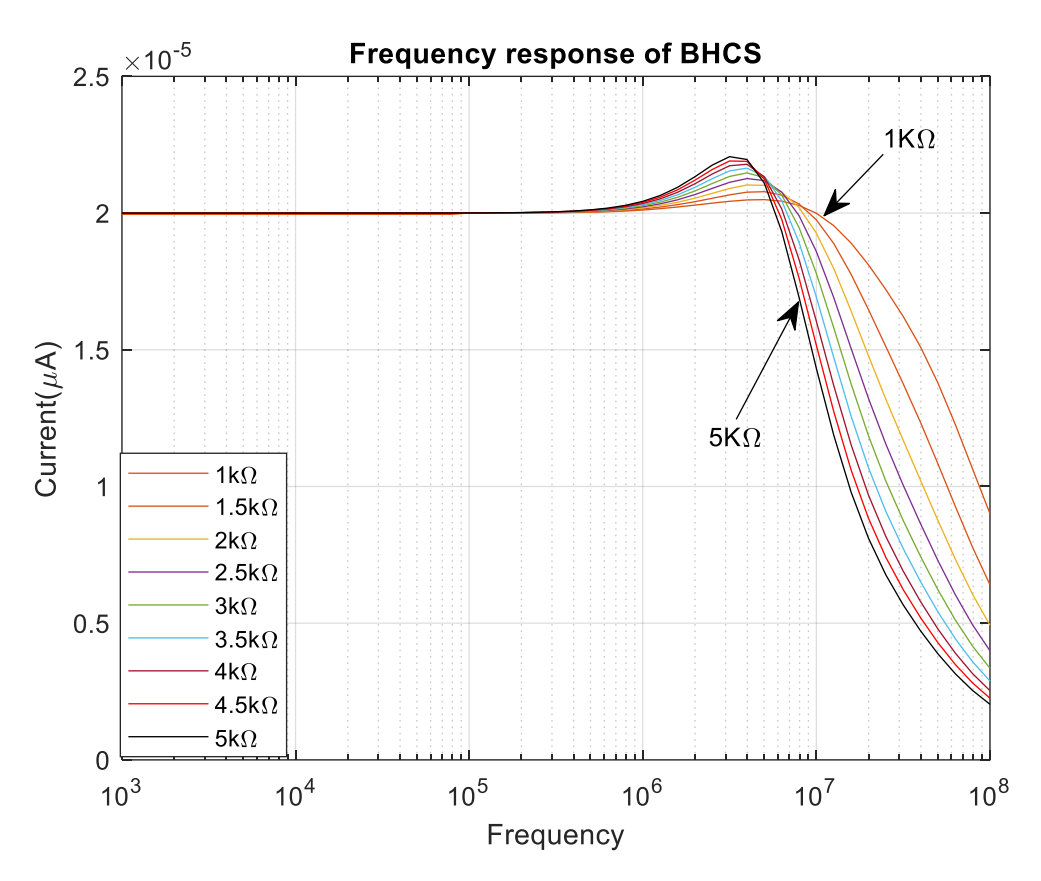


Figure 4. 4 Current output of BHCS for varying resistive Loads.

Figure 4.4 shows the frequency response of BHCS for input reference volage V_{in} of 1V peak, and resistive load voltages spanning from 1K Ω to 5K Ω . The output current I_{out} was notably 20 μ A agreeing with the calculations. In contrast, Figure.4.5 presents the frequency response of the Enhanced Howland Current Source (EHCS), which demonstrates an output current of 1mA for the same load values and parameters as used in the BHCS. This indicates that, with identical parameters, the EHCS is capable of driving a significantly higher current into the load compared to the BHCS. As a result, the current source adapted in this project is a derivative of EHCS.

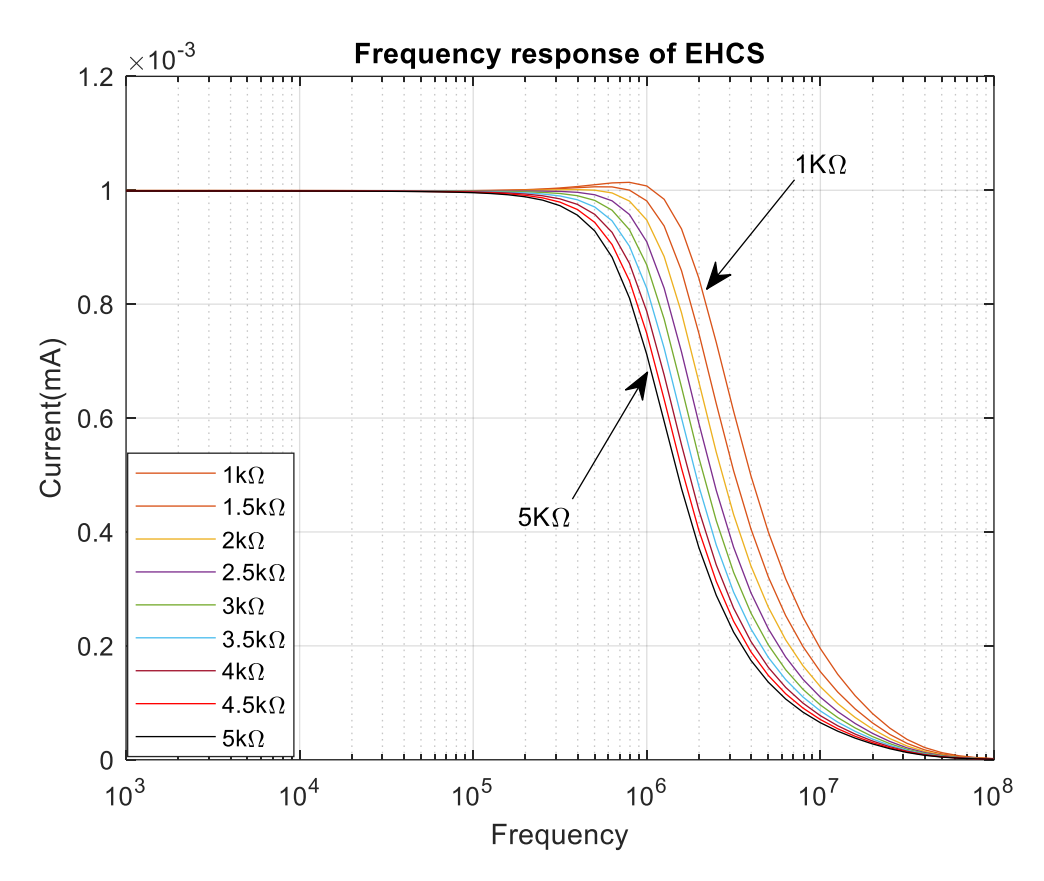


Figure 4. 5 Current output of EHCS for varying resistive Loads

4.2 Sources of Error with Drive Circuit (HCS)

There are many sources of errors and considerations that can potentially degrade the performance of a Howland current source. These include non-idealities of components such as the operational amplifiers, feedback resistors tolerances, printed circuit board layouts, parasitic capacitances, and the op amps circuit's slew rate limitations etc.

4.2.1 Effects of Resistor Tolerance (T) on the output impedance of Howland current source.

Resistor tolerances can impactfully degrade the performance of HCS by degrading the output impedance of the HCS following eq.4.32

$$Z_o = \frac{(R_1 + R_2 - R_{2b})//R_{2b}}{1 - \beta_{fb}} * \frac{(1 - T)^2}{\pm 4T}$$
 4.32

Eq.4.32 indicates that the output impedance of the Howland Current Source (HCS) is directly affected by the tolerance of the matching resistors[93]. Specifically, resistors with higher tolerance values will result in a decreased output impedance. In contrast, resistors with very low tolerance values will maintain a higher output impedance, thereby improving the overall performance of the HCS. This relationship underscores the importance of selecting precision

resistors with minimal tolerance to ensure optimal impedance characteristics and reliable operation of the current source.

The tolerance of the resistors also leads to an imbalance between the positive and negative inputs of the Howland Current Source (HCS), which adversely affects the Common-Mode input voltage the circuit. As shown in Equation 4.33, the CMRR of the HCS is inversely proportional to the tolerance of the feedback resistors. This means that as the tolerance of the resistors increases, the CMRR decreases, resulting in reduced ability to reject common-mode signals. Conversely, using resistors with lower tolerance enhances the CMRR, thereby improving the system's performance in rejecting common-mode noise and maintaining signal integrity. Therefore, selecting precision resistors with minimal tolerance is crucial for achieving high CMRR and ensuring the accurate and stable operation of the HCS[93], [94].

$$CMRR = 1 + \frac{1}{2T} * \left(1 + \frac{R_{2a}}{R_1}\right) \tag{4.33}$$

4.2.2 Effects of Mismatches in the Resistor Network in the accuracy of HCS output current.

While the non-ideal behaviour such as the input offset voltages of the op amp can degrade the performance of HCS, however mismatches in the feedback and resistor network can also induce some error in the output current[92]. i.e if

$$\frac{R_3}{R_1} \neq \frac{R_4}{R_{2a} + R_{2b}}$$

This can induce an error term and imbalance according to eq.4.34

$$I_{out} = \frac{1}{R_{2b}} * \frac{1 - \beta_{fb}}{\beta_{fb}} (V_{in}) - \frac{1}{R_{2b}} (R_1 I_{b+} - R_3 I_{b-})$$

$$4.34$$

Eq.4.34 shows that the input bias currents of the op amp and respectively I_{b+} and I_{b-} could lead to an error in the output current if there is a mismatch in the resistors.

4.2.3 Degradation of Output Impedance of HCS by Parasitic Capacitances.

The most crucial characteristic of current sources is the accuracy of their output current over a range of frequencies[58], [95], [96], [97]. To achieve this, the output impedance must be very high, ideally approaching infinity. However, several factors introduce parasitic capacitance at the output, including cable capacitances, stray capacitances from VCCS and tracks, and the sense circuit. These parasitic capacitances reduce the output impedance at higher frequencies and resulting in a decay of the current source's performance.

While some of the sources of errors of Howland current source can be mitigated with appropriate component selection, the decay in output impedance of a HCS is often due to

multiple factors, many of which can be beyond the designer's control. This has led to the development of various HCS variants aimed at improving output impedance.

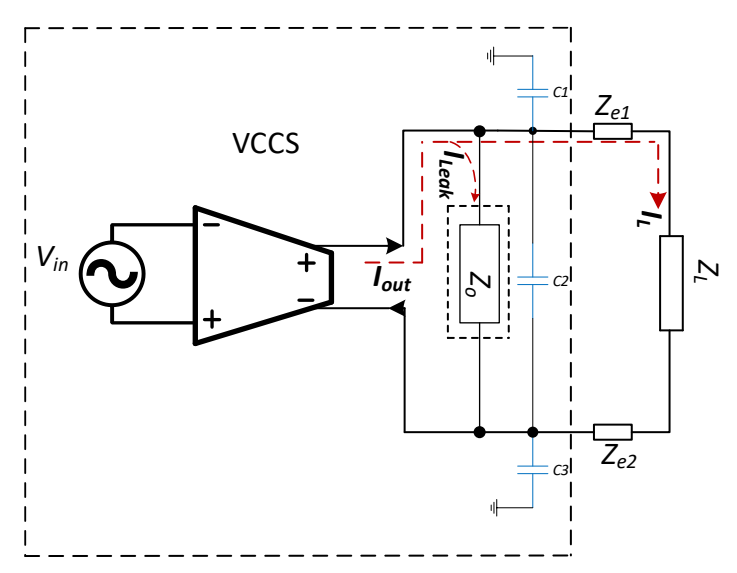


Figure 4. 6 Block diagram of VCCS with the parasitic capacitances C1, C2 and C3 C3 [1].

Analysing the circuit in Figure 4.6

$$XC_1//XC_3 = (C_1 + C_3) = C_{cm}$$
 for frequencies >>1MHz 4.35

As such electrode contact impedances Z_{e1} , Z_{e2} and Z_L will not to taken into account when accounting for the output impedance in this calculation.

$$Z_o / / X C_2 = \frac{Z_o * X C_2}{Z_o + X C_2}$$
 4.36

$$Z_o / / X C_2 = \frac{\frac{Z_o}{j\omega C_2}}{Z_0 + \frac{1}{j\omega C_2}}$$
 4.37

$$Z_o//XC_2 = \frac{\frac{Z_o}{j\omega C_2}}{\frac{Z_oj\omega C_2+1}{j\omega C_2}}$$

$$4.38$$

$$Z_o / / X C_2 = \frac{z_o}{z_{oj} \omega c_2 + 1}$$
 4.39

$$XC_{cm} = \frac{1}{j\omega C_{cm}}$$
, $XC_2 = \frac{1}{j\omega C_{diff}}$ 4.40

Total output Impedance Z_{oT} (i.e Z_o with the reactance of the parasitic capacitances)

$$Z_{oT} = \frac{Z_o}{Z_o j \omega C_{diff} + 1} / / \frac{1}{j \omega C_{cm}}$$
 4.41

$$Z_{oT} = \frac{\frac{Z_o}{(Z_o)\omega C_{diff} + 1)j\omega C_{cm}}}{\frac{Z_oj\omega C_{cm} + Z_oj\omega C_{diff} + 1}{j\omega C_{cm}(Z_oj\omega C_{diff} + 1)}}$$

$$4.42$$

$$Z_{oT} = \frac{Z_o}{Z_oj\omega C_{cm} + Z_oj\omega C_{diff} + 1}$$
 4.43

From the eq.4.43, at high frequencies, Z_{oT} approaches zero and at very low frequencies, $Z_{oT} \approx Z_o$.

4.3 Output impedance compensation of HCS

There have been several modifications and variants of EHCS in bid to improve the output impedance of the HCS and as such improve the accuracy. Some of which are the buffered feedback topology, negative impedance converter, generalised impedance converter, mirrored enhanced Howland current source.

4.3.1 Buffered feedback Topology

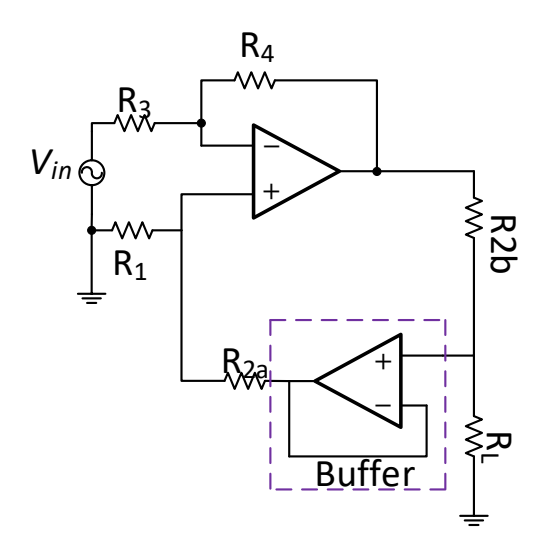


Figure 4. 7 Buffered feedback topology for HCS [98]

In the buffered feedback topology as shown in Figure 4.7, the buffer configured in the feedback path maintained a virtual ground point at the inputs. Effectively increasing the impedance in the positive feedback loop of the current source that otherwise would have caused instability if this was to be done by the using large values of resistors [93]. Following equation 4.44 Click or tap here to enter text..

$$Z_o = (R_{2b}//(R_1 + R_{2a} - R_{2b}))(1 + A\beta_{fb})$$
4.44

Where A is the open loop gain of the op. amp. Thus, it can be seen that with increase in the positive resistance R_{2a} , the output impedance increases.

4.3.2 Negative Impedance Converter (NIC).

The NIC circuit as shown in Figure 4.7 utilizes positive feedback through the capacitor Cn to counter the current flowing into the output parasitic capacitances of the current source. By injecting a current that is 180 degrees out of phase and equal in magnitude to the current flowing into the output parasitic capacitance, the net current flow is effectively reduced to

zero. This cancellation increases the output impedance of the current source, enhancing its performance by mitigating the effects of parasitic capacitance.

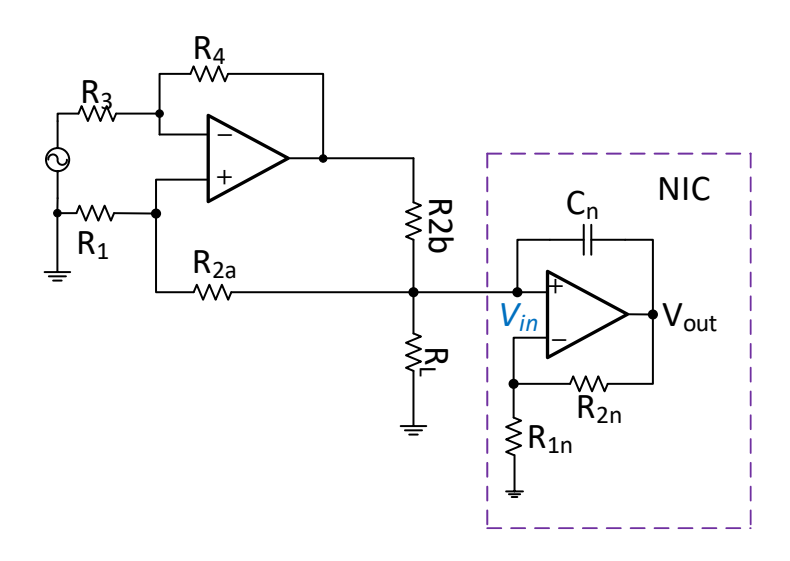


Figure 4. 8 EHCS with negative impedance converter [98]

Further analysing Figure 4.8,

$$V_{out} = \left(1 + \frac{R_{2n}}{R_{1n}}\right) V_{in} \tag{4.45}$$

Current flowing through the feedback capacitor $\mathcal{C}_n \ = \ I_n$

$$I_n = \frac{V_{in} - V_{out}}{Z_c}$$
 where Z_c is the impedance due to the feedback capacitor C_n 4.46

$$I_n = \frac{V_{in} - \left(1 + \frac{R_{2n}}{R_{1n}}\right) V_{in}}{Z_c}$$
 4.47

$$I_n = \frac{V_{in} \left(1 - 1 - \frac{R_{2n}}{R_{1n}}\right)}{Z_c}$$
 4.48

$$I_{n=} -\frac{R_{2n}}{R_{1n}} * \frac{V_{in}}{Z_c}$$
 4.49

$$Z_{NCC} = \frac{V_{in}}{I_n} \tag{4.50}$$

$$Z_{NCC} = \frac{V_{in}}{\frac{-R_{2n_*}V_{in}}{R_{1n}}\frac{V_{in}}{Z_C}}$$
 4.51

$$Z_{NCC} = -\frac{R_{1n}}{R_{2n}} * Z_C 4.52$$

For $R_{2n} = R_{1n}$, the input impedance of the converter thus appears as negative impedance due negative capacitance reactance[99].

$$Z_{NCC} = -Z_c 4.53$$

4.3.3 Mirrored Enhanced Howland Current Source (MEHCS)

The Mirrored Enhanced Howland Current Source is another topology that achieves symmetrical current generation by connecting two Enhanced Howland Current Sources (EHCS) with opposite polarities in series. This configuration is designed to generate both sourcing and sinking currents, resulting in differential voltages across the load.

One of the primary advantages of the MEHCS topology is that it facilitates a truly floating load, meaning the load is electrically isolated from the ground. However, a notable consideration in this design is the effect of the combined output impedances of the individual EHCS units. Since the output impedances of the two EHCS are connected in series, they sum up, effectively increasing the total output impedance that the load experiences.

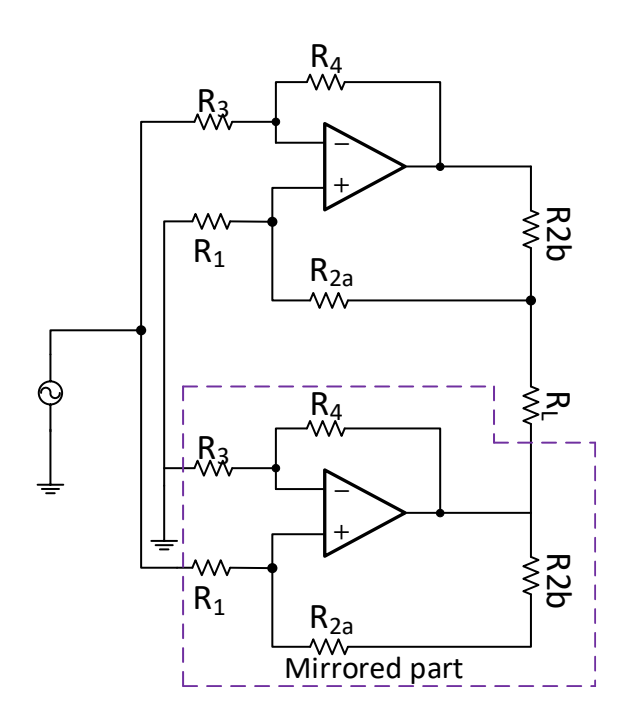


Figure 4. 9 Mirrored Enhanced Howland Current Source (MEHCS) [97]

4.3.4 Generalised impedance converter (GIC).

The GIC-based topology employs two operational amplifiers and five adjustable impedances, configured to provide either a frequency-dependent negative resistance or an inductive behaviour. To cancel the parasitic capacitances at the output of the Current Source, the inductive behaviour of the GIC is preferred. When the reactance of the parasitic capacitance matches the reactance of the GIC-generated inductance, the net current flow becomes zero, resulting in a high impedance at the output of the current source. Figure 4.10 shows the diagram of GIC based HCS topology.

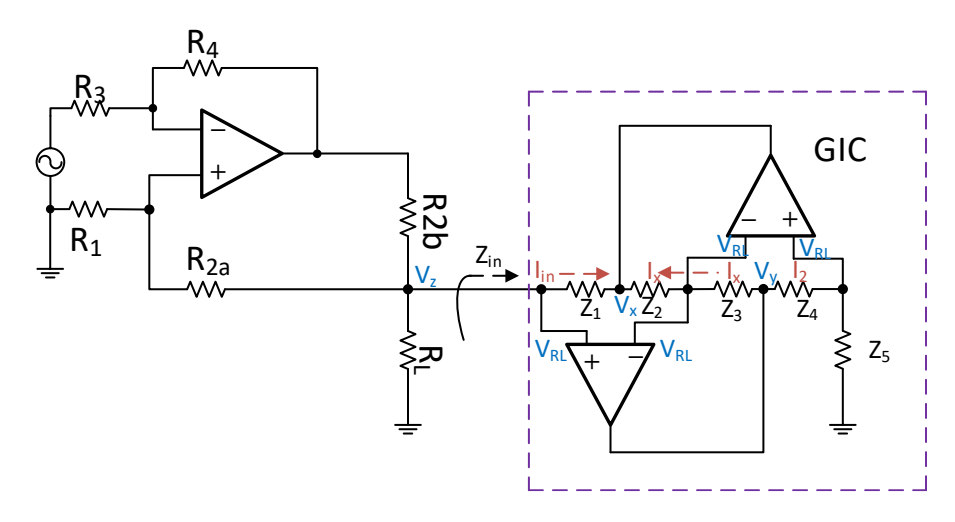


Figure 4. 10 EHCS with GIC for output impedance improvement [98].

Analysing Figure 4.10

$$V_z = I_2 Z_5$$
 4.54

$$V_z = I_{in} Z_{in} 4.55$$

Where \mathcal{Z}_{in} is the input impedance of GIC

$$V_z - V_x = I_{in} Z_{in} = I_x Z_2 4.56$$

$$I_{\mathcal{X}} = \frac{I_{in}Z_1}{Z_2} \tag{4.57}$$

$$V_y - V_z = I_x Z_3 = I_2 Z_4 4.58$$

$$I_2 = \frac{I_X Z_3}{Z_4}$$
 4.59

Substituting equation 4.57 in equation 4.59

$$I_2 = \frac{I_{in}Z_1}{Z_2} \cdot \frac{Z_3}{Z_4} \tag{4.60}$$

Substituting eq.4.54 and eq.4.55 in eq.4.60

$$\frac{V_Z}{Z_L} = \frac{Z_3}{Z_4} \cdot \frac{Z_1}{Z_2} \cdot \frac{V_Z}{Z_{in}}$$
 4.61

$$Z_{in} = \frac{Z_1 Z_3 Z_5}{Z_2 Z_4} \tag{4.62}$$

Assuming $Z_1 = R_1$, $Z_2 = R_2$, $Z_3 = R_3$, $Z_4 = \frac{1}{XC_4}$, $Z_5 = R_5$

$$Z_{in} = \frac{R_1 R_3 R_5 \frac{1}{X C_4}}{Z_2} \tag{4.63}$$

$$L = \frac{R_1 R_3 R_5 C_4}{R_2} \tag{4.64}$$

The output impedances of the Howland current source and the variants is shown in Figure 4.11.

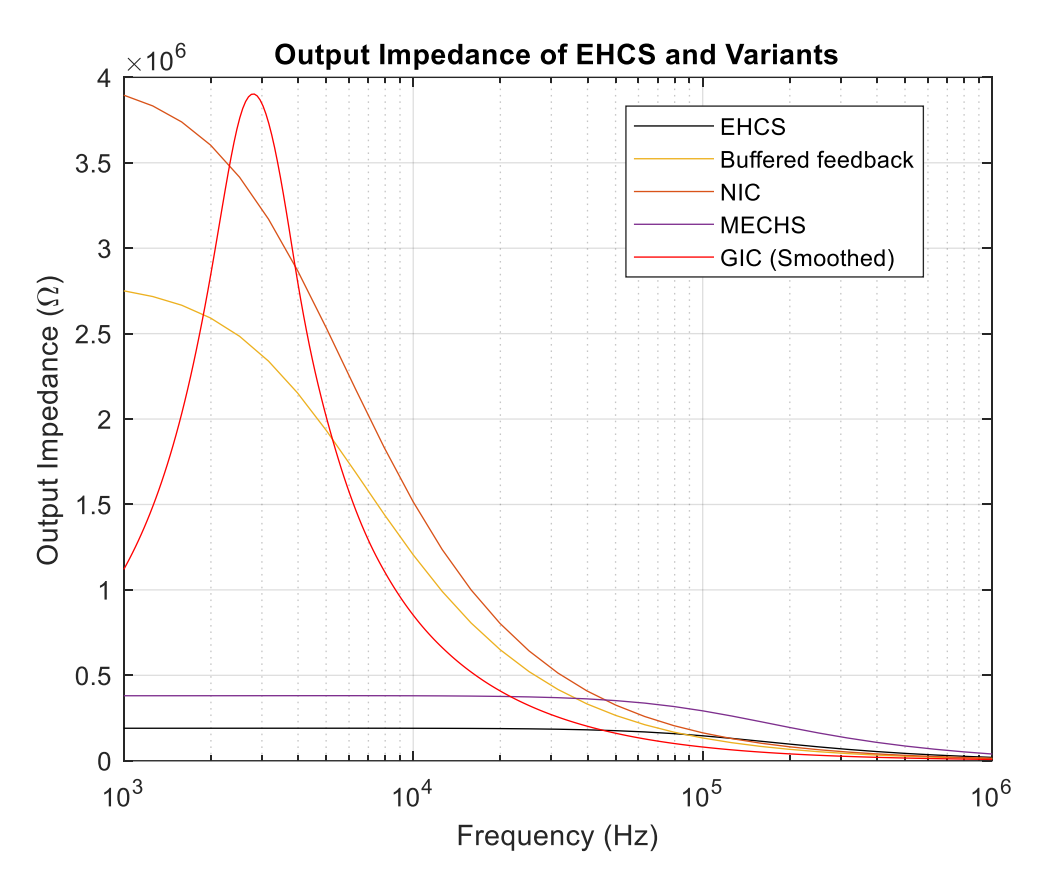


Figure 4. 11 Output impedances of EHCS and the corresponding variants.

To measure the output impedances, the input of the current sources was shorted to ground and an ideal current source was connected at the output and a constant current amplitude of 1mA was injected at the output of the current sources and the output impedances were calculated following equation 4.65-4.66

$$\frac{I_{inj}*Z_L}{Z_L*Z_o} = I_{Zo} 4.65$$

 $I_{Zo} = I_{inj} - I_{ZL}$

$$Z_o = \left(\frac{I_{inj} \cdot Z_L}{(I_{inj} - I_{ZL}) Z_L}\right) \tag{4.66}$$

While NIC and GIC presented with the highest amplitude in output impedance, it could be seen that GIC only has effect on a specified frequency and a change in frequency would need recalculation of the components used. In this case, the output capacitance of interest to cancel was approximately 17pF, and for a centre frequency of 3kHz gives reactive impedance of 3.6M Ω , while for the respective values of $R_1=R_3=R_5=100k\Omega$, C4=100pF, $R_2=600\Omega$ gives reactive impedance of 3.14M Ω . Thus, by matching the parasitic impedance due to parasitic capacitances of the current sources to the impedance due to the inductive behaviour of the GIC, output impedance is improved at the frequency of interest. While most bioimpedance designers concentrate on enhancing the output impedance of the EHCS to improve bandwidth, limitations persist in various topologies. For instance, GIC topologies are

frequency-dependent, and NIC topologies are influenced by the parasitic capacitance of components like electrodes and operational amplifiers. These factors often require recalibration when component characteristics change. The work presented here explores alternative methods to maintain the accuracy of current output amplitude without the need to further increase the output impedance.

4.4 The sense Circuit.

The voltage measured between two electrodes placed on tissue primarily depends on the injected current and the electrical properties of the tissue. Although various topologies exist for bioimpedance measurement systems, they all incorporate a voltage-sensing amplifier to detect the voltage drop caused by the tissue's impedance. Among these, the three op-amp instrumentation amplifier is widely utilized in the front-end of bioimpedance voltage sensing due to its high input impedance, which is achieved through its dual pre-amplifier stages. Additionally, this configuration is highly effective in minimizing common-mode voltage.

4.4.1 Instrumentation Amplifier

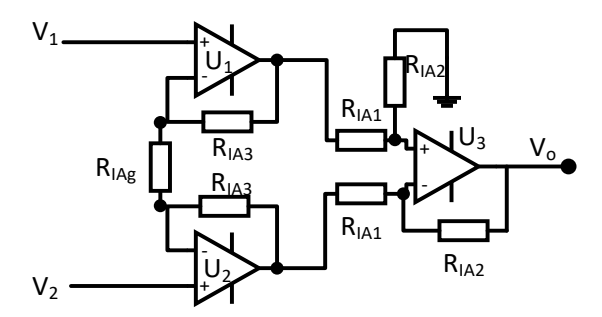


Figure 4. 12 schematic diagram of instrumentation amplifier

In Figure 4.12 V_1 and V_2 are connected to the electrodes which are placed on the subject/tissue and for a common mode signal at both inputs, the net current flow though the gain setting resistors R_{IA3} R_{IAg} and R_{IA3} is zero and hence, no amplification. Since no current flows through R_{IA3} (and, therefore, through both R2 resistors, amplifiers U_1 and U_2 will operate as unity-gain followers (buffers). Since the input voltage at the outputs of amplifiers U_1 and U_2 appears differentially across the three-resistor network, the differential gain of the circuit can be varied by just changing the value of R_{IAg} .

The voltage output from the differential op-amp U3 which is a subtractor, is simply the difference between its two inputs (V_1-V_2) and which is amplified by the gain of A3 can also unity, (assuming that $R_{IA1}=R_{IA2}$). Then we have a general expression for overall voltage gain of the instrumentation amplifier circuit as:

$$V_{o} = (V_{1} - V_{2}) \left[1 + \frac{2R_{IA3}}{R_{IAg}} \right] \left(\frac{R_{IA2}}{R_{IA1}} \right)$$
 4.67

4.4.2 Common Sources of Errors in Instrumentation Amplifiers

The performance and the measurement accuracy of the instrumentation amplifiers could be notably affected by their common sources of errors, some of which are:

4.4.3 Measurement Electrode Impedance mismatch.

Ideally, the common-mode gain of the pre-amplifiers should be zero. To work out the common mode gain, let's assume that there is only a common mode DC voltage of V_{cm} present at the inputs, i.e., $V_1 = V_2 = V_{cm} = 5$ V. As there is no voltage drop across the gain setting resistor R_{IAg} , the voltage on the outputs of each of the amplifiers, U1 and U2, should ideally be equal to V_{cm} . However, Instrumentation amplifiers are not perfect and undesired signals are also amplified due to incomplete rejection of common-mode signals, and an undesired component due to electrode impedance imbalance.

Common mode rejection errors of the instrumentation amplifier were tested with and without electrode impedance (Z_{e1} and Z_{e2}) imbalance connecting to the input of the buffers, U1 and U2. In the first instance where Z_{e1} = Z_{e2} =10k Ω , in the second instance where Z_{e1} =10k Ω and Z_{e2} = 5k Ω . R_{IA1} = R_{IA2} = R_{IA3} = 1k Ω , R_{IAg} = 100k Ω , Vcm =5V and connected as in Figure.4.13 with simulations in LT_Spice.

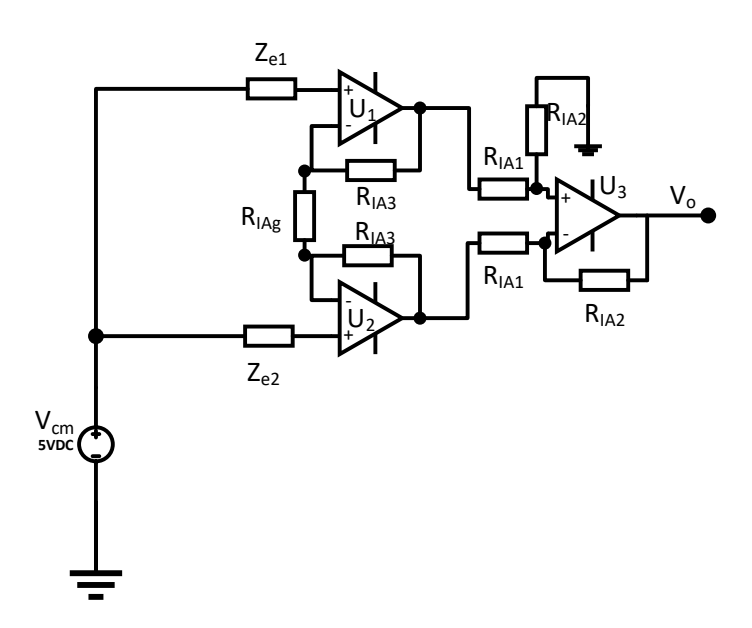


Figure 4. 13 Schematic diagram of instrumentation amplifier with common mode inputs

Figure 4.14 demonstrates that a SPICE simulation of an imbalance in electrode impedance can degrade the common mode rejection of the instrumentation amplifier, leading to the conversion of common-mode signals into differential signals, which then appear at the output. The Figure also shows that when the electrode impedances are equal, the common-mode voltage at the output of the instrumentation amplifier is significantly reduced to $390\mu V$, compared to 3.41mV when the impedances are unequal. This disparity can pose challenges in biosensing applications. However, techniques such as using a tetrapolar electrode

configurations, implementing a high-pass filter at the pre-amplification stage, and employing FET-input stage op-amps can mitigate these effects

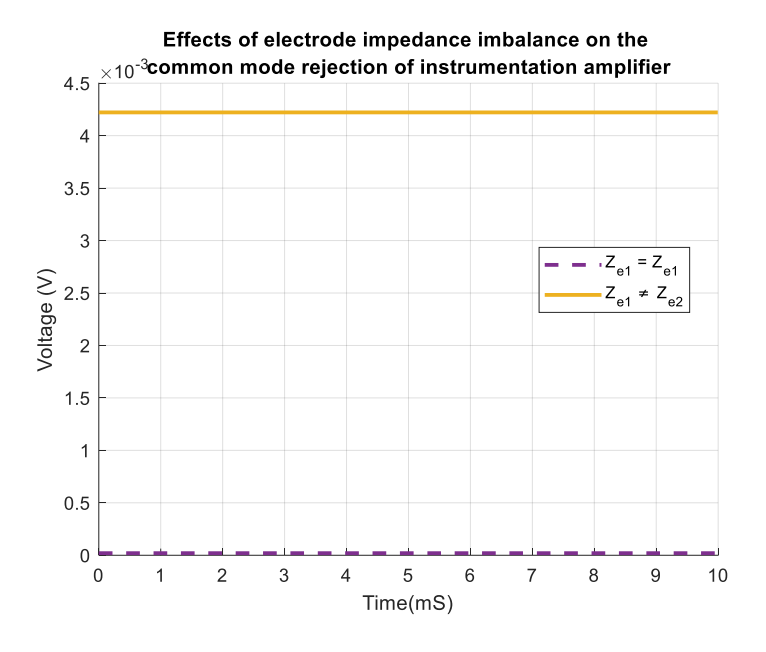


Figure 4. 14 Effects of electrode impedance on common mode signals rejection of the IA.

4.4.4 Effects of mismatches in the Sense circuit differential amplifier feedback resistors.

In addition to the impedance mismatch at the electrodes, mismatches in the differential amplifier feedback resistors R_{IA1} and and R_{IA2} can also degrade the common-mode rejection ratio (CMRR) of the instrumentation amplifier, as described by equation 4.68.

$$CMRR = 20Log\left(\frac{gain*100}{\%mismatch}\right)$$
 4.68

This can be mitigated by using application-specific integrated circuit (ASIC) instrumentation amplifiers, where the resistors are laser-trimmed for precise matching.

4.4.5 Effects of Input and Output Capacitances of Instrumentation Amplifiers.

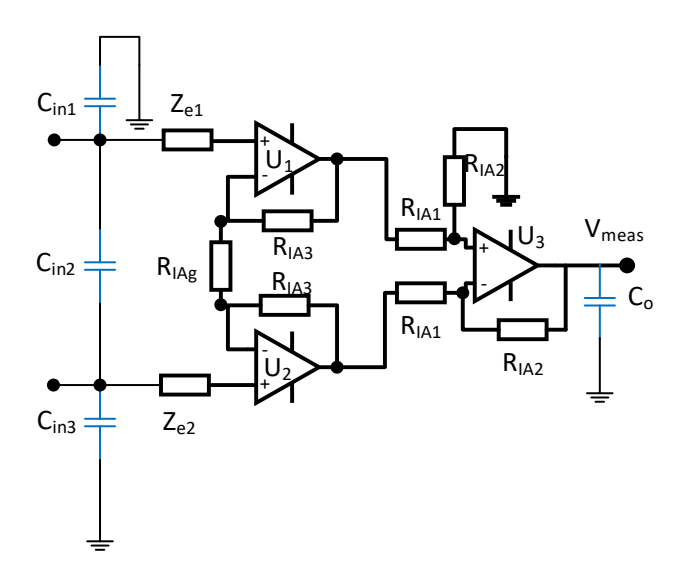


Figure 4. 15 Schematic diagram of instrumentation amplifier showing input and output parasitic capacitances.

The input and output parasitic capacitances can significantly degrade the performance of an instrumentation amplifier. These stray capacitances often arise in leads, switches, input capacitors, and PCB traces, with a substantial portion occurring between the traces that connect the circuit components. These parasitic capacitances also introduce erroneous phase shifts to the measurement output (V_{meas}), making the accuracy of the output frequency-dependent. Although methods such as incorporating a load in the loop [1] have been employed to minimize stray capacitances, they restrict the current source to a grounded load. Proper PCB layout techniques can also mitigate these effects, but they may sometimes be beyond the designer's control. Designs covered in this work also aims to develop a system that significantly reduces the phase shift effects of these stray capacitances on measurements.

4.5 Bioimpedance measurement system

There are several types of impedance measurement systems ranging from Inductance, Resistance, and Capacitance (LRC) meters, Bridges, Network Analysers, Impedance Analysers [51]. However, the work done here had focused on the most commonly adopted system for bio-impedance measurements, namely Synchronous demodulation(SD), Synchronous sampling(SS), and Magnitude and phase system(MP).

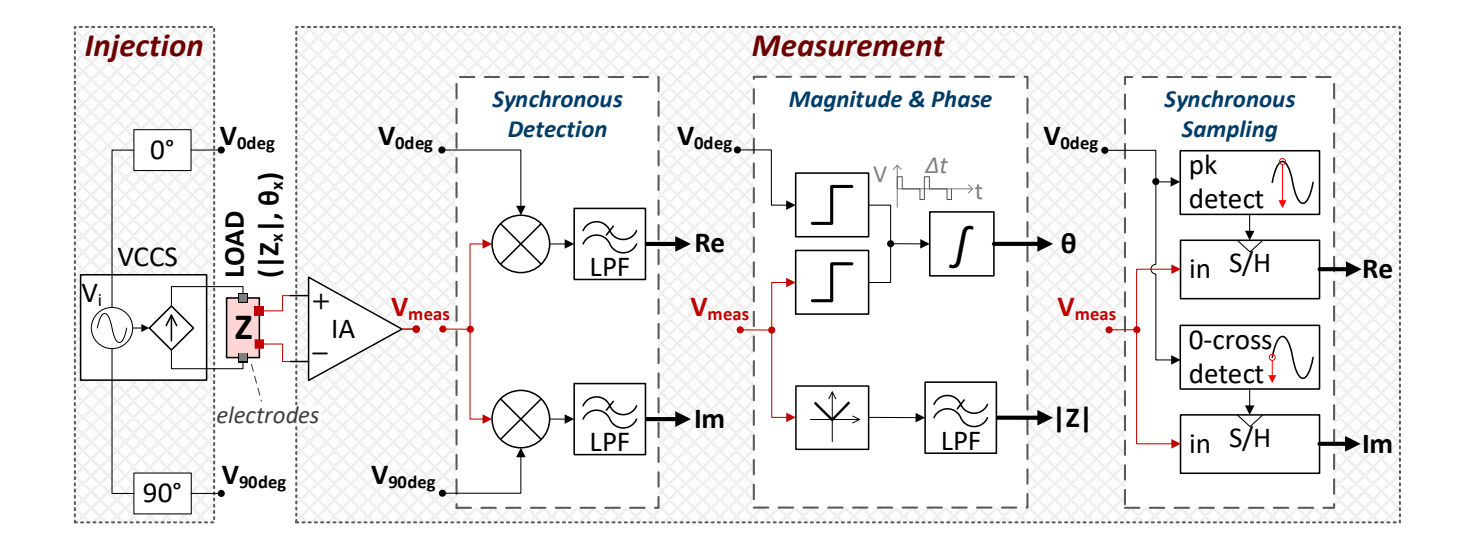


Figure 4. 16 System-level block diagram of the three designs: SD, MP and SS systems [58], [59]

In Figure 4.16, all three systems connect to the load through an instrumentation amplifier that would be included in each system and the signal is provided by a voltage-controlled current source (VCCS) driven by a signal generator which also produces unity amplitude sinusoids at 0° and 90° phase shifts. The known amplitude of the injected current is used in post processing to derive the exact value of the unknown load magnitude. Details about the functions of the various systems will be explained in their subsequent circuit diagrams.

4.5.1 Synchronous demodulation bioimpedance system and analysis.

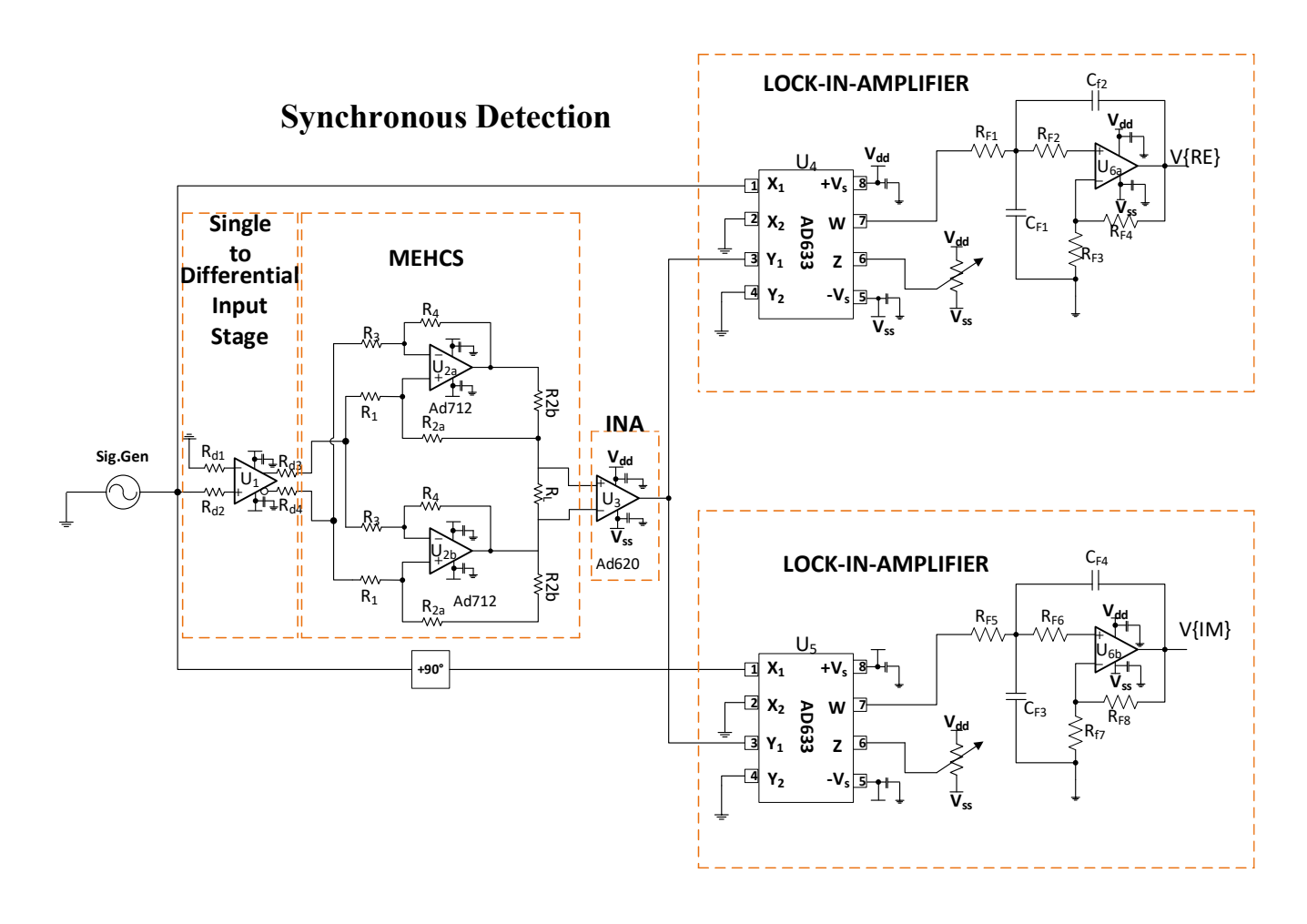


Figure 4. 17 Synchronous demodulation system.

Figure 4.17 illustrates the synchronous demodulation system for bioimpedance measurement designed and implemented in this work. The synchronous demodulation method for bioelectrical impedance measurement utilizes the principles of lock-in amplifiers. This approach involves multiplying two sine waves: one is the signal carrying the resultant voltage measurement from the current injection and the other is a reference signal with a chosen frequency and phase. In this topology, a voltage-controlled MEHCS injects a constant alternating current of fixed amplitude into the tissue through a pair of electrodes. The resultant potential across another pair of measurement electrodes, measured by the instrumentation amplifier, is multiplied by a signal in phase with the injected current. The output is then filtered by a low-pass filter to obtain the DC component, which corresponds to the real part V{RE}. Similarly, a reference signal that is phase-shifted by 90 degrees is used to multiply the resultant voltage to obtain the imaginary part of the signal V{IM}. Equations 4.69 to 4.88 further described the process.

The injected current into the biological tissue

$$i_0 \sin(\omega t)$$
 4.69

Resultant measured voltage across the tissue is

$$v_{meas} = A_v i_0 z_x \sin(\omega t - \varphi) \tag{4.70}$$

To further extract the impedance data from v_{meas} , demodulation signals are utilized. These include the in-phase lock in signals (v_{-0}) and the quadrature sinusoidal signal v_{-90} defined as:

$$v_{-0} = v_0 \sin(\omega t) \tag{4.71}$$

$$v_{90} = v_0 \sin(\omega t + 90^\circ)$$
 4.72

In phase multiplier output can further be analyzed as

$$v_{mult0deg} = A_v i_0 z_x \sin(\omega t - \varphi) * v_0 \sin(\omega t)$$
4.73

$$\sin(\omega t - \varphi) * \sin(\omega t) = \frac{1}{2} \left[\cos((\omega t - \varphi) - \omega t) - \cos((\omega t - \varphi) + \omega t) \right]$$
 4.74

$$\sin(\omega t - \varphi) * \sin(\omega t) = \frac{1}{2} [\cos(-\varphi) - \cos(2\omega t - \varphi)]$$
 4.75

Substituting back the constants,

$$v_{mult0deg} = A_v i_0 z_x \sin(\omega t - \varphi) * v_0 \sin(\omega t) =$$

$$\frac{1}{2}A_v i_0 z_x v_0 [\cos(-\varphi) - \cos(2\omega t - \varphi)]$$

$$4.76$$

$$v_{mult0deg} = \frac{1}{2} A_v i_0 z_x [cos(-\varphi) - cos(2\omega t - \varphi)]$$
 4.77

Ignoring the right-hand frequency components, as would be eliminated by the low pass filter, as such, the DC signal that would appear at the output would be.

$$VLPF_{0deg} = \frac{i_0 A_v Z_x v_0}{2} cos(\varphi)$$
 4.78

Hence the Real part of the impedance {RE}

$$Re\{Z\} = \frac{2*VLPF_{0deg}}{i_0A_vv_0}$$
 4.79

Similarly, the quadrature demodulation procedure involves multiplying v_{meas} by $v_{_90}$, yielding the output of quadrature multiplier ($v_{mult90^{\circ}}$).

$$v_{mult90^{\circ}} = A_v i_0 z_x \sin(\omega t - \varphi) * v_0 \sin(\omega t + 90^{\circ})$$

$$4.80$$

$$\sin(\omega t + 90^{\circ}) = \cos \omega t \tag{4.81}$$

$$v_{mult90^{\circ}} = A_{v}i_{0}z_{x}\sin(\omega t - \varphi) * v_{0}(\cos\omega t)$$

$$4.82$$

$$\sin(\omega t - \varphi) * (\cos \omega t) = \frac{1}{2} \left[\sin((\omega t - \varphi) + \omega t) + \sin((\omega t - \varphi) - \omega t) \right]$$
 4.83

$$sin(\omega t - \varphi) * (cos\omega t) = \frac{1}{2}[sin(2\omega t - \varphi) - sin(\varphi)]$$
 4.84

Substituting back the constants,

$$v_{mult90^{\circ}} = A_v i_0 z_x \sin(\omega t - \varphi) * v_0 \cos(\omega t) =$$

$$\frac{1}{2}A_v i_0 z_x v_0 [\sin(2\omega t - \varphi) - \sin(\varphi)]$$

$$4.85$$

$$v_{mult90^{\circ}} = \frac{1}{2} A_v i_0 z_x v_0 \left[\sin(2\omega t - \varphi) - \sin(\varphi) \right]$$

$$4.86$$

Ignoring the right-hand frequency components, as would be eliminated by the low pass filter, the DC signal that would appear at the output would be.

$$VLPF_{90deg} = \frac{i_0 A_v Z_x v_0}{2} \sin(-\varphi)$$

$$4.87$$

$$Im\{Z\} = \frac{2*VLPF_{90deg}}{i_0 A_v v_0}$$
 4.88

Figure 4.18 below presents the experimental data, showcasing the outputs from different circuit stages within the synchronous demodulation system for bioimpedance measurement.

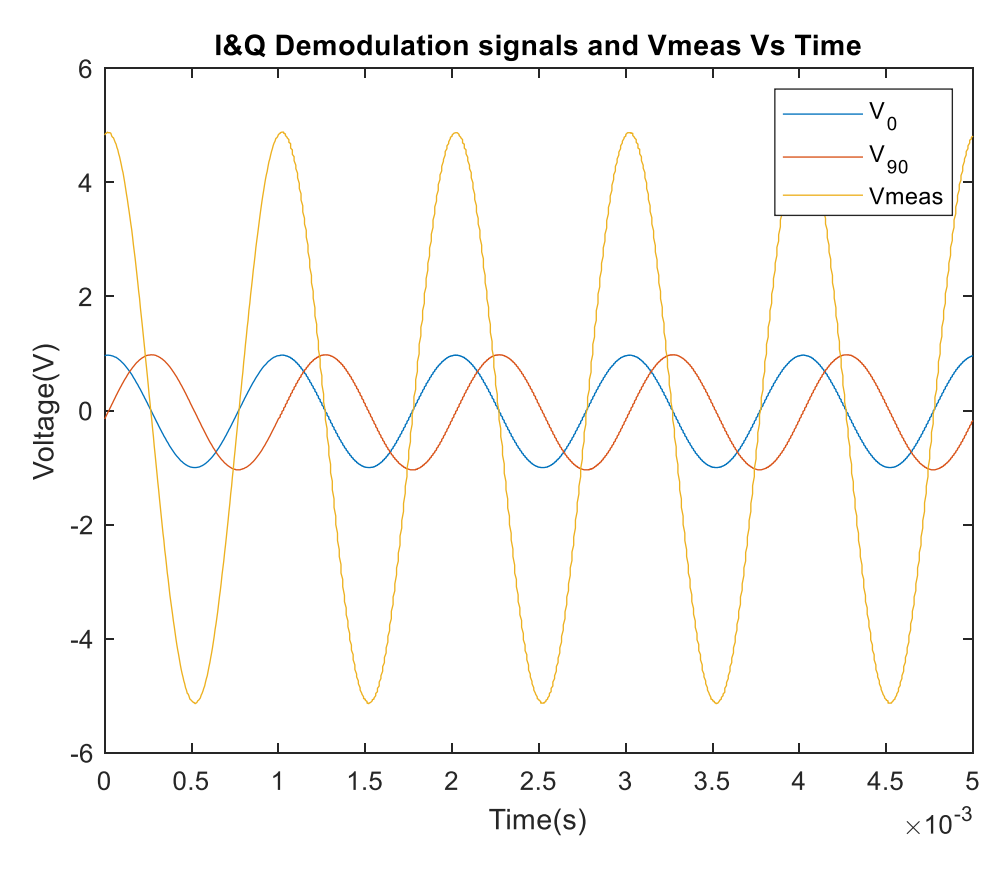


Figure 4. 18 Demodulation signals and V_{meas} as a function of Time.

Figure 4.18 illustrates a graphical plot of the I&Q demodulation signals of the synchronous demodulation system for a constant current of 1mA across a $5k\Omega$ resistive load. The resultant measured voltage of 5V is then multiplied by the in-phase and 90-degree modulation signals

of 1V peak amplitude to yield the corresponding real (V{RE}) and imaginary (V{IM}) components, as illustrated in Figure 4.19.

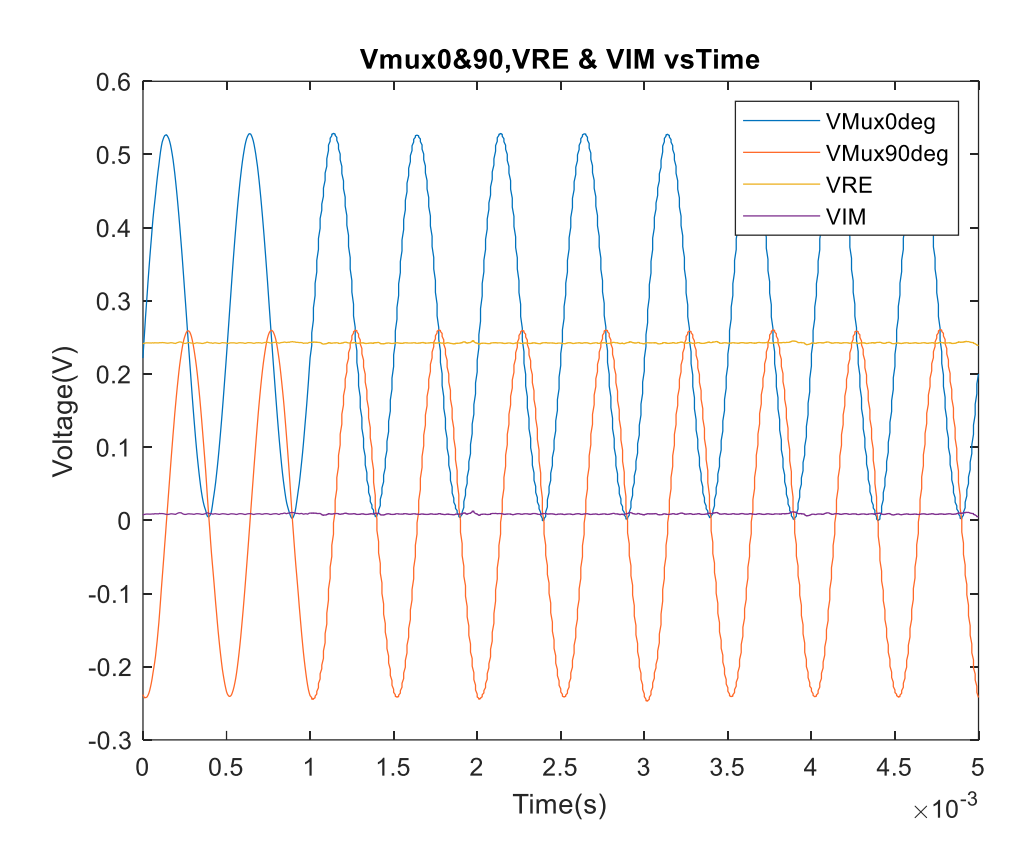


Figure 4. 19 Multiplier and low pass filter outputs for 5V peak of Vmeas at no phase shift

The results presented in Figure 4.19 show that, with a multiplier scale factor of 10 and a purely resistive 5 k Ω load, the voltage output of the filter corresponding to the real part of the impedance (V{RE}) is approximately 250 mV. This represents the average DC output of the multiplier. As expected for a purely resistive load, the imaginary component (V{IM}) is ideally zero, although minor offsets exist due to system nonidealities.

4.5.1a Potential Sources of error of SD system.

- ▶ Phase shift between VCCS and the measurement Instrumentation Amplifier: The phase shift introduced by the current driver due to factors such as parasitic output capacitance of VCCS, is a significant source of error reported in the literature for synchronous demodulation systems [43]. These errors become more pronounced at higher frequencies, leading to a degradation output impedance and hence measurement accuracy.
- > DC offsets of the filter: Errors in form of dc offsets from Low pass filter could also exist in the measurement.

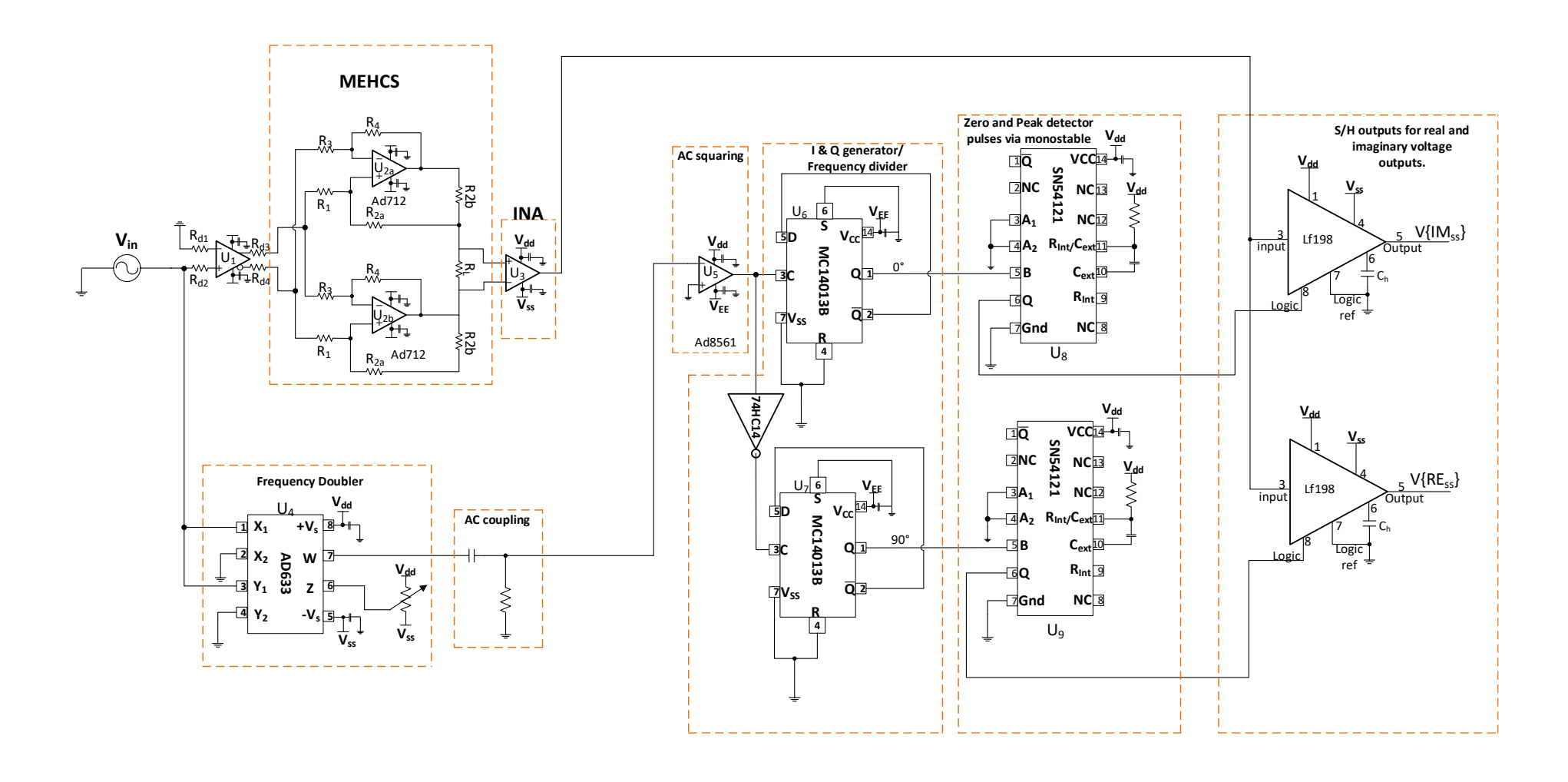


Figure 4. 20 Synchronous Sampling system implemented in this work

4.6 Synchronous Sampling system and analysis:

Another popular system for measuring the bioelectrical impedance of tissue is synchronous sampling. In this approach, the signal is sampled at points where the injected signal peaks and crosses zero, allowing for the determination of the real and imaginary components of the tissue impedance[100]. Unlike synchronous detection, which locks onto a specific input signal frequency, synchronous sampling can utilize a band-pass filter to mitigate unwanted signals, in multifrequency measurements[59]. Figure 4.20 is the schematic of the synchronous sampling circuit designed and implemented in this work.

In the implementation shown in Figure 4.20, the reference signal $V_{\rm in}$ is multiplied by itself using the AD633 multiplier [U4], effectively doubling the frequency and adding a DC offset. The output of the multiplier is then AC-coupled through a high-pass filter with a cut off frequency more than 10 times less than the doubled frequency to minimize any impact of the filter on the phase and amplitude of the measured signal. The signal, now free of DC components, is squared by the AD8561 comparator [U5] and fed into a D-type flip-flop composed of [U6] and [U7], generating 0° and 90° phase-shifted square wave pulses relative to $V_{\rm in}$ at the same frequency as the reference signal $V_{\rm in}$. These 0° and 90° phase-shifted pulses are fed to inputs of monostable circuits [U8] and [U9] to further generate sharp pulses of approximately 3 μ s, corresponding to the zero crossing and peak pulses of the reference signal $V_{\rm in}$. These timing pulses are used to trigger sample and hold circuits [U10] and [U11], thereby sampling the measured signal v_{meas} . The resulting outputs of the sample and hold circuitry corresponds to the real and imaginary components of the measured impedance. This process is described in detail in Equations 4.89–4.97.

Recall

$$v_{meas} = A_v i_0 z_x sin(\omega t - \varphi)$$
 4.89

A sample of v_{meas} at the zero crossing of the reference signal V_{in} at t=0 gives

$$V\{IM\}_{ss} = A_v i_0 z_x sin(\omega t) cos(\varphi) - A_v i_0 z_x cos(\omega t) sin(\varphi)$$
4.90

$$V\{IM\}_{SS} = A_{\nu}i_0z_x\sin(0)\cos(\varphi) - A_{\nu}i_0z_x\cos(0)\sin(\varphi)$$

$$4.91$$

$$V\{IM\}_{ss} = -A_{v}i_{0}z_{x}sin\varphi 4.92$$

$$\frac{V\{IM\}_{SS}}{A_{v}i_{0}} = -z_{x}sin\varphi$$

$$\{IM\}_{SS} = -z_x sin\varphi = \frac{V\{IM\}_{SS}}{A_v i_0}$$
 4.93

Hence, a sample of v_{meas} taken at t=0 yields the imaginary part of the impedance.

The Real part of the impedance value is also derived from sampling v_{meas} at the peak of the reference signal V_{in} at $t=\frac{\pi}{2}$

$$\omega t = \frac{\pi}{2} \tag{4.94}$$

$$t = \frac{\pi}{2\omega} \tag{4.95}$$

$$V\{RE\}_{ss} = A_v i_0 z_x sin\left(\omega.\frac{\pi}{2\omega}\right) cos(\varphi) - A_v i_0 z_x cos\left(\omega.\frac{\pi}{2\omega}\right) sin(\varphi)$$

$$4.96$$

$$V\{RE\}_{SS} = A_v i_0 z_x sin\left(\omega.\frac{\pi}{2\omega}\right) cos(\varphi) - A_v i_0 z_x cos\left(\omega.\frac{\pi}{2\omega}\right) sin(\varphi)$$

$$4.97$$

$$V\{RE\}_{ss} = A_{\nu}i_0z_xcos(\varphi)$$
 4.96

$$\frac{V\{RE\}_{SS}}{A_{vio}} = z_{x}cos(\varphi)$$
 4.97

$$\{RE\}_{SS} = \frac{V\{RE\}_{SS}}{A_v i_0} = z_x cos(\varphi)$$

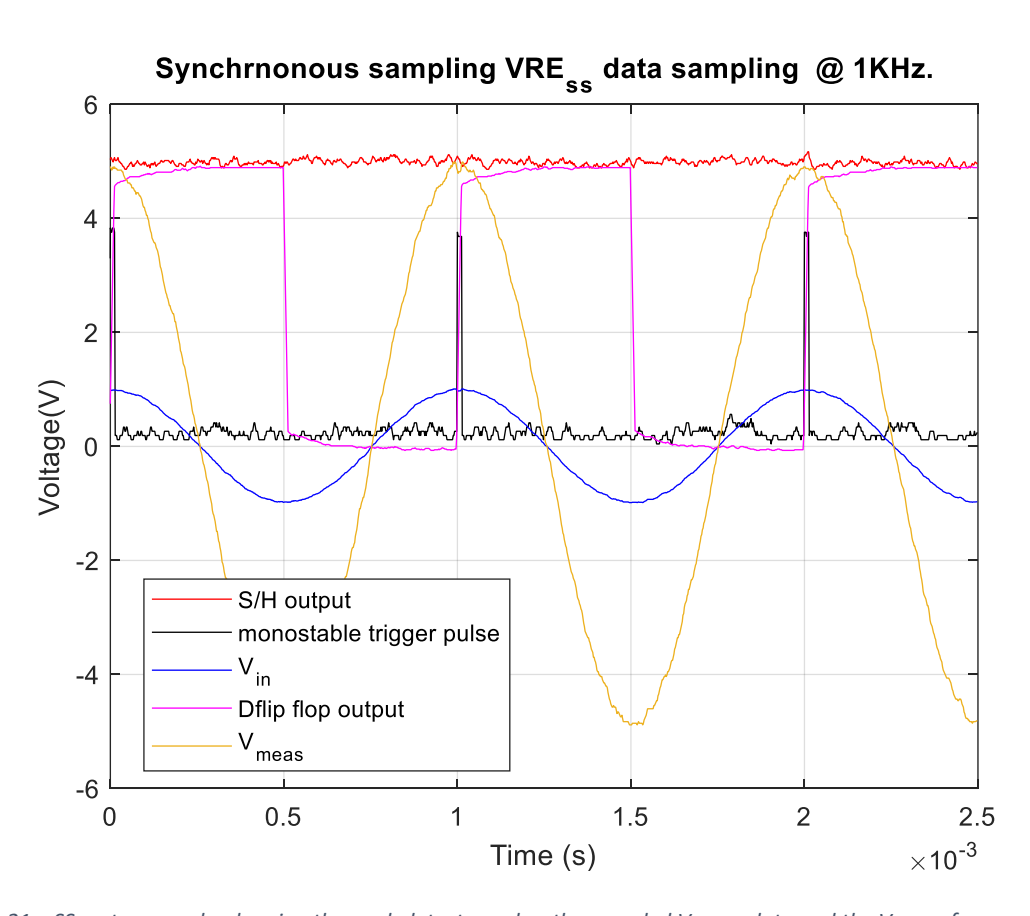


Figure 4. 21. SS system graphs showing the peak detector pulse, the sampled Vmeas data and the Vmeas for a purely resistive load of $5k\Omega$ for an injected current of 1mA.

The data in Figure 4.21 illustrates the results obtained from a sample of Vmeas data for a resistive load of 5 k Ω . One of the outputs from the D-type flip-flop is displayed as a square wave, which is phase-shifted by 90 degrees relative to the reference signal V_{in} . This phase-shifted output is used to generate a trigger pulse for the monostable circuit, which in turn produces the pulse used by the peak detector sampling. The resulting peak detector pulse is

observed in the diagram. Additionally, the Sample-and-Hold (S/H) output (VRE_{SS}) accurately reflects the peak amplitude of the measured data, confirming the expected 5V output.

The trigger pulses obtained at 100kHz is further shown in Figure.4.22.

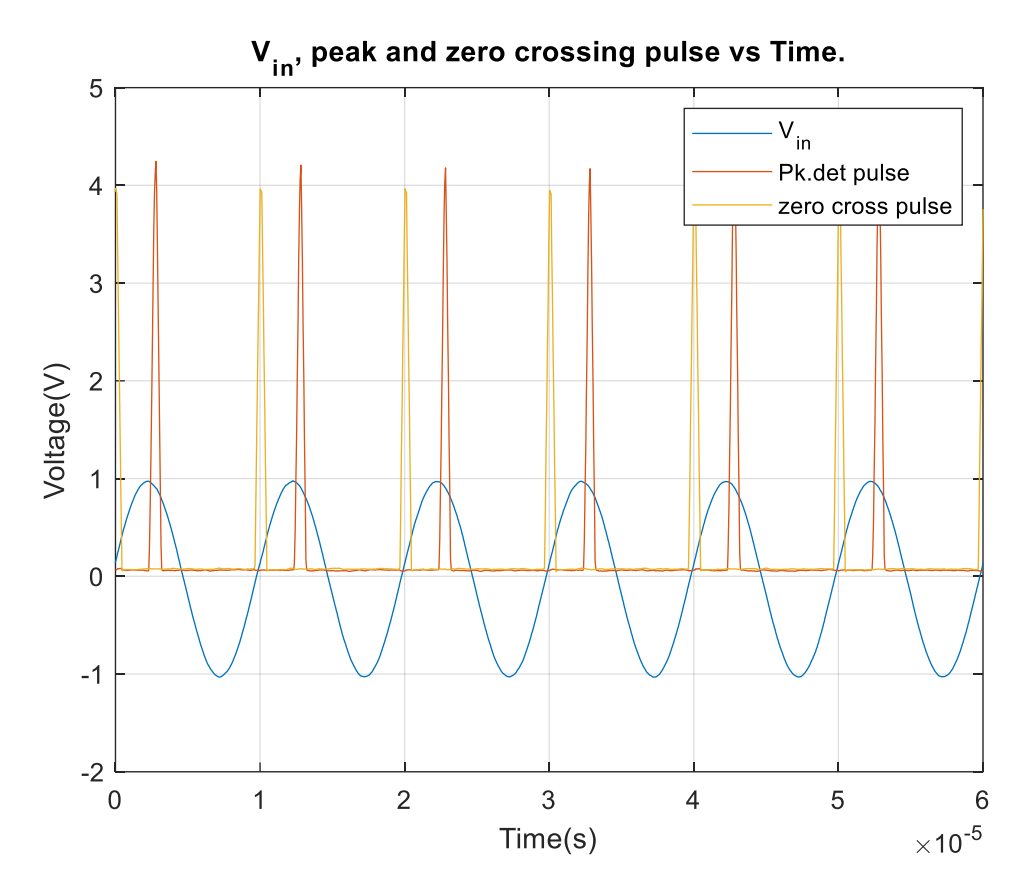


Figure 4. 22 Sampling pulses of synchronous sampling at 100kHz

4.6.1a Potential Sources of errors in Synchronous Sampling System.

- ➤ Aperture Time Error: This error is the duration it takes for the S/H circuit to switch from sampling the input signal to holding its value. Ideally, this transition should be instantaneous, but in practice, it takes a finite amount of time. During the aperture time, the input signal might change, causing the held value to deviate from the true value at the precise moment the hold command was given, as such introducing an error.
- > DC offsets of the measurement Instrumentation Amplifier filter[U3]: Any DC offsets introduced by the instrumentation amplifier would cause an erroneous output in the sampling and hold system.

4.7 Magnitude and Phase Bioimpedance system and analysis.

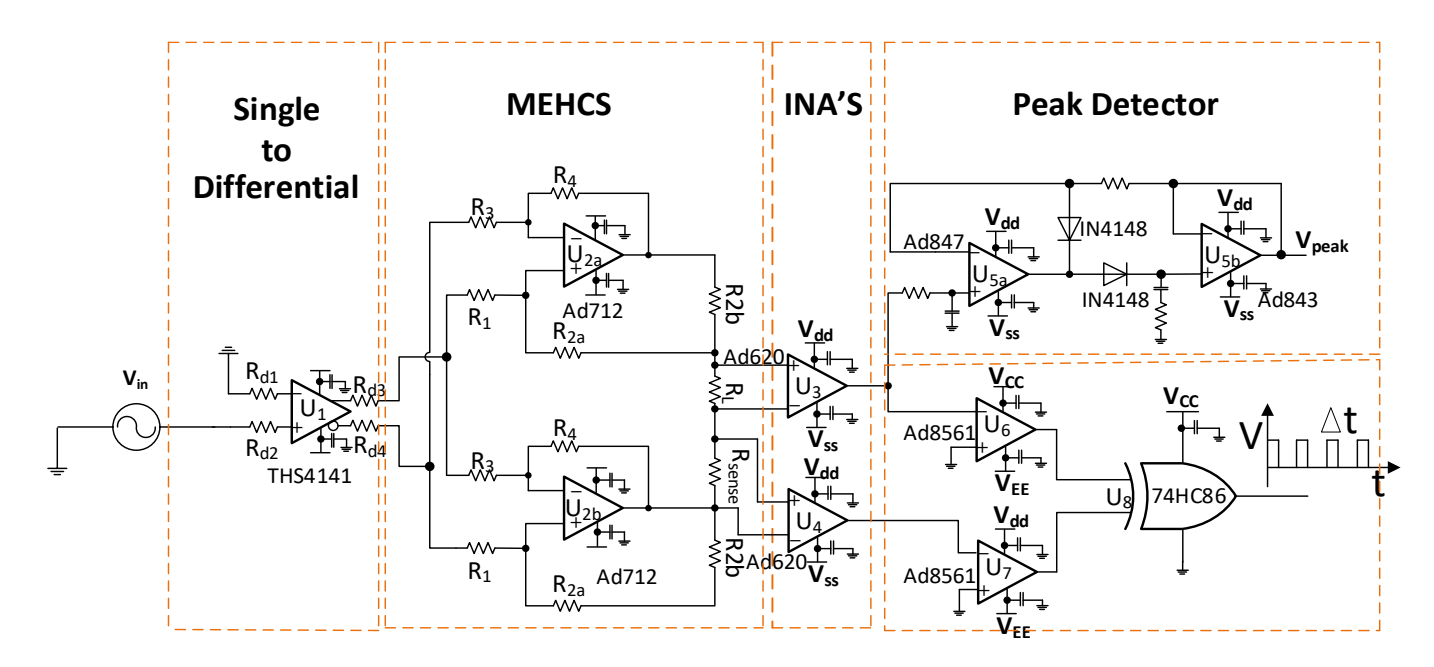


Figure 4. 23 Magnitude and Phase Bioimpedance system implemented in this work

In the magnitude and phase method illustrated in Figure 4.23, a process similar to synchronous detection is employed on the injection side. A constant current with a fixed amplitude is injected into the load sample via a pair of electrodes. This current is then measured by another pair of electrodes connected to an instrumentation amplifier [U3]. The peak detector circuit, comprising [U5a] and [U5b], captures the peak amplitude of the measured signal V_{meas}, which is then used to calculate the impedance magnitude using Ohm's law.

The phase difference is determined using a complex circuit involving comparators, a reference sense resistor, and an XOR gate [U8] [101]. The reference resistor (R_{sense}) is a small resistor connected in series with the Load (R_L) sample under test, and the voltage across this resistor is measured using a separate instrumentation amplifier [U4]. This voltage is then converted into a square wave by feeding it through a comparator [U7], which compares the signal to ground(OV).

Similarly, V_{meas} is squared by comparing it to zero ground using another comparator [U6]. The outputs from both comparators [U6] and [U7] are fed into an XOR gate [U8], which generates a pulse signal. The width of this pulse corresponds to the phase delay (Δt) introduced by the load at the set frequency.

The magnitude and phase values of the load are derived using the equations 4.98—4.99

$$|Z| = \frac{V_{peak}}{A_n i_0}$$
 4.98

$$\varphi = 360 * \Delta t * freq$$

Figure 4.24 further illustrates the measurements stages for magnitude and phase detection system at 1kHz.

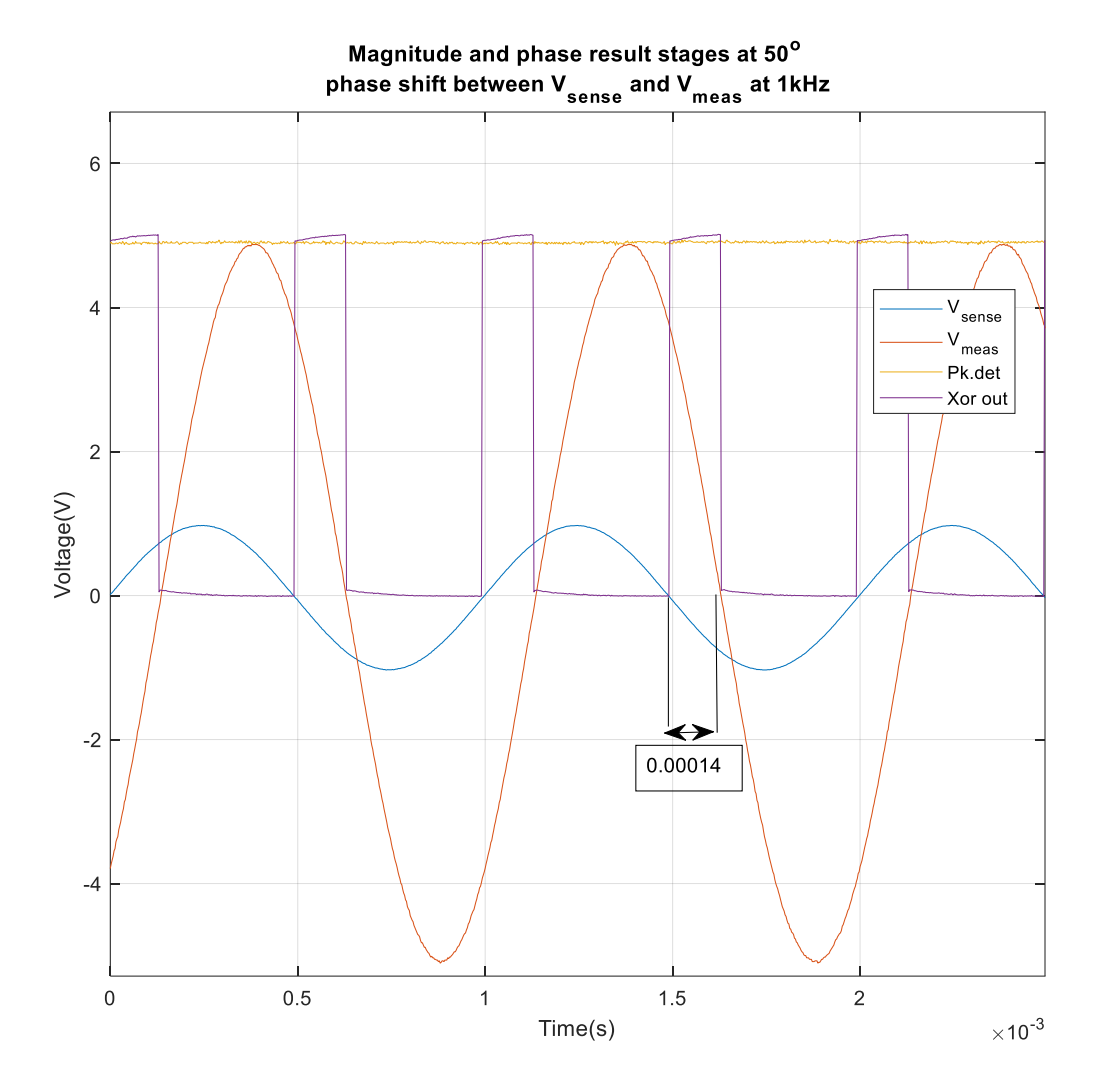


Figure 4. 24 Magnitude and phase measurement result measurement stages of measurements at 1kHz

Figure 4.24 shows an experiment where the signal generator was directly employed to inject a 5V amplitude sinusoidal waveform across $1k\Omega$ resistor RL connected across instrumentation amplifier [U3] as V_{meas} . A further 1V sinusoidal waveform was applied across $1k\Omega$ sense resistor instrumentation amplifier [U4] as V_{sense} . Vmeas is 50° phase shifted relative to V_{sense} . The peak detector circuit accurately detects the peak amplitude of V_{meas} , which is V_{peak} .

The output of the XOR gate produces a pulse with a duration of approximately 0.00014 seconds, corresponding to a phase shift of 50 degrees following eq.4.99. This result effectively verifies the initially introduced phase shift, further verifying the initial added phase.

- 4.7.1a Potential sources of errors for Magnitude and Phase detection System.
 - Phase shift and dc offsets introduced by Instrumentation amplifiers: If the measurement instrumentation amplifiers [U3] and [U4] are not well matched to achieve low offset voltage and phase drifts. They will respond differently to external stimuli, and as such introducing phase and offsets errors in the estimated impedance phase.
 - ➤ Propagation delays and DC offsets introduced by comparators amplifiers: If the comparators are not well-matched, they may introduce varying levels of delay, which can lead to inaccuracies in the phase measurement.

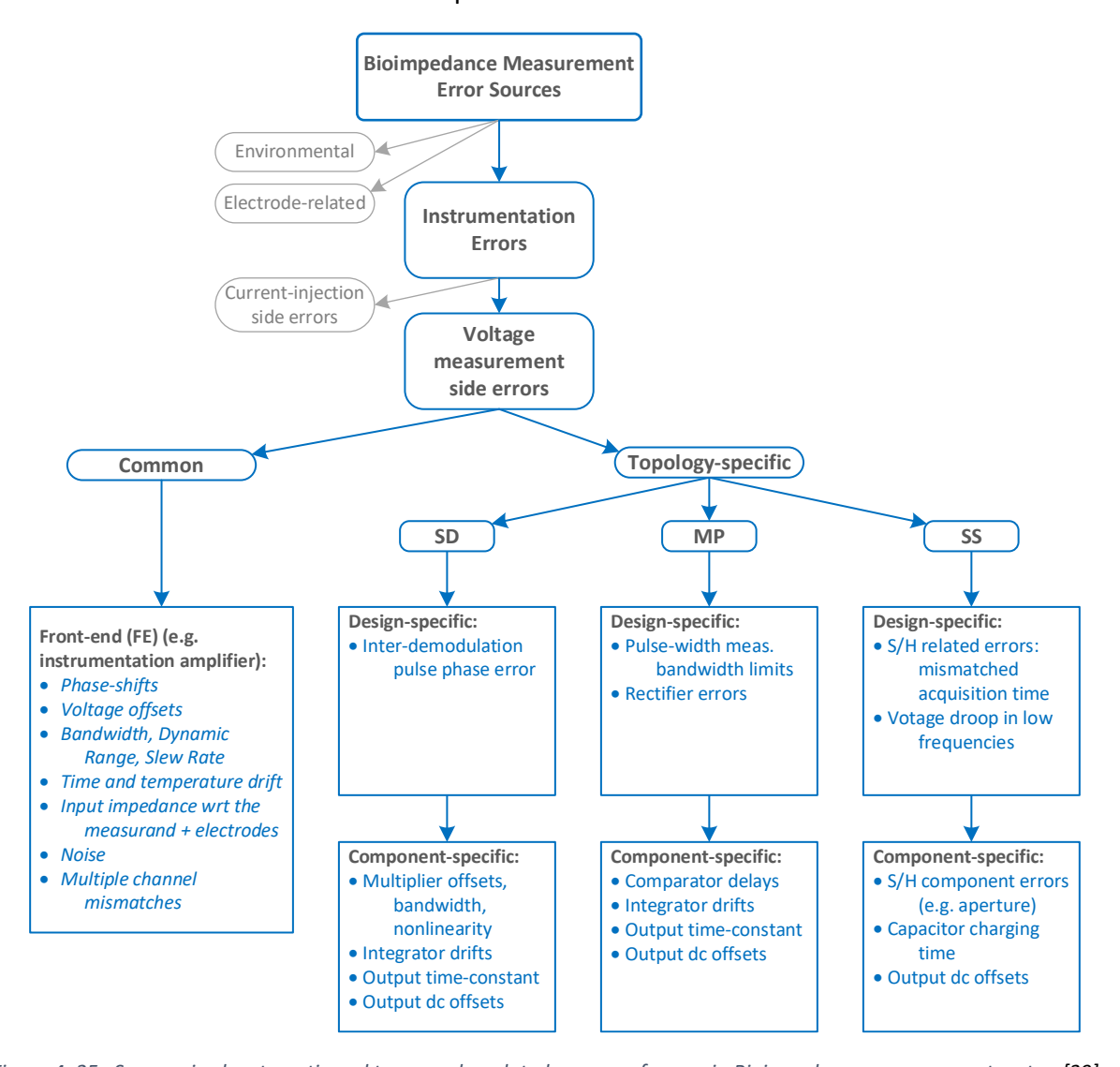
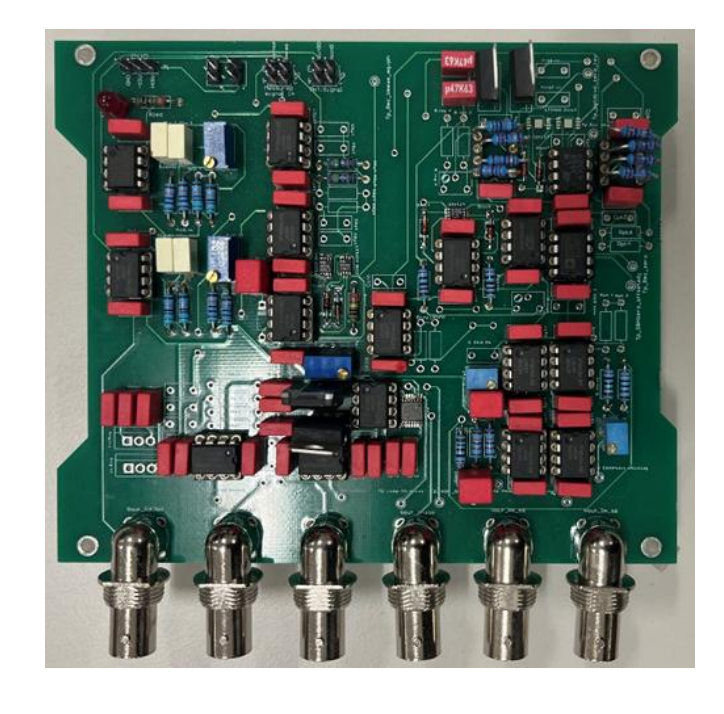


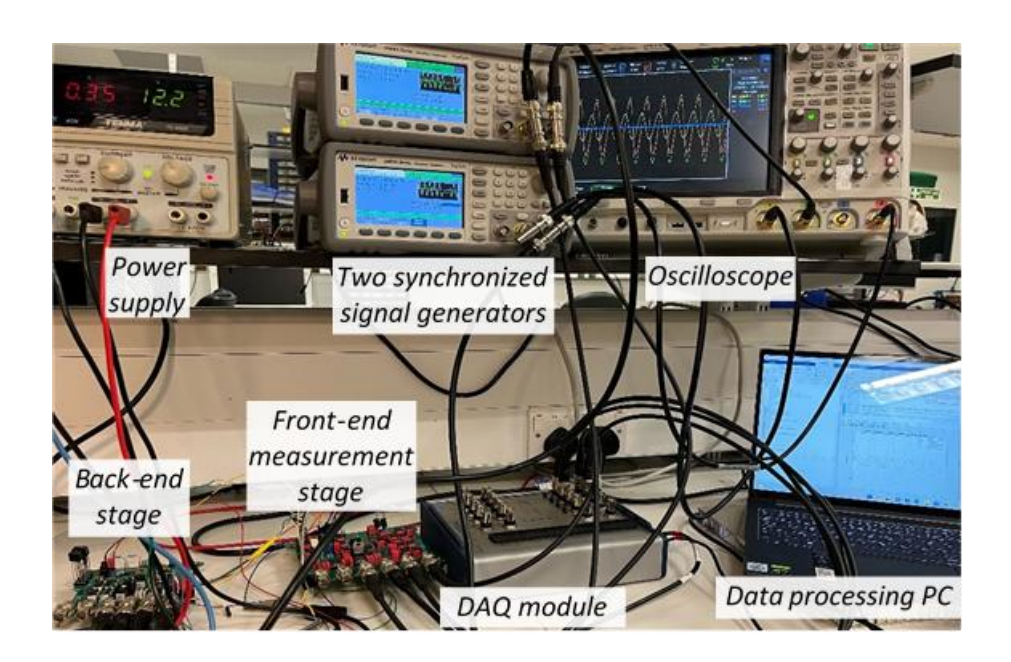
Figure 4. 25 Summarized systematic and topography related sources of errors in Bioimpedance measurement system[39], [43], [102]







(4.26b) Measurement Circuits(MP,SD,SS)



(4.26c) Experimental set-up

Figure 4. 26 PCB photographs of the MECHS and SD, SS, and MP systems designed in and explained in this chapter

4.8 Conclusion on Chapter 4:

In conclusion, Chapter 4 has analysed the current injection and voltage measurement circuits used in bioimpedance systems. The chapter focused on three primary bioimpedance systems: the synchronous detection system, the synchronous sampling system, and the magnitude and phase bioimpedance system. Results derived from these systems provided deeper insights into the mathematical models and analyses previously discussed, enhancing the understanding of their operation.

Through both mathematical and experimental analyses, potential sources of errors were identified. The next chapter will explore the effects of these identified errors on the accuracy of the measurements, which guided and had influenced the final selection of the bioimpedance system optimized in this thesis.

Chapter 5

Effects of the systematic sources of errors on the measurement accuracy of the bioimpedance measurement system.

The previous chapter, chapter four discussed the types of drive circuits and sense circuits used in various bioimpedance systems, highlighting the potential sources of errors. However, it is not straightforward to identify the characteristics of an impedimetric system that are best suited for the application considered in this this thesis and in this case, bioimpedance for skin cancer. There is insufficient information in the research literature when it comes to any systematic categorization of biomedical applications in terms of required design specifications of such systems. Moreover, and more importantly, the system-level characteristics of the aforementioned three designs are not clearly defined when it comes to their respective advantages or disadvantages for any specific application. As a result, new research and development in this area often includes some level of recycling of some of these designs randomly or optimizing some of their characteristics towards the desired performance. However, this is mostly done without a clear indication as to whether a different design might have been preferable for a specific application. This lack of clarity in the literature hampers future design decisions, especially in new application areas. As such, in this chapter and in order to take this line of research forward more systematically, a clear classification of the advantages and disadvantages of these designs in relation to the requirements of different applications was demonstrated, in addition to level of the accuracy degradation in the presence of their potential source of errors. This will help in identifying the best suited system for the bioimpedance for skin cancer application considered in this thesis.

Through experiments and system-level simulations, I proposed an approach to classifying these designs in terms of their appropriateness for different applications, by: a) briefly categorizing applications in terms of technical specifications of the measuring instrumentation; b) identifying the main systematic error sources of each design; c) comparing systems within the context of such systematic errors; and d) assessing the appropriateness of each system for each application category. Through this systematic comparison, I aimed at making a choice for which system to optimise for the bioimpedance for skin cancer application proposed in this work. To this effect, a brief category on the bioimpedance application category based on the system specifications were further analysed.

5.1 Bioimpedance Application classification in terms of system specifications

Depending on the application, a bioimpedance measurement system may have to interrogate samples that are relatively stable during the acquisition time or tissues that are dynamically

varying in composition. This was labelled here as "static" and the second one "dynamic" application as in (Figure. 5.1). A brief overview of the two categories follows below.

> Static Application Category: From an impedimetric system perspective, the first category applications might have constraints related to achieving repeatable and accurate measurements of either magnitude or phase, often requiring a wide frequency range of operation[23], [73]. Systems that are appropriate for applications in this category will not necessarily be required to operate over a wide range of magnitudes, especially if standard electrode geometries are used in combination with prior knowledge or look-up tables of reference values. Low amplitude currents are often used, necessitating a low-noise, high gain first stage at the front end of the measurement stage. Bioimpedance measurements in this category are either localized, across body segments, or over the whole body. Examples of the first include applications that assess cell integrity e.g. skin cancer[23] and applications that detect variations (spatially or in comparison with healthy tissue) of cell geometric disposition over small areas e.g. in the case of impedance myography [73]. In both of these examples the measurement of phase over a wide frequency range is essential and accuracy of measurement will result in better detection of localized variations of tissue properties. Segmental measurements as in limb bioimpedance analysis involve average measurements from certain body sections scaled to specific anatomical features [103] In such cases low system drift and accurate relative magnitude readings at specific frequencies are essential. Whole body measurements involve obtaining and analysing impedance measurements of the whole human body using standardized electrode positions as used in determining body composition [104]. Figure 5.1 further illustrates the categories of bioimpedance application diagrammatically.

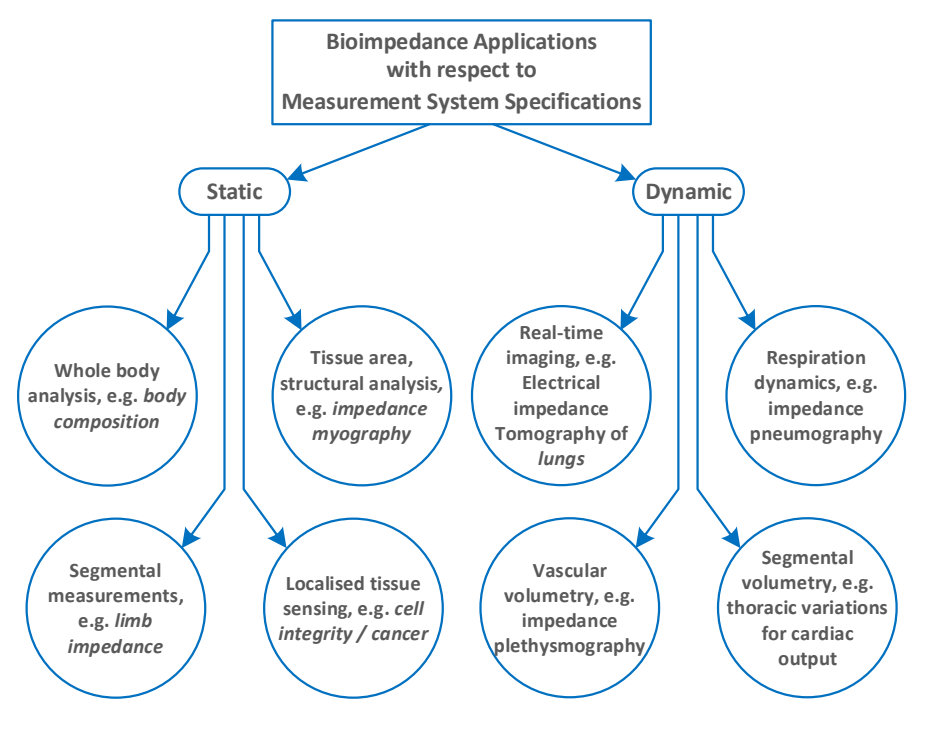


Figure 5. 1 Categories of bioimpedance applications in relation to the impedimetric system specifications required.

> Dynamic Application Category: The second application category requires fast settling systems often at one or more fixed frequency values with a wide dynamic range, as impedance values may change with time even by an order of magnitude. One of the major applications, bioimpedance plethysmography (or electrical impedance plethysmography – IPG)[105] involves impedance measurements through the skin relating to venous or arterial blood volumetric variations, often at extremities, synchronized to the heart rate [105]. In impedance cardiography, cardiac volume variations are assessed through thoracic impedance variations corresponding to blood volumetric variations across the chest area [106]. In both cases the 0.6-2Hz frequency of variation sets the response time of the instrumentation to at least double that frequency and capturing features like the "dicrotic notch" may require responses of up to 10 milliseconds or faster. Given that all impedimetric systems aim at generating dc values that correspond to magnitude / phase or real /imaginary readings, their outputs are often slow varying low-pass filter type stages with relatively long-time constants[106]. Impedance pneumography, a respiratory plethysmographic method requires similar specifications, albeit with higher dynamic range but much slower response requirements[107]. If measurements need to be used for imaging, electrical impedance tomography (EIT) applications range from static to dynamic biological functions including assessment of swelling, stroke, intracerebral blood perfusion and lung function [108] [109]. Irrespective of the biological dynamics, all real-time imaging applications should be considered as dynamic as number of measurements per frame and number of frames per second are often generated, with fractions of milliseconds response times required in some cases. Magnitude only measurements are usually made requiring only half of the instrumentation, while linearity over a wide dynamic range is required[58]. Good matching between identical instrumentation channels is also important.

5.2 Methods employed to analyse and compare bioimpedance systems.

In order to comparatively assess the impact of the aforementioned systematic errors on the performance of the three topologies, system level parametric simulations were caried out using a range of applied magnitudes and phases corresponding to different impedance measurands, calculated using eq. (5.1) and (5.2). These were followed by experimental analysis on the speed and accuracy of measurements of the systems for multifrequency inputs. Figure.5.2 shows the three topologies which were simulated in Matlab Simulink in the presence of some of the major error sources mentioned previously.

$$\frac{1}{Z_{t}} = \frac{1}{R_{t}} + j\omega C_{t} \Rightarrow \begin{cases} |Z_{t}| = \frac{1}{\sqrt{\left(\frac{1}{R_{t}}\right)^{2} + (\omega C_{t})^{2}}} \\ \varphi = \tan^{-1}(-\omega C_{t}R_{t}) \end{cases}$$

$$(5.1)$$

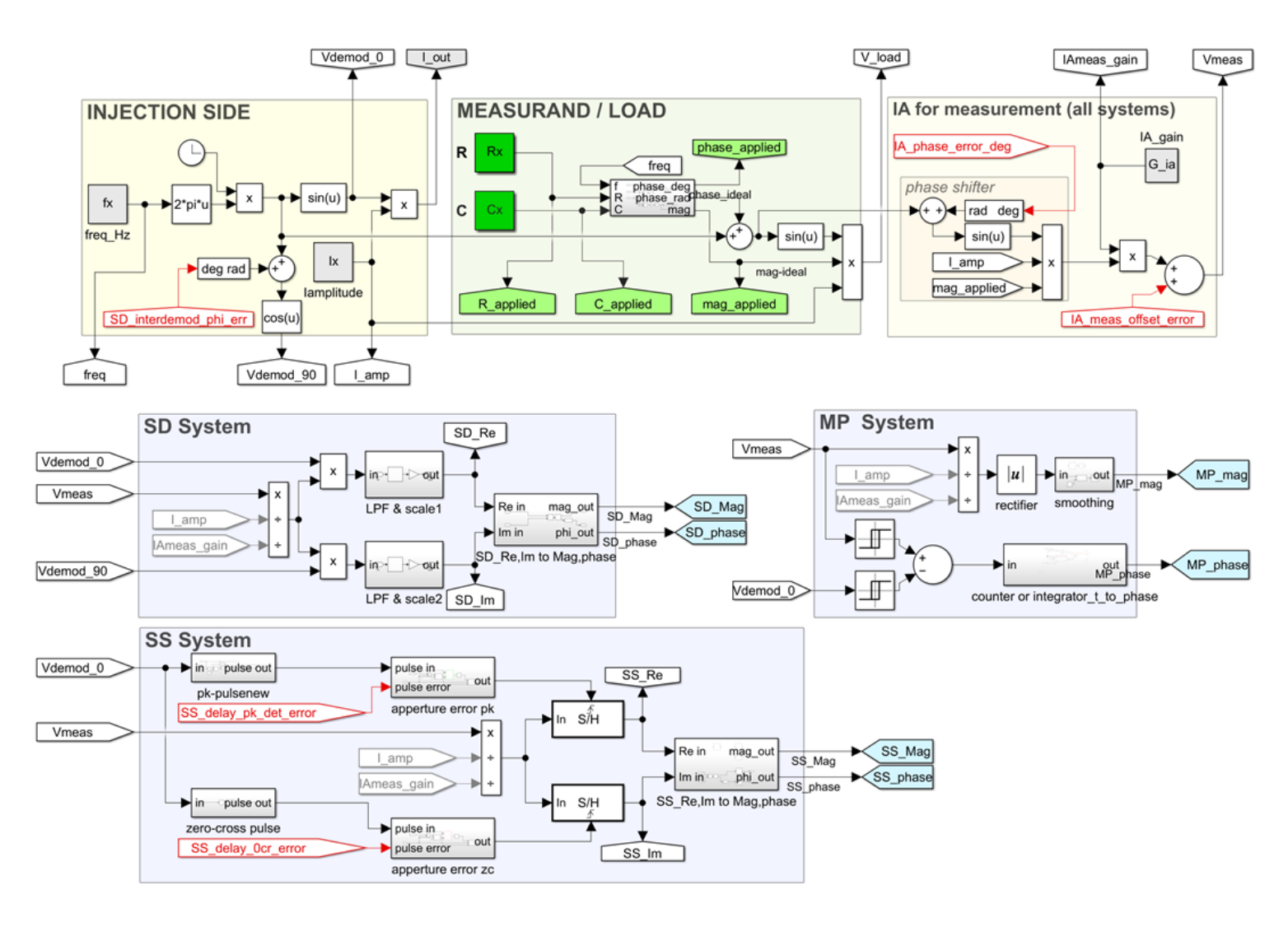


Figure 5. 2 Simulink model developed for the comparative assessment of the three impedimetric topologies.

In Figure. 5.2, a sine and a cosine waveform were generated respectively representing the $V_{\rm 0deg}$ (V_0) and $V_{\rm 90deg}$ (V_90) signals, both with unity 1V amplitudes and a frequency = 100Hz. A transconductance gain stage of 0.001 was subsequently applied to the first to represent the injected current of 1mA. The resistive and capacitive input values R_t and C_t (Table 1) forming the load representing tissue impedance were converted to ideal magnitude and phase using mathematical blocks representing eq. (5.1) and (5.2). The magnitude was multiplied with the injected current to represent the voltage (V_{meas}) appearing across the load with a subsequent stage of scaling representing the V_{meas} instrumentation amplifier and its gain.

Table 5.1. Applied R_x , and parallel R_x - C_x values in the simulations	
Resistive load $(Z_t = R_t)$	Parallel R-C load $(Z_t = R_t C_t)$
1ΚΩ	50KΩ 20nF
5ΚΩ	5KΩ 50nF

Table 5. 1 Applied R_{x_y} and parallel R_x - C_x values in the simulations

Systematic sources of error including common errors affecting all which is the error of measurement instrumentation amplifier. The error injection blocks will be discussed further in this chapter, as well as the individual blocks of the topologies as represented in Figure.5.2. To further understand the model and system block diagram as shown in Figure.5.2, the individual blocks has further been explained in the subsequent paragraphs.

5.3.1 Injection, load and measurement Side Simulink Block and analysis

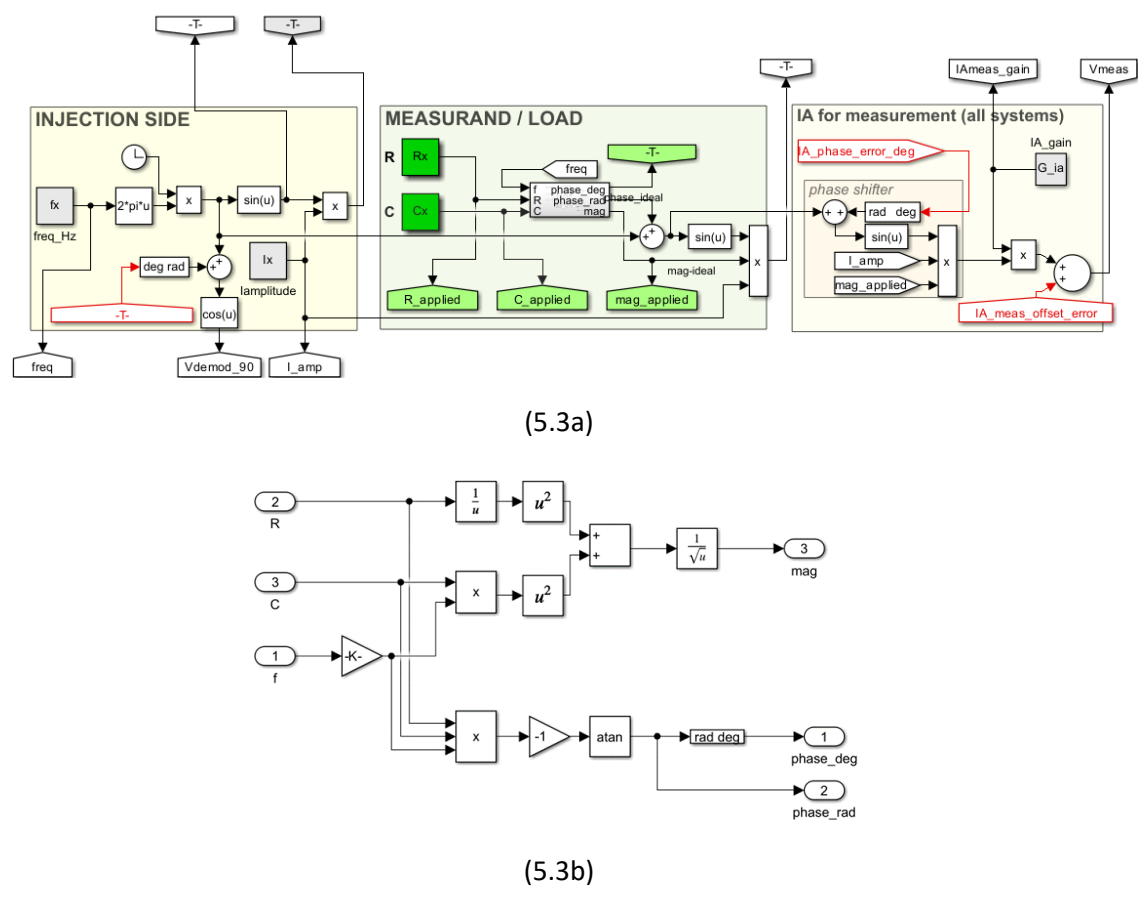
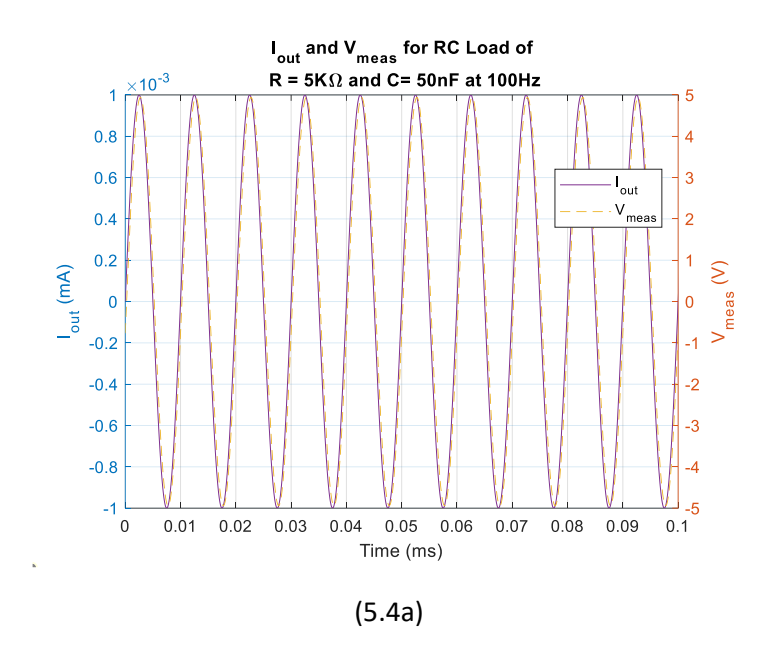


Figure 5. 3 Showing the details of (5.3a) current injection, and (5.3b) load measurement stages of Bioimpedance system

Simulink block.

In the input stage shown in Figure 5.3a, the injection signal, assumed to be a VCCS signal, is a generated sinusoidal waveform with a 1V amplitude. This signal produces a sinusoidal output current, I_{out} , with a transconductance gain of 0.001, giving an output current of 1mA. The output current is then multiplied by the respective load, whether it's a resistive load (R_{Load}), a capacitive load (C_{Load}), or an RC load, to generate the resultant voltage, V_{meas} , which is measured across the instrumentation amplifier, also with a gain of 1.

The ideal impedance magnitude and phase, used for cross-referencing and comparing with the other impedimetric systems mentioned, are calculated using equations 5.1 and 5.2 and determined by the block diagram in Figure. 5.3b. To further demonstrate the stage outputs shown in Figure 5.3, Figure 5.4 presents the measurement result V_{meas} along with the computed magnitude and phase for an RC load of 5 k Ω in parallel with 50 nF at a frequency of 100 Hz.



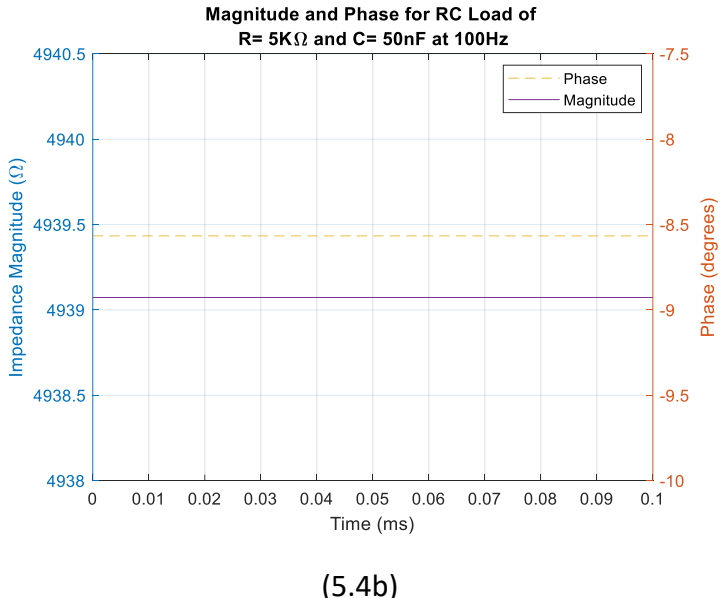


Figure 5. 4 Details of (5.4a) the injected current and measured voltage and (5.4b) Magnitude and phase graph for 5KΩ//50nF simulation graph of Simulink.

Figure 5.4 (a) and (b) demonstrate that, for a unity gain instrumentation amplifier, the measured voltage (V_{meas}) across a parallel RC load of 5K Ω and 50nF at 100Hz, for an injected current of 1mA, is 4.939V. The ideal impedance magnitude and phase for the same RC load were also computed using the Simulink block shown in Figure 5.3(b), yielding the result |4939|<-8.927°. These Simulink-based results were further confirmed through mathematical calculations which gave the same result.

With the accuracy of the injection and sensing blocks of the Simulink model verified in the absence of errors, the precision of the bioimpedance systems—specifically SD, SS, and MP was then evaluated before introducing error injections for comparison.

5.4 Synchronous detection Simulink Block.

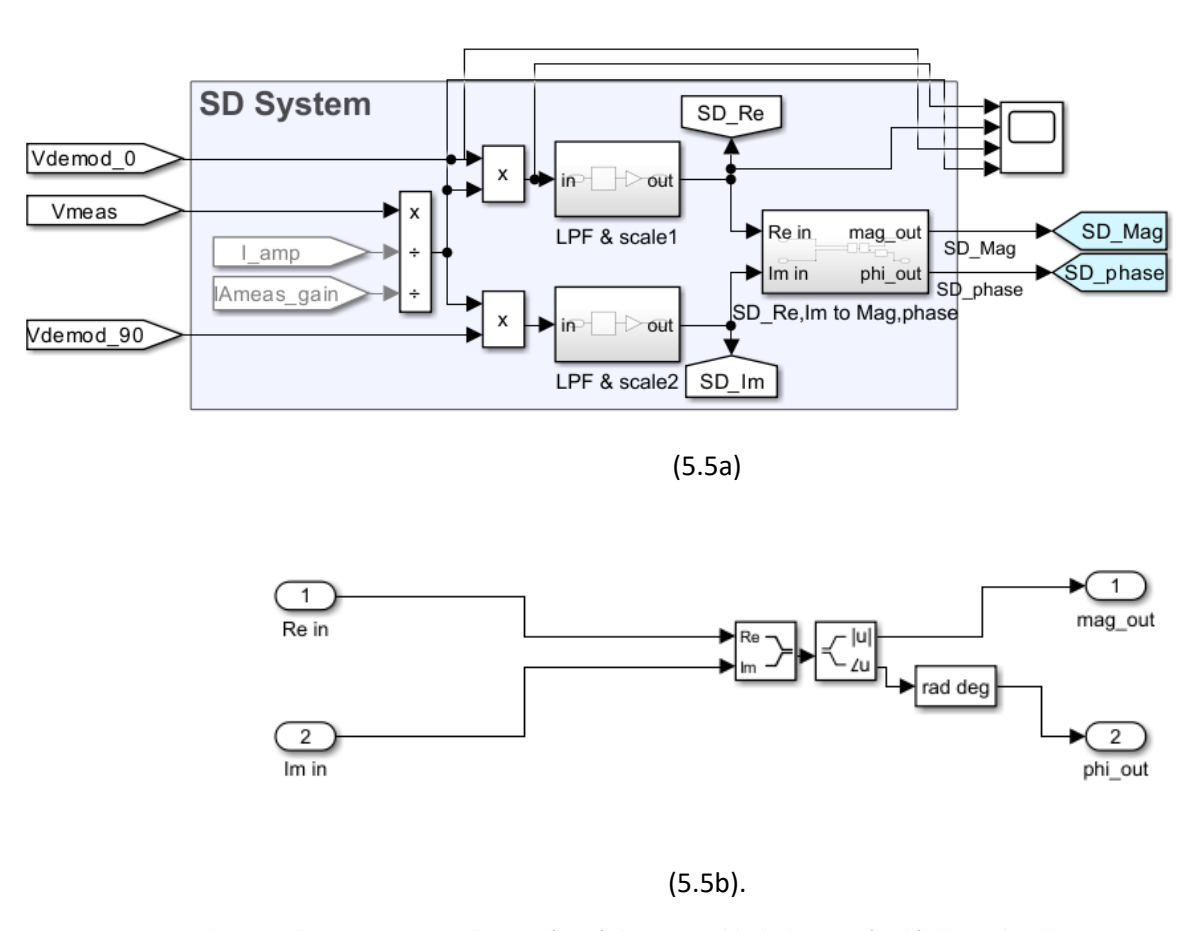
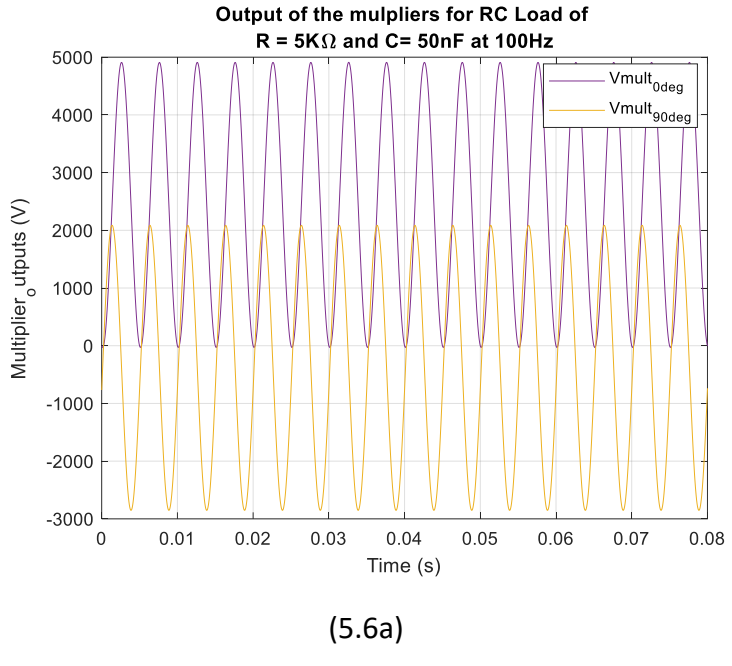


Figure 5. 5 Synchronous detection system showing (5.5a) the system block diagram (5.5b) The real and Imaginary to Magnitude and phase block diagram

Figure 5.5(a) shows the system simulating the SD topology. The scaled V_{meas} was fed into two channels, each featuring a multiplier, respectively multiplying the signal with V_{Odeg} and V_{90deg} before low-pass filtering stages generated the real and imaginary outputs. These were converted into magnitude and phase signals to better compare the performance of the systems by the Simulink block in Figure 5.5(b)



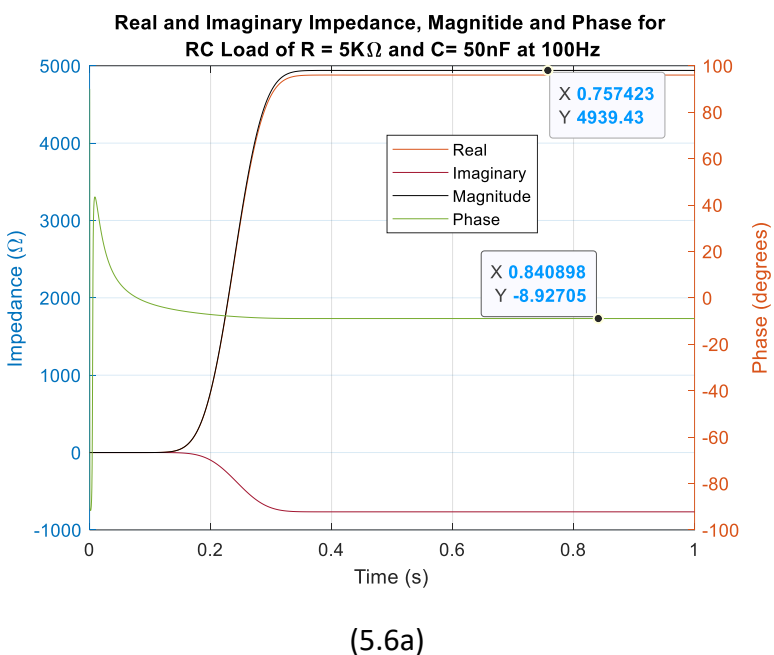


Figure 5. 6 Illustrating the measurement stages for SD system showing (5.6a) the multiplier outputs and (5.6b) Real and imaginary measurements results and their converted magnitude and phase values.

The results shown in Figure 5.6a shows the multiplication of V_{meas} from Figure. 5.5a with the 1V amplitude signals, V_{0deg} and V_{90deg} . The generated real and imaginary outputs are then transformed into magnitude and phase signals. In the absence of errors, the results remained the same with the mathematically computed data, yielding $|4939| < 8.927^{\circ}$.

5.5 Synchronous Sampling Simulink Block and analysis.

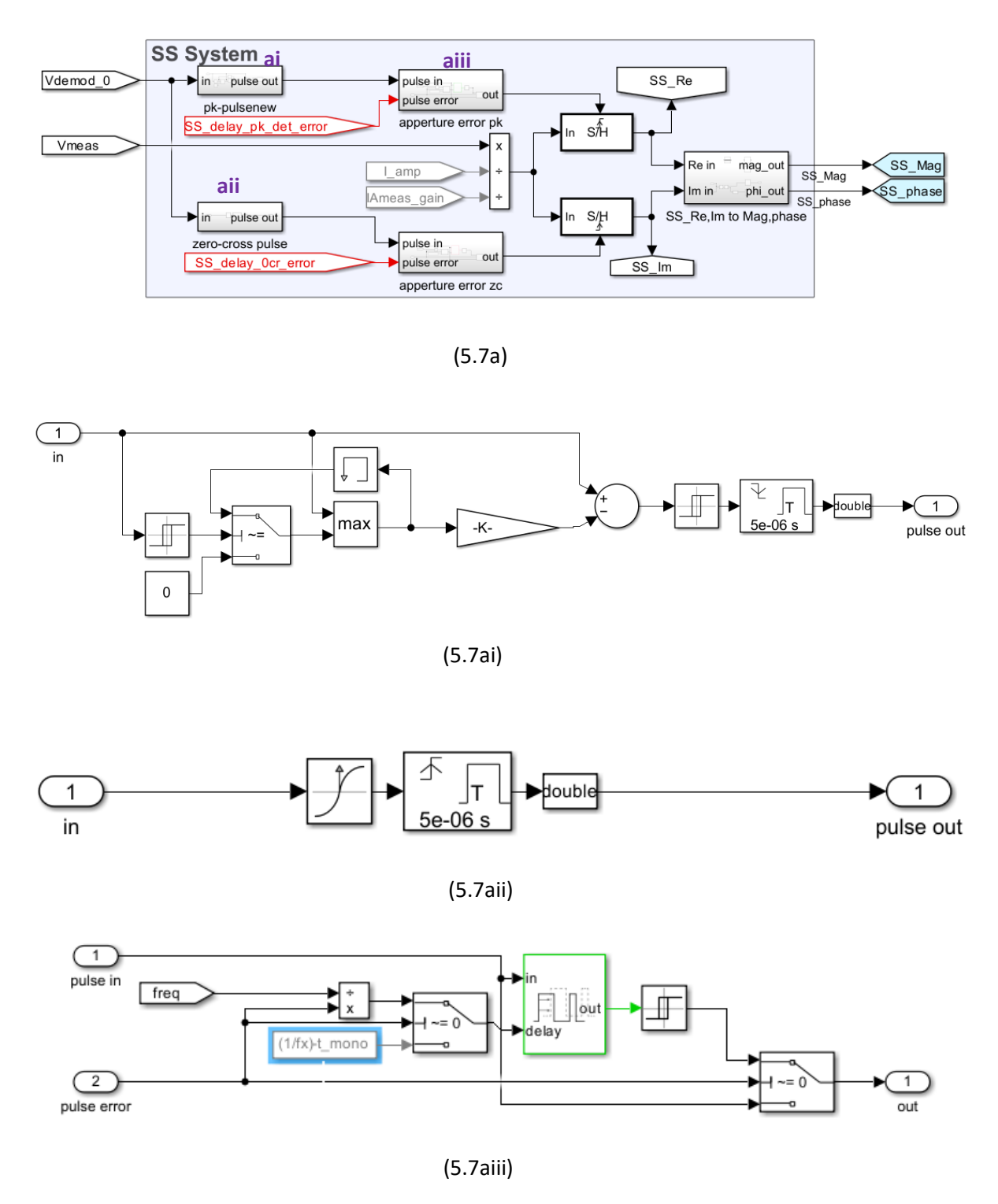


Figure 5. 7 Synchronous Sampling system Simulink blocks showing (5.7a) SS system block diagram, (5.7ai) The peak amplitude pulse generation block, (5.7aii) Zero crossing detection pulse and (5.7aiii) Error injection block

In the SS system, the real impedance $V\{RE\}_{ss}$ is sampled at $t=\frac{\pi}{2}$ of the zero-degree demodulation pulse (Vdemod_0), as shown in Figure 5.7ai. The peak of the in-phase demodulation pulse (Vdemod_0) is continuously tracked by a maximum detection block.

Once the signal reaches its peak amplitude, this value is stored in memory by the maximum detection block.

When the demodulation pulse (Vdemod_0) reaches its peak amplitude, it marks the start of a 90° phase. The stored peak amplitude of (Vdemod_0) is then multiplied by a gain of 0.9999 and subtracted from the original (Vdemod_0). This subtraction results in a small positive value.

This small positive difference is used to generate a pulse by comparing it to a very small threshold value (epsilon) in a relay switch. The relay is turned on or off depending on whether the difference exceeds this epsilon threshold. A falling-edge monostable with a pulse duration of 5*10⁻⁶s is triggered by the relay pulse, producing the SS peak detection pulse. This process repeats, resetting at each zero crossing of Vdemod_0 to track the next peak.

Figure. 5.7aii is the zero-crossing sampling pulse circuit. In this circuit, a zero-crossing detector block detects the zero crossing of Vdemod_0 signal and a rising edge monostable with a pulse duration of $5*10^{-6}$ s is used to capture a sharp rising pulse, thereby creating zero crossing sampling pulse.

Similarly, Figure 5.7aiii represents the error-adding block, which simulates aperture delay errors. This block introduces delays using variable transport delay blocks to the sampling pulses as the error increases, as illustrated in Figure 5.8. The error injection block will be further discussed later in this chapter

The respective zero crossing and peak detect trigger pulse of Vdemod_0 is further used to trigger the sample and hold(S/H) block which now samples the measured signal (V_{meas}). Their respective outputs of the S/H blocks corresponded to the real and the imaginary parts of the impedance load, subsequently further filtered and converted to magnitude and phase for comparison with the other systems.

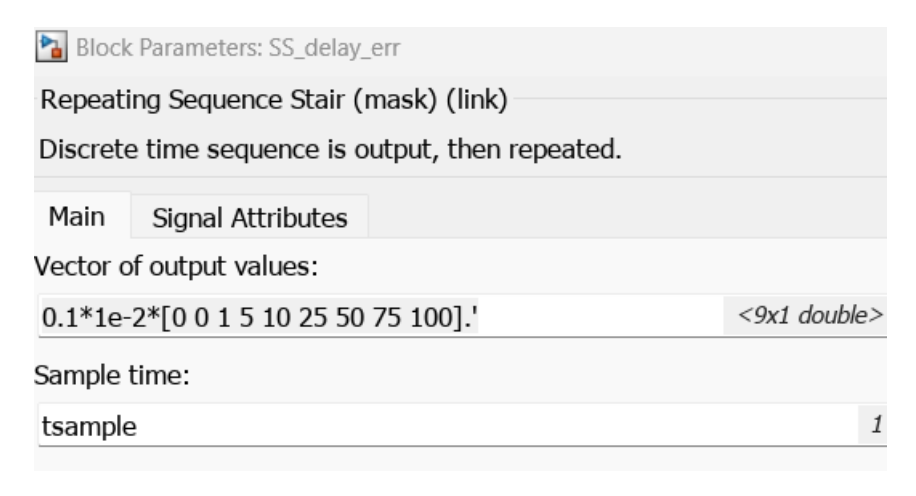


Figure 5. 8 Error values for SS system trigger pulses.

$Vdemod_0, Vdemod_0$ Peak Amplitude, $Vdemod_0$ Peak sampling Pulse for RC Load of R= $5K\Omega$ and C= 50nF at 100Hz8.0 0.6 0.4 0.2 Voltage(V) 0 -0.2 -0.4 -0.6 $Vdemod_0$ Vdemod₀ Peak Amplitude -0.8 Vdemod_∩ Peak sampling pulse 0.05 0.06 0 0.01 0.02 0.03 0.04 0.07 0.08 0.09 0.1 Time (s)

Figure 5. 9 SS Peak sampling pulse derivation graphs.

Figure. 5.9 provides a more detailed graphical explanation of the sub-circuit presented in Figure. 5.7ai, showing the derivation of the peak sampling pulse in the synchronous sampling system. The graphs illustrating the zero-crossing detection pulse, along with the circuit block previously shown in Figure. 5.7aii, are shown in Figure.5.10.

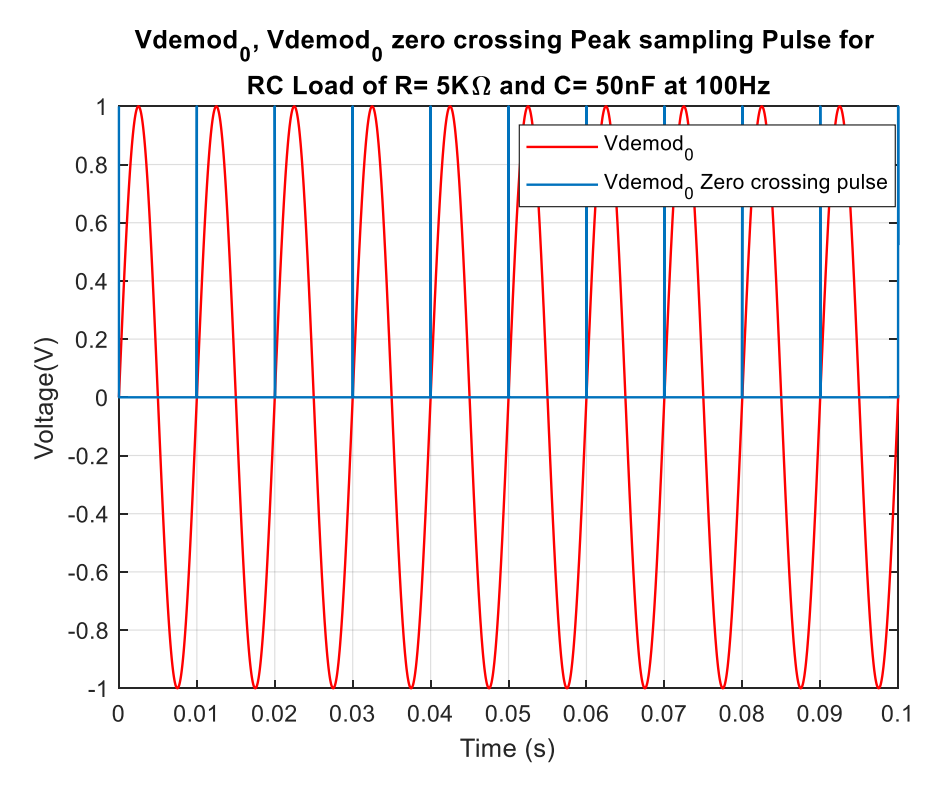


Figure 5. 10 SS Peak sampling pulse derivation graphs.

 V_{meas} sampled at the time, ωt =0, (zero crossing) and at time $\omega t = \frac{\pi}{2}$ (peak detect pulse) of the Vdemod_0, divided by the injected current, gives the real and Imaginary impedance values for RC load of $5K\Omega$ and 50nF at a frequency of 100Hz using a synchronous sampling system. These values here are in the absence of the errors and are in shown in Figure 5.11. These have also been further converted to their magnitude and phase values for comparison with other systems.

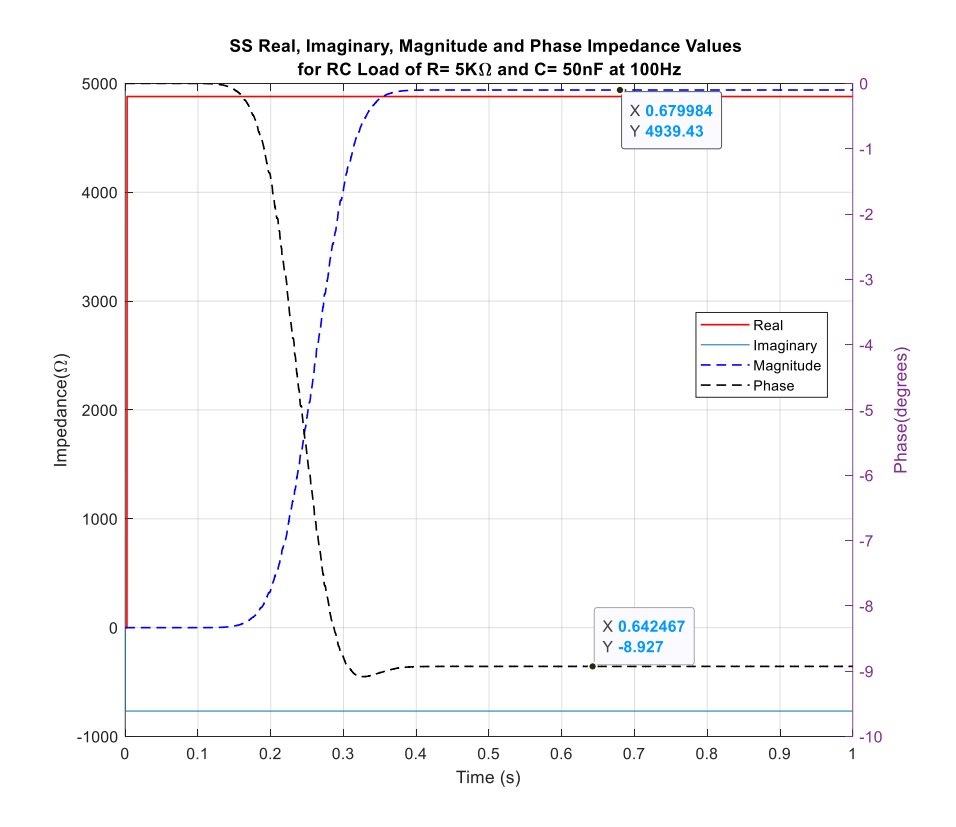


Figure 5. 11 SS systems showing the result of Real, Imaginary, Magnitude and Phase Impedance values for RC load of $5K\Omega$ | | 50 for an injected current of 1 mA.

In the absence errors, SS system magnitude and phase impedance values for RC load of $5K\Omega||50nF$ at 100Hz remained the same with the mathematically computed data, yielding $|4939|<-8.927^{\circ}$ and which is also the same as the SD System.

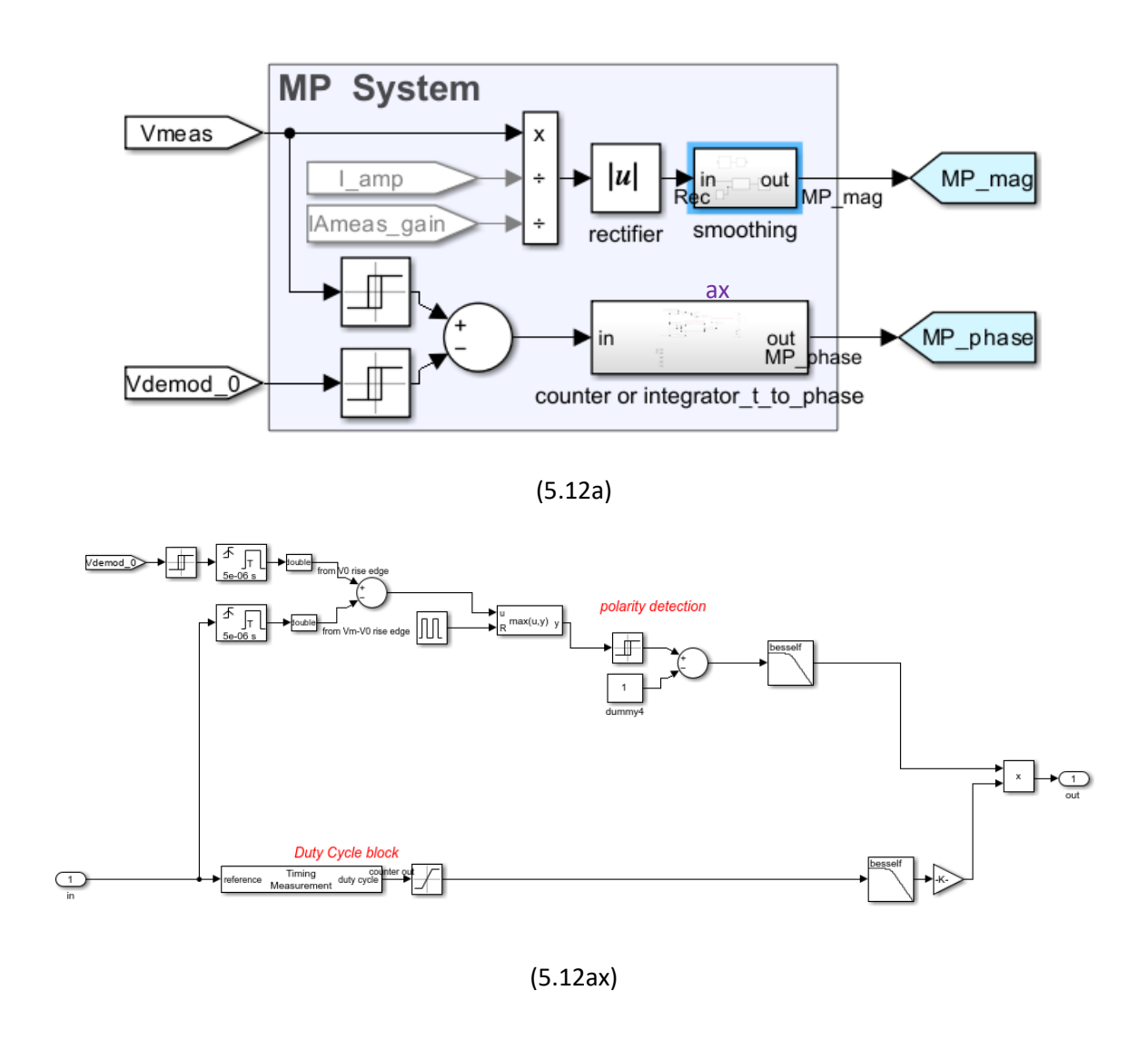
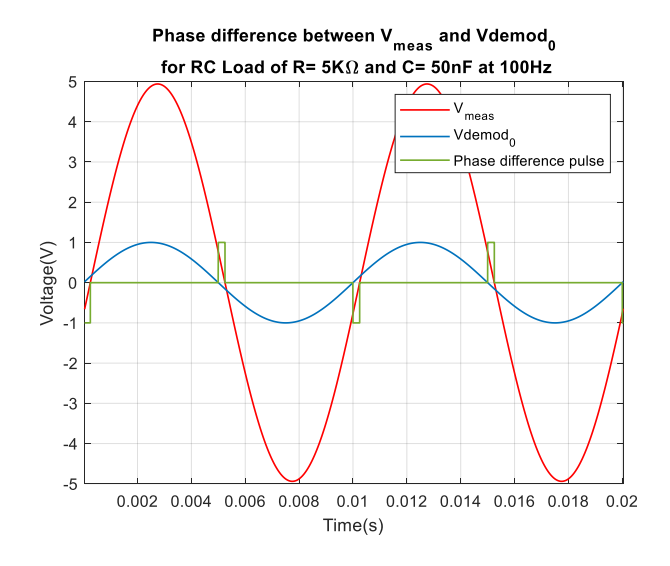


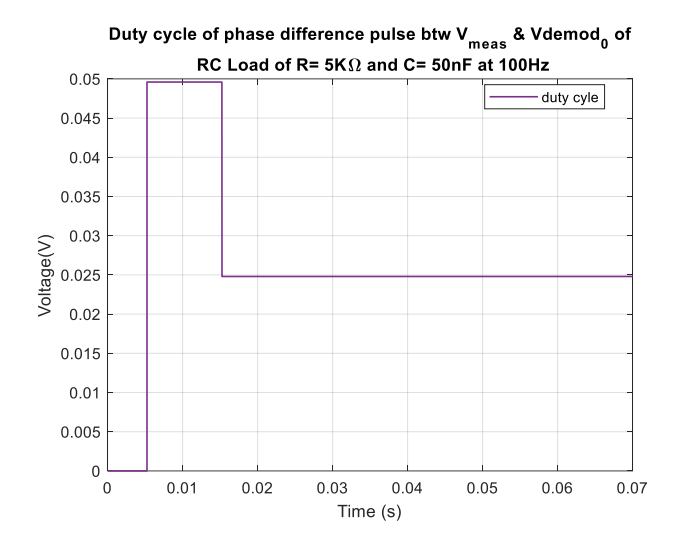
Figure 5. 12 MP system showing (5.12a) the system block diagram and (5.12ax) The polarity and phase detection block diagram.

Figure 5.12 shows the magnitude and phase system block diagram. In this block, V_{meas} is divided by the injected current of 1mA and its peak amplitude is obtained using a max-min block giving the Impedance magnitude. The phase is detected by converting both V_{meas} and V_{demod} into square waves using comparator blocks, and a subtractor block is used to obtain the pulse corresponding to the phase difference between the two square waves.

A duty cycle detection block, which is part of a subsystem shown in Figure 5.12ax, captures the duty cycle of the pulse from the subtractor circuit. A gain of 360 is applied to the detected duty cycle to calculate the phase value. Additionally, the subsystem block in Figure 5.12ax functions as a type II phase detector, determining whether V_{meas} is leading or lagging. The graphs of Figure.5.13 shows the result stages of the of the Simulink blocks for the magnitude and phase bioimpedance measurement system.



(5.13a)



(5.13b)

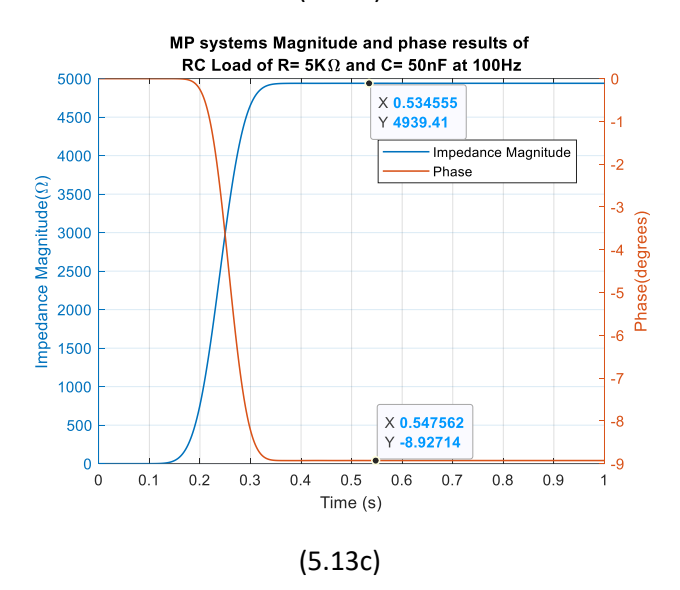


Figure 5. 13 Illustrates the measurement stages of the MP system showing (5.13a) Detected phase with MP system, (5.13b) Duty cycle and (5.13c) Magnitude and Phase measurement.

In the absence of errors, the final results for an RC load of 5 k Ω in parallel with 50 nF at a frequency of 100 Hz for MP system remained the same with the mathematically computed data, yielding |4939|<-8.927° and which is also the same as the SD and SS System.

5.7 Systematic errors of Bioimpedance measurement system

Two categories of errors were considered: common errors, arising from the measurement instrumentation amplifier connected to the input of all systems, and topology-specific errors, which comprises of errors related to synchronous detection and synchronous sampling. The MP topology specific error were considered as part of originating from the common errors of the VCCS and IA, as such, MP specific were not simulated separately.

The five errors simulated here are not exhaustive as there many more errors peculiar to these systems, however, these errors are considered to be most popular and reported in the literature [43][110][111]. The common for all the systems considered here are:

- Phase errors noted at the sense circuit, i.e output of the measurement instrumentation amplifier $(\phi_{\text{er}_{ia}})$
- Dc Offsets voltage of measurement instrumentation amplifier (Vof_ia)

The topology specific errors considered here are

- Intermodulation phase errors ($\phi_{\text{er_demod}}$) of the synchronous demodulation system. i.e when the I & Q demodulation pulses are not perfectly locked to 0° and 90° phase apart.
- \triangleright Aperture errors ($\tau_{\text{er-pk}}$, $\tau_{\text{er-zer}}$) of the S&H circuit of the Synchronous sampling system.
- ➤ Comparator phase shifts and offsets of the M&P phase detection block, however this was considered to have been introduced by the common errors from the measurement IA.

5.8 Errors Injection block and analysis.

The error Simulink block in Figure 5.14 consists of six multiport multiplexer switches, each with seven selectable ports. These six multiplexers are connected to a central control port, where selecting a specific port number activates the error source connected to the corresponding multiplexer, while all other ports are shunted to 0. Each of the five errors considered, $\{\phi_{\text{er_ia}}, V_{\text{of_ia}}, \phi_{\text{er_demod}}, \tau_{\text{er-pk}}, \tau_{\text{er-zer}}\}$ were varied through 7 percentage levels of their highest value: 1%, 5%, 10%, 25%, 50%, 75% and 100% using the repeating sequence stair.

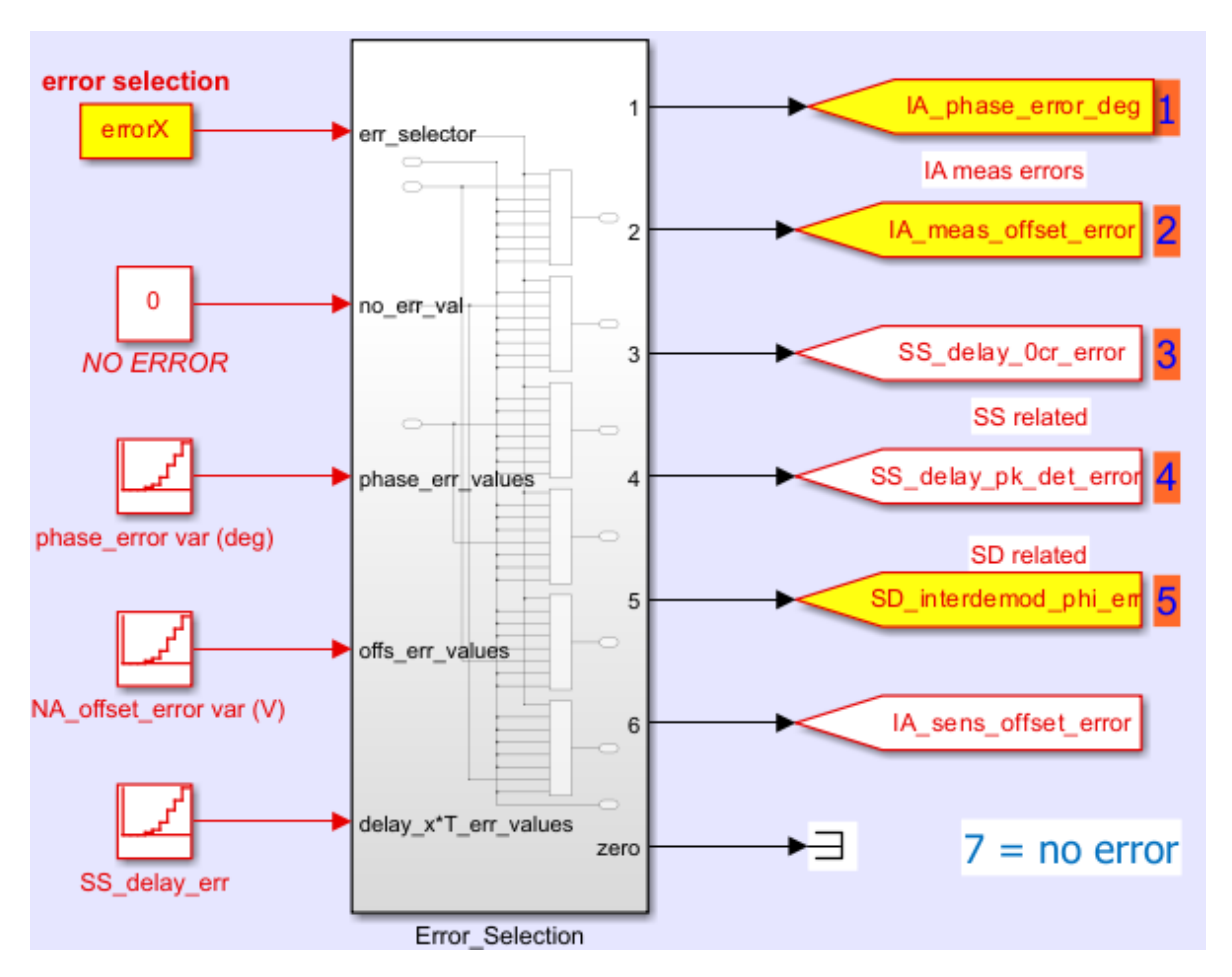


Figure 5. 14 Error selection and injection block.

For phase errors $\phi_{\text{er_ia}}$ and $\phi_{\text{er_demod}}$ the highest error value considered was 45°; for the offset error $V_{\text{of_ia}}$ the maximum value was set to 500mV; and for sample and hold aperture delays, errors $\tau_{\text{er-pk}}$ and $\tau_{\text{er-zer}}$ of up to 100ms was used.

5.7.1. Effects of IA phase errors on the MP measurements of the systems.

The magnitude and phase measurements result of the systems were compared against the ideal measurements when phase errors at the output of instrumentation amplifier was introduced. Figure 5.15 shows introduced phase errors.

Phase errors of up to 45° were incrementally introduced at the sensing block. The measured and converted magnitude and phase impedance and their percentage error values for all the systems are illustrated in Figure 5.16-Figure 5.19.

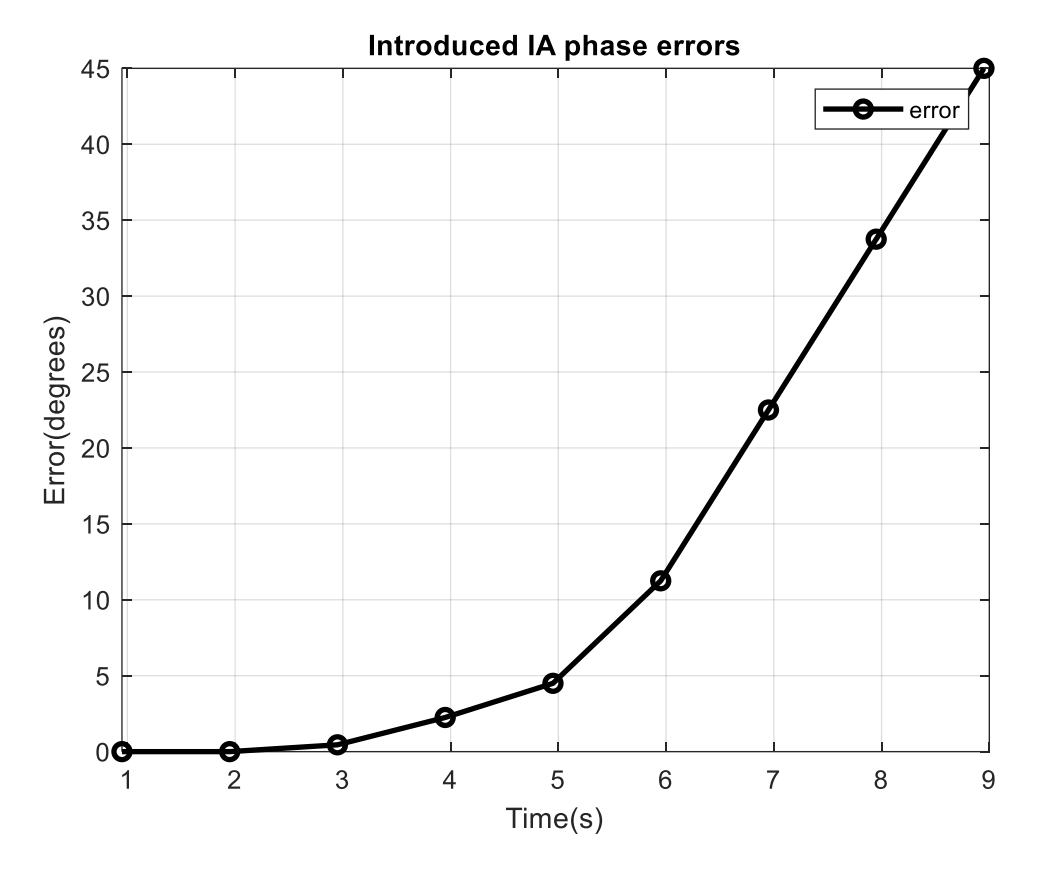


Figure 5. 15 Introduced phase errors at the output of sensing block.

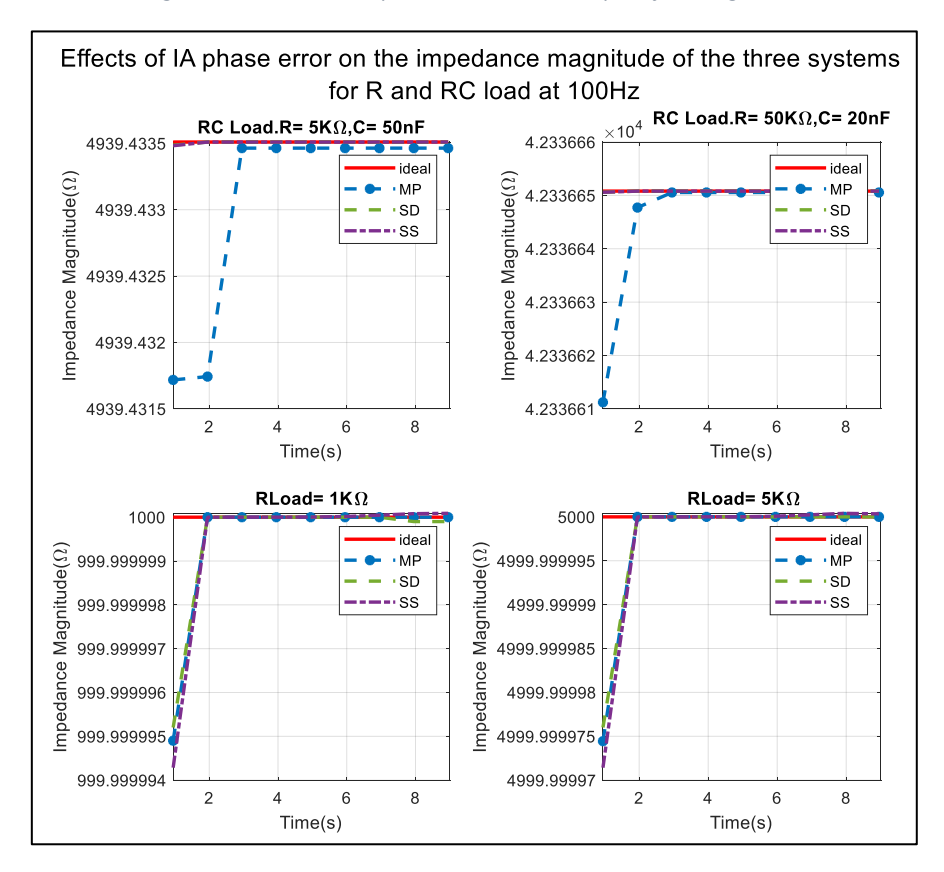


Figure 5. 16 Effects of IA phase errors on the Impedance magnitude results of all the system.

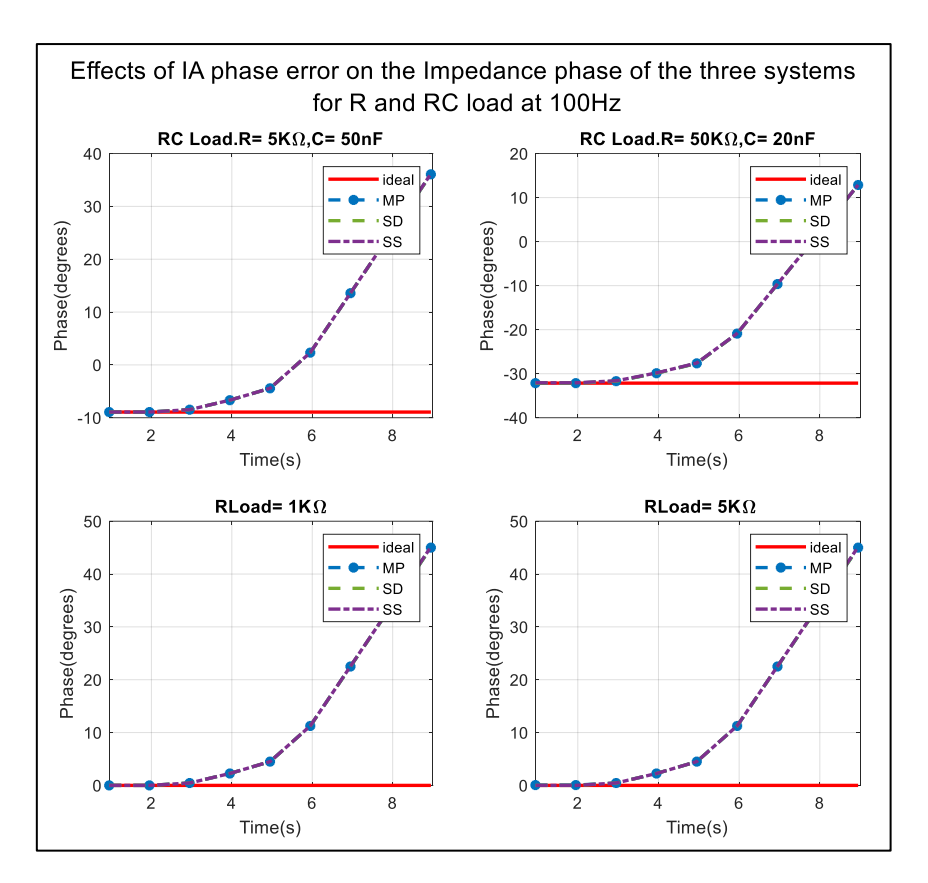


Figure 5. 17 Effects of IA phase errors on the Impedance phase results of the all the system.

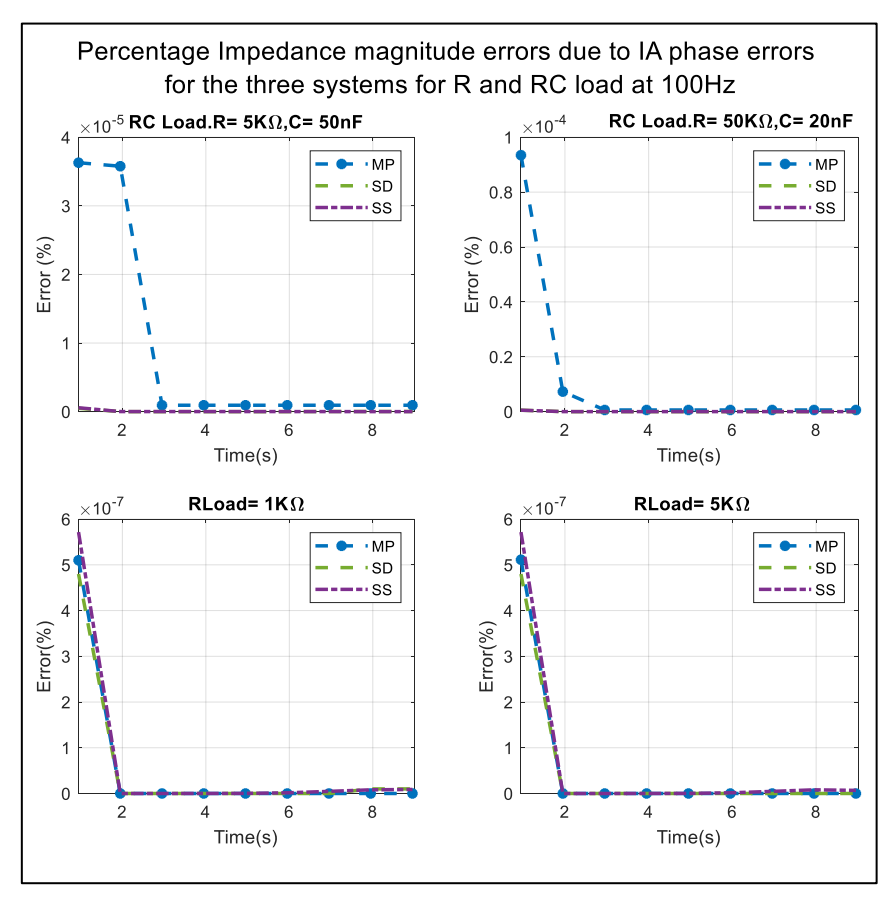


Figure 5. 18 Relative percentage impedance magnitude errors of R and RC loads due to added IA phase shifts errors.

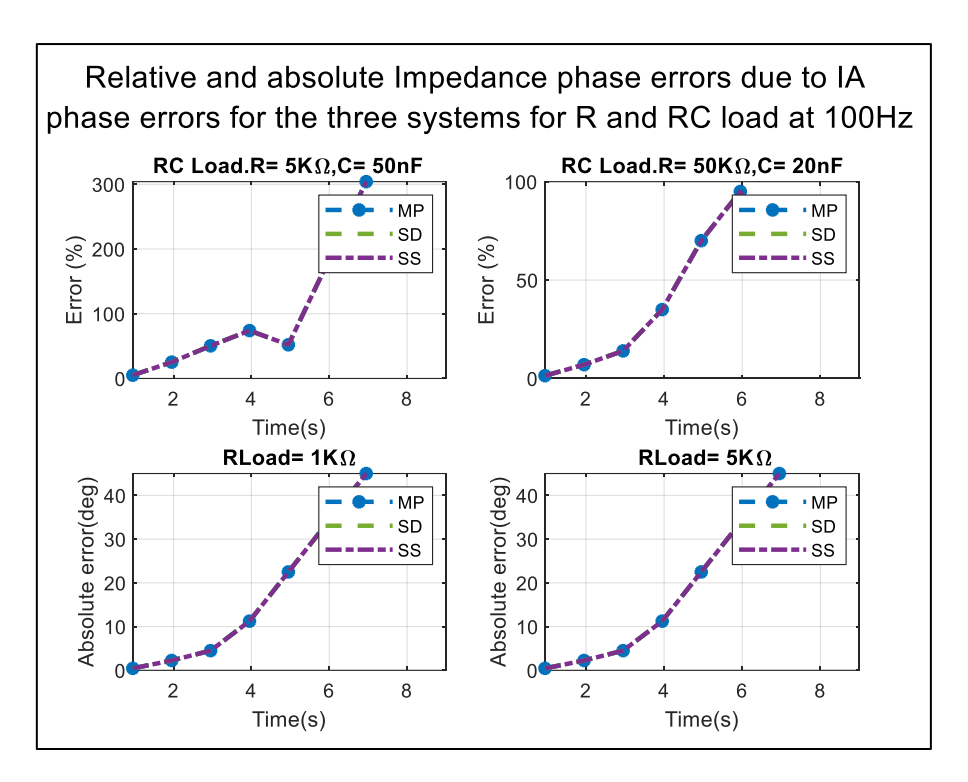


Figure 5. 19 Relative and absolute impedance phase errors of R and RC loads due to added IA phase shifts.

Figure 5.16 - Figure 5.19 shows the effects erroneous phase shifts of the sense circuits on the magnitude and phase measurement results of both R and RC loads. The relative and absolute errors of Figure 5.18 and Figure 5.19 further shows that while erroneous phase shifts of sense circuit affect the phase values of all the systems, the impedance magnitude remained unaffected.

Recall the measured resultant voltage out of the instrumentation amplifier sense circuit is from equation 4.89 is

$$v_{meas} = A_v i_0 z_x sin(\omega t - \varphi)$$

As such with additional erroneous phase shifts added

$$v_{meas} = A_v i_0 z_x sin(\omega t - \varphi - \Delta \theta)$$
 (5.1)

For MP system,

The Impedance magnitude $|z_x|$ is peak amplitude of v_{meas} divided by the peak amplitude of the injected current.

$$|z_x| = \frac{A_v i_0 z_x}{A_v i_0}$$
 . no effects of phase shift (5.2)

For SS system,

$$v_{meas} = A_v i_0 z_x sin(\omega t - \varphi - \Delta \theta)$$

A sample of v_{meas} at the zero crossing of the reference signal $V_{\rm in}$ at $~\omega t=0$ further gives the Imaginary impedance component $V\{IM\}_{ss}$

$$V\{IM\}_{ss} = A_{v}i_{0}z_{x}sin(-\varphi - \Delta\theta)$$
(5.3)

$$\frac{V\{IM\}_{SS}}{A_{v}i_{0}} = -z_{x}sin(\varphi + \Delta\theta)$$
 (5.4)

The Imaginary part of the impedance is hence

$$\{IM\}_{SS} = \frac{V\{IM\}_{SS}}{A_v i_0} = -z_x sin(\varphi + \Delta\theta)$$
(5.5)

A sample of v_{meas} at the peak of the reference signal V_{in} at $\omega t = \frac{\pi}{2}$ further gives

$$\frac{V\{RE\}_{SS}}{A_{\nu}i_0} = z_{\chi}Cos(\varphi + \Delta\theta) \tag{5.6}$$

$$\{RE\}_{SS} = \frac{V\{RE\}_{SS}}{A_v i_0} = z_x Cos(\varphi + \Delta\theta)$$
 (5.7)

The impedance magnitude is:

$$|Z_x| = \sqrt{\{RE\}_{SS}^2 + \{IM\}_{SS}^2}$$
 (5.8)

$$\{RE\}_{SS}^2 = (z_x Cos(\varphi + \Delta\theta))^2 = z_x^2 cos^2(\varphi + \Delta\theta) =$$
(5.9)

$$\{IM\}_{SS}^2 = (-z_x Sin(\varphi + \Delta\theta))^2 = z_x^2 Sin^2(\varphi + \Delta\theta)$$
 (5.10)

$$z_x^2 cos^2(\varphi + \Delta\theta) + z_x^2 Sin^2(\varphi + \Delta\theta)$$
 (5.11)

$$z_x^2((\cos^2(\varphi + \Delta\theta) + \sin^2(\varphi + \Delta\theta))$$
 (5.12)

$$(\cos^2(\varphi + \Delta\theta) + \sin^2(\varphi + \Delta\theta) = 1$$
 (5.13)

$$|z_x| = \sqrt{{z_x}^2 * 1} \tag{5.14}$$

Hence the magnitude is not affected by phase errors in Synchronous sampling system

For SD system,

$$v_{-0} = v_0 \sin(\omega t) \tag{5.15}$$

$$v_{90} = v_0 \sin(\omega t + 90^\circ) \tag{5.16}$$

The in-phase demodulation procedure involves multiplying v_{meas} by v_{-0} , yielding the output of in-phase multiplier

$$v_{multodeg} = \frac{A_v i_0 Z_x v_0}{2} \left[\cos(\varphi + \Delta \theta) - \cos(2\omega t - \varphi - \Delta \theta) \right]$$
 (5.17)

The output of the multiplier $v_{mult0deg}$ is also passed through a low pass filter to eliminate high frequency components leaving out the DC components. The output of the low pass filter for the in-phase demodulation is

$$v_{LPF0deg} \approx \frac{A_v i_0 Z_x v_0 (\cos(\varphi + \Delta \theta))}{2}$$
 (5.18)

Hence the real part of the impedance is
$$Re\{Z_x\} = (cos(\varphi + \Delta\theta)) = \frac{2*v_{LPF0deg}}{A_v i_0 v_0}$$
 (5.19)

Similarly, the quadrature demodulation procedure involves multiplying v_{meas} by $v_{_{90}}$, yielding the output of quadrature multiplier ($v_{mult_{90}}$ °).

$$v_{mult90^{\circ}} = \frac{A_{v}i_{0}Z_{x}v_{0}}{2}\left\{\sin(2\omega t - \varphi - \Delta\theta) + \sin(-\varphi - \Delta\theta)\right\}$$
 (5.20)

 $v_{mult90^{\circ}}$ is also passed through the low pass filter from where the imaginary part of the Impedance (Im) is derived as in eq. (5.19).

$$v_{LPF90^{\circ}} = -\frac{A_v i_0 Z_x v_0}{2} \sin(\varphi + \Delta\theta)$$
 (5.21)

$$Im(Z_{\chi}) = (sin(\varphi + \Delta\theta)) = \frac{2*v_{LPF90^{\circ}}}{A_{\nu}i_{0}\nu_{0}}$$
 (5.22)

The impedance magnitude is:

$$|Z|=Z_{\chi}\sqrt{cos^2(\varphi+\Delta\theta)+sin^2(\varphi+\Delta\theta)}=1$$
 : magnitude is unaffected by $\Delta\theta$ in SD system.

5.7.2. Effects of IA dc offsets errors on the MP measurements of the systems.

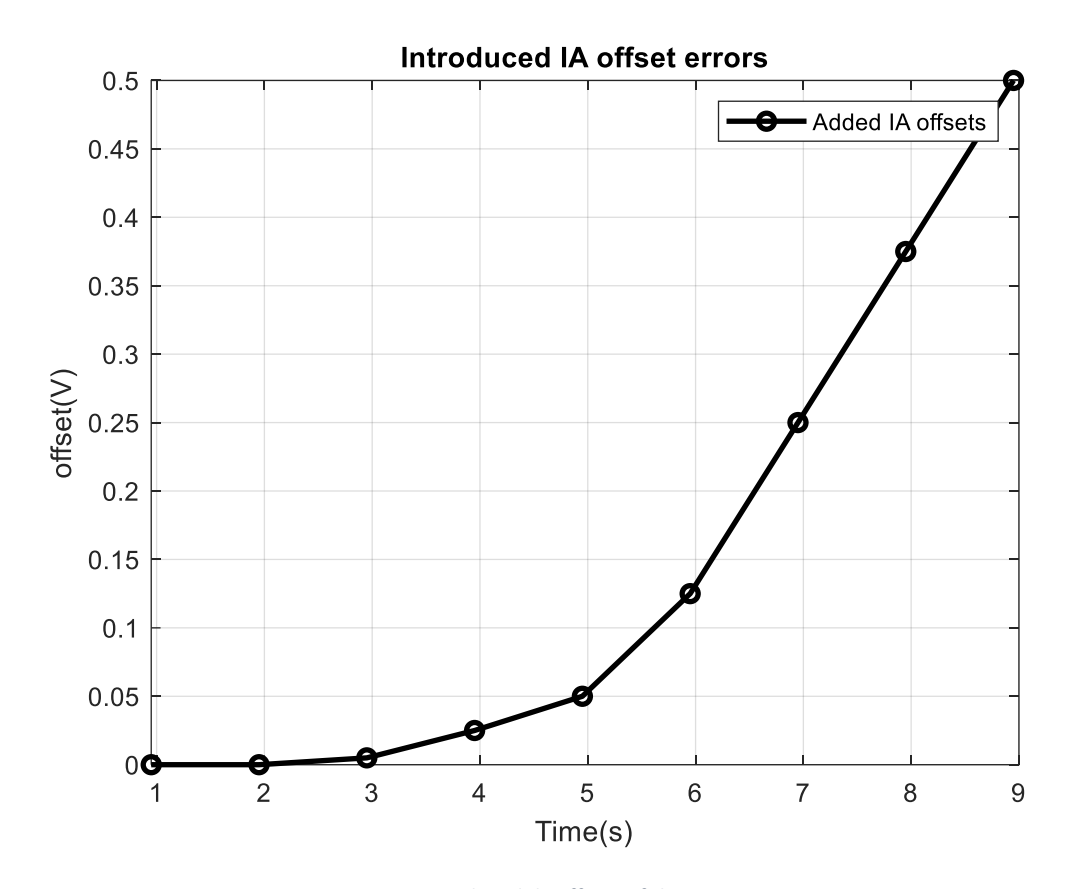


Figure 5. 20 Introduced dc offsets of the sense circuits

One of the key requirements for sense circuits is a high Common-Mode Rejection Ratio (CMRR) to effectively reject common-mode voltages at the input of the instrumentation amplifier (IA)[111]. However, mismatches in electrode impedances and DC offsets from the Voltage-Controlled Current Source (VCCS) can introduce DC offsets at the output of the IA. Since the final outputs of the system are DC-measured values, any DC offsets at the IA output will impact the accuracy of these measurements.

To investigate the effect of these DC offsets on the overall system accuracy, offsets of up to 500 mV were introduced in the sensing block, as shown in Figure 5.20.

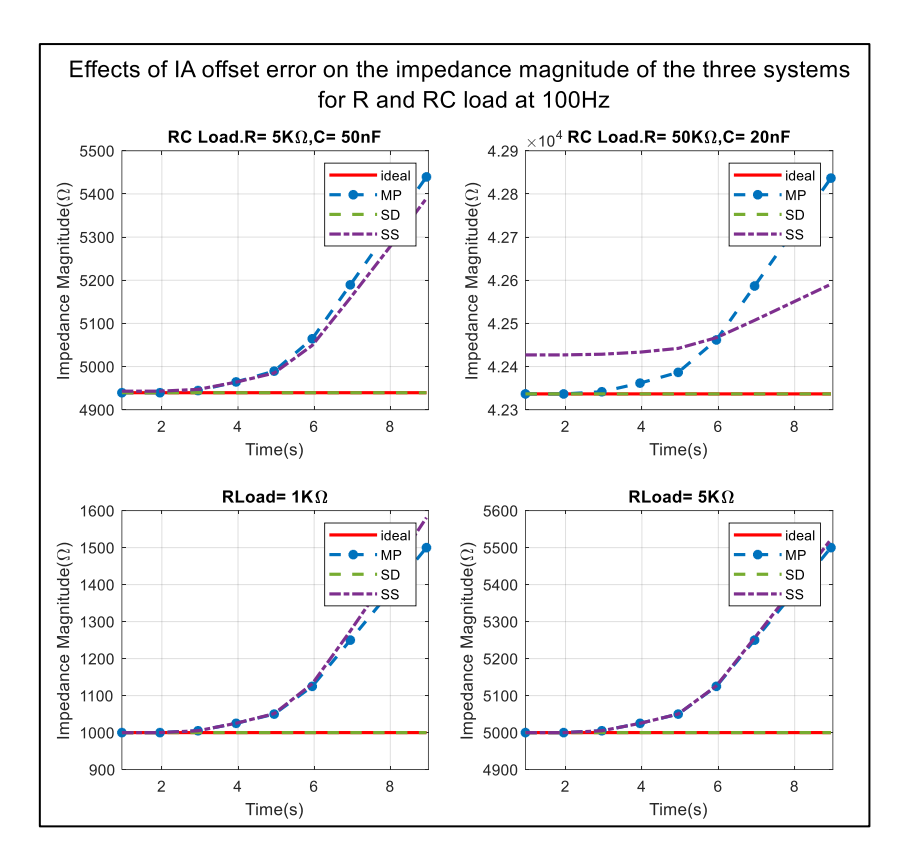


Figure 5. 21 Effects of IA offset errors on the Impedance magnitude results of the all the system.

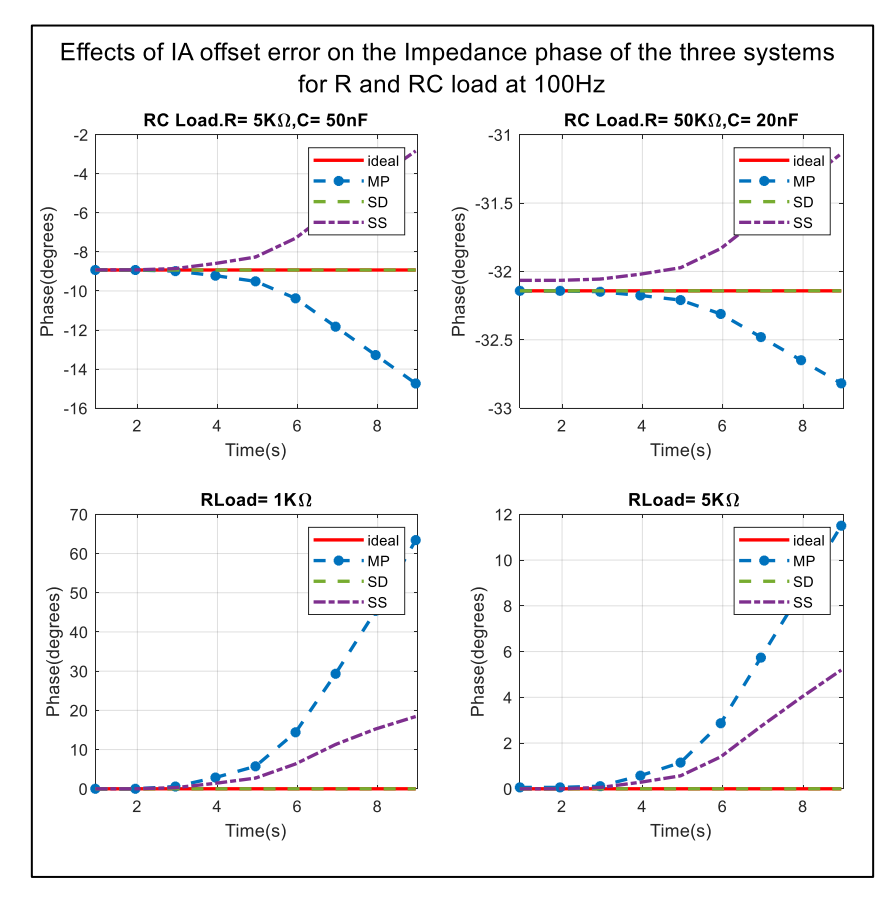


Figure 5. 22 Effects of IA offset errors on the Impedance phase results of the all the system.

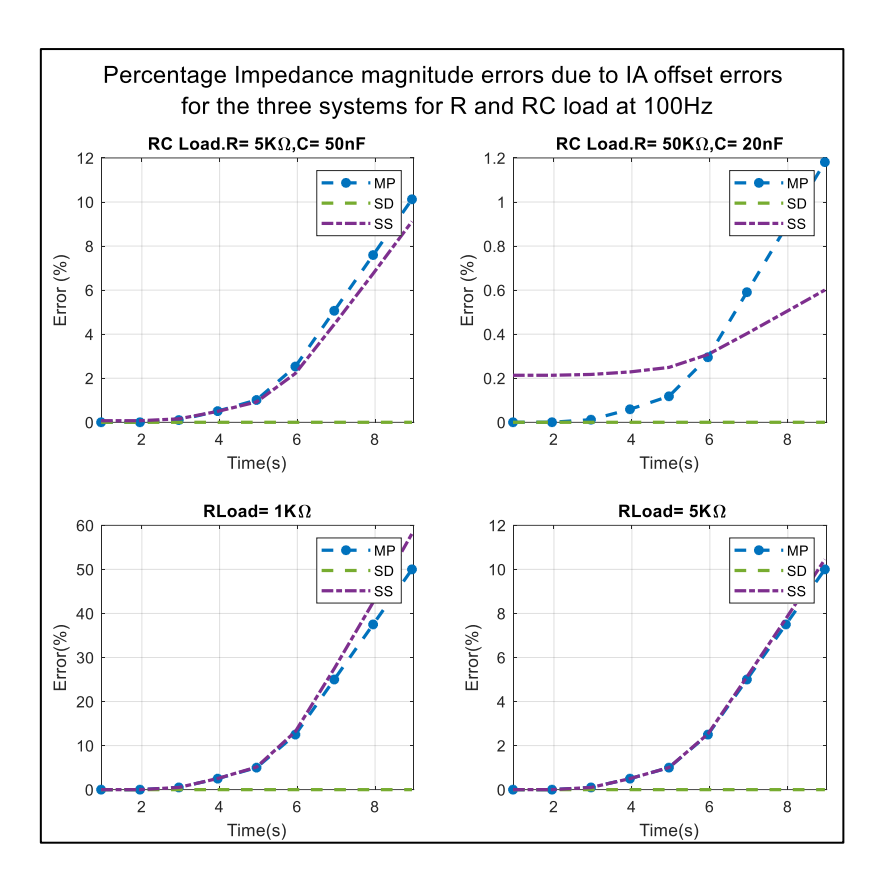


Figure 5. 23 Relative percentage impedance magnitude errors of R and RC loads due to added IA offset errors.

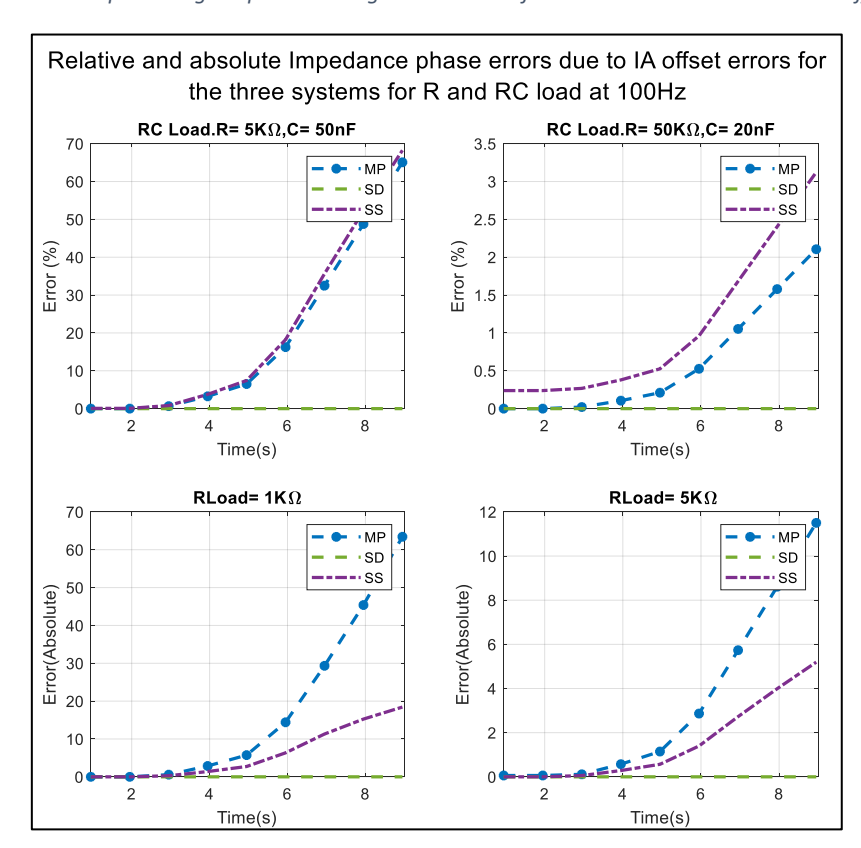


Figure 5. 24 Relative and absolute impedance phase errors of R and RC loads due to added IA offset errors.

Figures 5.20 to Figures 5.24 illustrate the effects of erroneous DC offsets in the IA circuit on the magnitude and phase measurement results for both R and RC loads. The relative and

absolute errors shown in Figures 5.23 and Figures 5.24 further demonstrate that, while the erroneous DC offset in the sense circuit affects the magnitude and phase measurements in both the MP and SS systems, the impedance magnitude and phase measurements in the SD system remain unaffected. This was further mathematically analysed below:

Recall

$$v_{meas} = A_v i_0 z_x sin(\omega t - \varphi)$$

In the presence of IA offsets VDC,

$$v_{meas} = A_v i_0 z_x sin(\omega t - \varphi) + VDC$$
 (5.23)

In-phase multiplication becomes

$$v_{mult0deq} = A_v i_0 Z_x \left(\sin(\omega t - \varphi) + VDC \right) * v_0 \sin(\omega t)$$
(5.24)

$$v_{mult0deg} = A_v i_0 Z_x \sin(\omega t - \varphi) * v_0 si n(\omega t) + VDC * v_0 si n(\omega t)$$
(5.25)

$$A_v i_0 Z_x \sin(\omega t - \varphi) * v_0 si n(\omega t) = \frac{A_v i_0 Z_x v_0}{2} [\cos(-\varphi) - \cos(2\omega t - \varphi)]$$
 (5.26)

$$VDC * v_0 si n(\omega t) = VDC v_0 si n(\omega t)$$
(5.27)

Following a low pass filter stage

$$v_{LPF0deg} = \frac{A_v i_0 Z_x v_0}{2} \left[\cos(-\varphi) \right]$$
 (5.28)

 $VDCv_0si\ n(\omega t)$ will not contribute to the final Component of the DC output of the filter because it oscillates at frequency (ω) and will be removed by the Low pass filter. Therefore, SD is immune to the DC Offsets of the IA sense circuits.

5.7.3. Effects of inter-demodulation phase shift errors of SD system.

One of the main sources of error in SD systems occurs when the intermodulation signals lose their 0–90-degree phase synchronization. This can happen if the signals are not accurately locked to a 90-degree phase shift or if the phase oscillator used is temperature-sensitive, as is the case with RC oscillators, where tolerance and temperature variations can impact the accuracy of the phase values. To further investigate how these factors affect the accuracy of magnitude and phase measurements in SD systems, phase shifts of up to 45° (Figure 5.20) were incrementally introduced to the 90-degree intermodulation signals for both R and RC loads at a frequency of 100 Hz.

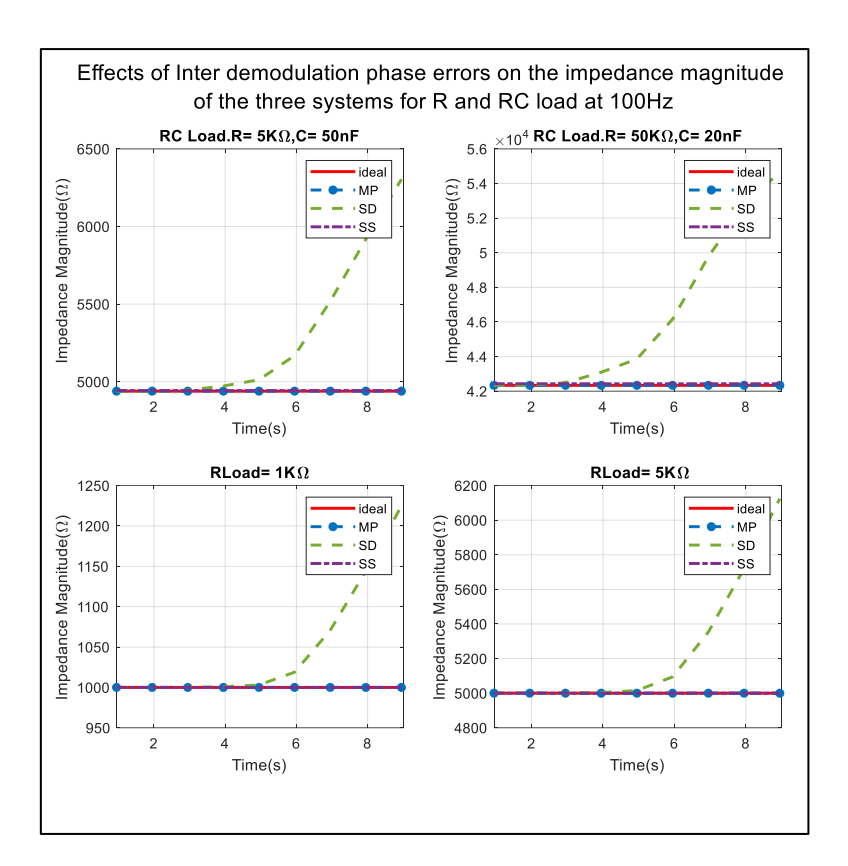


Figure 5. 25 Effects of SD inter-demodulation phase errors on the Impedance magnitude results of SD system.

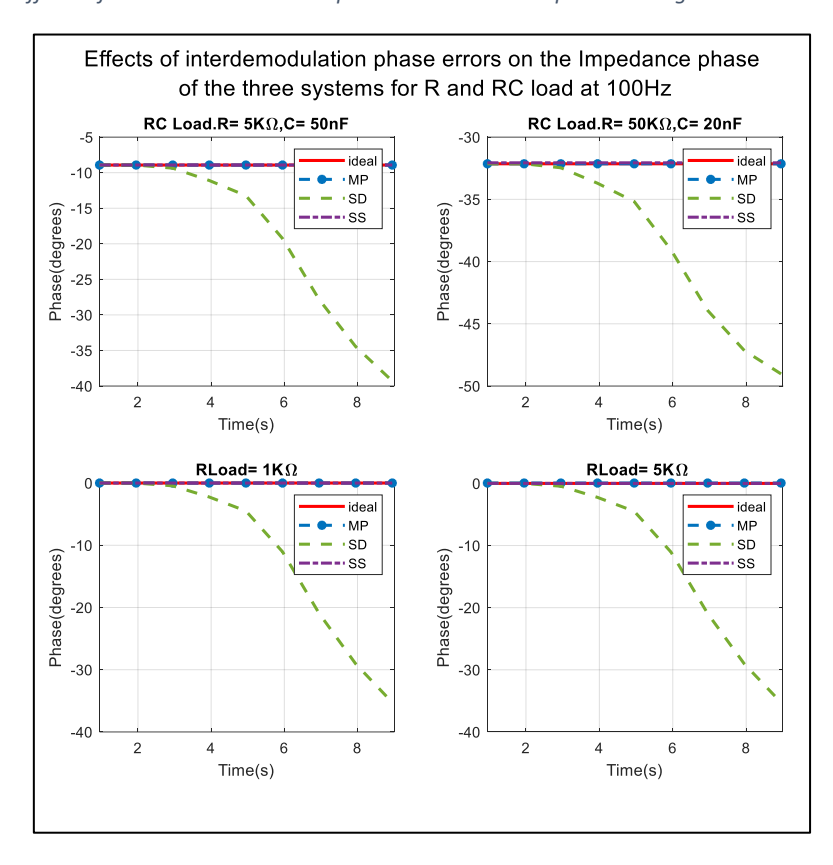


Figure 5. 26 Effects of SD inter-demodulation phase errors on the Impedance phase results of SD system

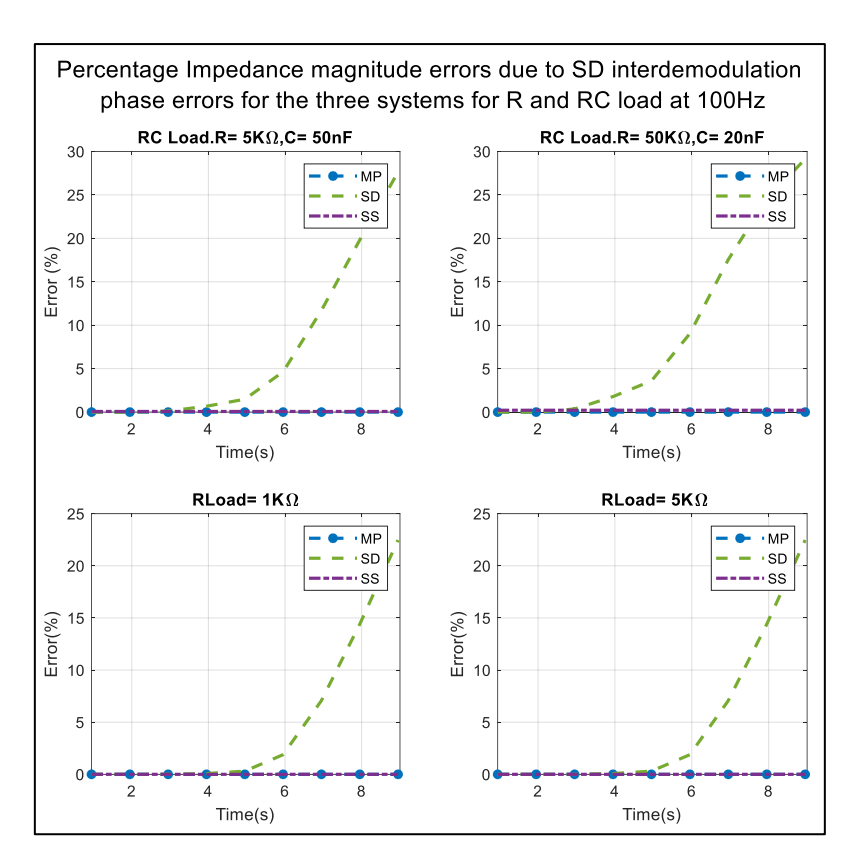


Figure 5. 27 Relative percentage impedance magnitude errors of R and RC loads due to added SD inter-demodulation phase errors.

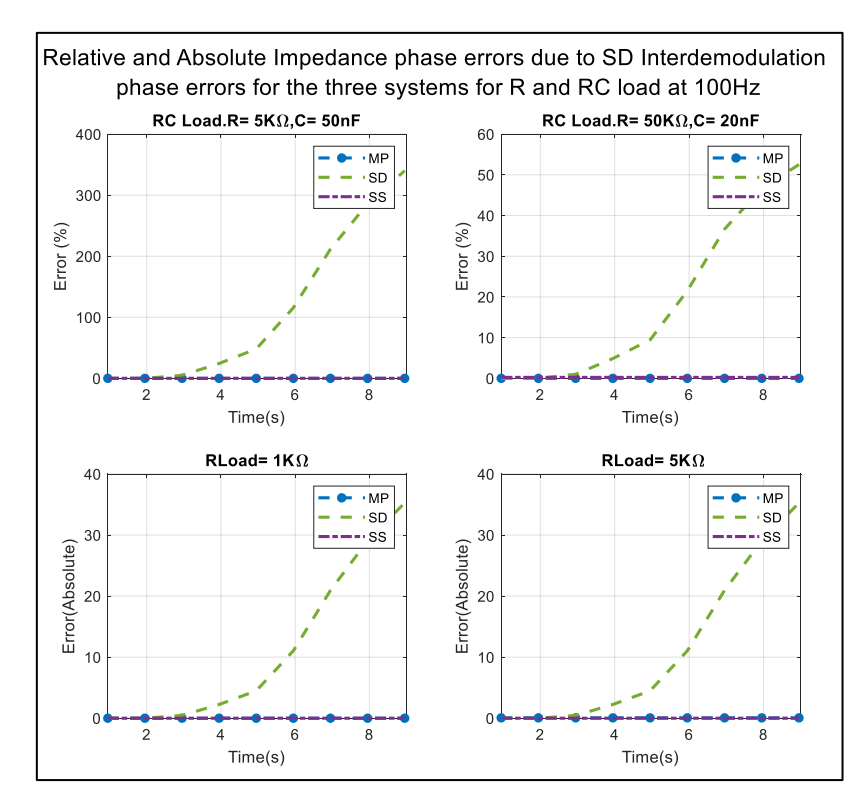


Figure 5. 28 Relative and absolute impedance phase errors of R and RC loads due to added SD inter-demodulation phase errors.

Figures 5.25 to Figures 5.28 illustrate the effects of intermodulation phase errors on the resultant magnitude and phase measurements using the SD system. While the other systems

show no impact from these errors, as they are topology-specific to the SD system, the SD system exhibits a relative error exceeding 100%, particularly in the phase measurements, significantly affecting the accuracy of the results.

5.7.4. Effects of Aperture delay error of the S/H circuit of SS system.

Timing inaccuracies in the sampling process of an analogue-to-digital converter (ADC) in the S/H could cause errors in the measurements. This error is most critical at high frequencies because where a sampling pulse width may not significantly affect the accuracy of a sampled signal at lower frequencies, at higher frequencies, the pulse width will play a significant role as the period of the sampled signal will be relatively small compared to the period of the signal at lower frequencies, making the contribution of this error significant. To simulate the effects of this error on the magnitude and phase of the measured data using SS system, the zero crossing and peak detect sample and hold pules where delayed in time for a maximum delay of up (.01* pulse period) where the period 10ms. The injected pulse delays which simulate the apertures delays is shown in the Figure 5. 29.

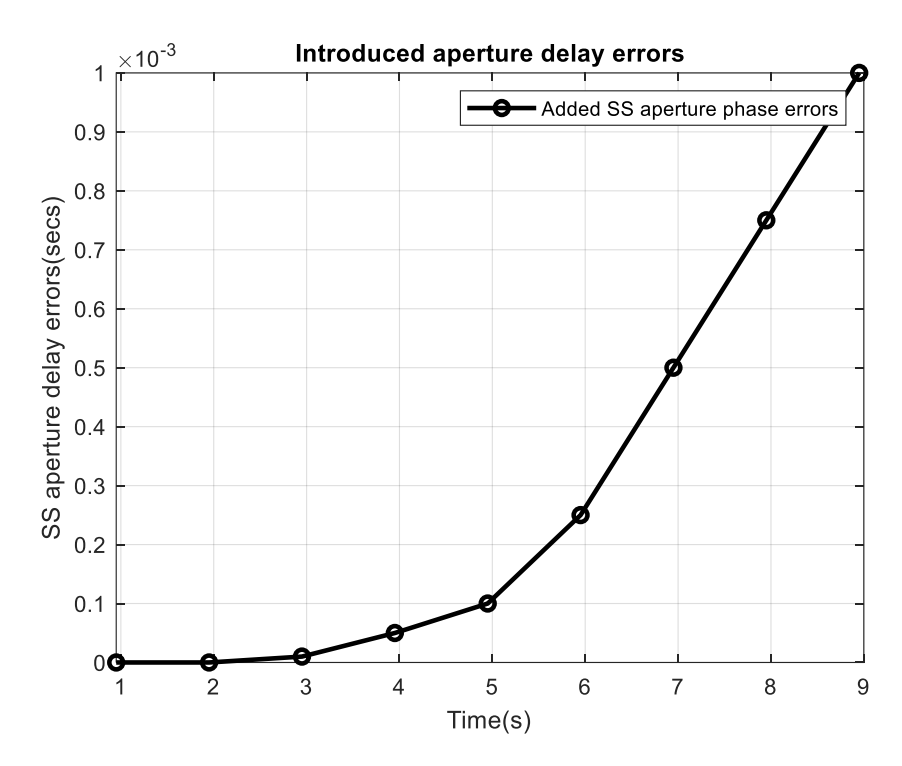


Figure 5. 29 Introduced Aperture delays errors.

The aperture phase delay errors illustrated in Figure 5.29 were gradually introduced by adding a specific time delay to both the zero-crossing and peak detection pulses at intervals of 1 second. These errors were applied simultaneously to both types of pulses with the effects shown in Figures 5.30 to 5.33.

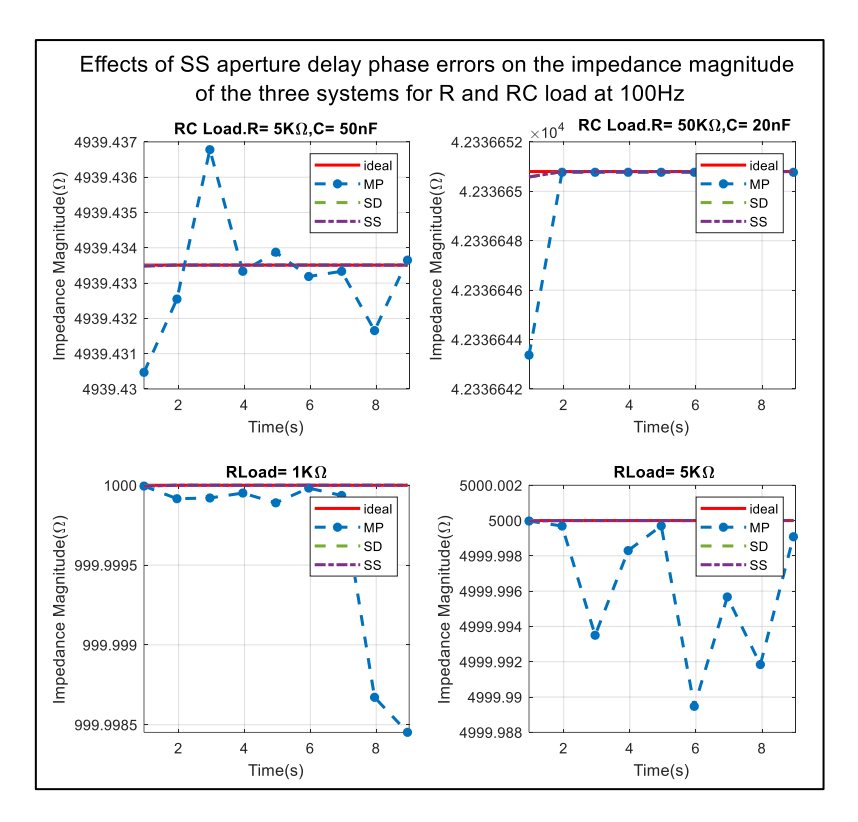


Figure 5. 30 Effects of SS aperture errors on the Impedance magnitude results of the all the system

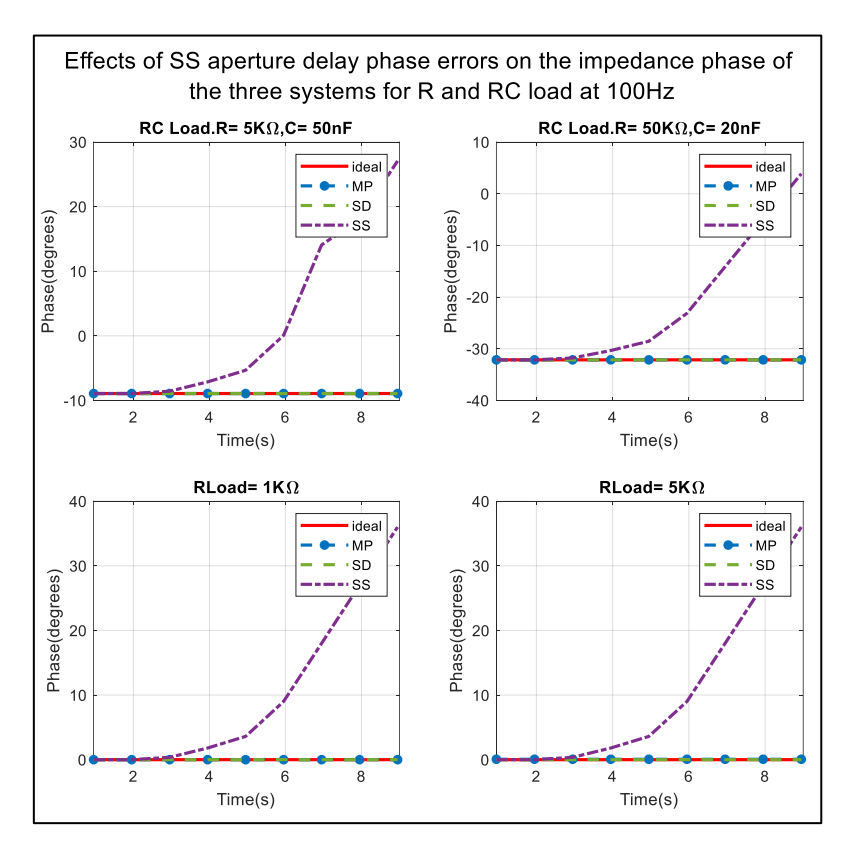


Figure 5. 31 Effects of SS aperture errors on the Impedance phase results of the all the system

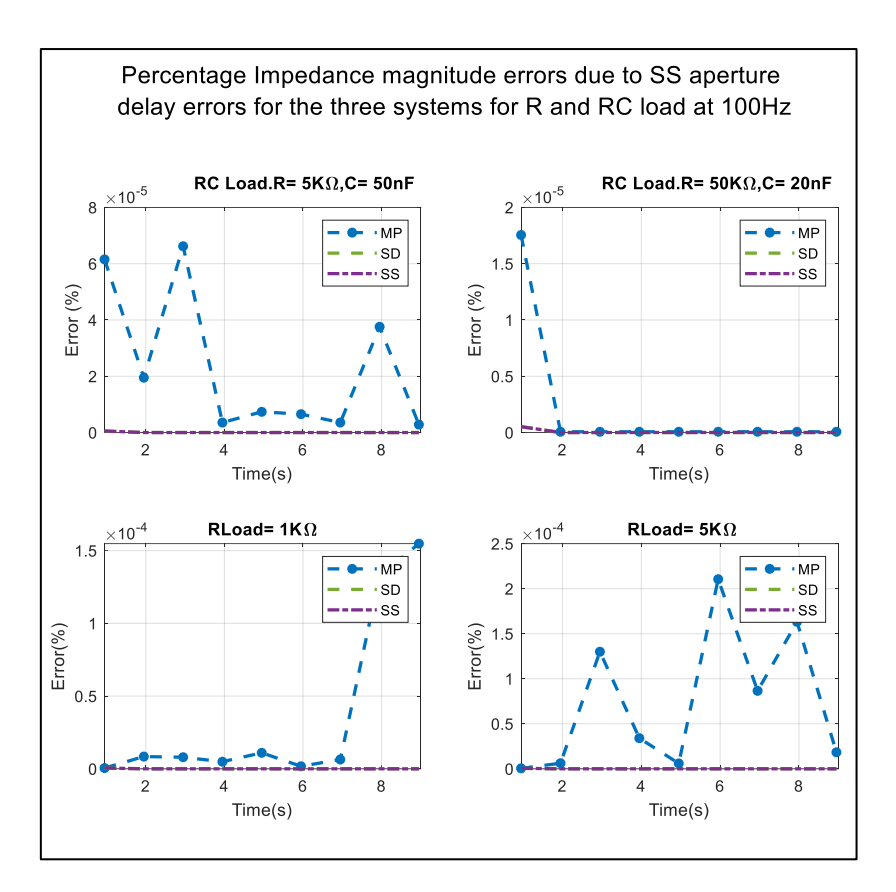


Figure 5. 32 Relative percentage impedance magnitude errors of R and RC loads due to added SS aperture errors

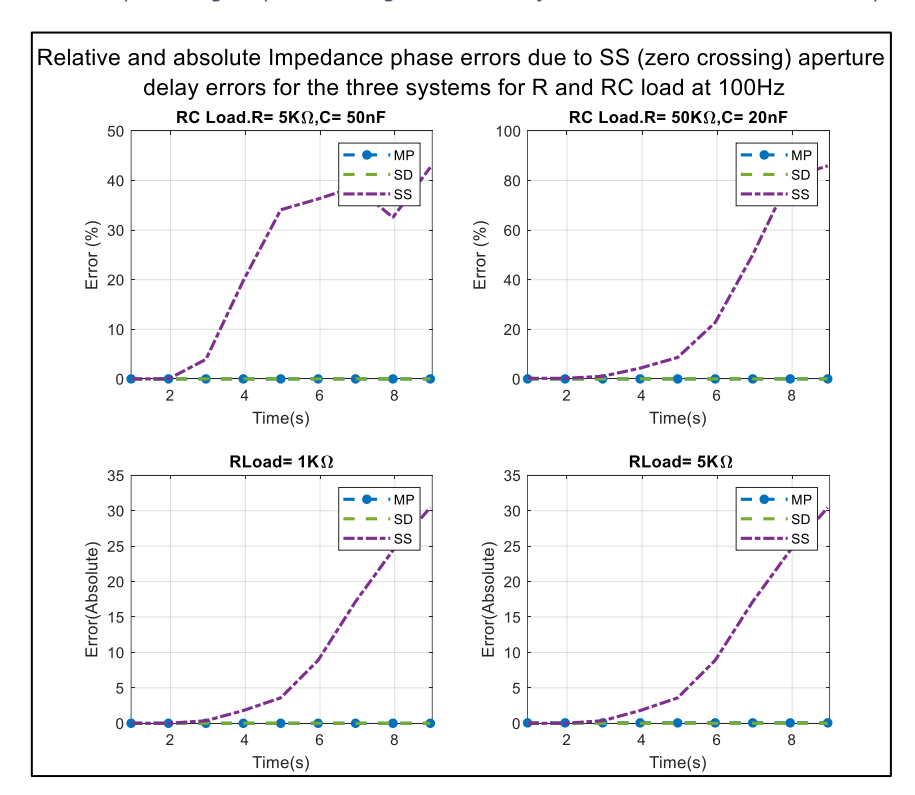


Figure 5. 33 Relative and absolute impedance phase errors of R and RC loads due to added SS aperture errors.

As shown in Figures 5.30 and Figures 5.31, when the aperture errors of the SS systems are simultaneously added to both the zero-crossing and peak detection pulses, the impedance magnitude derived from their respective real and imaginary measured results remains

unaffected. This behaviour is consistent with other topologies without this error and aligns with the mathematical derivations presented in equations 5.3 to 5.14. However, the phase results for SS systems exhibited a relative percentage error of up to 90%.

In contrast, when the aperture delay errors are not simultaneous or not identical such as when the zero-crossing pulse and peak detection pulse circuits are not ideally matched the impedance magnitude and phase are affected, unlike when the delays are matched and introduced simultaneously. To further illustrate this, the aperture delay error was introduced only to the zero-crossing delay pulse, and the relative percentage error and absolute error were calculated for both the impedance magnitude and phase for the R and RC loads used in the simulations. These results are displayed in Figures 5.34 and Figures 5.35

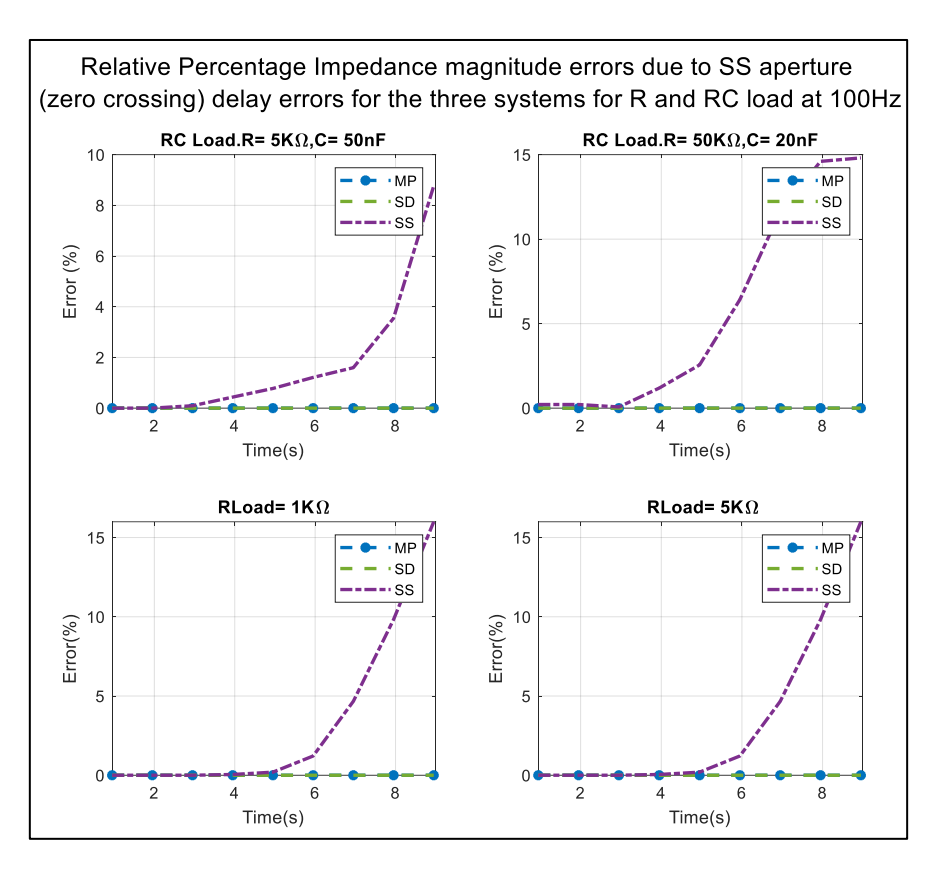


Figure 5. 34 Relative percentage impedance magnitude errors for R and RC loads due to added SS aperture (zero crossing) errors.

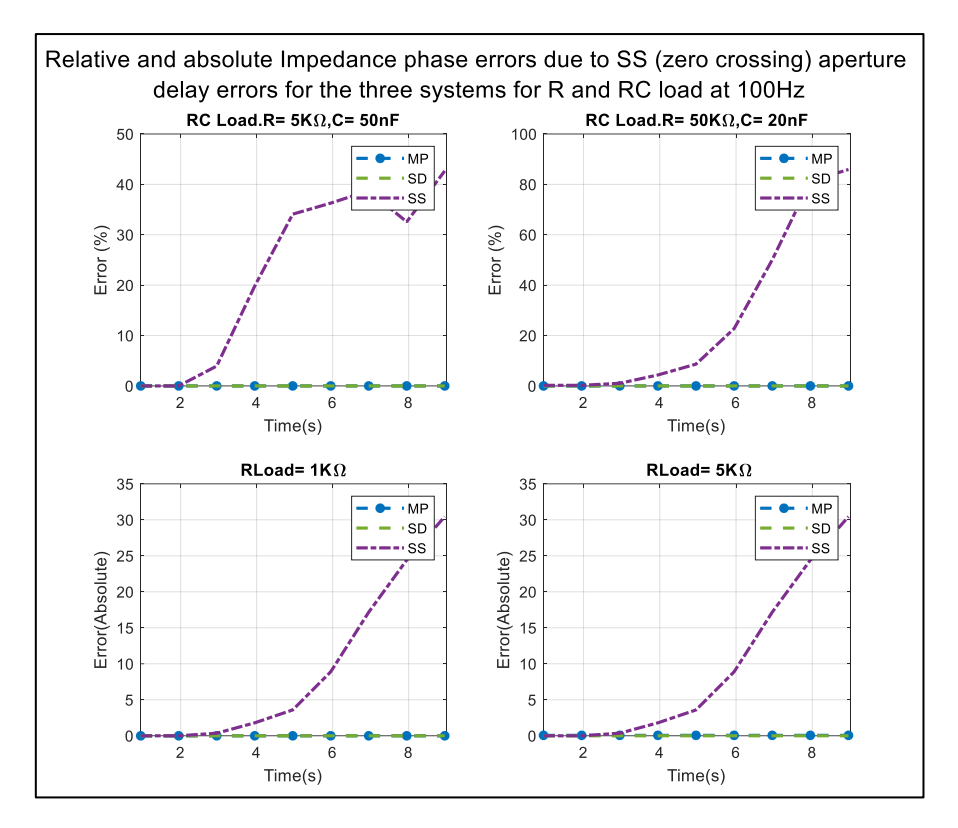


Figure 5. 35 Relative and absolute impedance phase errors for R and RC loads due to added SS aperture (zero crossing) errors.

5.8 Multifrequency Measurements with the three (SD, MP, SS) bioimpedance systems.

Figure 5.36 illustrates the injection circuit used for the multifrequency experiment. This involved the front-end injection and measurement side circuit arrangement.

These systems were tested for their ability to maintain accuracy during applications that require multifrequency signal injections, such as neuromuscular disease assessment as in the case of bioimpedance myography and impedance for cancer [23], [73], [112]. To achieve this, a summation of voltage signals of different amplitudes and frequencies were fed into the instrumentation amplifier of via a summing amplifier stage as $V_{\textit{meas}}$.

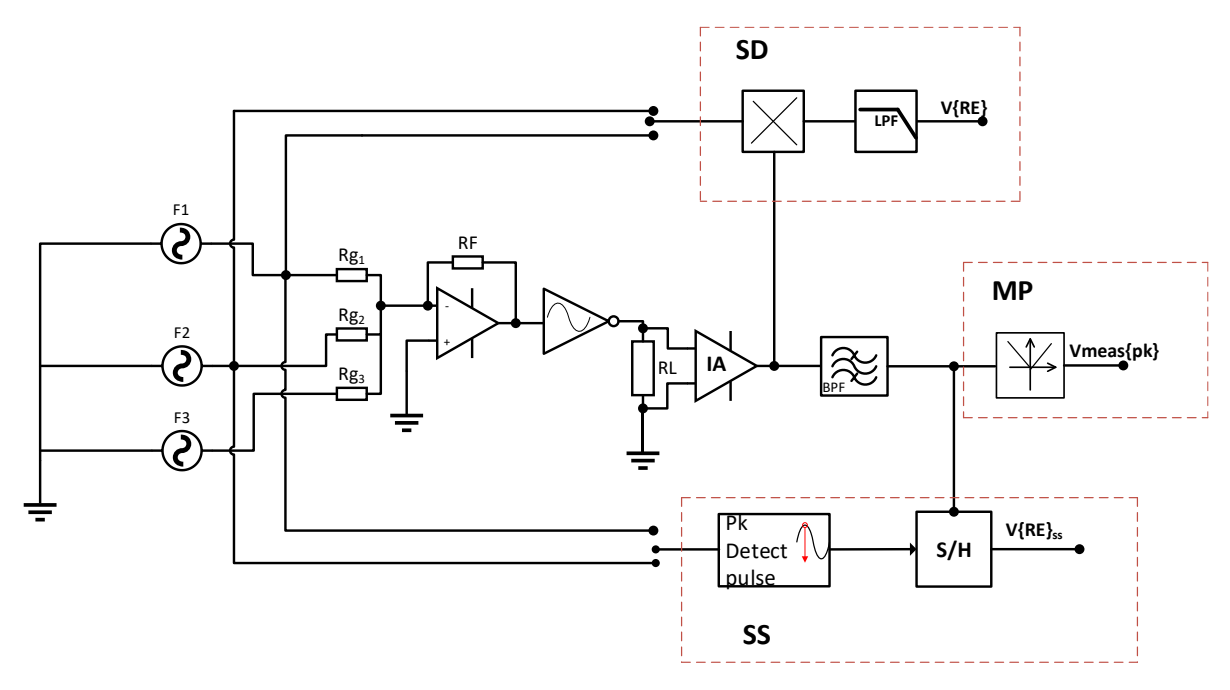


Figure 5. 36 Diagram of circuit used for multifrequency experiment.

In this summation, signals at frequencies of 100 Hz and 53 kHz were of primary interest, while the 100 kHz signal was introduced as noise. The respective peak amplitudes of the individual signals 1 Vpk, 5Vpk, and 4Vpk were fed into the summing amplifier. These amplitudes ideally represent the product of the injection current (1 mA) and load magnitudes of resistive loads (1 k Ω , 5 k Ω , and 4 k Ω). The test loads were assumed to be purely resistive, eliminating any need for phase shifting the signals.

In the SD system, the summed output from the summing amplifier is multiplied by modulation signals whose frequencies is the same as that of the signals of interest (100 Hz and 53 kHz). The band-pass filter's cut-off frequencies were tuned accordingly, as shown in Table 5.2, to isolate the desired signals.

Amplitudes(V)	Frequencies (Hz)	Band pass filter	Band pass filter	Centre	
		lower cut off	Higher cut off	Frequency	
		frequency (Hz)	frequency (Hz)	f _c (Hz)	
1	100	10	1K	100	
5	53k	10K	282K	53K	
4	100k	Introduced in the sum as signal interference			
Table 5.2. Amplitudes and frequencies of summed signals for multifrequency experiment					

Table 5. 2 Amplitudes and frequencies of summed signals for multifrequency experiment

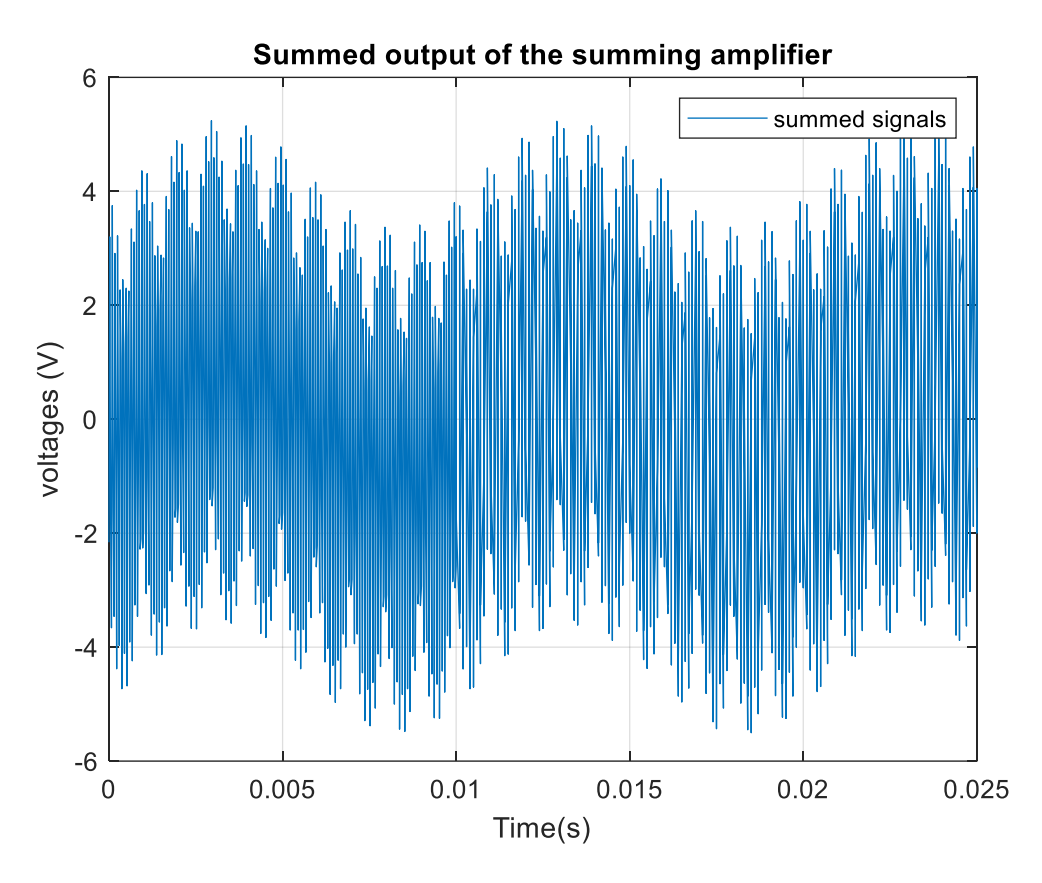


Figure 5. 37 Summed signals at the output of the instrumentation amplifier.

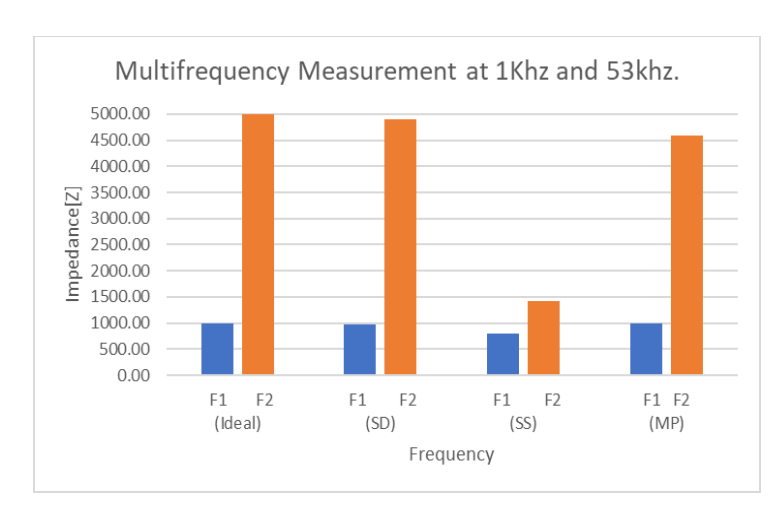


Figure 5. 38 Impedance magnitude of the three bioimpedance systems with a summed input.

Figure 5.38 shows that with summed input, SD remained the most accurate of all the systems. This system uses locking effect of the multiplier to lock to the measured signal of interest and ignoring the interferences of different frequencies that are contained in the sum. MP and SS systems relies entirely on the filtering ability of the band pass filters tuned individually for centre frequencies corresponding to the frequency of the signals of interests i.e. at 100hz and 53KHz.

Results shows that SD retained a better accuracy than MP and SS systems, with SS suffering the worst performance and most particularly when the difference between stop band frequencies and the signal interferences/noise are less than a decade apart. This is because of the phase locking advantage of SD system against MP and SS systems that employs filters to segregate frequencies. The locking mechanism of the SD can further be mathematically be proven below

Recall

$$v_{meas} = A_v i_0 z_x sin(\omega t - \varphi)$$

Assuming $A_v i_0 z_x$ for two different summing Amplifier gains $(A_v) = V_{m2} V_{m3}$.

Assuming there are two frequencies of interest namely ω_1, ω_2

The output of the multiplier ($v_{mult0deg}$), multiplying the signal at the summed frequencies with a signal at a reference frequency

$$v_{mult0deg} = [V_{m2}\sin(\omega_1 t - \varphi) + V_{m3}\sin(\omega_2 t - \varphi)] * v_0\sin(\omega_1 t)$$
(5.29)

Where $v_0 \sin(\omega_1 t)$ is the reference signal oscillating at the reference frequency ω_1

$$v_0 \sin(\omega_1 t) * V_{m2} \sin(\omega_1 t - \varphi) + v_0 \sin(\omega_1 t) * V_{m3} \sin(\omega_2 t - \varphi)$$
 (5.30)

Applying product to sum identity

$$v_0 V_{m2} \sin(\omega_1 t) \sin(\omega_1 t - \varphi) = \frac{v_0 V_{m2}}{2} [\cos(\varphi) - \cos(2\omega_1 t - \varphi)]$$
 (5.31)

This generates:

Frequency term at
$$2\omega_1 = \frac{v_0 V_{m2}}{2} [\cos(2\omega_1 t - \varphi)]$$
 (5.33)

$$v_0 \sin(\omega_1 t) * V_{m3} \sin(\omega_2 t - \varphi) \tag{5.34}$$

$$v_0 V_{m3} \sin(\omega_1 t) \sin(\omega_2 t - \varphi) = \frac{v_0 V_{m3}}{2} \left[\cos((\omega_1 - \omega_2)t + \varphi) - \cos((\omega_1 + \omega_2)t - \varphi) \right]$$
(5.35)

This generates:

$$ightharpoonup$$
 Difference frequency term: $\cos((\omega_1 - \omega_2)t + \varphi)$ (5.36)

$$\triangleright$$
 Difference frequency term: $\cos((\omega_1 + \omega_2)t - \varphi)$ (5.37)

Hence

$$v_0 \sin(\omega_1 t) * V_{m2} \sin(\omega_1 t - \varphi) + v_0 \sin(\omega_1 t) * V_{m3} \sin(\omega_2 t - \varphi) =$$

$$v_{multodeg} = \frac{v_0 V_{m2}}{2} \left[\cos(\varphi) - \cos(2\omega_1 t - \varphi) \right] + \frac{v_0 V_{m3}}{2} \left[\cos((\omega_2 - \omega_1)t - \varphi) - \cos((\omega_2 + \omega_1)t - \varphi) \right]$$

$$(5.38)$$

Further analyzing

 $\begin{array}{l} \Rightarrow \ \, \frac{v_0 V_{m2}}{2} \cos(\varphi) : \text{DC constant term} \\ \Rightarrow \ \, \frac{v_0 V_{m2}}{2} \cos(2\omega_1 t - \varphi) : \text{High frequency term at } 2\omega_1 \\ \Rightarrow \ \, \frac{v_0 V_{m3}}{2} \cos((\omega_1 - \omega_2)t + \, \varphi) : \text{Difference frequency term oscillate at } \omega_2 - \omega_1 \\ \Rightarrow \ \, \frac{v_0 V_{m3}}{2} \cos((\omega_1 + \omega_2)t - \varphi) : \text{Sum frequency term oscillate at } \omega_2 + \omega_1 \end{array}$

This same procedure applies with 90 degrees out of phase modulation. Therefore, passing the output of the multiplier through a low pass filter would remove the frequency components, leaving out only the DC terms which corresponds to the frequency components of the reference signal $v_0 \sin(\omega_1 t)$.

While multifrequency experiments offer various advantages, environmental factors such as mains noise and motion artifacts [39] can negatively impact the accuracy of the measurements. This necessitates continuous filtering of the signals. Since noise frequencies can fluctuate, systems like MP and SS require continuous tuning of the filter cut-off frequency. In contrast, SD systems lock onto the frequency of the reference signal, maintaining measurement accuracy and preserving signal integrity.

5.9 Comparing the Systems response to input step change

Some bioimpedance applications requires faster response than others. For example, electrical impedance tomography (EIT) measurements are performed at relatively high frame rates to allow multiple acquisitions per second[113], [114]. To assess the speed of these systems, their settling times were compared by applying a step input. A time-varying signal with a sudden amplitude change was introduced to the input of all systems via the instrumentation amplifier (IA), and their responses to this change were analysed. Figure 5.39 presents the graph of their respective responses.

While MP and SS exhibit similar performance in terms of speed, SD appears to respond more slowly to changes in the input signal. The SD system incorporates a low pass filter at its output, with a cut-off frequency of less than 1 Hz, a feature not present in the other systems.

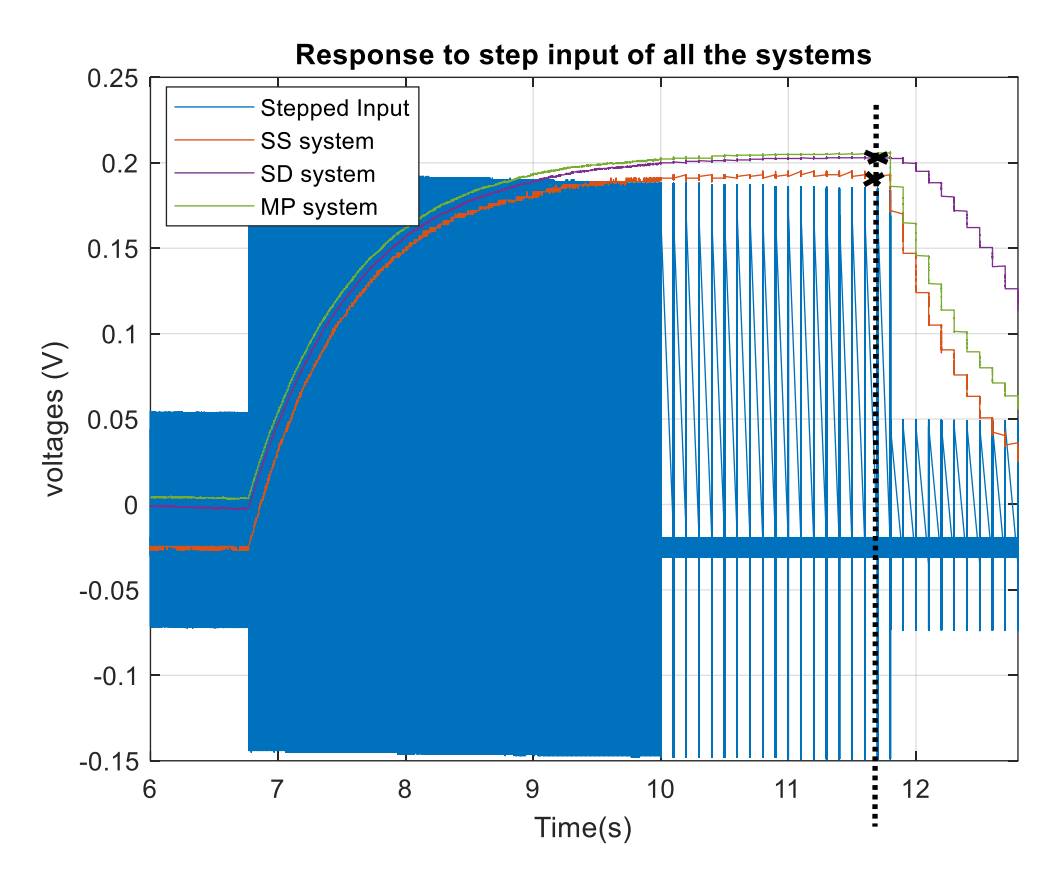


Figure 5. 39 Comparing the response of the systems in response to step change.

5.10 Discussion on the System Comparison

Having analyzed the systems both mathematically and in simulations, they will now be categorized according to specifications as below

- ➤ **Speed**: Dynamic bioimpedance applications such Impedance plethysmography which are measurements through the skin relating to venous or arterial blood volumetric variations, synchronized to the heart rate. Impedance for Tomography requires high frame for mapping out the conductivity boundary voltages as a result of injected currents would require fast response time and, SP and MP system responded faster to the step change experiment as such can be adapted for any of these applications. This is mainly because SS and MP does not have the delays introduced by low pass filter of the SD system which tuned at a low cut off frequency, further delays the response of the signal and hence measurements.
- Multifrequency measurements: In static body measurements such as impedance for body composition, multifrequency measurement provides a more precise estimate of total body water (TBW) and extra cellular water (ECW). This could be limited to single frequency measurements. The ability to differentiate Intracellular water, extracellular water and the total body water using multifrequency measurements is particularly important in assessing clinical situations such as renal diseases[115]. Multifrequency measurements in impedance for

compositions proves more powerful and more sensitive in detecting the variations in the ratio of ECW:TBW. An increase in the ECW/TBW could be indictive of diseases such as edema which multifrequency measurements would be more sensitive to even when they are no visible changes to body weight. This is will not be possible with single frequency measurements. Furthermore, in cell integrity measurements, Impedance of skin cancer and in neuromuscular application such Impedance myography where multifrequency injections has been known to provide richer assessment of disease status[73], SD system performs better. Though it can be argued that swept frequency applications may achieve similar result, however, in many bioimpedance systems, the sense circuit are normally designed with a filter at the output [58]to remove any unwanted signals in the measurements, as such in swept applications, it will need for the filter to be continually re-tuned for each frequency, where SD will automatically lock to the reference frequency providing a better accuracy.

- ➤ Complexity: Some bioimpedance applications such as impedance for skin hydration often times will have no requirements for speed and multifrequency injections, relatively needing a system that will determine the impedance magnitude of skin as a measure to monitor its hydration status[90]. MP system is relatively less complex for impedance magnitude only measurements. As such less complex system like MP would for such an application.
- ➤ Motion artefact Tolerance: Bioimpedance impedance technique has been adopted in water balance monitoring in preterm neonates because they show variable needs of fluid replacement [116]. A reduced fluid intake can cause dehydration, electrolyte imbalance, and arterial hypotension[116]. The studies that assessed TBW in neonates reported a good correlation with bioelectrical impedance analysis, however measurements in neonates can be challenging due to motion artefacts. This is because motion artifacts result from the movement or interaction between the electrode and the skin, they affect the electrodes unevenly and cause variations in the impedance signal, leading to baseline drift or DC offsets[117]. However it is proven, SD system is immuned to a Dc offsets errors of the sense circuits and hence suitable for neonatal measurements.
- Impedance Phase Diagnostic factors. Some Impedance applications like Impedance for cancer and Myorgraphy, albeit could benefit from the multifrequency assessment uses phase as diagnostic factors for disease such as skin cancer and neuromuscular diseases respectively[23], [73], [118]. However, all systems reviewed are affected by erroneous phase shifts in the sense circuits, particularly at high frequencies, which compromises phase measurement accuracy. Further optimization is required to mitigate these errors for applications where phase detection is critical.

5.10 Conclusion on chapter 5.

This chapter provided a detailed discussion and comparison of three major bioimpedance systems, using both Simulink models and mathematical analyses. The findings informed the selection of appropriate systems for specific applications. SD system has better wide range applicability and immunity to errors such as DC offsets. However, just like every other system, it suffers from phase errors which may however limit its applicability too. The next chapter will focus on optimizing the phase measurement performance of the SD system through experimental validation and simulations to improve its accuracy for phase-based diagnostic applications, such as bioimpedance in skin cancer diagnostics.

Chapter 6

Phase Optimisation for SD system.

Chapter 5 has compared various bioimpedance measurement systems through which it was highlighted that most of the systems are affected by the erroneous phase shift at the output of the sense circuit.

SD system has been identified as most suitable for measurements on the skin due to its lock in amplifier mechanism. Research in improving SD based systems is predominantly focused on minimising systematic errors that affect the measured impedance magnitude, including bandwidth limitations and issues related to output current amplitude degradation at frequencies higher than 100kHz[58][119]. Minimal research and attention have been devoted to rectifying inaccuracies in SD phase detection system and most notably the erroneous phase shift between the demodulation signals and the measurements. In this Chapter, the phase errors could further be analysed and optimisation method discussed and designed.

6.1 SD Phase error analysis.

As earlier stated, the injected current into the biological tissue $i_{out}=i_o\sin(\omega t)$, where i_o = the amplitude of the injected constant current of the current source. The measured voltage v_{meas} relative to the reference voltage V_{in} and affected by the erroneous phase shifts of the VCCS can be expressed as

$$v_{meas} = A_v i_0 z_x \sin(\omega t - \varphi - \Delta \theta)$$
 (6.1)

where A_v is the gain of the measuring instrumentation amplifier, $|Z_x|$ is the measured impedance magnitude, $\angle Z_x$ is the measured impedance phase, φ = tissue impedance phase (ideally equal to $\angle Z_x$), $\Delta\theta$ = erroneous phase to due the frequency dependent delay by VCCS.

Recall from chapter 5 that real and Imaginary Impedance measurements using SD system are respectively

$$Re = z_{\chi}(cos(\varphi + \Delta\theta)) = \frac{2*v_{LPFodeg}}{A_{\nu}i_{0}v_{0}}$$
(6.2)

$$Im = -z_{\chi}(sin(\varphi + \Delta\theta)) = \frac{2*v_{LPF90^{\circ}}}{A_{\nu}i_{0}\nu_{0}}$$

$$\tag{6.3}$$

$$\angle Z_x = tan^{-1} \left(\frac{\sin^2(\varphi + \Delta\theta)}{\cos^2(\varphi + \Delta\theta)} \right) :: \underline{phase\ measured\ is\ affected\ by\ \Delta}\ \theta \tag{6.4}$$

The work presented here introduces a Phase Error Compensated Synchronous Demodulation system (PECSD): an SD based bioimpedance measurement system with automatic phase error correction achieved by introducing a delay block, injecting a delay to the I and Q demodulation signals equal in phase to the erroneous phase shift at sense circuit output. The block diagram of Figure.6.1 illustrates the phase correction circuitry adopted in this project.

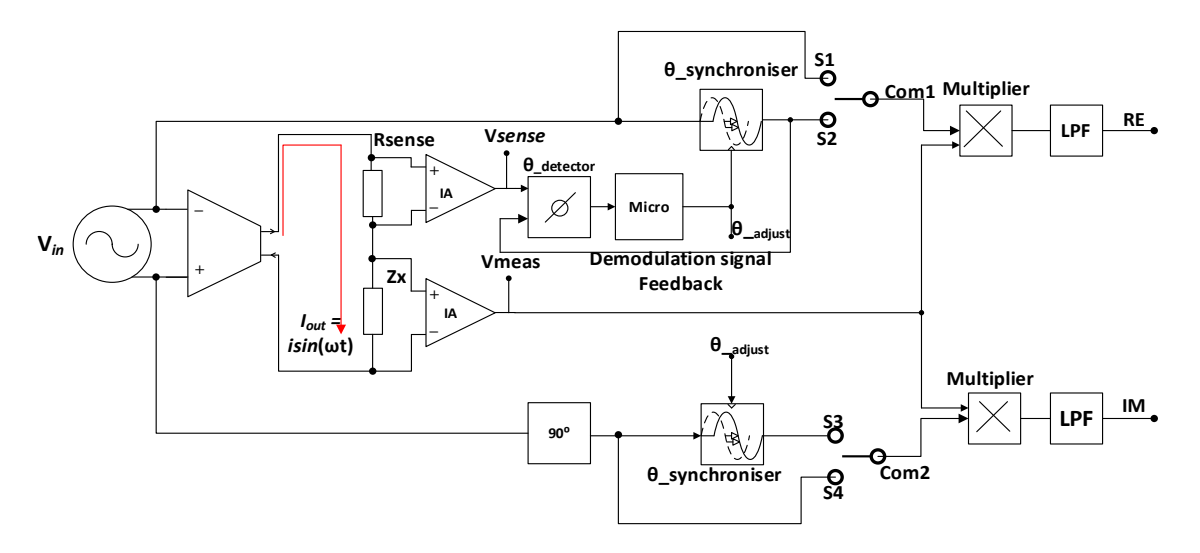


Figure 6. 1 Block diagram of the automatic Phase Error Compensated Synchronous Demodulation system (PECSD).

The block diagram shown in Figure 6.1 illustrates the SD system block incorporating phase correction methodology proposed in this project. With switches S2 and S3 closed to com 1 and com 2, respectively, the system functions in a closed-loop system, activating the phase compensation mechanism. The output current (Iout) from the current source undergoes constant phase monitoring facilitated by a very low tolerance (Rsense) carbon film resistor in series with load impedance. The voltage output (Vsense) of Rsense is precisely measured via an Instrumentation Amplifier (IA) placed very close to Rsense, mitigating parasitic capacitance induced by long signal tracks. Subsequently, phase differences between Vsense and the reference sinusoidal voltage (Vin) are compared using a Type II phase detector. Phase differences provide a pulse that tunes the phase synchroniser delay block via a microcontroller until an equivalent phase delay is added to the I and Q demodulation signals. This step causes the phase detector pulse to become low and remain low until another phase difference occurs. Vmeas is now multiplied with demodulation signals after phase correction, and low-pass filtered to eliminate AC components. The resultant DC voltages are further analysed after the low-pass filter to obtain real and imaginary components of the impedance and further expressed them in polar form.

To achieve the block diagram as shown in Figure.6.1, Vin was initially designed using a synthesiser circuit shown in Figure. 6.2

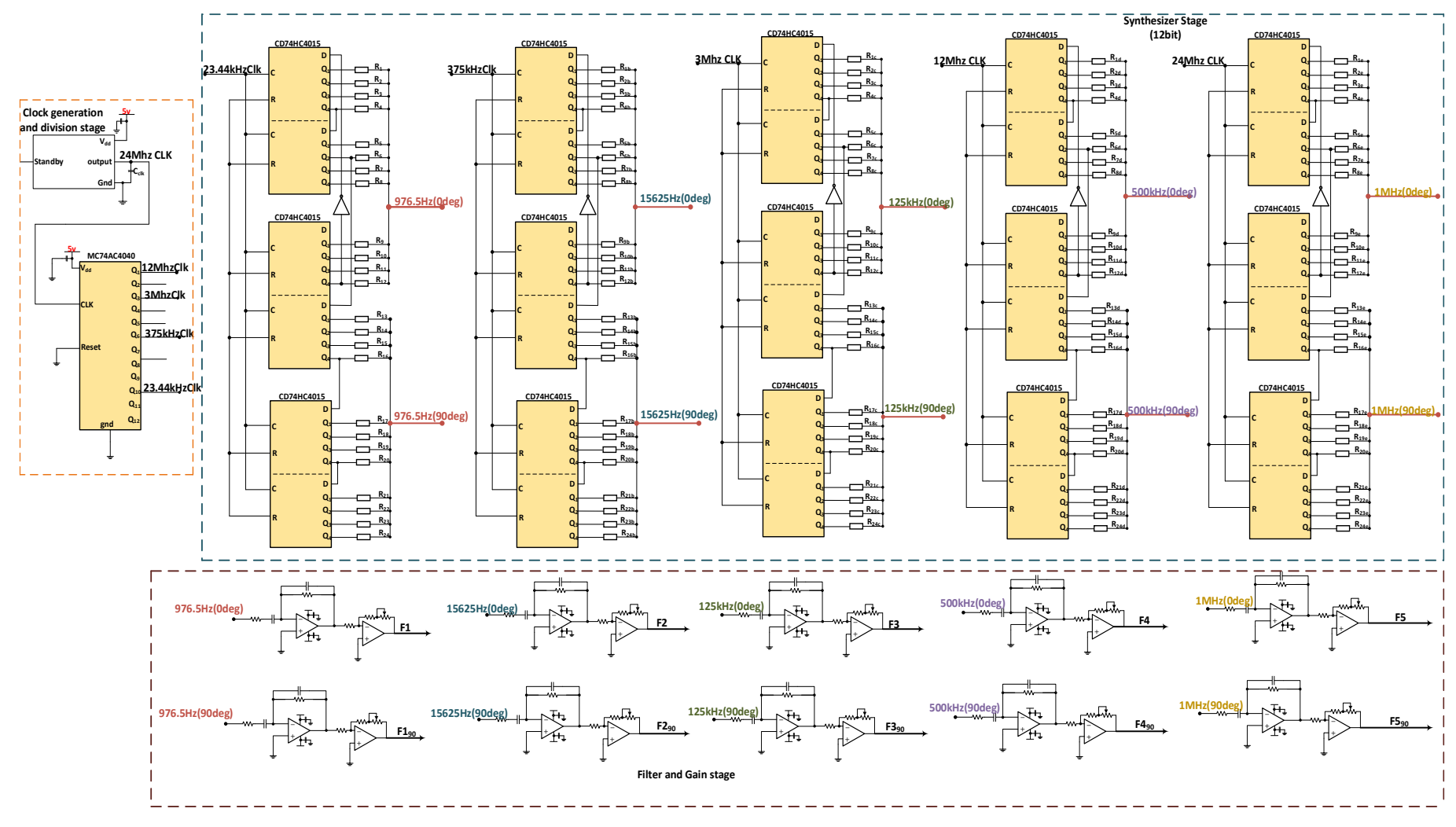


Figure 6. 2 Frequency Synthesizer Circuit designed for this project

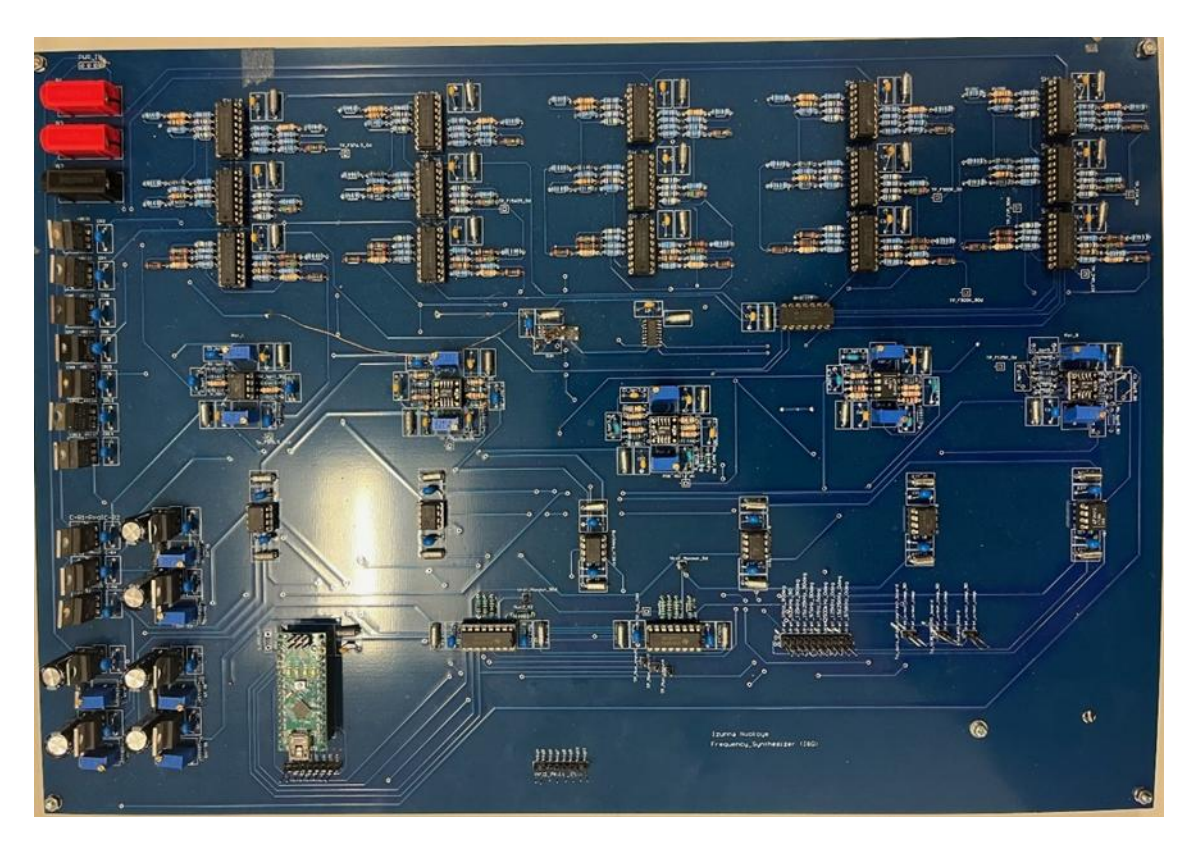


Figure 6. 3 PCB photo of Frequency synthesizer

6.2 The reference sinusoidal signal (V_{in}) Generation.

V_{in} was initially generated using the synthesizer circuit shown in Figure 6.3. A common clock pulse drives the CD4015 4-bit shift registers, cascaded to form a 12-bit configuration, which recirculates a pattern of 12 zeros and 12 ones with the aid of an inverter.

The design of resistor networks R_1 through R_{12} using trigonometric functions (sine values) for calculating the resistances in a stepped or sequential manner for an "n-stage" counter could be derived from equation 6.1. [121]

1;
$$\frac{\sin\frac{k\pi}{n}}{\sin\frac{\pi}{n}}; \dots \dots \dots \dots \frac{\sin\frac{(k-1)\pi}{n}}{\sin\frac{\pi}{n}}$$
 (6.1)

Where n is the no of stages in the counter and k is the step number ranging from 2 to k-1

The stepped sinusoidal output waveform of the shift registers is further filtered to remove clock-pulse feedthrough and stepped-edge transients and a subsequent gain stage applied.

Since each of the step produces 15° phase shift from each other (360/24steps), to further achieve a 90 degrees phase shifted output (90°/15), Q2 which is the 6th stage of the first 12 stage counters is fed as the data input of the second 12 stage counters.

The I&Q signals development stages are shown in Figure 6.4 and Figure 6.5.

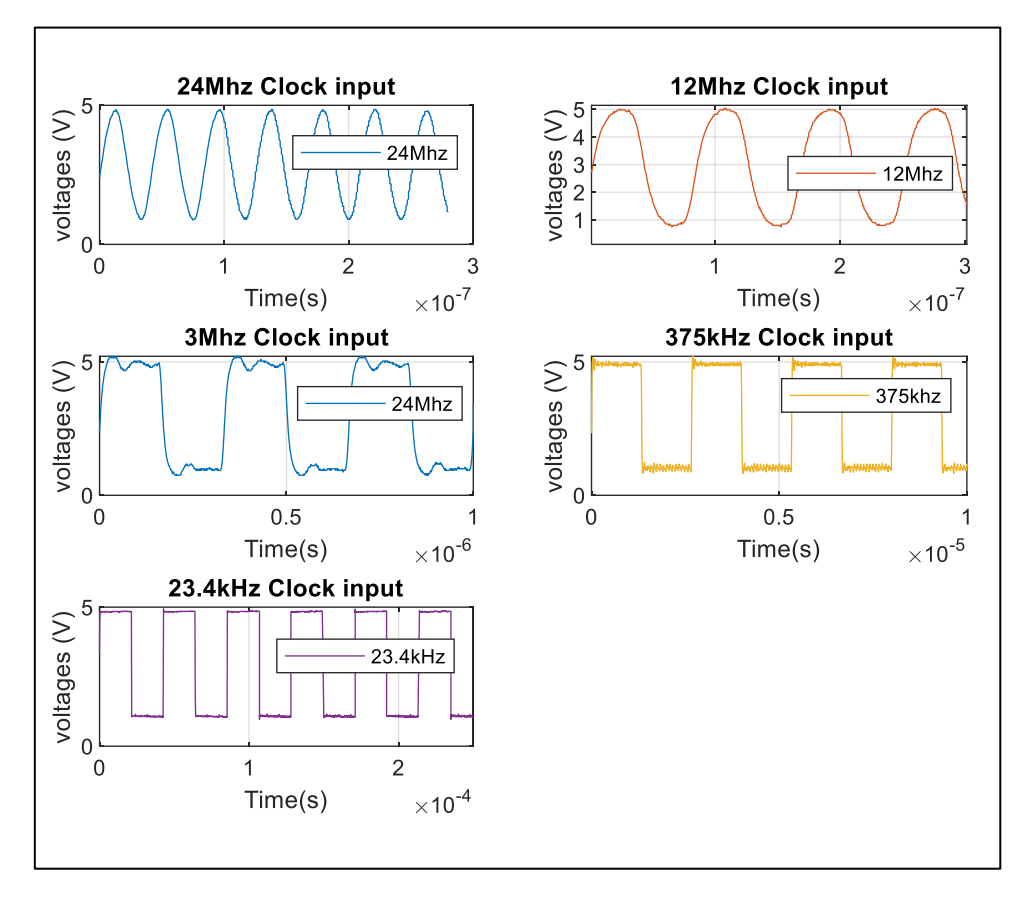


Figure 6. 4 I&Q generated signals from the digital synthesizer circuit

Ref Clock (MHz)	dividing counter state	Counter output	Signal Frequencies
	N/A	N/A	1MHz
	2 ¹	12MHz	500kHz
24	2 ³	3MHz	125kHz
	2 ⁶	375kHz	15.62kHz
	2 ¹⁶	23.44kHz	965Hz

Table 6. 1 Shift register clock signals and the subsequent output of the dividing counter

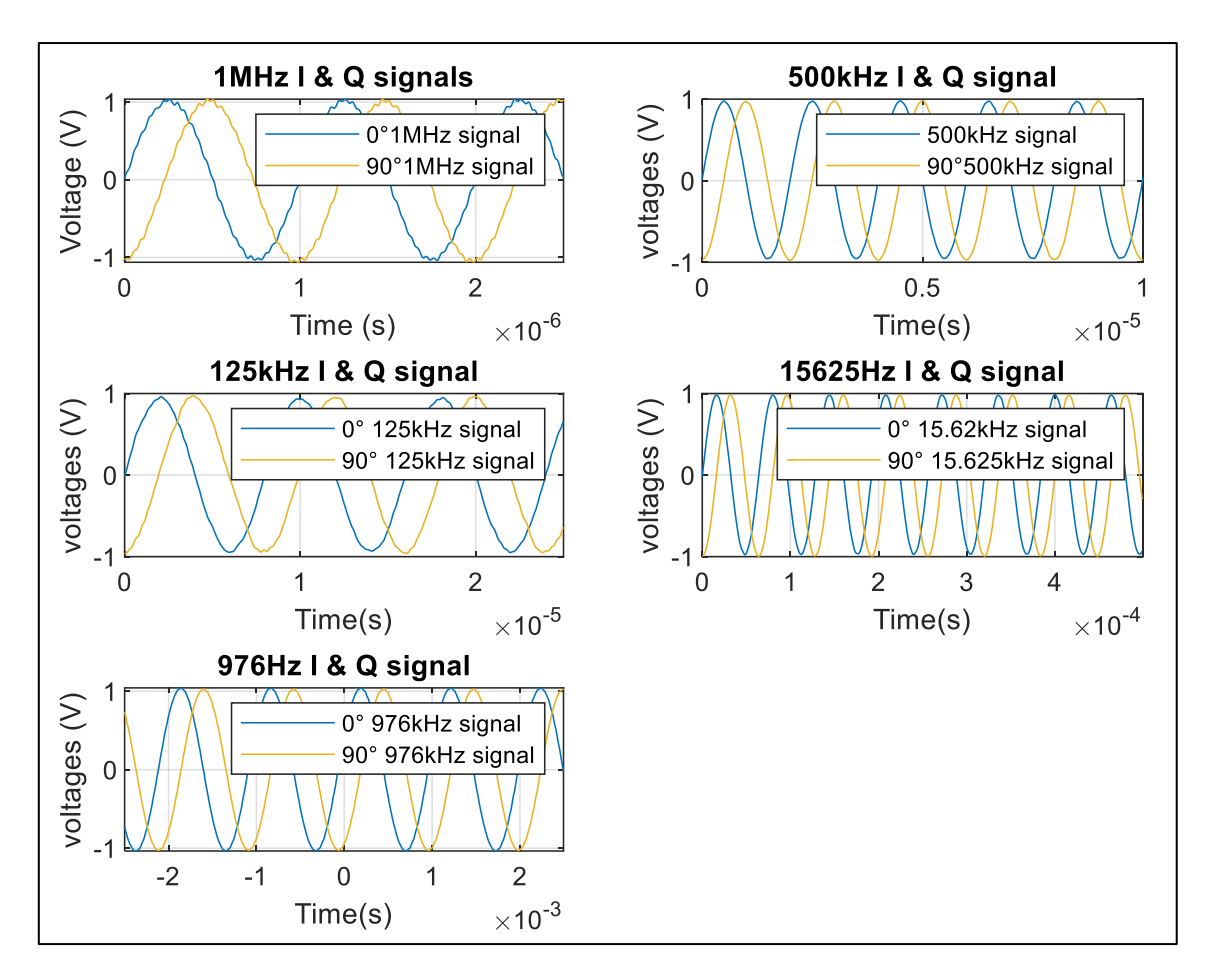


Figure 6. 5 I&Q generated signals from the digital synthesizer circuit

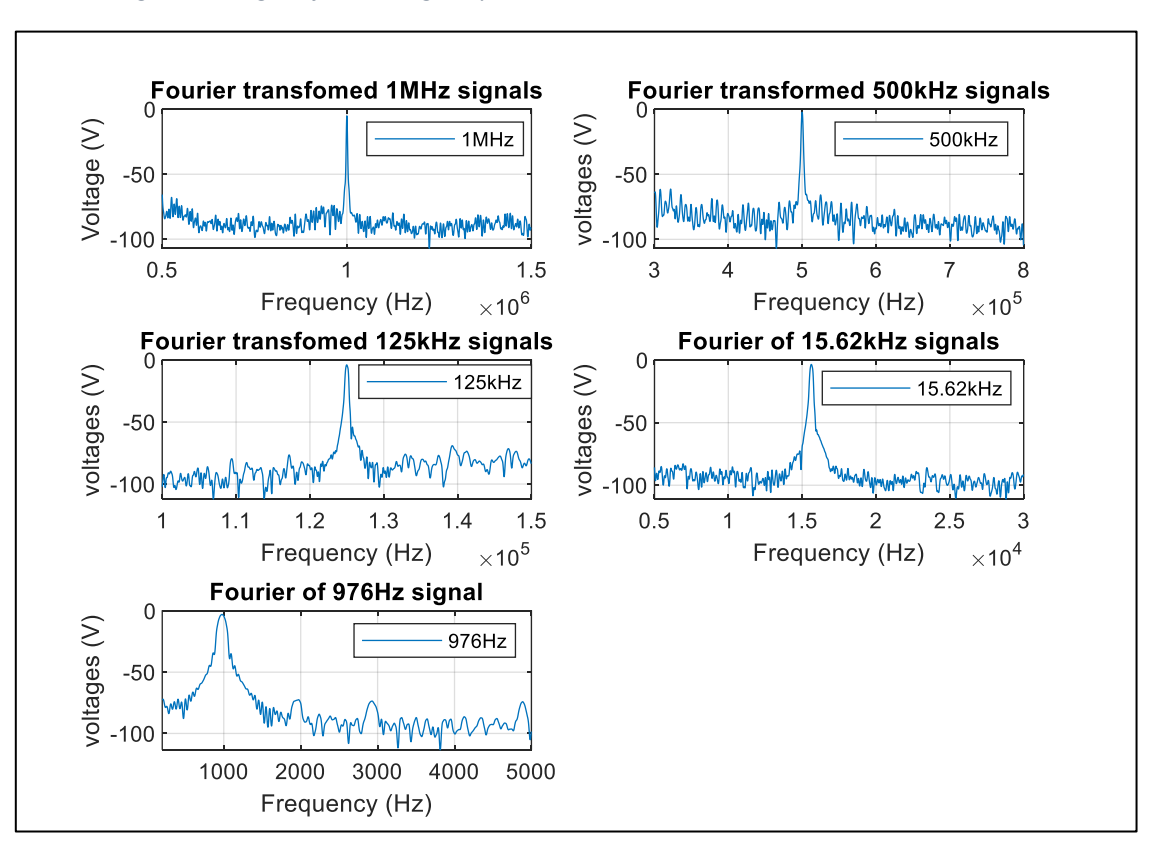


Figure 6. 6. Fourier analysis of I&Q generated signals from the digital synthesizer circuit

6.3 PECSD Circuit diagram and analysis.

In the implementation of the phase synchroniser in Figure 6.7, the current source is driven is by U1, unity gain single to differential op amp in a way to increase common mode rejection and also minimize dc offset[94]. The current source is made of U2 and U3 op amp arranged to give Mirrored enhanced Howland current source (MEHCS), ensuring true floating load, as such the output current flowing through the load impedance Z_L and sense resistor Rsense is

$$I_{out} = g_m V_{in} ag{6.1}$$

where g_m is the transconductance of the Howland current source given by [97].

$$g_m = \frac{R_4}{R_3 * R_5} \tag{6.2}$$

U4 and U5 are instrumentation amplifiers used to measure the resultant voltages across Rsense and the Load. These amplifiers are implemented in a three-op-amp configuration using the LT1364. In the closed-loop system, Vsense and Vin which should ideally be in phase are squared using comparators U11 and U12, respectively. The outputs of U11 and U12 are then compared in phase through a type II phase detector, which utilizes D type flip flops U13 and U14, along with P and N channel MOSFETs (U19 and U20).

The MOSFETs are driven by parallel AND and OR gates (U17 and U18) to enhance their drive strength and improve switching speed by discharging the gate capacitance more quickly. U16 simultaneously resets U13 and U14 when the phases of Vsense and Vin are synchronized.

When Vin leads, a positive charge pump is activated. Conversely, when Vin lags Vsense, the negative charge pump is activated. However, only one of these conditions occurs at a time, ensuring that either leading or lagging is compensated, but never both simultaneously.

The type II phase detector produces lead and lag pulse outputs, centred around 2.5V due to the potential divider formed by R8 and R9. These outputs are sent to comparators U21 and U22, which generate pulses with wider voltage levels (0-5V) to eliminate the possibility of false triggering by the microcontroller.

Upon detecting a phase shift between Vsense and Vin, the microcontroller (U6) initiates a corrective response to cancel the phase shift by delaying Vin by an equivalent phase interval. This adjustment is made by automatically changing the position of the wipers on the digital potentiometers R9a and R9b, which are part of the all-pass filter circuits (U7 and U8).

The all-pass filters phase adjustment follows the eq. 6.3-eq.6.8

$$V_{oa} = \frac{1 - j2\pi f(R_{9a} + R_{24})C_1}{1 + j2\pi f(R_{9a} + R_{24})C_1} *V_{ia}$$

$$6.3$$

Where V_{ia} and V_{oa} are respectively the input and output of the all-pass filter

Recall Impedance magnitude $|Z| = \sqrt{x^2 + y^2}$ where x and y are the real and imaginary impedance.

For numerator
$$1 - j2\pi f(R_{9a} + R_{24})C_1$$
, $x = 1$, $y = -j2\pi f(R_{9a} + R_{24})C_1$ 6.4

For Denominator,
$$1 + j2\pi f(R_{9a} + R_{24})C_1$$
, $x = 1$, $y = -j2\pi f(R_{9a} + R_{24})C_1$ 6.5

Representing eq.6.4 and eq.6.5 in their magnitudes, reduces eq.6.3 to 1 as in eq.6.6

$$\frac{v_{oa}}{v_{ia}} = 1 ag{6.6}$$

Phase
$$\theta = tan^{-1} = \left\{ \frac{-j2\pi f(R_{9a} + R_{24})C_1}{+j2\pi f(R_{9a} + R_{24})C_1} \right\}$$
 6.7

$$\theta = \left[-2tan^{-1} \left[2\pi f (R_{9a} + R_{24})C_1 \right] \right]$$
 6.8

As such, the signal passes through all pass filter at unity gain as can be seen in eq.6.6 but can be modified in phase by introducing delays by varying either R_{9a} , R_{24} or C_1

At the same time, the microcontroller switches the inputs to the lock-in amplifiers to the delayed signals from the all-pass filters using the double pole double throw relay contacts of U23 and U24.

Additionally, the input to the type II phase detectors is switched by another set of contacts on the U23 relay, allowing Vsense to be compared with the newly delayed Vin signal, instead of the reference one.

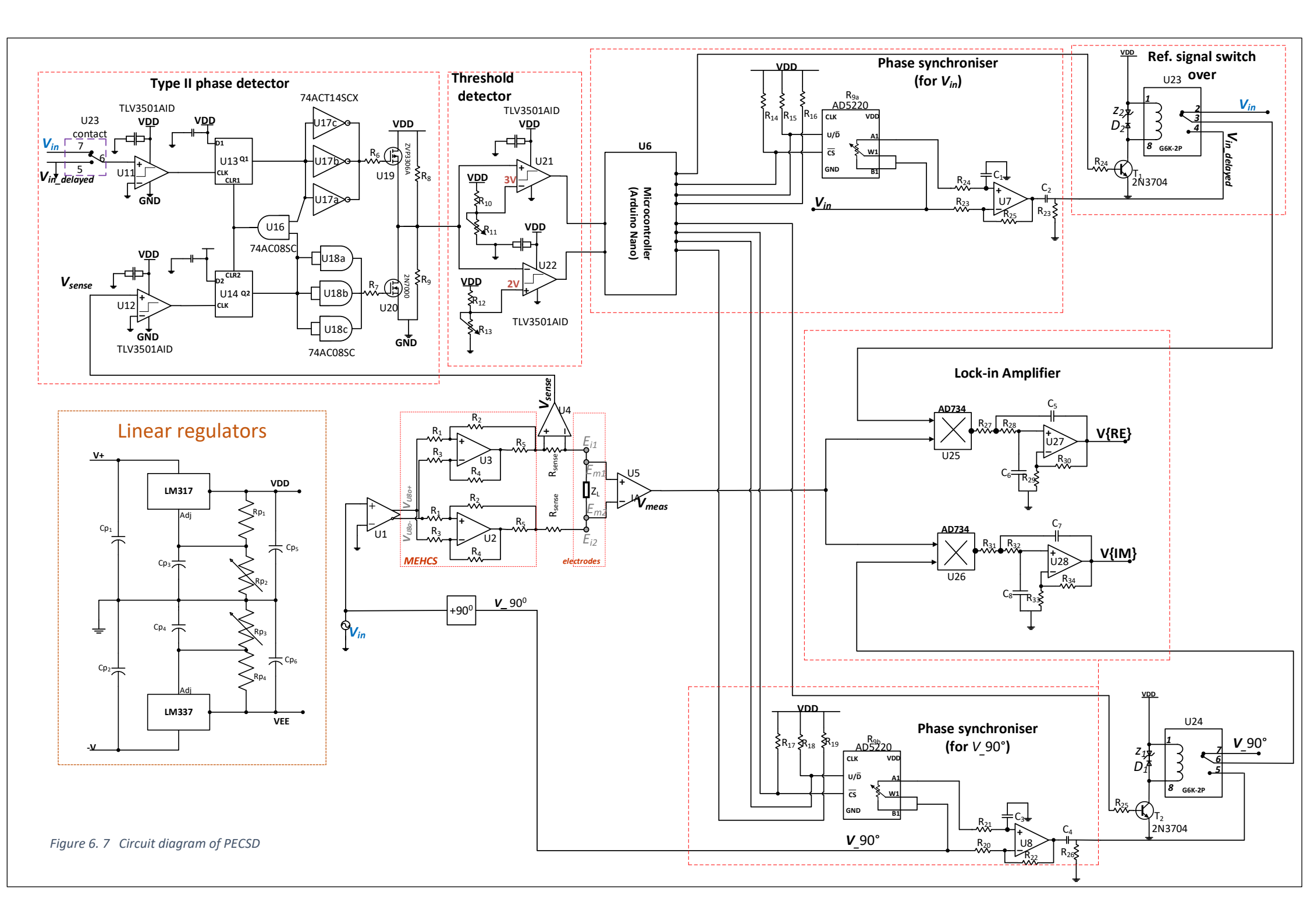




Figure 6. 8 PCB design of PECSD

Once the necessary phase compensation is achieved, the digital potentiometers store the wiper positions in memory. Multiplication is then performed via the lock-in amplifier mechanism comprising U25-U28. The same procedure is repeated during the quadrature demodulation cycle.

The performance of some key components needed optimum performance of PECSD were determined via LT spice simulations and pre-experimental test in order to determine their performance and possible effects on result accuracy.

6.4 Effects of sensing resistor (Rsense) on the accuracy of the signal.

The accuracy of the PECSD depends to a greater extent on the sense resistor, however eliminating the contribution of phase errors of the sense resistor knowing that it may not be purely resistive is important. Therefore, properties of the sense resistor used in these simulations were modelled and simulated.

The sense resistor used in this work is High Precision Foil Resistor with TCR of \pm 2.0 ppm/°C , Tolerance of \pm 0.005 % and Load Life Stability of \pm 0.005 %[122]. The resistor typical parasitic capacitance is 0.5pF and parasitic inductance of 0.08uH, while the maximum parasitic capacitance and inductance are respectively 1pF and 0.1uH. These were modelled in Figure 6.9.

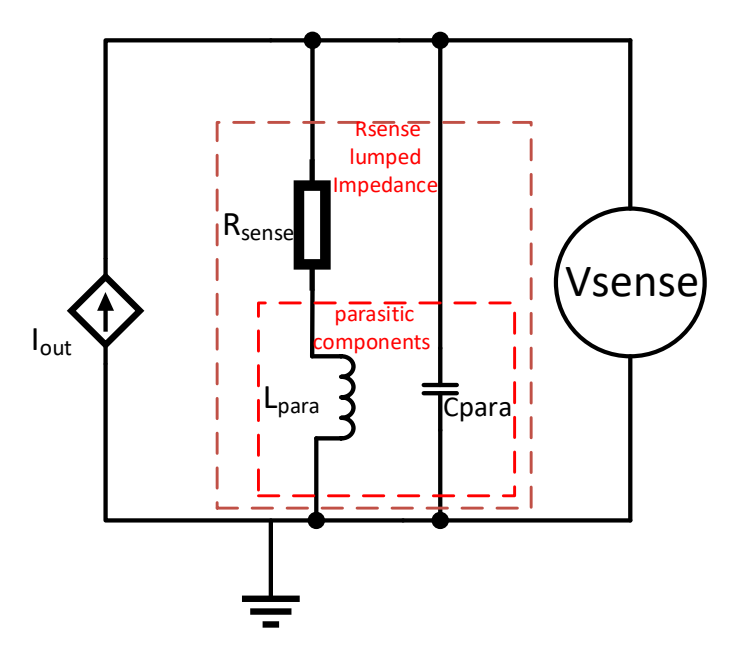


Figure 6. 9 Rsense Lumped Impedance model.

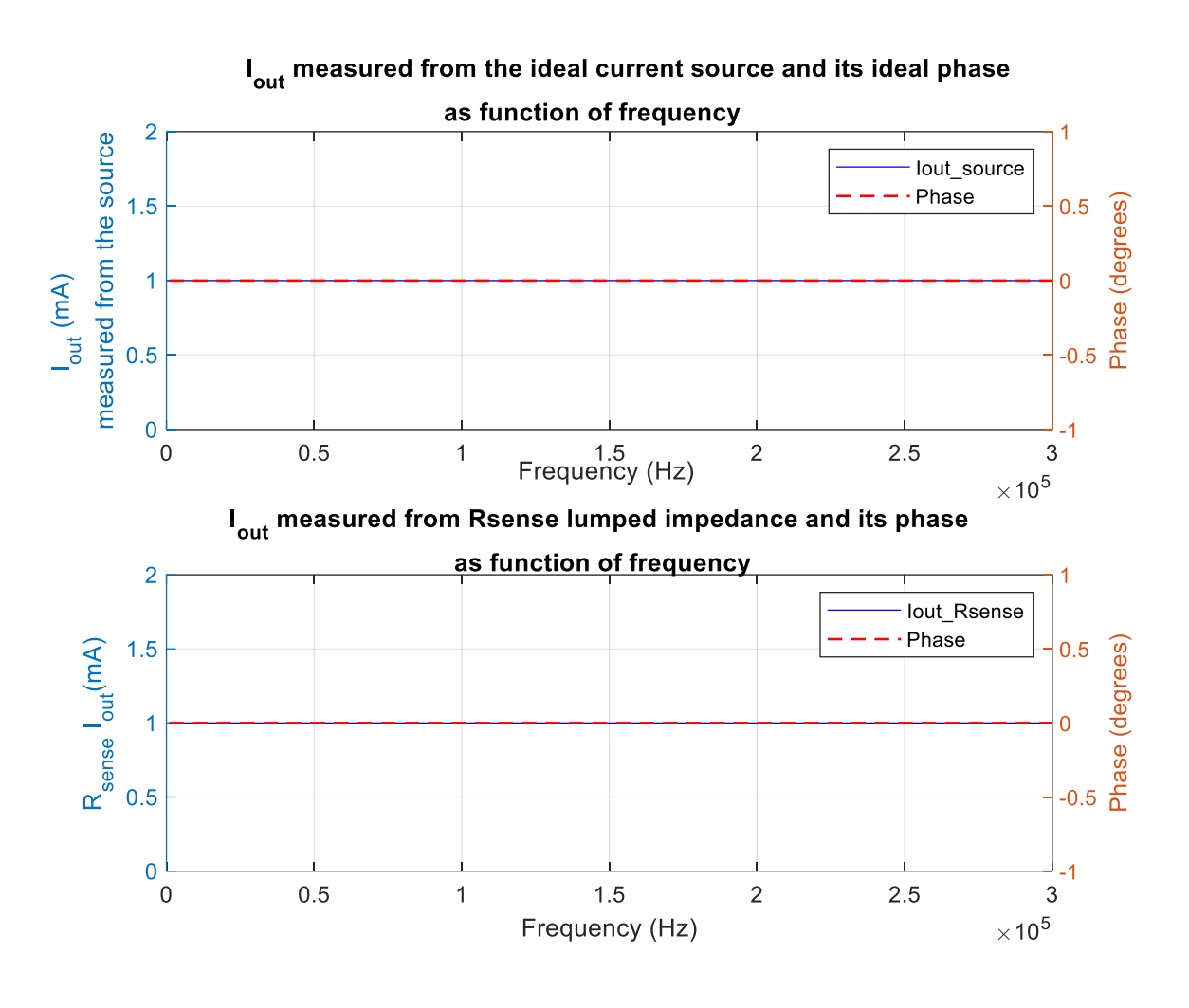


Figure 6. 10 Effects of Rsense on the phase errors of SD system.

An ideal current source was used to inject 1mA of constant current into the lumped impedance model of Figure 6.9 for a swept frequency between 0-300kHz. Measurements were taken across the ideal current source and across the lumped impedance model. Results shown in Figure 6.10 shows that the phase error contribution due the sense resistor is negligible and would not influence the accuracy of the topology proposed in the Figure 6.7

6.5 Effects of common mode offset voltage of IA on the accuracy of the PECSD.

The instrumentation amplifier used in the proposed PECSD topology was simulated to assess the impact of common mode offset voltage on measurement accuracy. As discussed in Chapter 4, any offsets at the output of the instrumentation amplifier (IA) can alter the overdrive of the comparators, leading to erroneous measurements. To evaluate this, the three op-amp IA in the PECSD system, with resistors matched to 0.1% tolerance, was subjected to a maximum common mode input voltage of 12V DC using a 15V power supply, with differential 1V amplitude input voltages as shown in Figure 6.11. The output of the IA was then compared to ground, and ideally (0V) using the comparator both with and without the presence of the common mode input offset voltage.

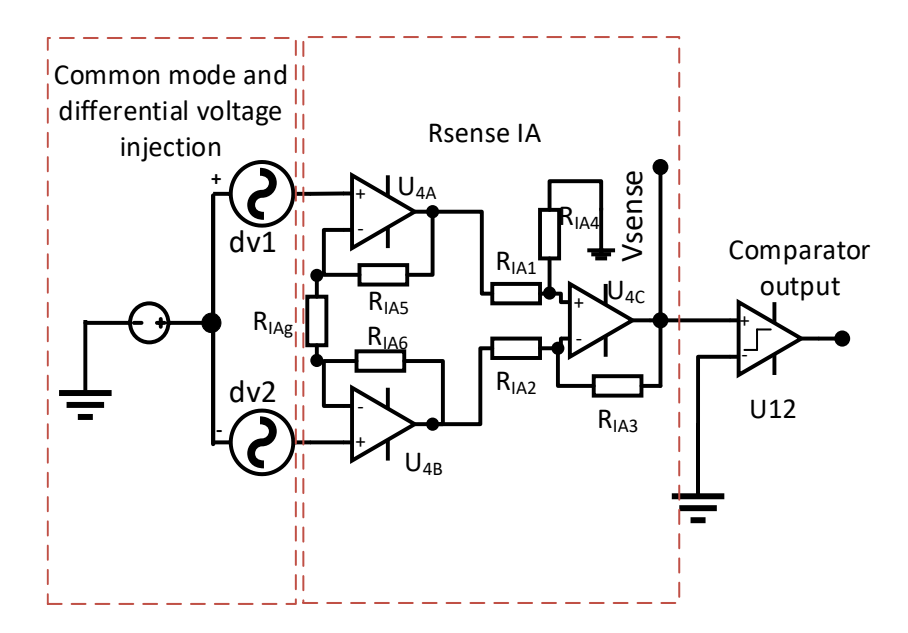


Figure 6. 11 Simulation of common mode offset voltage of the instrumentation amplifier

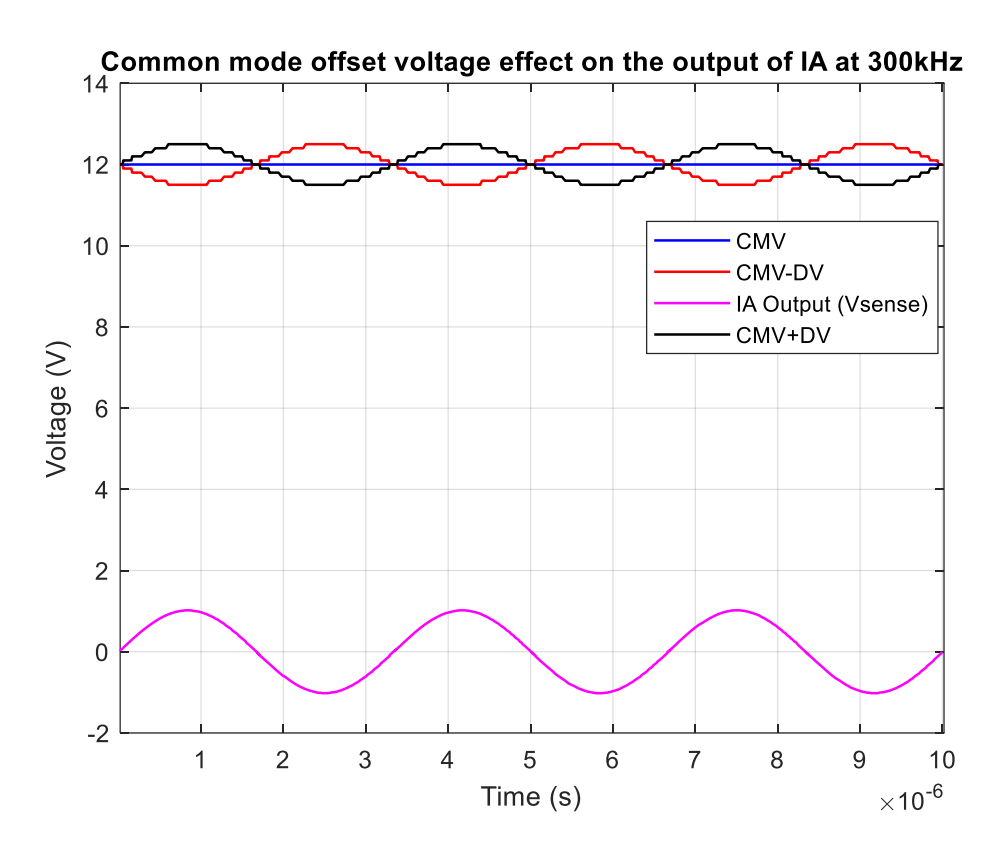


Figure 6. 52 Input and output of the Instrumentation amplifier with a common mode offset voltage of 12VDC.

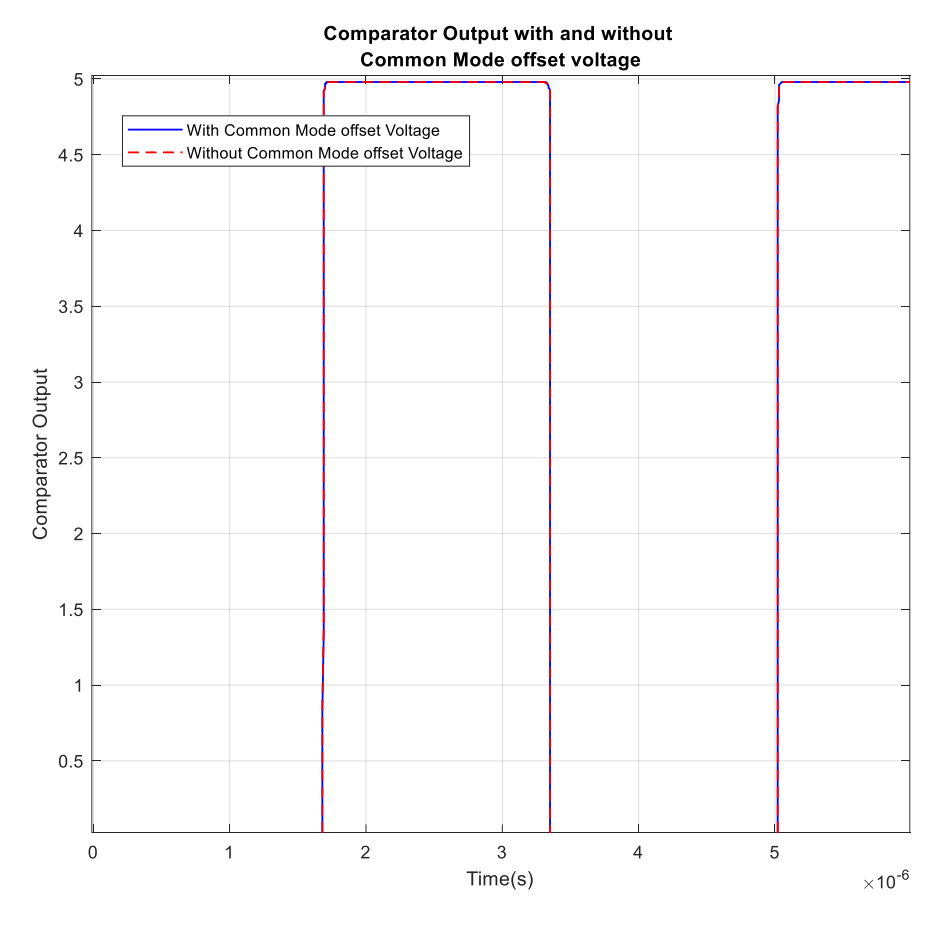


Figure 6. 63 Output of the comparator with and without the common mode offset voltage of IA.

Figure 6.12 further shows that IA designed has good rejection for common mode DC offsets inputs as the comparator overdrives remained the same. The common mode rejection ratio CMRR was also tested adopting a similar circuit in Figure 6.11 but in this case, the common mode signal was AC and tested for the full proposed system bandwidth of 300kHz. CMRR was determined following eq.6.9-6.10.

$$CMRR = \frac{A_D}{A_{CM}}$$
 6.9

$$CMRR(dB) = 20log10(CMRR)$$
6.10

Where A_D = Differential gain

ACM = Common Mode Gain

The resulting output a shown in Figure 6.14 shows a relatively high CMRR of IA, even at the higher end of the 300kHz bandwidth proposed.

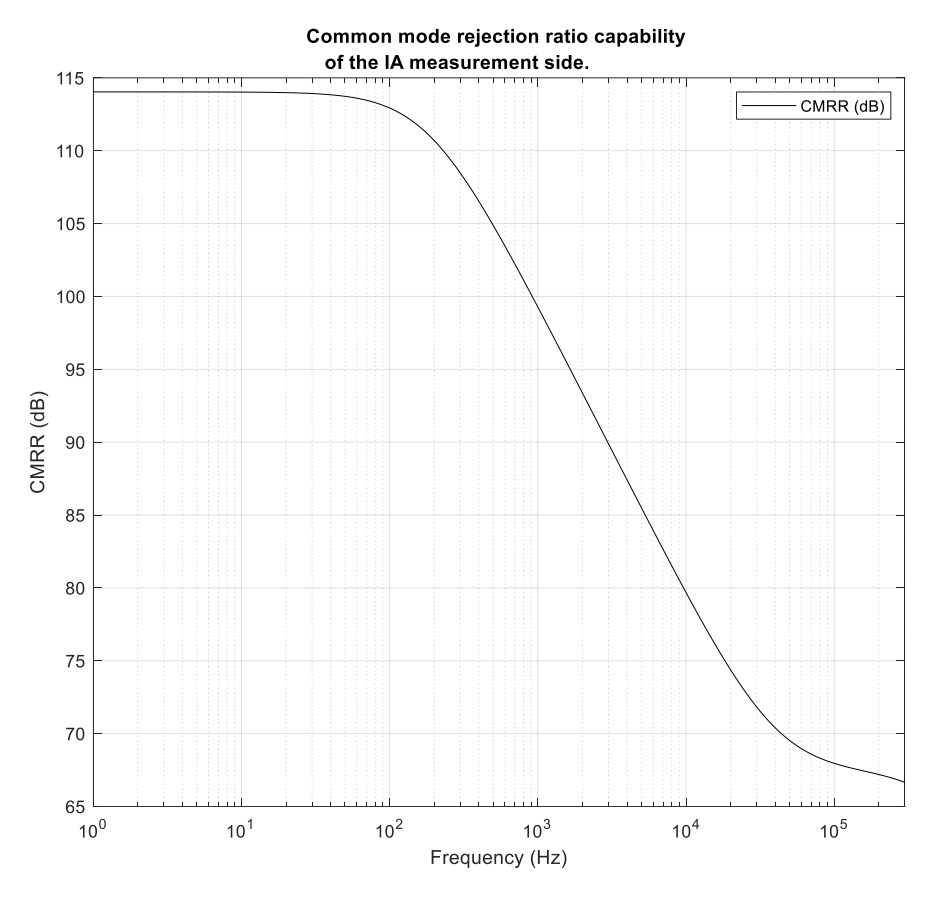
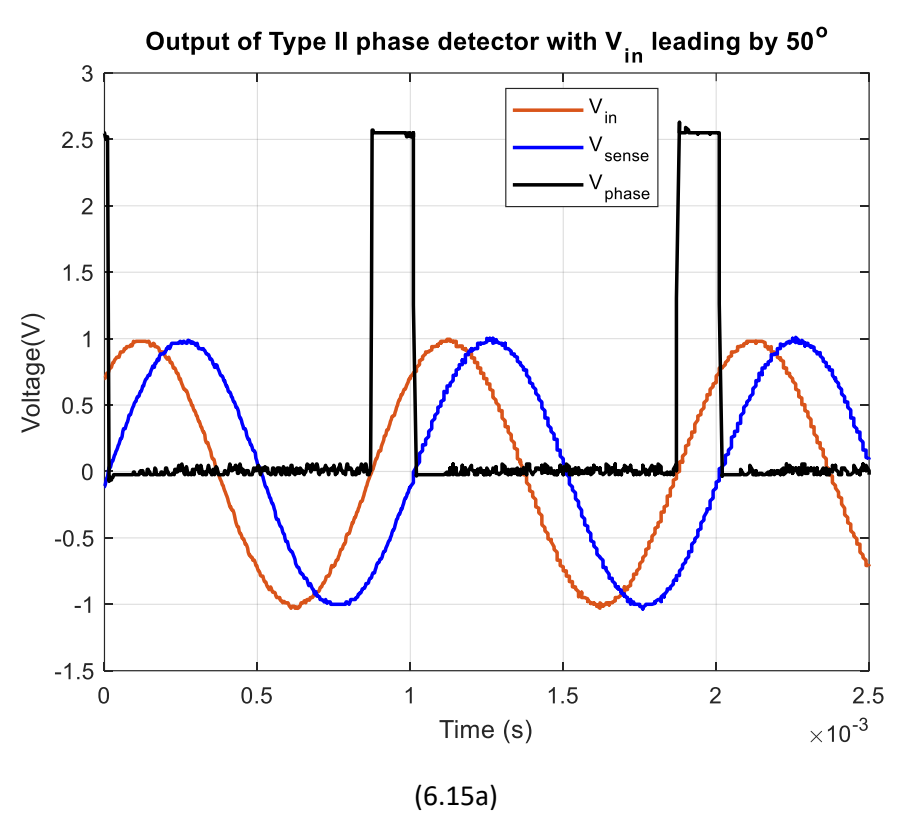


Figure 6. 7 CMRR of the measurement side IA.

6.6 Phase detector lead and lag phase pulses (from the implemented hardware).

Figure 6.15 a and Figure 6.15b shows the working of the type II phase detector pulses at lead and lag 50° phases of the Vmeas.



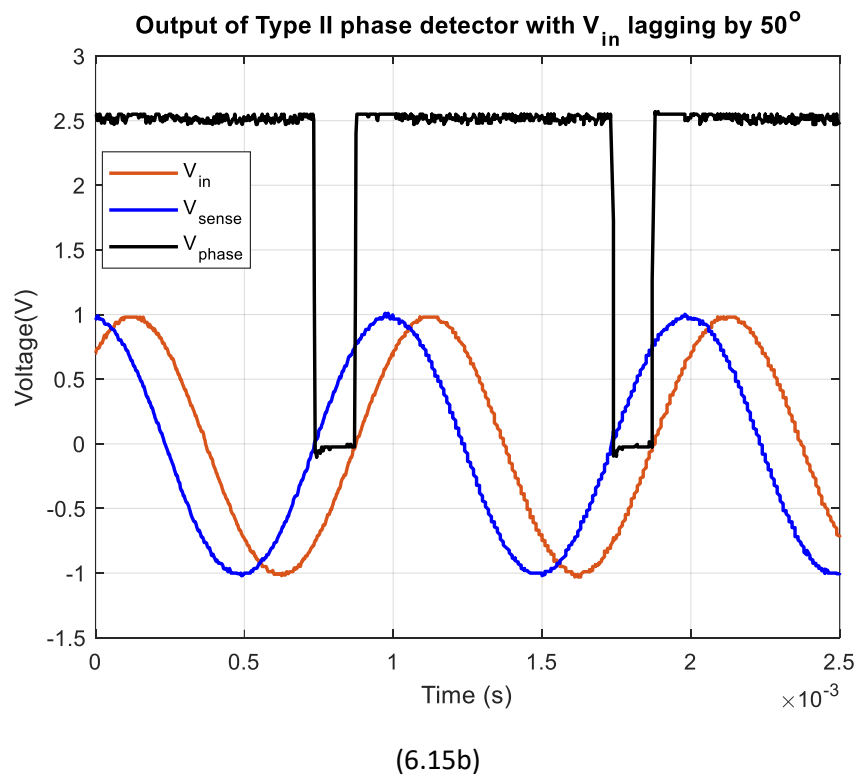


Figure 6. 85 showing (a) phase pulses due to V_{in} leading V_{sense} and (b) phase pulses due to V_{in} leading V_{sense} and (c) phase pulses due to V_{in} leading V_{sense} and V_{sense} are V_{sense} and V_{sense} and V_{sense} and V_{sense} are V_{sense} and V_{sense} and V_{sense} and V_{sense} and V_{sense} and V_{sense} are V_{sense} and V_{sense} and V_{sense} and V_{sense} are V_{sense} and V_{sense} and V_{sense} and V_{sense} are V_{sense} a

6.7 PECSD Experimental Set-Up.

The PECSD proposed in this thesis was tested under various loads and frequencies using the setup shown in Figure 6.16. Initially, a direct digital synthesizer (DDS) was used as the signal generator; however, due to bandwidth limitations, a standard lab waveform generator was employed instead. The experimental setup included a power supply, a signal generator, an oscilloscope, and a data acquisition (DAQ) module. Tests were conducted with both resistive and capacitive loads.

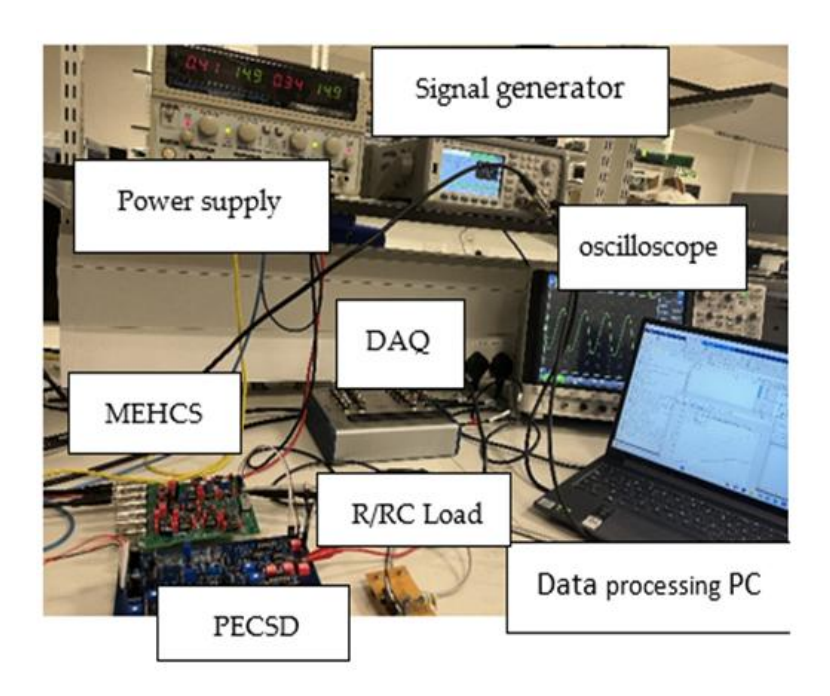


Figure 6. 9 Set up for Experiment with PECSD

Table 6.2 and Table 6.3 below further illustrate the impedance output variables for both phase-compensated and uncompensated synchronous detection systems for resistive loads, as well as resistive and capacitive loads.

Load	Frequency	Z _x With phase compensation	Z _x W/O phase compensation	arphi with phase compensation	φ W/O phase compensation
	1000	997.77	986.30	1.47	1.64
	10,000	996.32	986.13	1.03	1.27
	100,000	961.95	957.70	1.68	11.10
R =	200,000	891.03	880.59	0.12	18.86
1kΩ	300,000	818.70	826.89	4.04	23.39

Table 6. 2 Impedance output variables for both phase compensated and uncompensated synchronous detection system. R Load = $1k\Omega$, Rsense = $1k\Omega$. IA gains: $A_{Vsense} = 1$, $A_{Vmeas} = 1$. $I_{out} = 1mA$. $V_{in} = 1V$.

Table of Resultant Impedimetric Values for RC Load of $1K\Omega$ and 244pF Across a Range of Frequencies, Comparing SD with and without Phase Compensation

			Z _x	Z _x			
Load	Frequency	Z _x Ideal	With phase compensation	W/O phase compensation	arphi Ideal	φ With phase compensation	φ W/O phase compensation
	1000	999.99	991.54	986.23	0.08	1.85	1.48
RC = 1kΩ	10000	999.88	991.92	988.64	0.87	2.44	3.12
&	100000	988.46	974.38	973.84	8.71	9.31	18.81
244pF	200000	956.10	838.78	844.15	17.03	15.96	33.35
	300000	908.59	752.30	746.28	24.68	22.01	43.67

Table 6. 3 Impedance output variables for both phase compensated and uncompensated synchronous detection system. R Load = $1k\Omega$, RC Load = $1k\Omega+244$ pF. Rsense = $1k\Omega$. IA gains: AVsense = 1, AV_meas = 1. lout = 1mA. Vin = 1V.

6.8 PECSD Experimental Results.

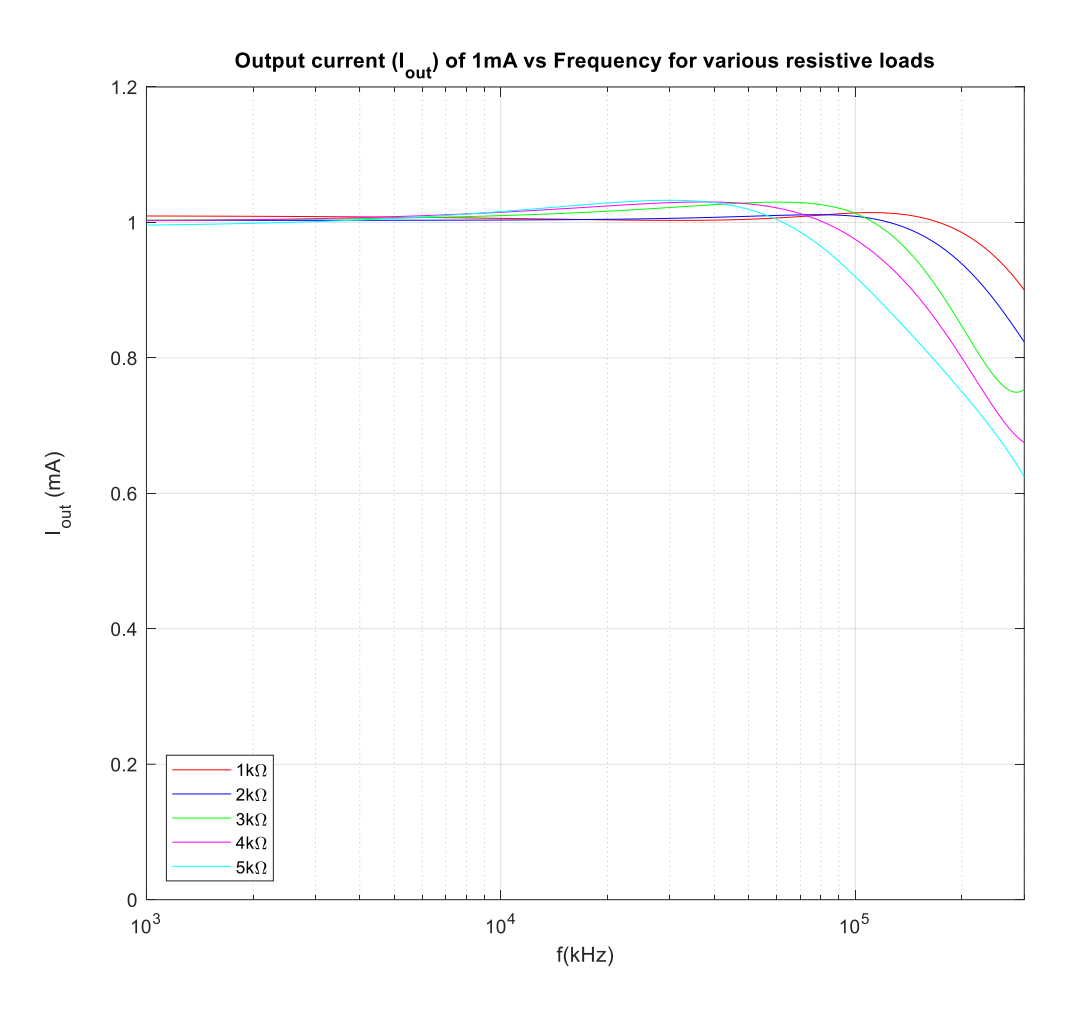


Figure 6. 10 Output current MECHS for a resistive load of 1-5K Ω

Figure 6.17 illustrates the frequency response of the MECHS in this experiment for output current I_{out} = 1mA. MECHS was tested with resistive Loads from 1k Ω to 5k Ω . The frequency response shown in Figure 6.17 was derived from Figure 4.9 already explained in the chapter 4. In Figure 4.9, $R_1=R_3=R_4=100K\Omega$, $R_{2a}=99K\Omega$, $R_{2b}=1K\Omega$.

As such Figure 6.18 illustrates the phase compensation mechanism employed in the proposed system. To demonstrate the phase error, measurements were taken both before and after applying the phase compensation.

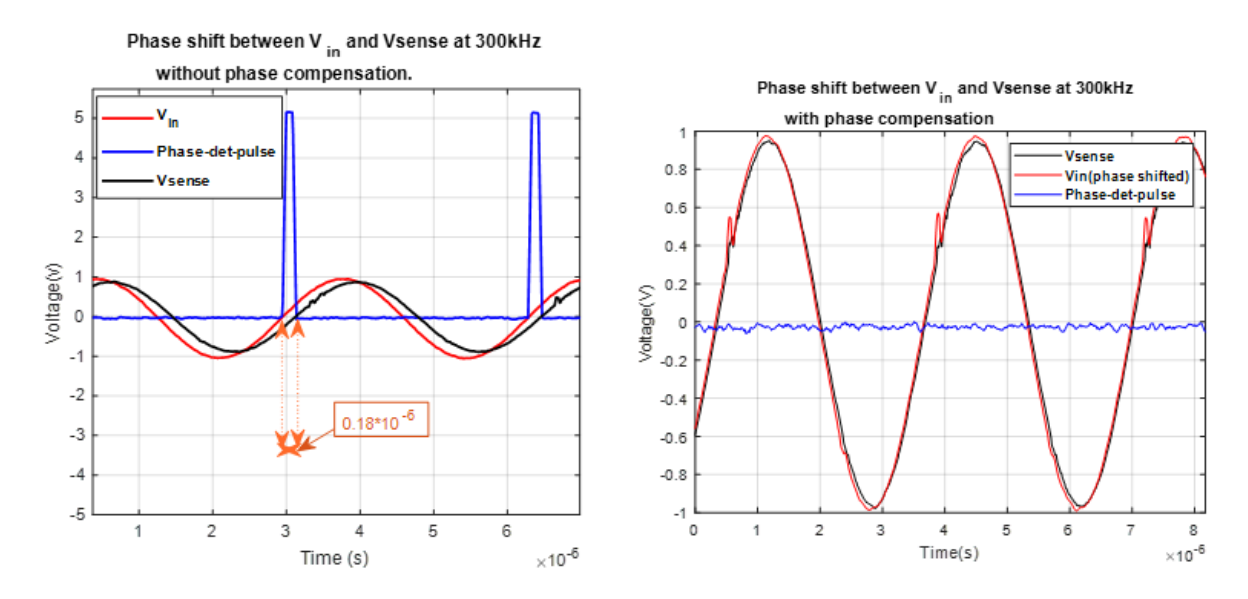


Figure 6. 11 showing (a) phase shift Vsense and V_{in} before and (b) after phase compensation at 300kHz.

The output of the Type II phase detector, phase-det-pulse, generates a pulse of 0.184 μ s at 300 kHz, which corresponds to the phase difference between the demodulator signal (Vin) and the measured signal (Vsense). According to Equation (4.99), this pulse width reflects a phase shift of approximately 19.44°.

This phase shift has significant clinical implications. In applications where tissue phase values are critical diagnostic indicators, such as cancer diagnostics and bioelectrical impedance myography, misinterpreting such a substantial phase error could lead to incorrect diagnoses and potentially endanger the patient [35]. Therefore, diagnostic results must be interpreted with the utmost precision and caution.

When phase compensation feedback is activated, Vin is delayed until it is in phase with Vsense. At this point, the Phase-det-pulse reduces to zero, indicating that there is no phase error between Vin and Vsense, as shown in Figure 6.8b.

The PECSD was evaluated using a parallel resistor and capacitor (RC) load combination to further assess its performance. The resulting real voltage component (VRE) and imaginary voltage component (VIM) at the low-pass filter output for RC loads are shown in Figures

6.19 and 6.20.

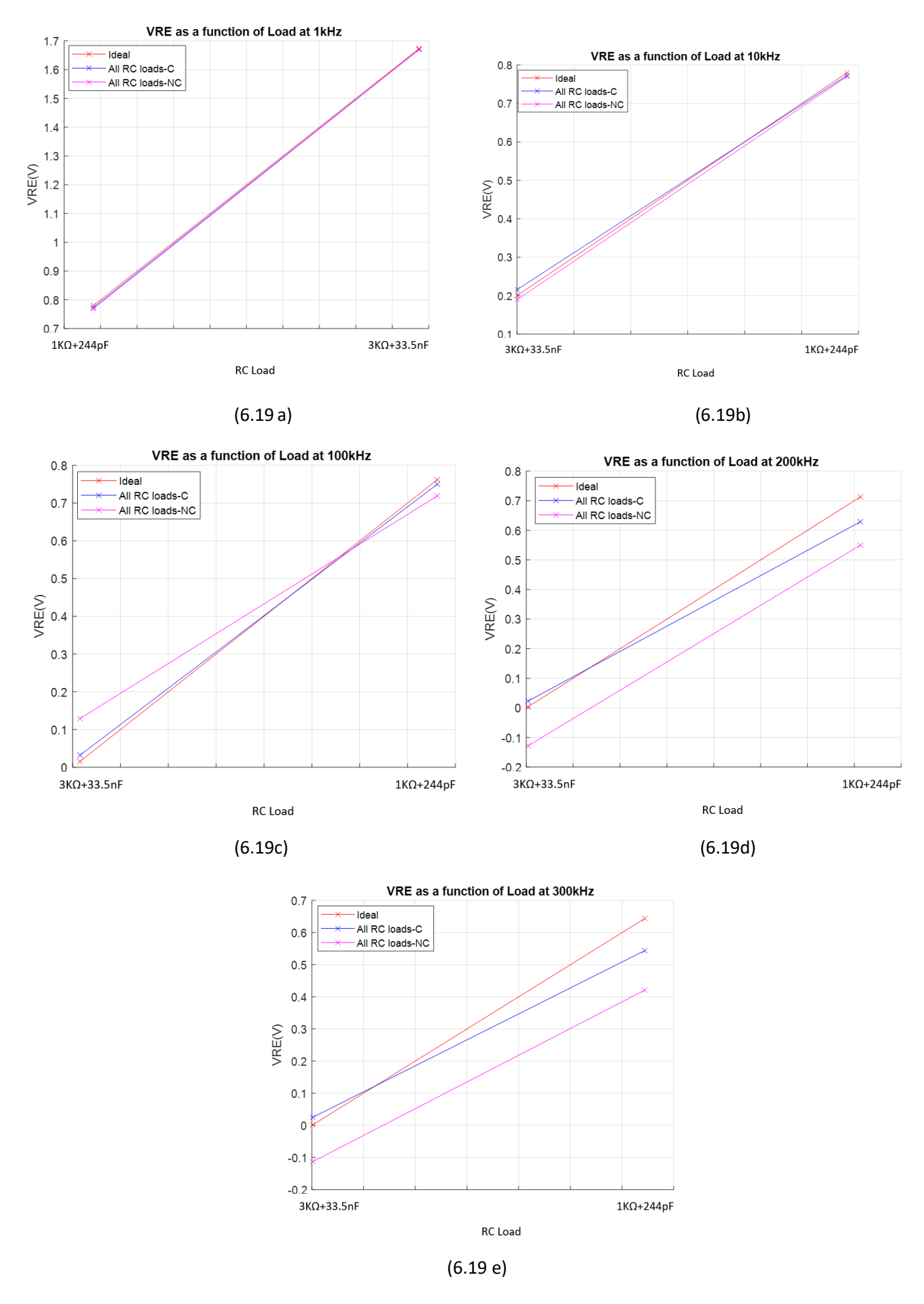


Figure 6. 12 V{RE} of the low pass filter as a function of RC load for (a) 1kHz (b) 10kHz (c) 100kHz (d) 200kHz (e) 300kHz

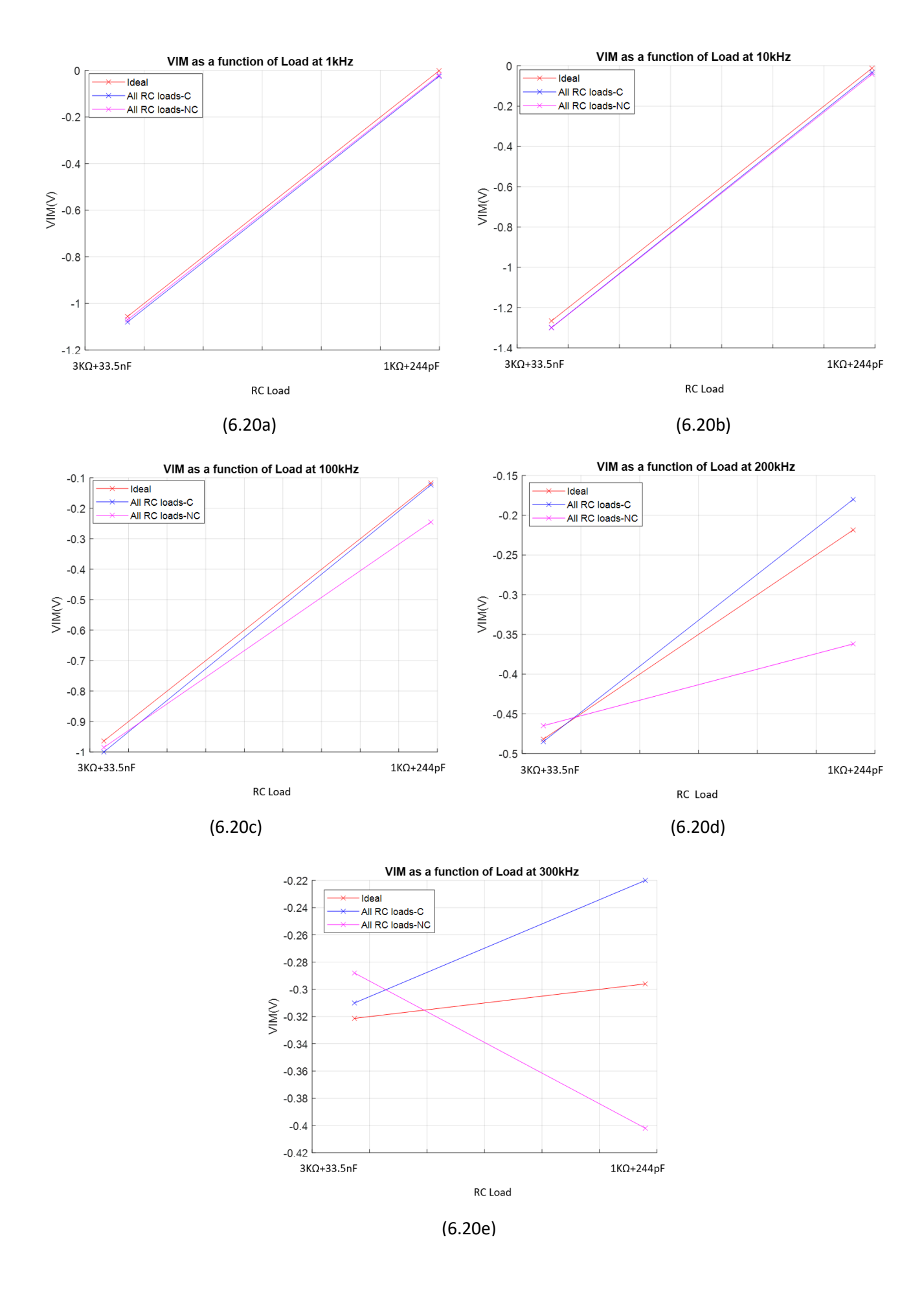


Figure 6. 13 V{IM} of the low pass filter as a function of RC load for (a) 1kHz (b) 10kHz (c) 100kHz (d) 200kHz (e) 300kHz.

Figures 6.19 and 6.20 above present the low-pass filter output of the SD system for RC loads of 1 k Ω + 244 pF and 3 k Ω + 33.3nF. The results indicate that with PECSD compensation, VRE and VIM align more closely with the ideal measurements compared to without compensation.

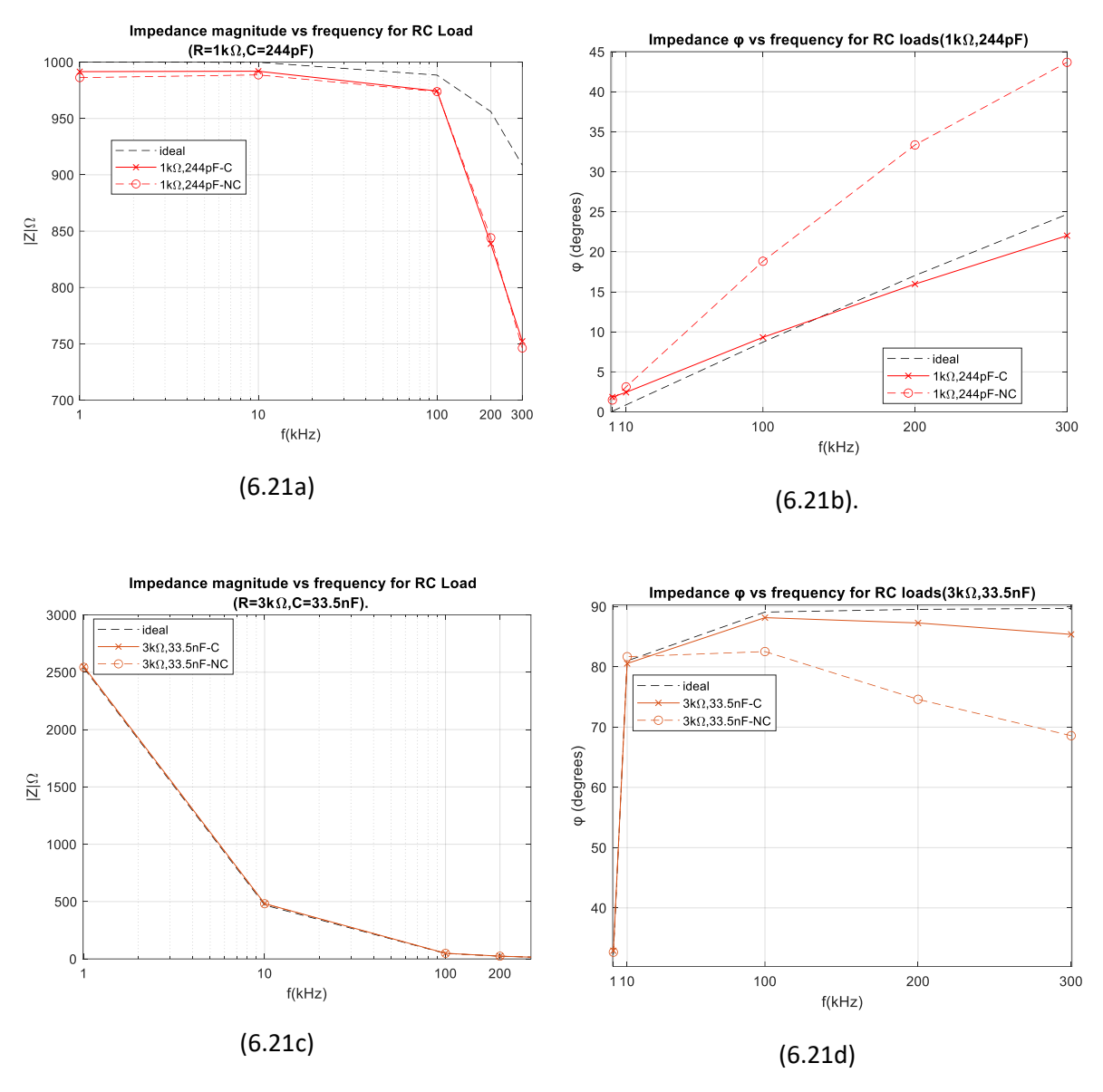
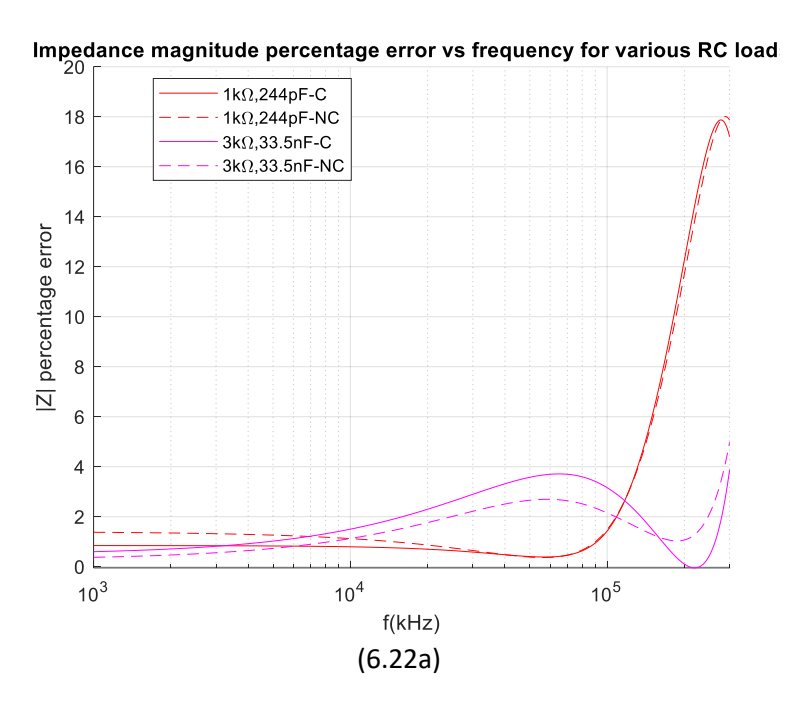


Figure 6. 14 Impedance magnitude and phase for RC loads (1 $k\Omega$, 244pF and 3 $k\Omega$, 33.5 nF) as a function of frequency

Figure 6.21a and Figure 6.21c showed the impedance magnitude as a function of frequencies for RC loads of ($1k\Omega$, 244 pF) and ($3k\Omega$, 33.5nF), respectively. Figure 6.21a, and Figure 6.21c shows no significant improvement with phase compensation unlike the counterpart Figure in Figure. 6.21b, d, which showed significant improvement in phase error correction. The percentage phase errors for Figure 6.21b, d, were further illustrated in Figure 6.22b, where the SD system without compensation for RC loads of ($1k\Omega$, 244 pF) and ($3k\Omega$, 33.5nF) exhibited phase errors of approximately 19% and 21% at 300 kHz, respectively. After phase compensation, however, they were significantly reduced to 2° and 4%. These findings underscore the critical role of phase compensation in enhancing accuracy. The clinical significance of these phase errors becomes evident considering previous research [35], where phase differences between healthy and cancerous tissues were approximately 20°, 17°, and

11° at frequencies of 100 kHz, 200 kHz, and 300 kHz, respectively. As such, without proper phase correction, there is a substantial risk of diagnostic unreliability, potentially leading to misidentifying healthy tissue as cancerous and vice versa. Therefore, accurate phase compensation in diagnostic procedures using SD systems is needed.



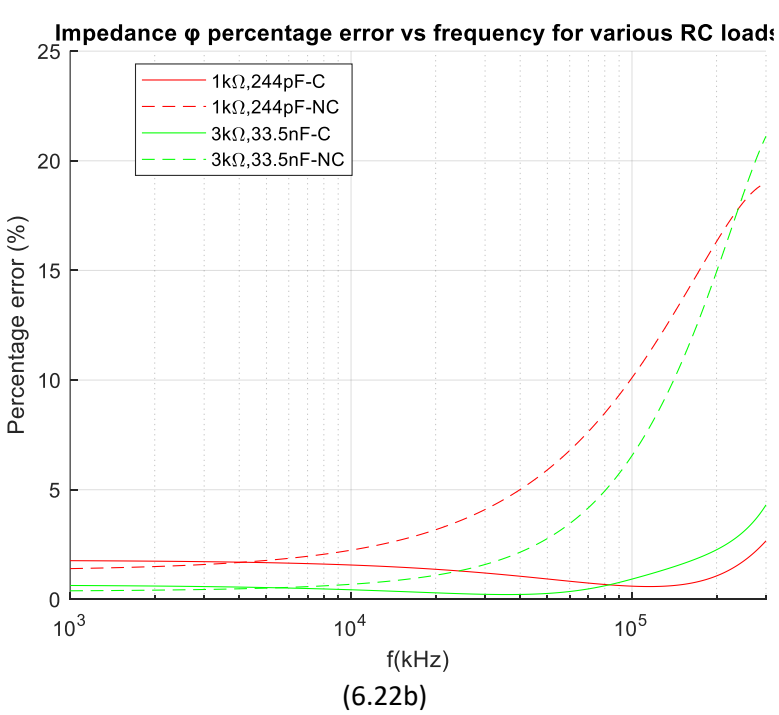


Figure 6. 15 showing (a) Impedance magnitude percentage phase error and (b) impedance phase percentage errors for RC loads.

After evaluating the performance of PECSD with RC loads, measurements were also conducted with purely resistive loads. Although resistive loads are not expected to exhibit phase elements, erroneous phase shifts introduced by the VCCS and the non-ideal characteristics of resistors can still cause phase deviations. PECSD is designed to minimize

these deviations through compensation. As such Figure 6.23a shows the impedance magnitude for various resistive loads, while Figure.6.23b displays their corresponding percentage errors. Notably, the bandwidth remains consistently at 10 kHz across all loads, beyond which the circuit's performance deteriorates, particularly for loads exceeding 1 k Ω . It is important to emphasize that phase compensation has minimal impact on the impedance magnitude of the SD system and this depends on the amplitude of the current output.

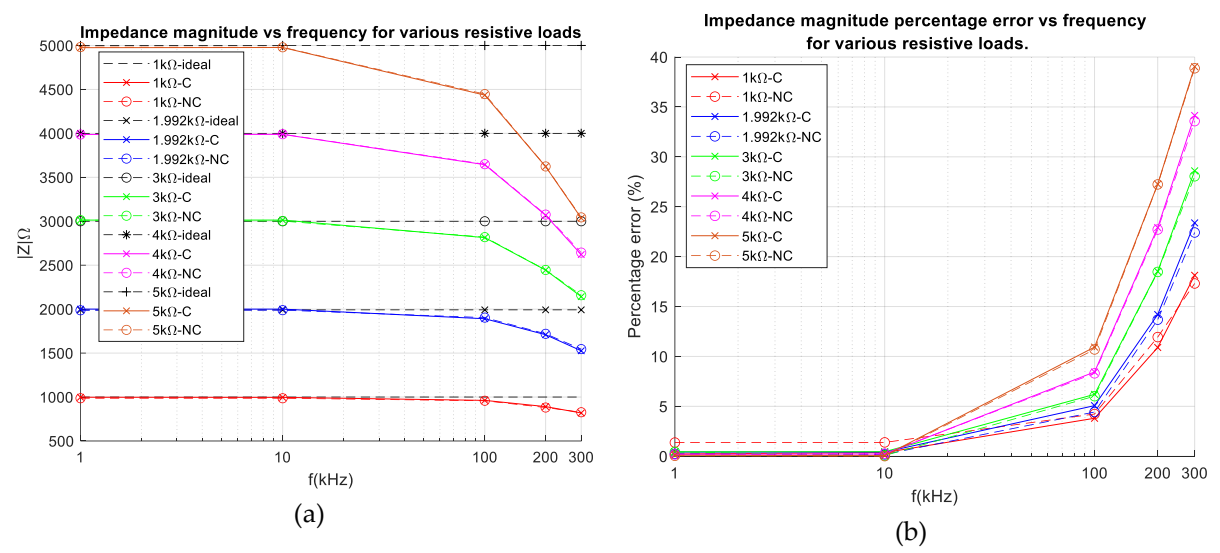


Figure 6. 16 (a) Impedance magnitude vs. frequency for resistive loads. (b) Impedance magnitude percentage error vs. frequency for resistive loads.

Figure. 6.24 illustrates a significant improvement in phase error correction, especially at higher frequencies. Without compensation, a resistive load of 5 k Ω at 300 kHz exhibited substantial phase errors of up to 38°. The phase errors after compensation error were notably reduced to 17° when phase compensation was applied under the same load and frequency conditions.

Although achieving ideal correction of an erroneous phase shift to 0° is theoretically desirable, it may be challenging. This challenge is likely caused by small mixer-induced errors, such as differential lags between inputs and filter offsets [123][124][125].

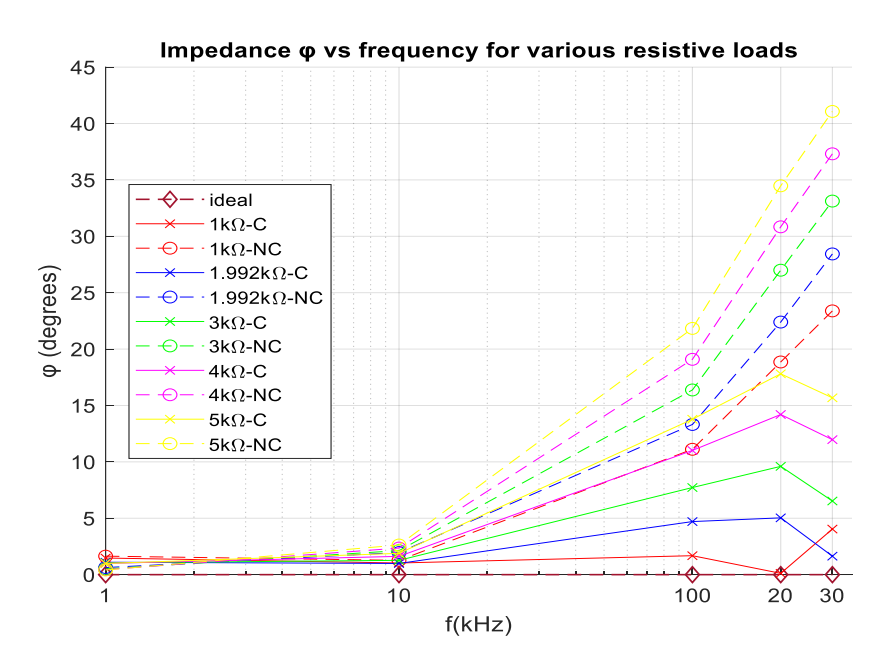


Figure 6. 17 Impedance phase errors for compensated and uncompensated SD systems as a function of frequency for resistive loads.

Figure. 6.24 further justifies the phase difference observed between the measured signal Vsense and demodulation signal Vin, as in Figure 6.18a, for a load of 1 k Ω and frequency of 300 kHz. Whilst the phase difference observed in Figure.6.18a is about 19.44°, as calculated from the phase detector pulse width, the erroneous phase observed in Figure.6.24 for 1 k Ω was notably 23°. As such, the additional phase difference of 4° may be due to non-idealities of the lock-in amplifier.

6.9 Settling Time of PECSD and Non compensated SD system

Figure 6.25a and Figure 6. 25b shows the settling time for conventional SD systems and for SD system with phase compensation respectively. The response time of conventional SD systems predominantly rely on the settling time of the filters used in the output stages. SD with phase compensation exhibits slightly longer response time in cases of step change in the amplitude of the input voltage. This is because, the final settled value of output low pass filters relies on the time required by the all-pass filter to add adequate delay in order to synchronize the sense voltage Vsense with the demodulation signals in phase.

The system's settling time at 1kHz and with a typical load ($4k\Omega$) was monitored by capturing the output of the Low pass filter at a step input of 0.9V. The settling time was measured as the time taken for the system to settle to 97% (1.74V) of the final expected value of 1.8V for a filter gain of 2. SD system with phase compensation was found to be 445ms slower than without compensation. It is noteworthy that this may not be a significant concern in most bioimpedance applications, where the measured impedance is relatively slow varying with

exceptions like applications where specific frame rate requirements are required for multiple channels recording as is the case with electrical impedance tomography [108], [113].

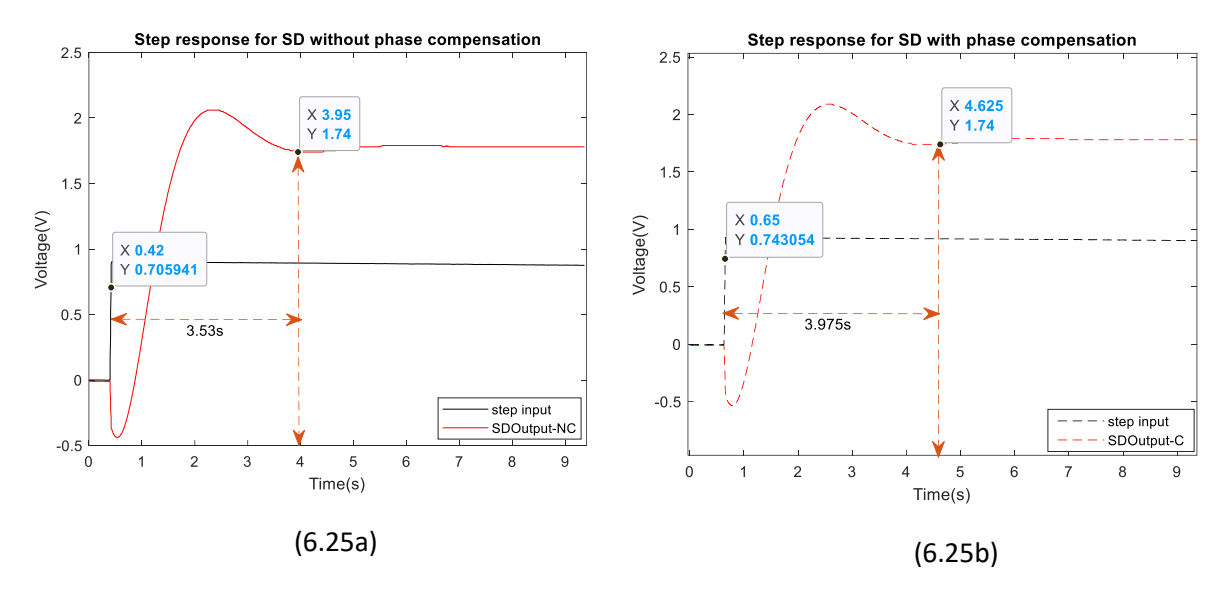


Figure 6. 18 System step response for SD system with (a) and without (b) compensation.

6.10 Analysing PECSD performance through simulations.

To validate these experimental findings, simulations were performed for both purely resistive and RC loads. Figure 6.26a and Figure 6.26b show the percentage error in impedance phase for both loads. Both sets of results showed lower errors compared to the experimental data, which may be attributed to the simulations not accounting for real-world experimental factors such as the non-idealities of certain components such as leads, connector terminals, and printed circuit boards.

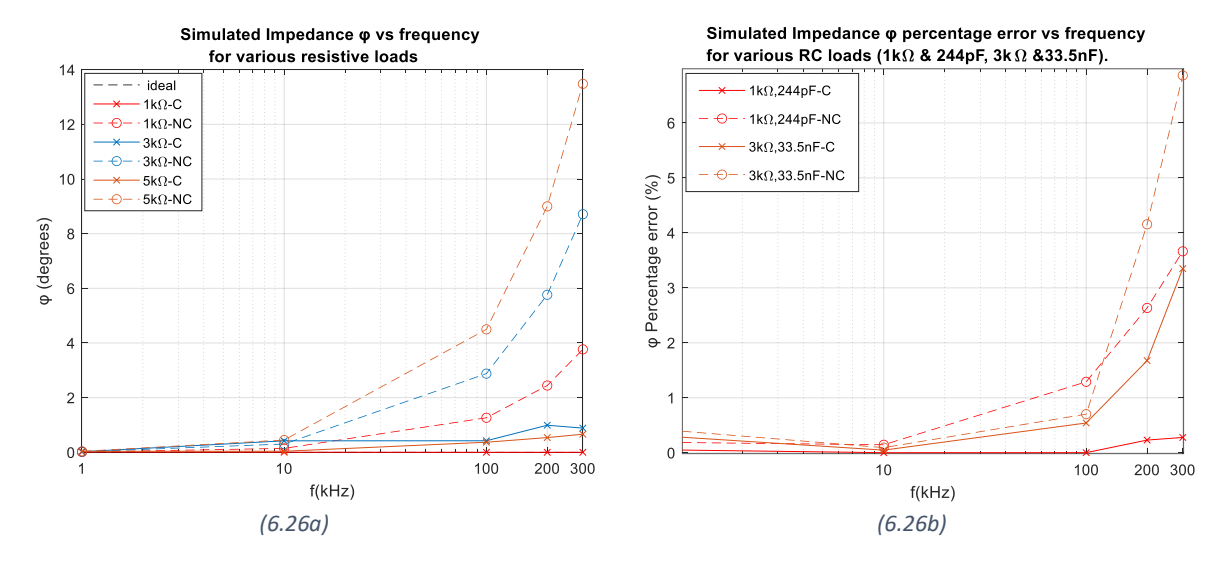


Figure 6. 19 Relative percentage errors (6.26a) and absolute phase errors (6.26) of the R and RC load before and after compensation.

Architecture	Discrete	
PCB Active area	130 mm × 162 mm	
Supply Voltage	±15 V	
Bandwidth	1 kHz-300 kHz	
Phase Measure	ement accuracy	
0/ Funes of Funesting autool DC leads @ full househoidth	≤5% with phase compensation	
% Error of Experimented RC loads @ full bandwidth.	≤21.1% without phase compensation	
	3.965 s with phase compensation	
Settling time @ 98% of final value	3.53 s without phase compensation	
	•	

Table 6. 4 Summary of Measured Performance of PECSD

6.11 Conclusion on Chapter 6.

The phase error compensated Synchronized Demodulation system presented in this Thesis featured a discrete component realization of the SD bioimpedance system featuring automatic phase error correction. It solely focused on eliminating a fundamental, systematic, and often unreported source of errors in bioimpedance measurement systems which particularly is the phase shifts between the VCCS output current and I, Q demodulation signals in the Synchronous Demodulation/Detection (SD) architecture.

The developed phase compensation method features an auto-adjustable delay block with an all-pass filter. The PECSD system achieved a substantial reduction in phase error at ≤5% across all RC loads compared with the uncompensated SD system, where errors could reach up to 21.1%. This improvement in measurement accuracy will significantly improve SD systems' applicability to diagnostic applications, particularly in scenarios where tissue phase values serve as crucial diagnostic indicators, such as in cancer diagnosis and others as bioelectrical impedance myography.

Although this system performed effectively, it is important to note that many bioimpedance applications that rely on phase differences as a diagnostic marker such as distinguishing between impaired and normal tissue in cases like skin cancer also depend on impedance magnitude. These measurements are typically conducted at relatively high frequencies. However, the VCCS used for PECSD suffered limitation in bandwidth, limiting the accuracy of the Impedance magnitude and could not be adopted relatively higher frequency above 300kHz..

One significant challenge with Voltage-Controlled Current Sources (VCCS) is the degradation of output impedance, which directly impacts the accuracy of the output current amplitude[126]. As such, the next chapter will be focused on optimising the Injection side circuit VCCS towards achieving a higher accuracy at a reasonable wider bandwidth.

Chapter 7.

Adaptive Howland Current Source.

The accuracy of bioimpedance measurements heavily relies on that of the front-end instrumentation [23], [41], which comprises two main stages, the current injection and the voltage measurement circuitry. The design of the current injection instrumentation usually involves an AC current source comprising a signal generator connected to a voltage-to-current converter [94], [127]. For precise BIM, the current source must deliver a constant amplitude (less than 1% amplitude variability [128][59]) AC current over a wide range of loads, typically from hundreds of Ω to tens of $k\Omega$ - respectively requiring injected currents of a few mA down to tens of μ A (sub-mA). Desired bandwidths range from 1kHz to several MHz, however nonidealities degrade the output impedance of current sources at high frequencies [126]. Consequently, the output current amplitude drops with frequency relative to its intended nominal value, resulting in considerable accuracy degradation.

Majority of bioimpedance circuitry makes use of discrete component versions of the Howland Current Source (HCS) [96], [129], which is a voltage-controlled current source (VCCS) topology. In the last few decades, several HCS variants have been suggested to improve the initial design's performance, mostly aiming to improve output impedance so as to avoid current fluctuations with frequency and load impedance [96].

7.1 Inaccuracies In Variants of Howland Current Source (HCS)

As earlier addressed in chapter 4, apart from the ASIC realisations, there are many variants of HCS with their unique advantages and disadvantages with most loosing accuracies at relatively higher frequencies. In addition to the aforementioned topologies and review in chapter 4, the NIC Tietze circuit [130], achieved a reported 1 MHz bandwidth; however, the current error was 2.33% and thus higher than 1%.

The current-to-voltage feedback topology [97] (CTVF-MEHCS) compensates for leakage current by sensing the output current and providing negative feedback to the MEHCS input, thereby effectively increasing the output impedance at higher frequencies. Experimental results employing this technique reported approximately a 1.5% error for a 1mA current amplitude over a 1MHz bandwidth, a significant improvement over MEHCS. However, its suitability for sub-mA output current is compromised, as accuracy degrades when generating lower current amplitudes. Additionally, the resistor matching requirements are greater than MEHCS [97].

Thus, Mirrored Enhanced Howland Current Source (MEHCS, Figure 4.9) is widely considered the best performing topology due to its true differential output and its overall simplicity and

robustness relative to other designs [94], [97] . Still, like all open-loop current sources, MEHCS also has drawbacks, including feedback resistor mismatches; operational amplifier limitations; stray capacitances in tracks and cables; and other issues degrading its output impedance, with the topology exhibiting more than 1% current error for bandwidths over a few hundred kHz [93].

7.2 Higher bandwidth requirements in Bioimpedance measurements.

At frequencies near and above 1MHz, tissue properties monitored are associated mainly with intracellular structures like with intracellular structures like cell membranes and organelles (part of β -dispersion bioimpedance frequency band) [50], [56]. Being able to monitor biological tissue accurately at frequencies above the abovementioned instrumentation limitations is crucial in bioimpedance applications like skin cancer detection and assessment [131], [132]. Still, to the authors' knowledge the "barrier" of sub-1% error over 1MHz for mA and sub-mA current amplitudes has not yet been surpassed.

To overcome this barrier, the work presented here introduces and experimentally evaluates a MEHCS-based automatic gain control (AGC) design offering a high bandwidth (3MHz) adaptive current source achieving significantly low amplitude error. I term this the "Adaptive Howland Current Source" (AHCS) and we have implemented it in a discrete-component realisation, in line with the majority of relevant literature [96]. This novel design adjusts the gain of the current driver automatically, to maintain the current output's accuracy, regardless of any output impedance degradation.

7.3 Automatic gain control (AGC) architecture.

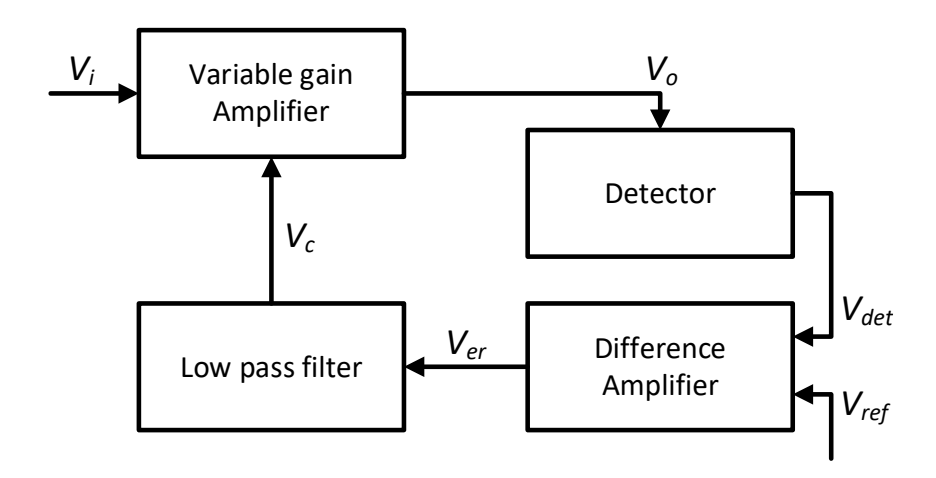


Figure 7. 1 AGC system for amplitude stabilisation. [133]

The system presented here in Figure 7.1 employs a standard automatic gain control (AGC) mechanism for amplitude stabilization, utilizing a variable gain amplifier (VGA). In a typical VGA-based AGC loop – like that in Figure 7.1 - the input signal V_{in} passes through the VGA to produce the output level V_{o} to be stabilized [133]. The detector's output (V_{det}) is compared against a desired output amplitude reference voltage (V_{ref}) producing an error signal (V_{er}). That is then integrated, producing a gain control feedback voltage (V_{c}) dynamically adjusting the VGA gain thus stabilizing the output to an amplitude (V_{o}) that tracks V_{ref}

7.4 Functional block diagram of the system Design

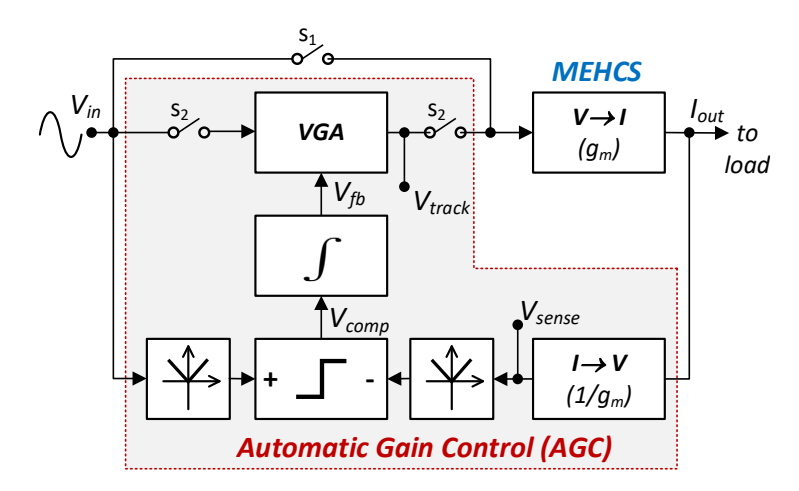


Figure 7. 2 Functional block diagram of the AHCS.

As shown in the block diagram in Figure 7.2, with switches s_1 on and s_2 off, the system operates as an open-loop MEHCS with a transconductance g_m converting the input sinusoidal voltage $V_{in}(t)$ to output current $I_{out}(t)$. As mentioned, its amplitude should ideally be constant to a nominal value I_{out} irrespective of its frequency. However, as its amplitude drops due to the leakage current I_{leak} "lost" through the output impedance - which decays at higher frequencies - the output current becomes $I_{outER} < I_{out}$ (eq. (7.1)):

$$I_{outER} = I_{out} - I_{leak} 7.1$$

Once the automatic gain control (AGC) stage is on (s_1 off, s_2 on), the output current $I_{out}(t)$ of the MEHCS is continuously monitored through a transimpedance stage with a gain of $1/g_m$, whose output amplitude is ideally $V_{sense} = I_{out}/g_m = V_{in}$ if the output current has the nominal value I_{out} . When the output current amplitude changes, $V_{sense} = I_{outER}/g_m \neq V_{in}$. The gain G_{COR} by which the present output I_{outER} needs to be multiplied to achieve the nominal output current I_{out} is given by Eq. 7.2:

$$G_{COR} = \frac{I_{out}}{I_{outER}} = \frac{I_{out}}{I_{out} - I_{leak}} = \frac{\frac{I_{out}}{g_m}}{\frac{I_{out} - I_{leak}}{g_m}} = \frac{V_{in}}{V_{sense}}$$

$$7.2$$

To compare their values, peak detectors extracting the amplitudes V_{sense} and V_{in} are connected differentially to a comparator. As indicated in Equation (7.3), its output $V_{\text{comp}}(t)$ assumes a "high" or a "low" state, represented respectively by a positive (+ V_{settle}) or a negative (- V_{settle}) DC voltage, depending on which of the inputs is higher. Once the inputs become equal, the comparator generates an oscillatory output at double the frequency of the injected signal, which is the dominant ripple frequency at the output of the peak detectors [134].

$$V_{comp}(t) = \begin{cases} +V_{settle,} V_{sense} < V_{in} \ (comparator \ output \ high \ DC) \\ -V_{settle,} V_{sense} > V_{in} \ (comparator \ output \ low \ DC) \\ V_{osc}(t), V_{in} = V_{sense} \ (comparator \ output \ oscilates) \end{cases}$$
7.3

The oscillatory output of the comparator can be ideally approximated as a square wave with amplitude V_{settle} and frequency ω_x . The Fourier series (up to 3rd harmonic) gives Eq(7.4):

$$V_{cosc}(t) = \frac{4V_{settle}}{\pi} \left(\sin(\omega_x t) + \frac{1}{3}\sin(3\omega_x t) + \frac{1}{5}\sin(5\omega_x t) + \frac{1}{7}\sin(7\omega_x t) \right)$$
 7.4

The comparator is connected to an integrator with time constant τ . The integrator's time constant is designed to be much higher than $1/\omega x$, assuming the dominant frequency of the comparator output oscillation when inputs are equal is the same as that of the injected signal or higher. The integrator's output $V_{fb}(t)$ is described by Eq.(7.5), where V_{fb0} is the integrator initial output at t=0, assumed to be zero.

$$V_{fb}(t) = \frac{1}{\tau} \int V_{comp}(t)dt + V_{fb0}$$
 7.5

When $V_{comp}(t)$ assumes its high or low DC value, the integrator output will respectively be a positive or a negative ramp given by Eq (7.6).

$$V_{fb}(t) = \begin{cases} \frac{V_{settle}}{\tau}t, & integrator outputing \ a + ive \ ramp \\ \frac{V_{settle}}{\tau}t, & integrator outputing \ a - ive \ ramp \end{cases}$$
 7.6

In the case examined here, $V_{\text{sense}} < V_{\text{in}}$ and the integrator will be a positive ramp. The integrator output controls the gain of a variable gain amplifier (VGA), whose initial gain is unity. Consequently, the amplitude of the VGA's output V_{track} can be expressed using Eq. (7.7)

$$V_{track}(t) = V_{in}(t) \left(1 + A_{vfb}(t) \right)$$
7.7

where $A_{vfb}(t) = V_{fb}(t)/1V$ is the integrator output expressed as unitless gain.

Thus, for $I_{\text{outER}} < I_{\text{out}}$, the amplitude of the MEHCS input voltage (now V_{track}) will ramp up in value until the transimpedance output amplitude of the Vsense reaches a value equal to V_{in} . At that point, the comparator will start oscillating (Eq. (7.3)), resulting in the integrator output shown in Eq. (7.8), comprised of a high frequency triangular wave (due to the square wave nature of Eq. (7.4)) around a dc value V_{fbDC} :

$$V_{fb}(t) = V_{fbDC} - \frac{4V_{settle}T_x}{2\pi^2\tau} \left(\cos(\omega_x t) + \frac{1}{9}\cos(3\omega_x t) + \frac{1}{25}\cos(5\omega_x t) + \frac{1}{49}\cos(7\omega_x t)\right)$$
7.8

Given that $\tau >> T_x$, the triangular wave can be considered a ripple of negligible amplitude, and therefore the integrator output will settle at DC voltage $V_{\rm fbDC}$, whose dimensionless value expressed as gain is $A_{\rm vfbDC}$. Replacing $A_{\rm vfb}(t)$ in Eq. (7.7) with $A_{\rm vfbDC}$ and dividing both sides by $g_{\rm m}$, the input to MEHCS will now settle to a $V_{\rm track}$ value that will generate the desirable $I_{\rm out}$ rather than $I_{\rm outER}$ generated by the open-loop MEHCS as given by Eq. (7.9) (expressed as amplitudes):

$$\begin{split} I_{out} &= I_{outER} \left(1 + A_{vfbDC} \right) \Rightarrow \\ &\Rightarrow 1 + A_{vfbDC} = \frac{I_{out}}{I_{out} - I_{leak}} \Rightarrow \\ &\Rightarrow 1 + A_{vfbDC} = G_{COR} \end{split}$$
 7.9

The AGC ensures that the integrator output and thus the VGA gain will settle to the value necessary for compensating the current error through scaling the input voltage to the MEHCS, rather than by attempting to increase the output impedance as seen in most of the aforementioned topologies[2], [135]. Attempting to compensate by somehow adding I_{leak} is also not straightforward, as it would have to be AC and precisely in phase with I_{out}

7.5 Circuit design.

During the design phase of the AHCS circuit, critical factors, including feedback resistor network tolerances, op-amp matching (same die amps) and open-loop gain, and PCB layout were considered to ensure a desirable output. In the implementation of the AHCS circuit in Figure 7.3, the MEHCS stage is comprised of U9 and U10 op-amps, with its input driven by a unity gain single-to-differential amplifier (U8) to increase common mode rejection, reduce DC offsets, and thus enhance load capability [136]. In the open loop (sw₁ to V_{in}), the output current I_{out} , flowing through R_{sense} and through the load Z_L , is given by

$$I_{out} = g_m V_{in} 7.10$$

where g_m is the transconductance of the MEHCS, given by [97].

$$g_m = \frac{R_{h4}}{R_{h3} \times R_{h5}}$$
 7.11

In MECHS, achieving high-output impedance requires R_{h1} to R_{h4} to be highly matched, high-value resistors [15] (in the range of 0.1–1 M Ω). Here, 0.01% tolerance 100 k Ω resistors were used. With the feedback on, the output current is continuously monitored via sensing resistor R_{sense} (inserted twice for output symmetry) and the sensing instrumentation amplifier U5, with gain A_{v_sense} , designed so that its output equals the MEHCS input voltage:

$$A_{v_sense} = \frac{1}{g_{m*R_{sense}}}$$
 7.12

The output current is now derived by replacing V_{in} with V_{track} in (7.10). V_{track} is the output of the AGC stage, comprised of two precision peak detectors ($U_{1,2}$ and $U_{3,4}$ combined with R_{r1-3} , $C_{r1,2}$, and D_{1-4}); a comparator (U6); an integrator (R_{int} , C_{int}); and a VGA realised through an AD734 multiplier that is fully AC coupled to a cut off frequency 10MHz to remove any DC offsets and set to a unity base gain through a 1V DC reference to avoid a multiplication by zero. The equation governing the multiplication by AD734 multiplier is as shown in eq.713

$$W = \frac{(X_1 - X_2) * (Y_1 - Y_2)}{(U_1 - U_2)} + Z_2$$
7.13

Where W is the multiplier output

$$U_1 = 1V$$
, $X_1 = V_{in}$, $Y_1 = Integrator output$, $X_2 = Y_2 = U_2 = 0$.

The AGC continuously monitors and compares the peak values of both V_{in} and V_{sense} . If the amplitude of I_{out} (i.e., V_{sense}) starts dropping, the comparator output becomes high, causing the integrator output to ramp up, effectively increasing V_{track} . Once the feedback achieves $V_{sense} = V_{in}$, the comparator starts oscillating, causing V_{int} to stabilise to a settled value.

Additionally, the AGC was designed with an overcompensation stage consisting of a differential amplifier with a gain of 200, set to output a voltage of 2 V for a differential input of 10 mV—the typical turn-on threshold for an N-channel MOSFET 2N7000. While this may be redundant under normal conditions, it becomes effective in cases where the AGC overcompensates or experiences an overshoot.

The measured voltage V_{meas} across the load Z_L is given by U11, the measuring instrumentation amplifier, with a gain of A_{V_meas} .

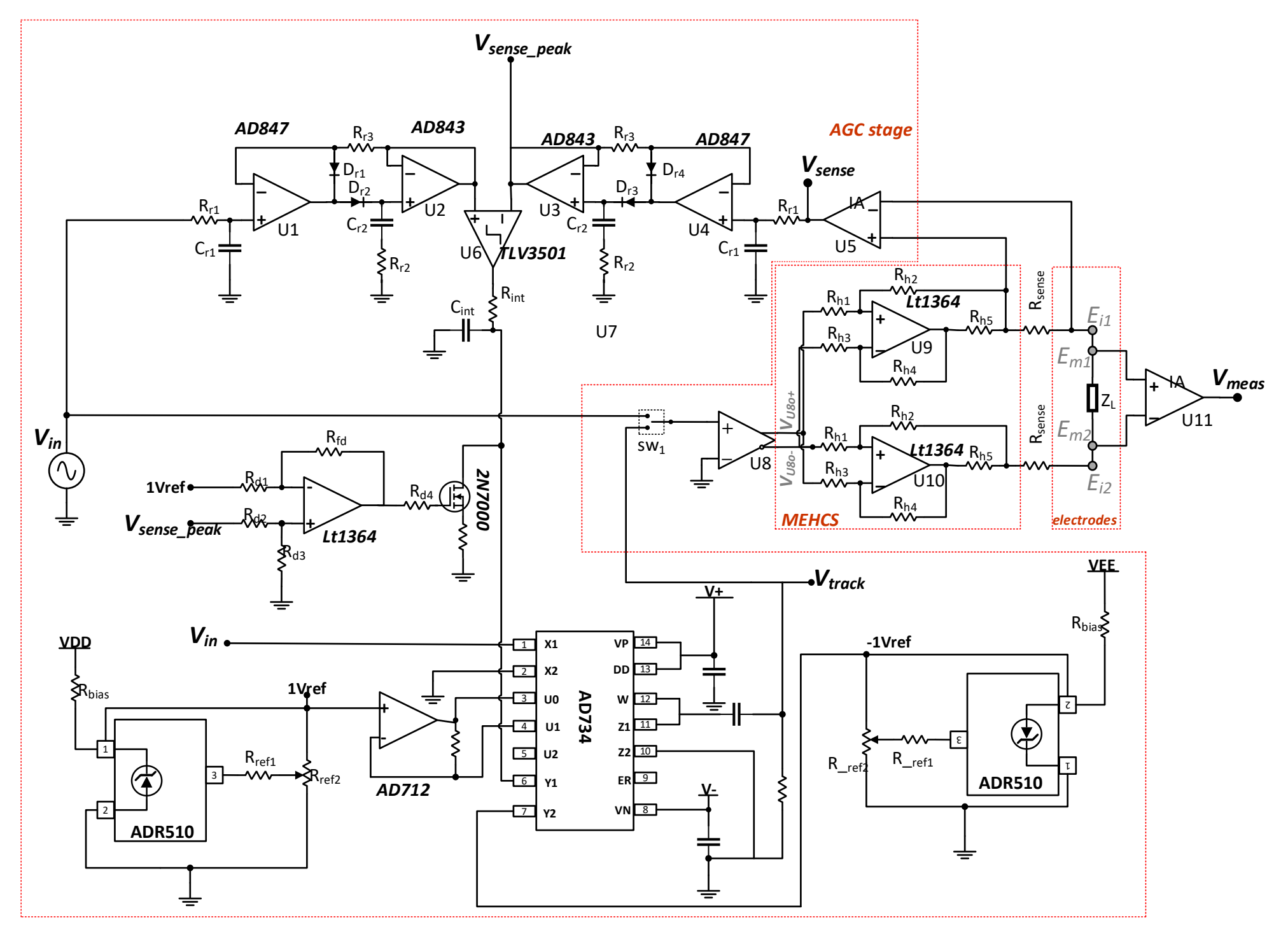


Figure 7. 3 Circuit Diagram of AHCS

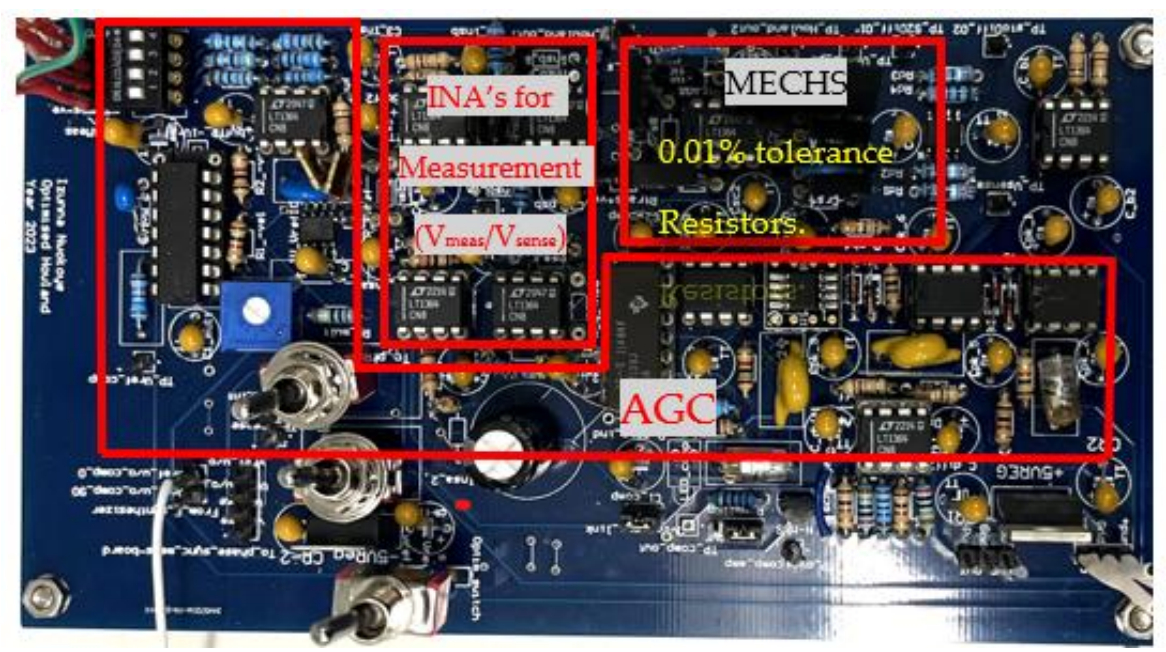


Figure 7. 4 Photograph of the AHCS circuit board with the main stages labelled.

7.6 ACHS Results and discussions

7.6.1 Frequency response

ACHS was tested for a range of resistive loads, the raw data presented in Figure 7.5 for the open-loop configuration (MEHCS) at 1 kHz for a 2 k Ω load and an output current I_{out} of 1 mA indicate that the amplitudes of V_{sense} and V_{meas} were respectively 1 V and 2 V, as expected. However, as shown in Table 1, their amplitudes decline at higher frequencies due to the degradation of output impedance, as described in the literature.

This is shown in Figure. 7.5b for 3 MHz, where $V_{sense} \neq V_{in}$ and V_{sense} , V_{meas} reached approximately half of their nominal values, indicating a reduction of approximately 50% in the amplitude of the generated current. However, when the AGC was enabled, the multiplier output amplitude V_{track} increased to compensate for the observed loss in I_{out} . This compensation continues until $V_{sense} = V_{in}$. At this point, the integrator ceases to charge, and V_{track} stabilises at its final value. The impact of the Automatic Gain Control (AGC) mechanism of the AHCS is demonstrated in columns 3 and 5 of Table 7.1.

Raw data for 1V pk input, 2K Ω load, 1mA \textit{I}_{out}

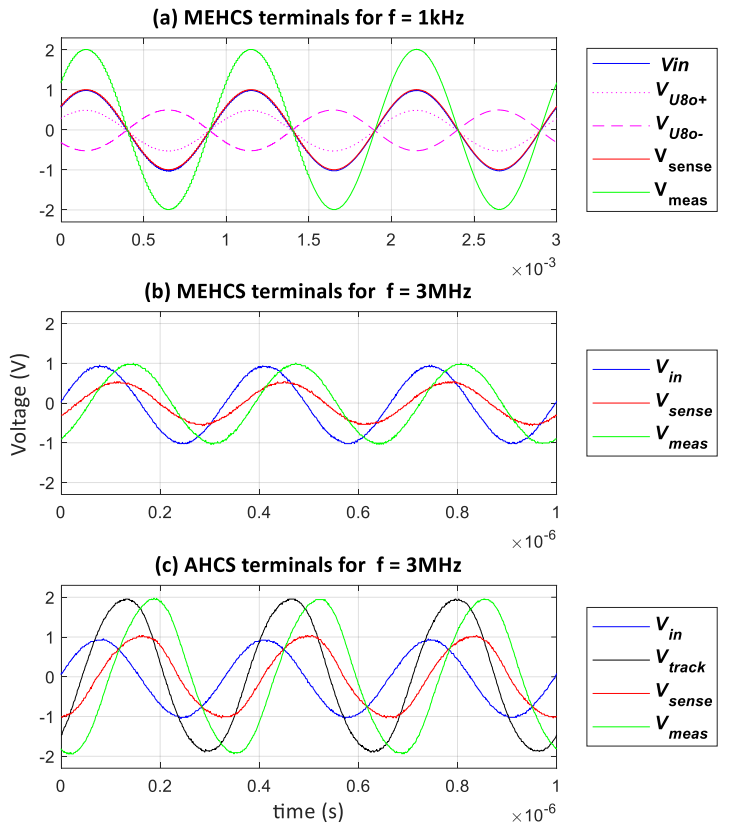


Figure 7. 5 Raw data: input and output voltages of the ACHS in open and closed loop for a 2 $k\Omega$ load

Table 7.1. MEHCS and AHCS measured peak outputs

f (Hz)	V _{sense}	_e (V)	V _{meas} (V)		
	MEHCS	AHCS	MEHCS	AHCS	
1k	1.018	1.021	2.011	2.002	
10k	1.020	1.011	2.002	2.016	
100k	1.032	1.012	2.014	2.015	
500k	0.861	1.021	1.620	2.015	
1M	0.600	1.016	1.201	2.013	
3M	0.211	1.001	0.480	2.011	

Table 7. 1 MEHCS and AHCS measured peak outputs for Load = 2 K Ω . R_{sense} = 100 Ω . IA gains: A_{V_sense} = 10, A_{V_meas} = 1. Nominal I_{out} = 1 mA. V_{in} = 1 V

Figure 7.6 shows the output current as a function of frequency derived by dividing the measured V_{sense} with A_{V_sense} across loads ranging from 1 k Ω to 5 k Ω . Measurements were taken with an applied voltage of 1V, with and without the AGC enabled. It is evident that the injected output current of AHCS remained stable at 1 mA over a wider bandwidth than with MEHCS. This was particularly evident with a resistive load of 1 K Ω , where a bandwidth of 3

MHz was attained, in contrast to MEHCS, which achieved acceptable accuracy (≤1% error) only up to 100kHz for the same load.

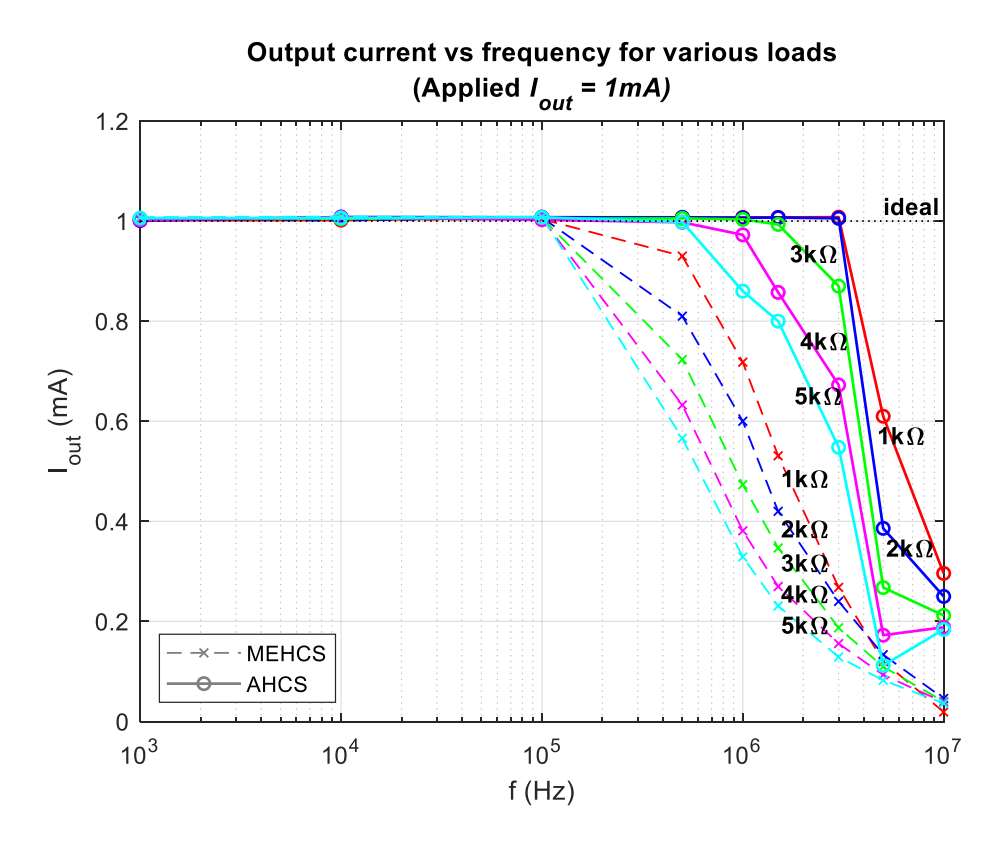


Figure 7. 6 Output current vs. frequency for various loads for MEHCS and AHCS.

This is better illustrated in Figure 7. 7, where the percentage errors of the trends in Figure 7. 6 are presented. The Figure illustrates all output current errors for loads ranging from 1 k Ω to 5 k Ω and the resulting mean error across all loads for all frequencies for the two systems. Significant errors from 100 KHz and above were observed from MEHCS compared to AHCS, for which output current decline (\geq 1%) occurred only for higher loads above 500 KHz. It could be seen that AHCS demonstrated significantly improved accuracy over a much wider bandwidth compared to the conventional MEHCS, especially for a 1 K Ω load, the load for which the highest reported bandwidth of 1 MHz was shown to be achieved with a 1.5% error in [97]. AHCS exhibited a sub-1% error for up to 3 MHz, i.e., a significantly lower error for three times the bandwidth, to our knowledge never reported before. With the same load, MEHCS recorded a 7% error at 500 KHz and 73% error at 3 MHZ. An error just above 1% was achieved for the same bandwidth of 3 MHz for a 2 K Ω load. It can be observed from Figure 7.6 and 7.7 that the AHCS performed better and accurately up to 1 MHz for all the loads and up to 3 MHZ for 1 K Ω .

Figure 7. 8 illustrates V_{meas} for MEHCS and AHCS as a function of load for specific frequencies. The data of Figure 7. 6 indicate that MEHCS exhibits inaccuracy above 100 kHz, and this is clearly illustrated in Figure 7. 8 for all loads from 500 kHz and above. This limitation in

bandwidth hinders the reliable assessment of bioimpedance tissue properties for a wide range of samples when using MEHCS. In contrast, the implementation of AHCS compensates for these limitations and delivers well-manifested improvement in bandwidth performance. The voltage responses obtained using AHCS remained accurate for all loads up to frequencies of 500 kHz.

Percentage error for all loads vs frequency for 1mA output current

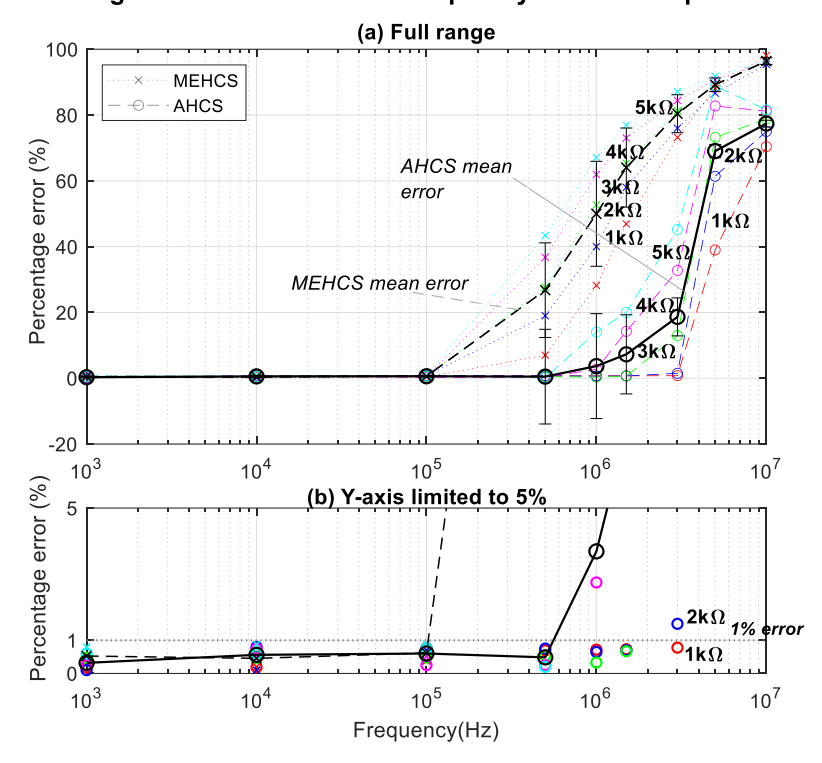


Figure 7. 7 (a) Percentage errors of 1 mA output current for MEHCS and AHCS for all loads at all frequencies and (b) scaled to 5%.

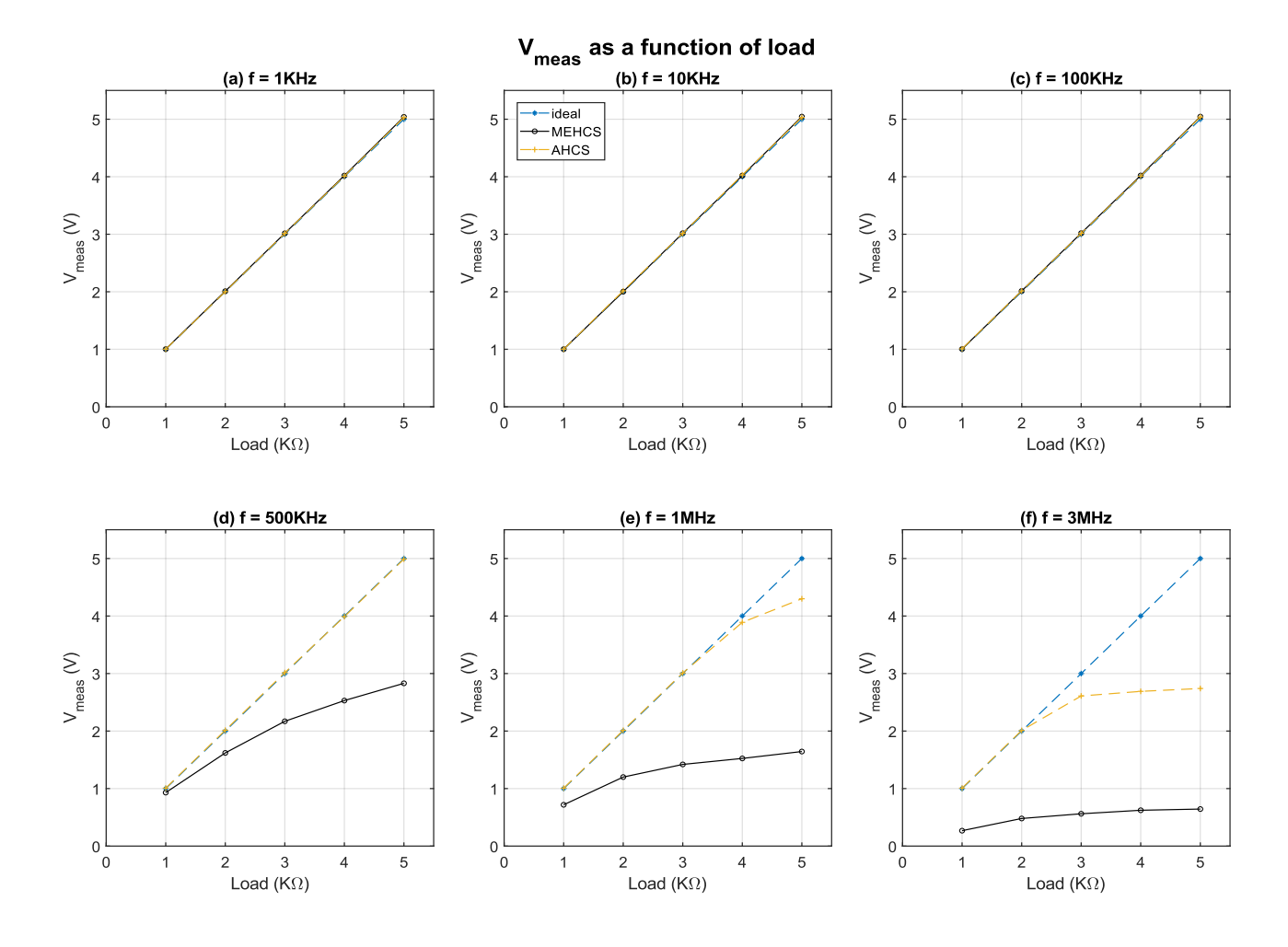


Figure 7. 8 Measured output voltage of MEHCS and AHCS compared to the ideal result as a function of load at frequencies from 1 kHz to 3 MHz for lout=1mA.

7.6.2 ACHS Performance for Smaller Output Current

The expanded bandwidth capability enables precise measurements of impedance across a broader range of frequencies in the β -dispersion, as mentioned previously. In addition to the above, Figure 7.8 also illustrates that AHCS exhibits exceptional accuracy even at higher frequencies, specifically up to 3MHz, for loads up to $1k\Omega$. This performance is noteworthy as it ensures reliable voltage responses and accurate bioimpedance measurements, even when these involve higher load tissues and at high frequencies, well beyond the capabilities of conventional MEHCS.

Designers of bioimpedance instrumentation prioritize output current amplitudes in the mA range, to maximize the signal strength relative to noise, and thus improve impedance measurement reliability. Nevertheless, in specific applications, e.g. in cell culture experiments, or for high contact impedance microelectrodes, sub-mA currents are necessary [137]. However, existing designs like e.g. CTVF-MEHCS cannot supply sub-mA currents ([97]).

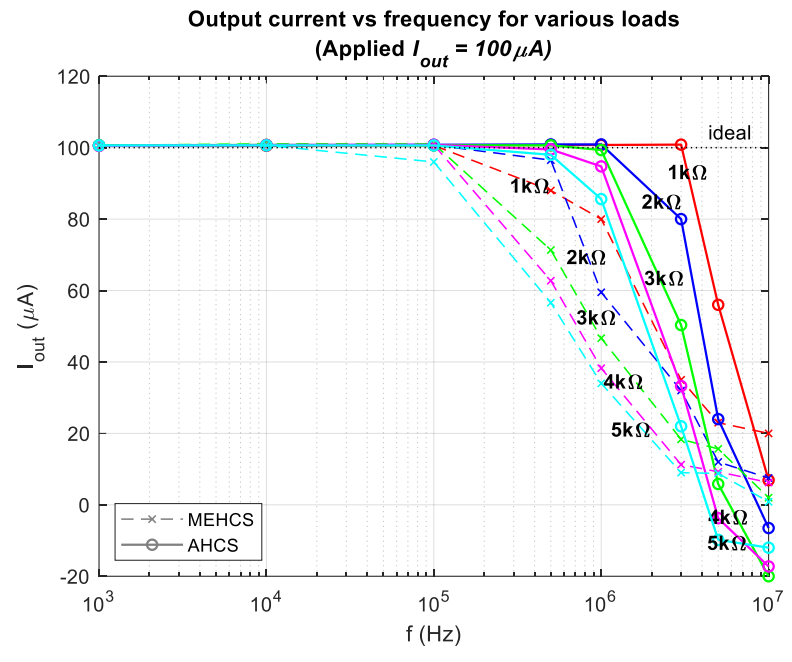


Figure 7. 9 Output current of 100 μ A as a function of frequencies for both MEHCS and AHCS.

Percentage error for all loads vs frequency for 100 μ A output current (a) Full range 120 **MEHCS** AHCS 100 80 Percentage error (%) AHCS mean error MEHCS mean error 20 0 -20 10³ 10⁴ 10⁵ 10⁷ (b) Y-axis limited to 5% Percentage error (%) 10³ 10⁴ 10⁶ 10⁵ 10⁷ Frequency(Hz)

Figure 7. 10 (a) Percentage errors of 100 μ A output current for MEHCS and AHCS and (b) scaled to low error values (up to 5%)

Figure 7.10 illustrates that AHCS enhances performance even for sub-mA currents. The accuracy and bandwidth results for AHCS are comparable for both 1mA and 100 μ A, as evidenced by the percentage error graphs in Figure 7.7 and Figure 7.10 respectively where the output current error is below 1% for 3MHz for a load of 1k Ω . In contrast, while with 1mA

 I_{out} MEHCS achieved below 1% percentage error all loads at 100kHz (Figure. 7.7), Figure. 7.10 indicates that when sourcing 100µA at the same frequency errors up to 4% were observed.

7.6.3 Output Impedance of MECHS and ACHS compared: Fully differential measurements.

The performance of the AHCS, demonstrated for a range of frequencies and loads, is based on the AGC essentially adjusting I_{out} to compensate for output current losses due to output impedance decay with frequency. Still, the measurement of the system's output impedance over the full bandwidth is of interest for comparison with prior state of art. Assuming a high op-amp open loop gain and very low and equal resistor tolerances, the minimum output impedance $Z_{O,min}$ for a single ended MEHCS can be calculated as in eq. (7.14) [96], [129]:

$$Z_{0,min}(\gamma) = \frac{R*R_{h5}}{2\gamma(R+R_{h5})}$$
 7.14

assuming that $R_{h1} = R_{h2} = R_{h3} = R_{h4} = R$. The factor γ represents resistor tolerances. Measuring the output impedance of MEHCS is a complicated procedure and often inaccurate. This is because the output impedance is conventionally derived through measurements between one output terminal and ground, in accordance to modelling the circuit as two single ended HCS current sources in series as shown in Figure 7.11(a).

As such the total impedance is then calculated as twice the measured single-ended output impedance [25], represented in Figure 7.11 (a) by $Z_{out1,2}$. According to [97] this can lead to errors.

Here, I initially attempted to measure the full differential Z_O using the E4980A precision LCR meter / impedance analyser, but the measurement was erroneous in low frequencies due to the MEHCS/AHCS output stage essentially connected as open circuit with the power on. Therefore, a different approach was adopted to achieve a more accurate measurement. A known, well-characterised resistive load $Z_L = 999~\Omega$ was connected at the output of the MEHCS/AHCS to ensure the output stage operates as a closed-circuit Norton equivalent, and the input to the system was grounded. Using the E4980A a measurement of $Z_T = Z_O || Z_L$ was carried out from 20Hz to 1MHZ as illustrated in Figure 7.11(b). This was done with both the AGC disabled (MEHCS) and enabled (AHCS), allowing for the output impedances of both MEHCS and AHCS to be derived from eq. (7.15) and generating the data for Figure 7.12.

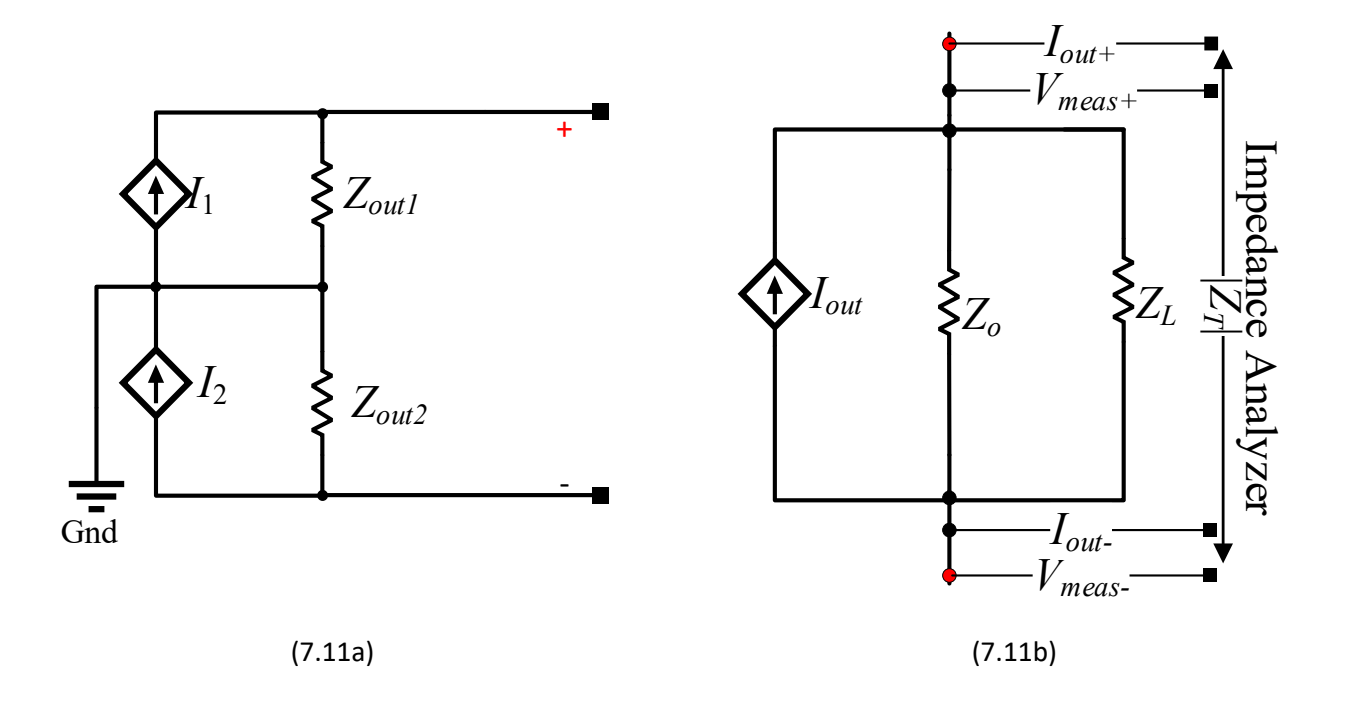


Figure 7. 11 (a) Equivalent MEHCS output impedance circuit and (b) The Measurement configuration.

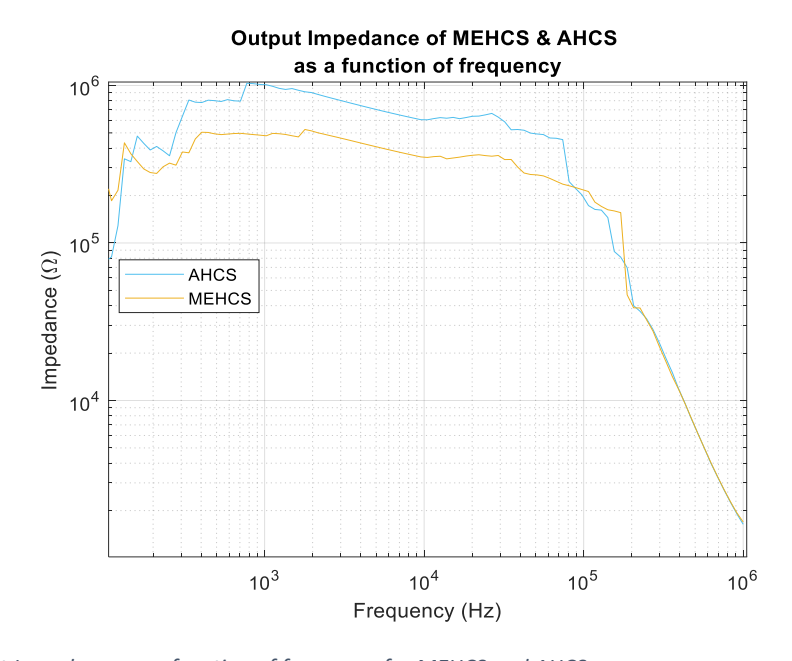


Figure 7. 12 Output Impedance as a function of frequency for MEHCS and AHCS

$$Z_0 = \frac{Z_T Z_L}{Z_L - Z_T} \tag{7.15}$$

It can be observed from the results in Figure.7. 12 that both MEHCS and AHCS exhibited a similar trend, with AHCS exhibiting higher output impedance at lower frequencies, up to 100 kHz.

7.7 ACHS Tracking Speed.

The response time of HCS based designs mostly depends on the settling time of the op-amps used (in absence of feedback capacitors). ACHS exhibits longer response time following abrupt input amplitude changes because of the AGC's integrator (here τ = 12ms). In Figure. 7.13, the integrator's settling time was measured to be 42.2ms at maximum V_{in} bandwidth (3MHz) with a typical load (1k Ω) with the feedback off and then on. It is noteworthy that this may not be a significant concern in most bioimpedance applications. Exceptions include applications where fast changes need to be monitored (e.g. plethysmography [105], [138]) or where specific frame rates across multiple channels are required (e.g. electrical impedance tomography (EIT [113]).

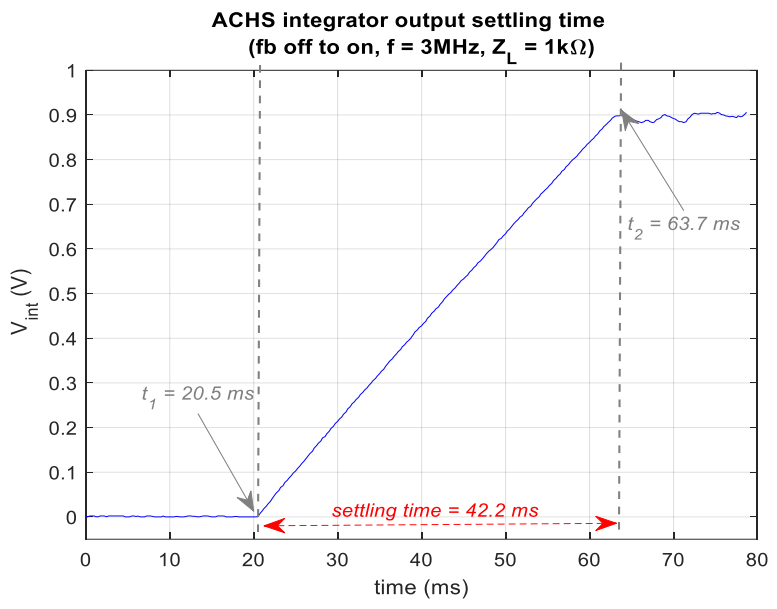


Figure 7. 13 AHCS settling time at its highest operating frequency of 3MHz.

7.8 Noise analysis of ACHS and MEHCS.

As mentioned previously, MECHS requires Rh1-4 to be in the order of $0.1-1M\Omega$, which results in increased thermal noise. During our performance analysis of AHCS it became apparent that with the AGC improving output current accuracy over a higher bandwidth independently of the system's output impedance allows for the use of lower value resistors in the MECHS substage. This reduces the overall noise exhibited at the output node. Error sources in MEHCS (Figure 7.14) can be identified through the analysis of half of the circuit (single ended HCS with grounded load). The noise sources detailed in the Figure translate to output and input referred RMS noise voltages, E_n (n,out) and E_n in respectively.

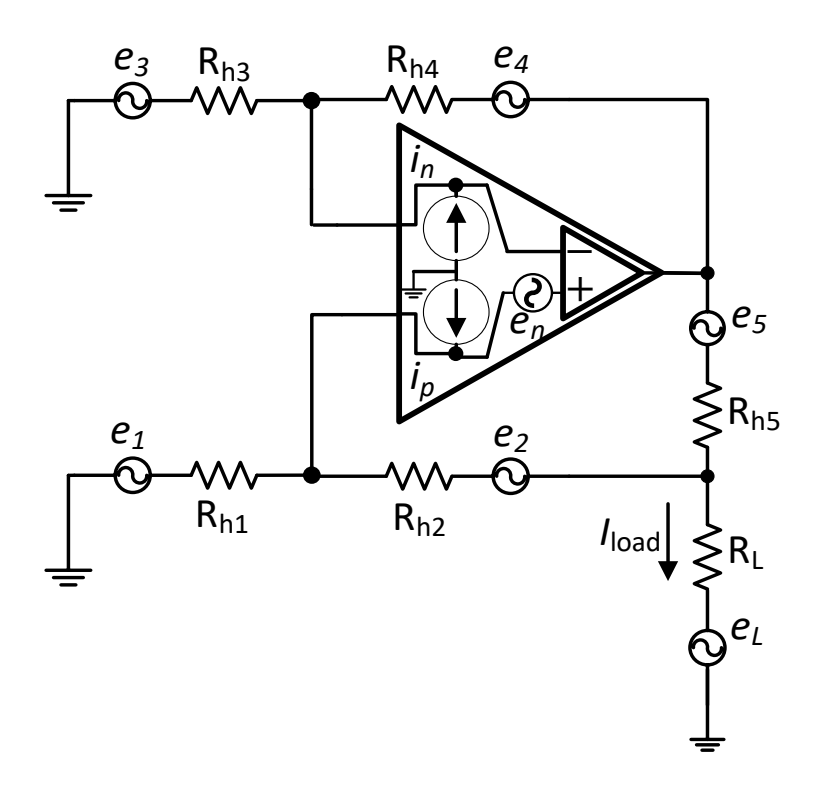


Figure 7. 14 Noise Analysis of single-ended Howland current source.

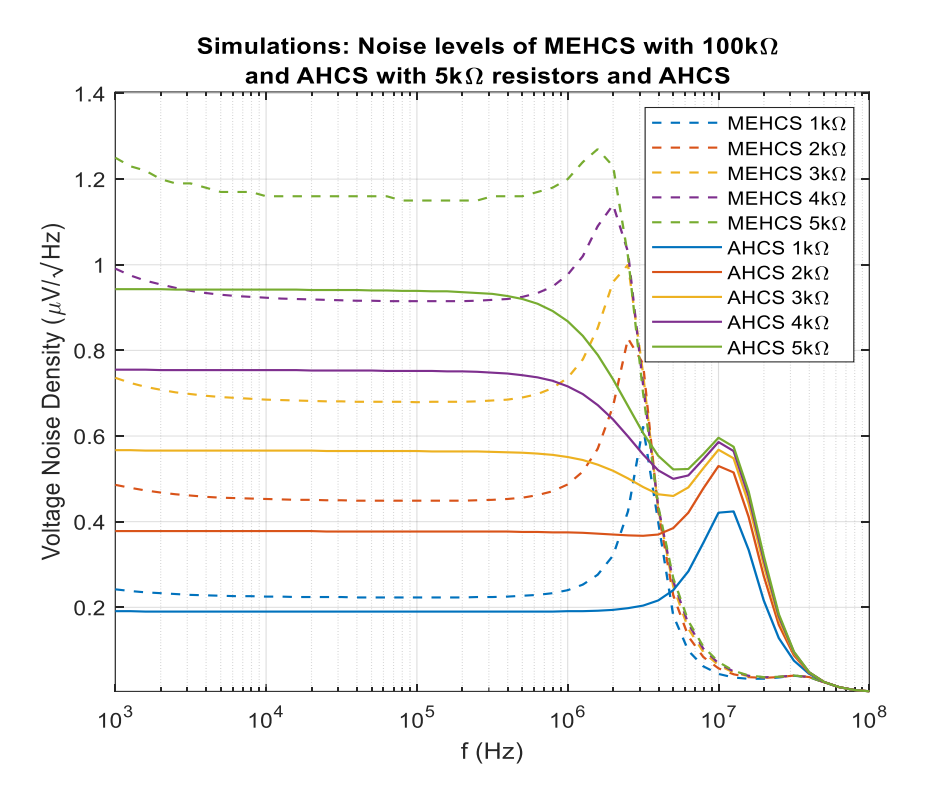


Figure 7. 15 Simulation: Voltage noise across different loads for single-ended MEHCS.

The governing equations can be seen from eq.7.16 to eq.7.28.

$$R_a = R_{h3} / / R_{h4} = \frac{R_{h3} * R_{h4}}{R_{h3} + R_{h4}}$$
 7.16

$$R_b = \left((R_{h5} / / R_L) + R_{h2} \right) / / R_{h1}. \tag{7.17}$$

$$R_b = \left(\left(\frac{R_{h5} * R_{hL}}{R_{h5} + R_{hL}} \right) + R_{h2} \right) / / R_{h1}.$$
 7.18

$$R_a = R_{h3} / / R_{h4} = \frac{R_{h3} * R_{h4}}{R_{h3} + R_{h4}}$$
 7.19

$$R_b = \left((R_{h5}//R_L) + R_{h2} \right) //R_{h1}. \tag{7.20}$$

$$R_b = \left(\left(\frac{R_{h5} * R_{hL}}{R_{h5} + R_{hL}} \right) + R_{h2} \right) / / R_{h1}.$$
 7.21

$$R_b = \frac{(R_{h5}R_{hL}R_{h1} + R_{h5}R_{h2}R_{h1} + R_{hL}R_{h2}R_{h1})(R_{h5} + R_{hL})}{(R_{h5}R_{hL} + R_{h5}R_{h2} + R_{hL}R_{h2} + R_{h5}R_{h1} + R_{hL}R_{h1})(R_{h5} + R_{hL})}$$
7.22

$$R_b = \frac{R_{h1}(R_{h5}R_{hL} + R_{h5}R_{h2} + R_{hL}R_{h2})}{(R_{h5}R_{hL} + R_{h5}R_{h2} + R_{hL}R_{h2} + R_{h5}R_{h1} + R_{hL}R_{h1})}$$
7.23

 $E_{n,in}$ has three components (eq. 7.24): the internal opamp voltage noise E_{nv} (not considered here as it is not affected by the size of R_{h3} and R_{h4}); the internal current-introduced noise E_{ni} ; and the resistor-related noise (thermal) E_{nr} (eq. 17).

$$E_{n,in} = \sqrt{E_{nv}^2 + E_{ni}^2 + E_{nr}^2} ag{7.24}$$

$$E_{ni} = \sqrt{(I_n R_a)^2 + (I_n R_b)^2}$$
 7.25

$$E_{nra} = \sqrt{4 * KT * R_a * NBW}$$
 7.26

$$E_{nrb} = \sqrt{4 * KT * R_b * NBW}$$
 7.27

$$E_{nr} = \sqrt{(E_{nra})^2 + (E_{nrb})^2}$$
 7.28

where BW_n = noise bandwidth of the op-amp, $k = 1.38 \times 10^{-23}$ J/K (Boltzmann's const.); $I_n = RMS$ noise current, and T = temperature (K).

Consequently, the total output-referred RMS noise voltage is

$$E_{n,out} = A_{v_CL} E_{ni} ag{7.29}$$

The contribution of the noise sources to the output current is

$$I_{load,TN} = \sqrt{\left(\frac{E^2_{nv} + E^2_{ni} + E^2_{nr}}{R^2_{h5}}\right)}$$
 7.30

Equations (7.25), (7.28), and (7.30) further indicates that selecting large values for R_{h3} and R_{h4} increases the noise levels in the MEHCS design. Attempting to lower the value of the R_h resistors from 100 k Ω (as used in the experiments) to 5 k Ω results in I_{out} degradation for the MEHCS. This is shown in the respective simulated I_{out} frequency responses in Figure 7 16a,

where MEHCS delivers the nominal current of 1 mA, and Figure 7. 16b, where the current delivered is lower than the nominal and changes for different loads. Figure 7. 16c indicates that the same reduction in R_h values does not affect the I_{out} frequency response of AHCS, which is 1 mA independent of load. Simulations were carried out in single-ended half-circuits with grounded loads.

Figure 7.15 demonstrates the noise spectrum for MEHS and AHCS for different loads. MEHCS is demonstrated with 100 k Ω R_h values as it is not operational for lower values, while lowering R_h values to 5 k Ω for the AHCS (still operational in Fig. 17) allows for improved noise performance, with AHCS achieving 17% lower noise for a 1k Ω load and 19% lower noise for a 5k Ω load within the bandwidth of interest

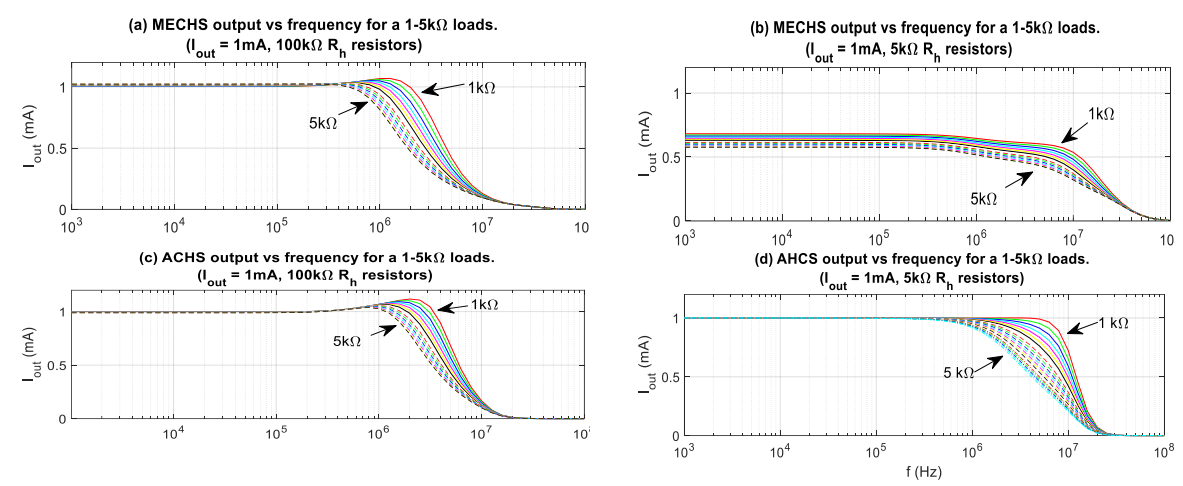


Figure 7. 16 Effects on I_{out} for lowering R_{h1-4} from (a) &(c) 100 k Ω to (b)& (d) 5 k Ω in single-ended MEHCS and AHCS.

7.9 Effects of AHCS feedback resistors Tolerance on circuit performance

The precision foil resistors used for R_{h1} – R_{h5} and R_{sense} have a TCR (temperature coefficient of resistors) of ± 2.0 ppm/°C and a tolerance of $\pm 0.01\%$. Nominal and calculated values for a 1 k Ω resistance of the same type as R_{sense} are presented in Table 2 for temperatures –20 °C, 0 °C, and 40 °C.

The impact of temperature on ACHS components and particularly the current sensing resistor R_{sense} was further examined through LTSpice simulations, spanning temperatures from $-20\,^{\circ}$ C to 40 °C, with a temperature coefficient set to the specified 2.0 ppm/°C as per the precision foil resistor datasheet. The reference temperature was set at 27 °C.

$$R_a = R_{ref}(1 + TCR(T_a - T_{ref})) 7.31$$

Replacing the R_h resistors with R_{α}, calculated using Equation (7.31), AHCS was once more assessed by generating its frequency responses for a range of loads (Figure 7.17) where T_a = Ambient temperature at which the resistance is measured, TCR =Temperature coefficient of

the resistance, T_{ref} is the reference temperature. The graphs demonstrate that extreme temperature variations do not have a significant effect on the system's performance. No different existed between the simulation at the two extreme temperatures.

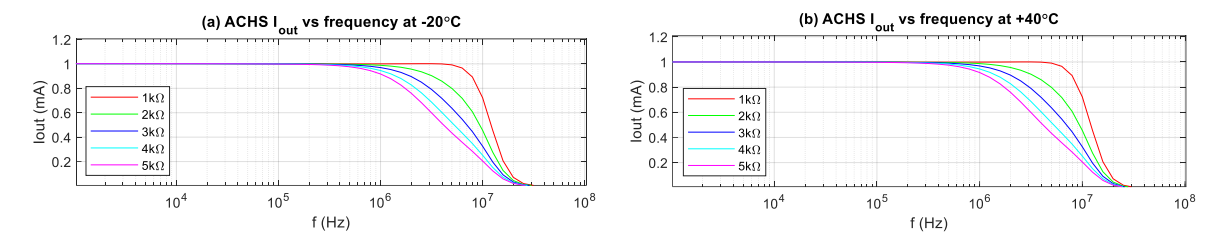


Figure 7. 17 Percentage errors of ACHS at extreme temperature variations (a) at -20° and (b) at 40°.

R_{ref} nominal (Ω)	TCR (ppm/°C)	T _a (°C)	R_a measured (Ω)
1000	2	-20	999.906
1000	2	0	999.946
1000	2	40	1000.026

Table 7. 2 Calculated resistance of the sense resistor (R_{sense}) at -20^o and 40^o extreme temperature variations

7.10 AHCS Performance Overview.

The overall performance of the AHCS system is summarised in Table 7.3, in comparison with six other architectures of AC current sources, including an ASIC approach featuring an OTA-based design. The AHCS architecture achieves a higher bandwidth than the ASIC for a less than 1% output current amplitude error. It also achieves outputs as low as 100 μ A, lower than the 500 μ A reported in [96]. The total harmonic distortion (THD) was measured to be less than 0.2% for 2 mA p-p output current. The system was also simulated with RC loads (Figure 7.18) comprising a 1 k Ω resistor in parallel with capacitors ranging from 5nF to 30nF. The bandwidth exhibited was stable for all loads.

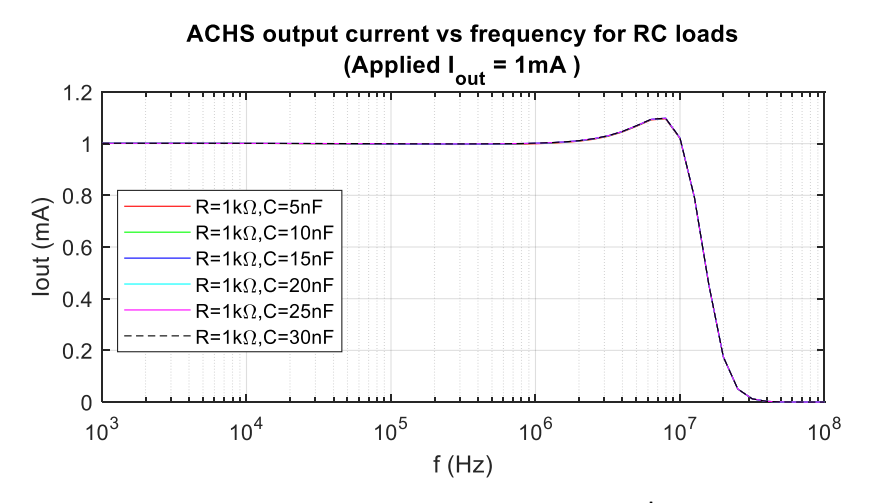


Figure 7. 18 Simulation: AHCS output current vs. frequency for RC loads (applied $I_{out} = 1 \text{ mA}$).

Main features of AHCS and comparison with other designs							
Architecture	CTVF-MEHCS [97]	EHCS [139]	Differential sinusoidal current gen. [140]	OTA - based ASIC. [59]	ACHS (This work)		
Bandwidth < 1% I _{out} err.	≤10kHz	<100Hz	90kHz	≤ 1MHz	≤ 3Mhz		
THD			0.81%@250μA _p -	0.69%@5mA _{p-p} 0.53% @ 2mA _{p-}	<0.2% @ 2mA _{p-p}		
Size and complexity			5 mm* 5 mm	6.18mm²	15.5cm*8.5 cm		
Max Output Current	2mA _{p-p}	<1.4A _{pk}	350μA _{p-p}	5mA _{p-p}	2mA _{p-p}		
Output Impedance	3.16MΩ@ 10kHz. 1.99MΩ @100kHz <32KΩ@1MHz		>100KΩ @ 90kHz	665KΩ @ 100kHz 372kΩ @ 500kHz	1MΩ @ 1kHz 200KΩ @ 100kHz. <1kΩ @1MHZ		
Output current accuracy	<1%eror @ 10kHz <2% @ 1MHz 68.5% @10MHz	<0.5% @<100Hz	≤1% @90kHz	<1%eror @ 1MHz	<1% @ 1mA @3MHz		
Supply Voltage	18V	±25V	1.25V	18V	±15V		
Technology	Discrete	Discrete	0.18μm CMOS	0.6μm CMOS HV	Discrete		
Table 7.3. Main features of AHCS and comparison with other designs Table 7.3. Main features of AHCS and comparison with other designs							

Table 7. 3 Main features of AHCS and comparison with other designs

7.11 Conclusion on chapter 7.

Conventional fixed-gain AC current source designs, commonly used in bioimpedance applications, exhibit output current amplitude decline at higher frequencies, limiting their bandwidth to around 100 kHz. Modified Enhanced Howland Current Source (MEHCS) design variants have shown promise with 1 MHz bandwidth and low output current errors of 1.5%. However, there remains a need for achieving less than 1% current errors, higher bandwidths, and operation with sub-mA currents in various bioimpedance applications, a feat not yet attained by existing optimised designs.

In this thesis, I introduced the Adaptive Howland Current Source (AHCS), which surpasses current systems by achieving sub-1% output current error over a bandwidth three times greater than the highest reported, including performance at smaller (100 μA) currents.. AHCS incorporates an Automatic Gain Control (AGC) to adapt input voltage amplitude, autonomously compensating for output current degradation. In contrast to conventional optimisation approaches, AHCS enhances accuracy across a wider bandwidth by dynamically adjusting the current driver reference voltage based on actual injected current output, offering flexibility for swept frequency applications and high performance for low amplitude currents, as needed in cell culture experiments.

AHCS's strength lies in maintaining constant amplitude AC current outputs with great accuracy over a significantly wider bandwidth, albeit with trade-offs such as increased complexity, power consumption, system size, and settling time. Despite these considerations, AHCS's wide bandwidth operation offers substantial performance improvements, making it conducive for highly accurate bioimpedance measurements at high frequencies. The envisioned applications encompass extending bioimpedance monitoring methods beyond research settings into mainstream clinical practice, assessing conditions like skin cancer.

To effectively detect skin abnormalities, such as skin cancer, it is essential for the circuit to accurately detect cells within a biological sample, particularly at higher frequencies. Chapter 8 will discuss the performance of the ACHS in biological samples, specifically by testing on lysed and unlysed blood samples.

Chapter 8

Assessment on the integrity of Blood cells using ACHS.

The application of bioimpedance for skin cancer detection depends on the instrumentation's ability to assess the integrity of biological cells. Following the evaluation of ACHS with electronic loads, it is essential to further characterize it using biological samples and benchmark its performance against a standard laboratory impedance analyzer. To achieve this, ACHS was employed to measure the impedance of in-vitro blood samples for haemolysis detection. The interface between the measuring circuit and the biological sample was established using a custom-designed PCB electrode, configurations in a square tetrapolar topology for a 6-well culture dish.

Impedance measurements were conducted with the MEHCS both with and without the implementation of the AGC feedback loop, and these results were compared to those obtained from the Agilent A4924A impedance analyzer. Haemolysis, indicating a loss of red blood cell integrity, was induced by rapid cooling of blood samples and confirmed through microscopy and haematocrit assessment. To undertake the experiments, several parameters were considered, including the electrode design as to determine the areas of best sensitivity.

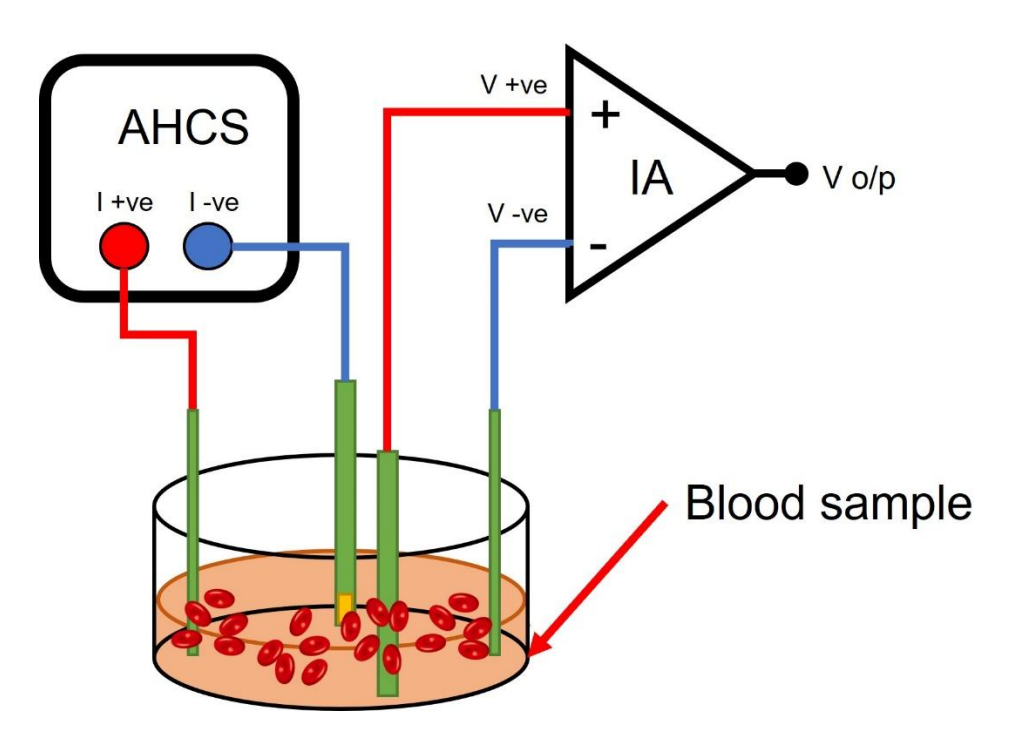


Figure 8. 1 Systematic block diagram interrogation of blood cells using ACHS

8.1 Electrode Design.

Custom electrodes were designed to fit a 6-well culture dish, enhancing previous work [141] through a PCB-based setup. The main board and electrodes were constructed from FR4 PCB material (Figure 8.2) with gold plating on the electrodes to ensure biocompatibility. The electrodes shown in Figure 8.2 are soldered onto the main board, which features connector points at one end for easy integration with external circuitry via jumper wires.



Figure 8. 2 PCB electrode setup for the 6-well culture dish

A finite element method (FEM) simulation of the electrode setup was conducted in COMSOL Multiphysics® (Figure. 8.3). The tetrapolar square electrode configuration (Figure. 8.3(a)) enhances sensitivity in the central region of the dish. The planar sensitivity distribution at the dish bottom (Figure. 8.3(b)) reveals a high-sensitivity area of 100 cm², indicating that the impedance of specimens placed within this central region will have the greatest impact on the overall measured impedance.

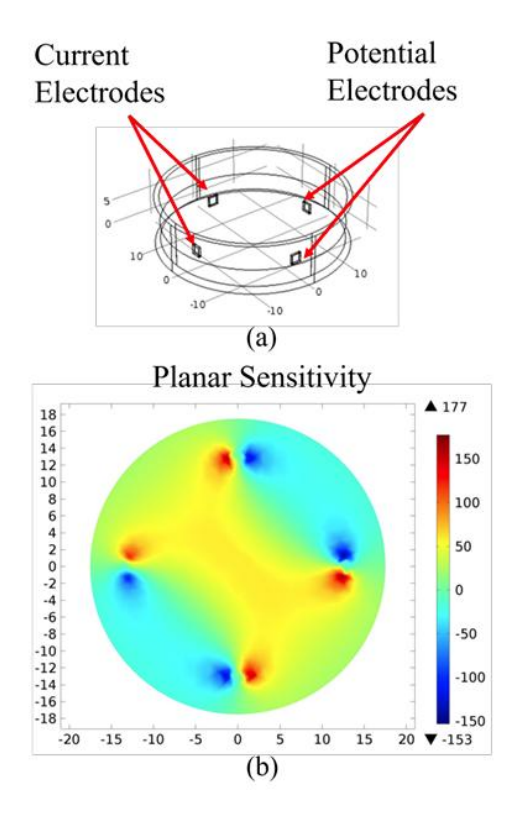


Figure 8. 3 COMSOL Multiphysics $^{\circ}$ simulation (a) Electrode configuration (b) Planar sensitivity

8.2 Blood Sample

Each sample consisted of 1.5 mL of whole human blood, treated with EDTA to prevent coagulation. Haematocrit (HCT) levels were measured using a haematology analyser (Dymind DH35). Transmission differential interference contrast (DIC) microscopy images were captured with an Amscope transmission microscope (Figure. 8.4(a)). Haemolysis was induced by freezing the blood at -80°C for 30 minutes, followed by thawing and warming to 22°C. Postlysis, HCT was measured again, and microscopy images were taken to evaluate the extent of haemolysis (Figure. 8.4(b)).

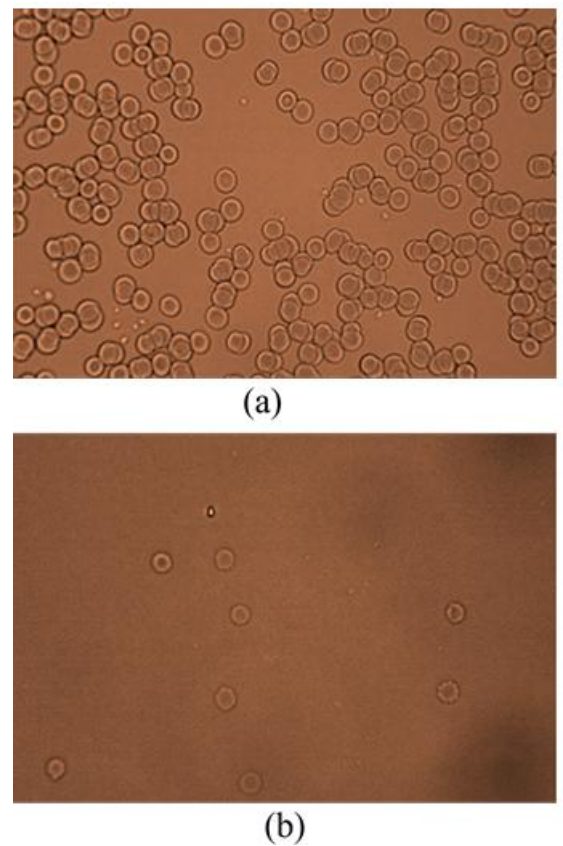


Figure 8. 4 Microscopic image of (a) whole blood (b) lysed blood

8.3 Experimental Procedure.

The electrode setup was placed in the dish so that the electrodes reached the bottom surface and 1.6 mm of the electrodes were dipped into the sample, with clean, disinfected electrodes. The sample covered the base of the culture dish and was maintained at 22°C. The setup was connected to the Agilent A4924A impedance analyser, with the injection current set to 1mA. The frequency was swept from 10kHz to 15 MHz with a bandwidth setting of 5 (high precision). Subsequently, the setup was also connected to the AHCS with a generated current Amplitude of 1mA. The Vmeas across the sample was captured using the oscilloscope. The frequency of the input signal ranged from 100 kHz to 4 MHz in decade intervals. Data from the oscilloscope was filtered in MATLAB®. The Impedance magnitude of the samples were

derived using ohms. This was repeated to determine the impedance of the blood sample following haemolysis. The set up for this experiment is further illustrated in Fig.8.5

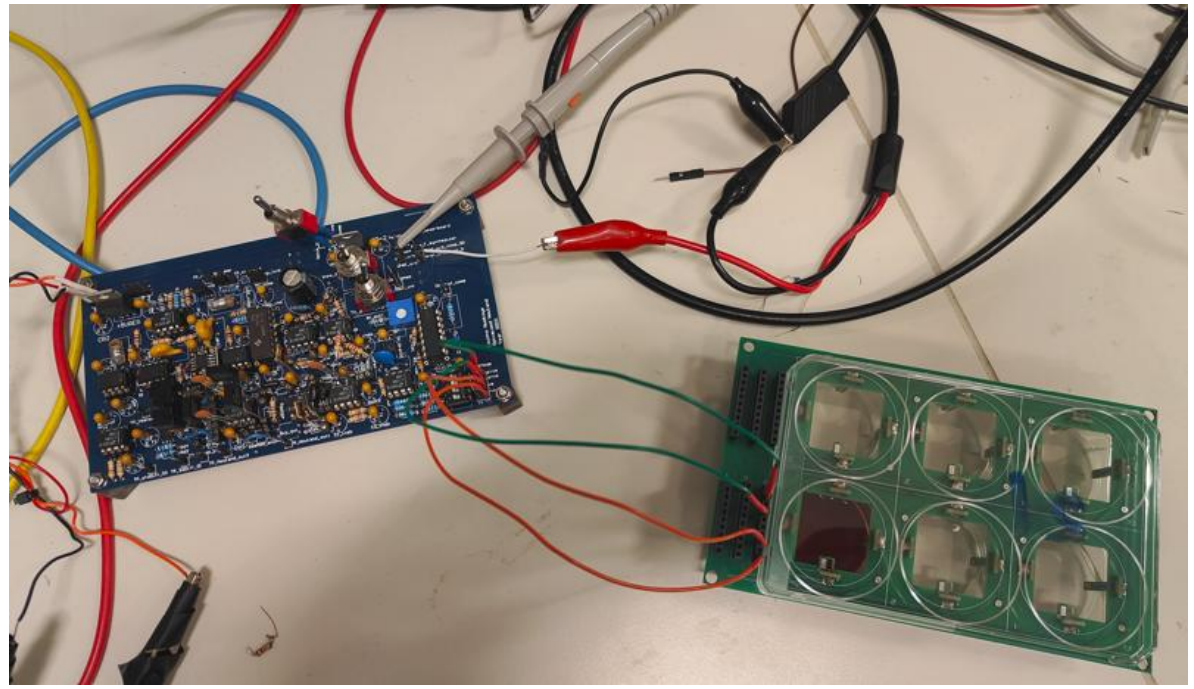


Figure 8. 5 Experimental set up featuring blood sample in one the wells, and the ACHS

8.4 Biological experimental result analysis.

The impedance of whole blood and lysed blood was measured using a standard Agilent A4924A impedance analyser over a frequency range from 100 kHz to 4 MHz. The impedance magnitude across this spectrum for both whole and lysed blood samples (S-1 and S-2) is shown in Figure 8.6. A clear difference is observed between the impedance magnitudes of whole blood and lysed blood across the frequency range, with lysed blood exhibiting higher impedance than whole blood. At approximately 5 MHz, impedance values for both whole and lysed blood converge. This distinction in impedance suggests that haemolysis can be detected through impedance measurements. Variability in impedance values at specific frequencies between the two samples likely reflects differing levels of haemolysis.

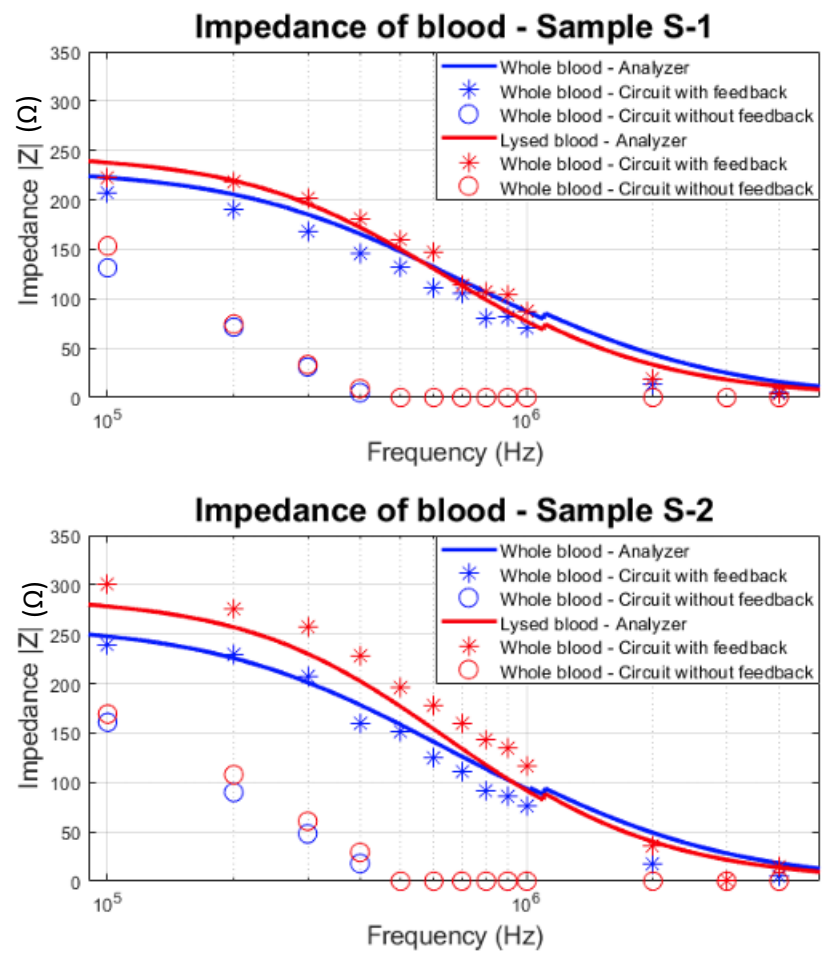


Figure 8. 6 Impedance spectrum of whole and lysed blood using the impedance analyser and the AHCS with and without feedback

The impedance of whole and lysed blood was measured using the Adaptive Howland Current Source (AHCS) over a frequency range of 100 kHz to 4 MHz Figure. 8.6 also compares the impedance measurements obtained with the AHCS (with and without AGC feedback) to those from the standard analyser. The results indicate that the circuit's performance improves with AGC feedback, showing a similar trend to the analyser's measurements at higher frequencies.

8.5 Conclusion on chapter 8.

In Chapter 8, AHCS was used as the injection side, with a front-end measurement side to assess the impedance of in-vitro blood samples for cell integrity assessment during haemolytic condition. To facilitate precise measurements, a custom-designed square tetrapolar configuration with printed circuit board (PCB) electrodes was implemented in a 6-well culture dish setup, enabling an effective interface between biological samples and the measurement circuitry.

Bioimpedance measurements were conducted under two conditions: with MEHCS and AHCS. These configurations allowed for a comprehensive evaluation of the AHCS's performance against a standard impedance analyser. Results revealed a robust correlation between the

AHCS circuit and the impedance analyser measurements, validating the AHCS's capability to reliably assess changes in the blood cells integrity.

The findings demonstrated that lysed blood samples exhibit significantly higher impedance values due to the resistive properties of the electrolyte medium in the absence of the capacitive contributions of intact cell membranes. This impedance variation, resulting from cellular breakdown, highlights the AHCS's sensitivity and confirms its capability to detect structural degradation and abnormalities within cell. Such sensitivity would be highly valuable in identifying skin-related pathologies, including skin cancer.

Chapter 9.

Conclusion on thesis.

This thesis presents a significant step forward in the design and validation of bioimpedance systems aimed at achieving more accurate, reliable, and portable solutions for skin health assessment and broader biomedical applications. Through an in-depth exploration of the limitations in current bioimpedance systems, this research proposes innovative architectures that address systematic sources of error and enhance the adaptability of bioimpedance technology for clinical and diagnostic purposes.

This thesis begins by establishing the clinical and research motivations behind improving bioimpedance technology, particularly for skin health monitoring. The introduction highlights the limitations of current bioimpedance methods, which suffer from high operator dependency, limited portability, and reduced accuracy. It sets out the primary objectives of this work, which include investigating error sources, performing systematic comparisons, conducting multimodal analyses, and advancing bioimpedance systems through phase error correction, bandwidth enhancement, and injection-side optimization. By setting these goals, this thesis emphasizes the potential of bioimpedance technology to transform non-invasive diagnostics in dermatology and other clinical fields.

Chapters 1-2 provides a theoretical exploration of bioimpedance, focusing on the electrical properties of biological tissues, with an emphasis on skin. It delves into skin anatomy and the equivalent circuit model used to represent its impedance, discussing key bioimpedance measurement configurations such as bipolar and tetrapolar setups, electrode models, and specific geometries for various applications. These insights establish the foundational understanding necessary for developing the innovative techniques presented later in the thesis.

A comparative analysis of skin hydration assessment methods is then presented in chapter 3, integrating bioimpedance and optical modalities. In addition to bioimpedance measurements, an optical sensor was developed to evaluate effectiveness alongside a conventional corneometer, the standard for hydration assessment. The results show that bioimpedance offers higher sensitivity to internal moisture levels. The multimodal approach highlights the potential of hybrid systems, providing a more comprehensive framework for skin diagnostics and offering a blueprint for future multimodal device development.

The thesis then provides an in-depth analysis of bioimpedance circuit designs and error sources in chapter 4. It explores the current injection and sensing mechanisms, comparing various Howland current source derivatives and topologies aimed at enhancing output impedance. A mathematical examination of key sources of error—such as phase shifts, frequency-dependent variations, and offset errors—is conducted to understand how these factors impact measurement accuracy. Through simulations and modeling, three bioimpedance circuit topologies are evaluated, leading to a robust understanding of error

propagation and the establishment of potential solutions and optimized circuit architectures to effectively mitigate these errors.

System-level simulations using MATLAB SIMULINK were then conducted to compare various bioimpedance configurations under simulated error conditions in chapter 5. This chapter examines configurations such as synchronous demodulation, magnitude and phase detection, and synchronous sampling, with each configuration subjected to systematic and topology-specific error simulations. The study identifies the unique strengths and limitations of each configuration, guiding the selection of an optimal bioimpedance architecture for applications like skin health assessment and cell integrity diagnostics. These findings inform the design of circuits that are optimized for diagnostic accuracy in real-world settings.

A significant contribution of this thesis is the development of a Phase Error Compensated Synchronous Demodulation (PECSD) system, which introduces automatic phase error correction to enhance measurement reliability n chapter 6. Experimental validation shows that this system reduces phase error by up to 95%, a substantial improvement over conventional bioimpedance systems that suffer from phase drift, especially at high frequencies. The PECSD system demonstrates strong performance in applications requiring high phase accuracy, such as the early detection of skin cancer, where precise phase information is essential for distinguishing malignant from healthy tissue.

To further expand bioimpedance capabilities, an Adaptive Howland Current Source (AHCS) with Automatic Gain Control (AGC) was introduced in chapter 7. The AHCS design addresses common limitations by ensuring a stable current output across a wide frequency range, which is crucial for applications requiring high-frequency stability, such as dielectric spectroscopy and detailed tissue characterization such as skin cancer. The AGC enables dynamic of the adjustments of the control drive voltage to keep the current amplitude constant, reducing errors and enhancing measurement consistency. Experimental results confirm that the AHCS system maintains accuracy and stability even at frequencies up to 3 MHz, marking a significant advancement in bioimpedance measurement systems.

The final experimental validation of AHCS systems is presented through experiment on blood samples where the integrity of blood cells were assessed by comparing the impedance of lysed and un-lysed blood cells in chapter 8. By employing a custom tetrapolar electrode configuration, distinct impedance patterns are detected, with lysed samples showing higher resistive values due to cellular breakdown. This chapter demonstrates the system's capability and versatility, suggesting its use in a variety of diagnostic applications, including tissue viability assessments as well as cell integrity assessments. The results underscore the potential of these optimized bioimpedance systems for real-time, non-invasive diagnostics in clinical settings. In conclusion, this thesis provides a substantial foundation for the development of next-generation bioimpedance systems that combine high measurement accuracy, reduced operator dependency, and adaptability across clinical applications. By addressing core issues such as phase accuracy, and bandwidth limitations, this work advances bioimpedance technology, making it a more viable and reliable tool for non-invasive diagnostics.

9.1 Future Work

Future research could focus on expanding the bandwidth of the Phase Error Compensated Synchronous Demodulation (PECSD) system to reach the MHz range. This bandwidth expansion is important as high frequencies injection reveals the conditions of the depth of the skin through which many skin conditions may be realised.

To achieve this bandwidth expansion, one promising approach would be to integrate a high-speed microcontroller capable of detecting fast pulses in the nanosecond range for the phase synchronization block. By incorporating advanced microcontrollers, the system could handle phase adjustments and performance synchronization more precisely, improving overall performance in applications where phase in a critical disease assessment factor. Additionally, the frequency synthesizer bandwidth could be further extended through careful circuit design, leveraging topologies optimized for high-frequency operations and incorporating ultra-fast clock/crystal oscillators.

Miniaturization of the entire system is another good direction for future work. By integrating components into a compact, all-in-one chip (ASIC), the system could be adapted for clinical trials and in-vivo applications, particularly in areas such as skin cancer diagnostics.

Further research should also explore the optimization of both the Adaptive Howland Current Source (AHCS) and PECSD for specific bioimpedance applications, such as dielectric spectroscopy, which requires operational frequencies up to 10 MHz. Incorporating radio frequency (RF) design techniques and adapting demodulation methods typically used in RF systems could facilitate this optimization. These would enhance measurement across a wider range of bioimpedance applications.

In summary, future research could yield transformative advancements by:

- 1. Extending PECSD bandwidth for MHz-level applications by Integrating high-speed microcontrollers for enhanced phase synchronization.
- 2. Expanding the frequency synthesizer's range by using with high-speed clock sources.
- 3. Optimizing AHCS and PECSD with RF techniques for applications up to 10 MHz.
- 4. ASIC realisations of ACHS and PECSD.

These steps would not only expand the versatility of this architecture but also establish it as a powerful breakthrough in precision medicine, supporting real-time, non-invasive diagnostics across various health care sector.

References

- [1] H. Nouri, D. Bouchaala, Y. Zhao, A. Y. Kallel, and O. Kanoun, "Load in the Loop Dual Howland Current Source for Wide Frequency Bandwidth and Wide Load Range Bioimpedance Measurements," *IEEE Trans Instrum Meas*, vol. 73, pp. 1–10, 2024, doi: 10.1109/TIM.2023.3325511.
- [2] P. Bertemes-Filho, P. B. Filho, R. G. Lima, and H. Tanaka, "An Adaptive Current Source using a Negative Impedance Converter (NIC) for Electrical Impedance Tomography (EIT) Biomechanical mdel for FESS View project Fast Electrical Biompedance Measuring System View project AN CURRENT SOURCE USING A NEGATIVE IMPEDANCE CONVERTER (NIC) FOR ELECTRICAL IMPEDANCE TOMOGRAPHY (EIT)," 2003. [Online]. Available: https://www.researchgate.net/publication/234833830
- [3] O. G. martinsen Sverre Grimmes, *Bioimpedance & Bioelectricity Basics*, 3rd ed. London UK: Elsevier Inc, 2015.
- [4] D. Naranjo-Hernández, J. Reina-Tosina, and M. Min, "Fundamentals, recent advances, and future challenges in bioimpedance devices for healthcare applications," *J Sens*, vol. 2019, 2019, doi: 10.1155/2019/9210258.
- [5] V. Narayanamurthy *et al.*, "Skin cancer detection using non-invasive techniques," *RSC Adv*, vol. 8, no. 49, pp. 28095–28130, 2018, doi: 10.1039/c8ra04164d.
- [6] J. R. González-Araiza, M. C. Ortiz-Sánchez, F. M. Vargas-Luna, and J. M. Cabrera-Sixto, "Application of electrical bio-impedance for the evaluation of strawberry ripeness," *Int J Food Prop*, vol. 20, no. 5, pp. 1044–1050, 2017, doi: 10.1080/10942912.2016.1199033.
- [7] L. M. Roa *et al.*, "Applications of bioimpedance to end stage renal disease (ESRD)," *Studies in Computational Intelligence*, vol. 404, no. 14, pp. 689–769, 2013, doi: 10.1007/978-3-642-27458-9_14.
- [8] D. C. Barber, "Electrical impedance tomography," *Biomedical Imaging*, vol. 500, no. 2, pp. 15-1-15–13, 2003, doi: 10.2174/157339809788190002.
- [9] B. Sanchez and S. B. Rutkove, "Electrical Impedance Myography and Its Applications in Neuromuscular Disorders," Jan. 01, 2017, *Springer New York LLC*. doi: 10.1007/s13311-016-0491-x.
- [10] P. C. Bolognini, C. B. Goy, M. A. G. López, and M. C. Herrera, "Tetrapolar Impedance Plethysmograph peripheral venous congestion for assessing," 2011.
- [11] M. E. Valentinuzzi, "Principles of applied biomedical instrumentation (third edition)," *J Biomed Eng*, vol. 14, no. 1, p. 86, 1992, doi: 10.1016/0141-5425(92)90043-k.
- [12] P. Åberg, I. Nicander, J. Hansson, P. Geladi, U. Holmgren, and S. Ollmar, "Skin cancer identification using multifrequency electrical impedance A potential screening tool," *IEEE Trans Biomed Eng*, vol. 51, no. 12, pp. 2097–2102, 2004, doi: 10.1109/TBME.2004.836523.

- [13] S. Krishnan *et al.*, "Multimodal epidermal devices for hydration monitoring," *Microsyst Nanoeng*, vol. 3, no. 1, p. 17014, Jun. 2017, doi: 10.1038/micronano.2017.14.
- [14] N. Kollias and G. N. Stamatas, "Optical non-invasive approaches to diagnosis of skin diseases," *Journal of Investigative Dermatology Symposium Proceedings*, vol. 7, no. 1, pp. 64–75, 2002, doi: 10.1046/j.1523-1747.2002.19635.x.
- [15] U. Birgersson, E. Birgersson, P. Åberg, I. Nicander, and S. Ollmar, "Non-invasive bioimpedance of intact skin: Mathematical modeling and experiments," *Physiol Meas*, vol. 32, no. 1, pp. 1–18, 2011, doi: 10.1088/0967-3334/32/1/001.
- [16] M. E. Darvin, "Optical Methods for Non-Invasive Determination of Skin Penetration: Current Trends, Advances, Possibilities, Prospects, and Translation into In Vivo Human Studies," *Pharmaceutics*, vol. 15, no. 9, p. 2272, Sep. 2023, doi: 10.3390/pharmaceutics15092272.
- [17] V. Narayanamurthy *et al.*, "Skin cancer detection using non-invasive techniques," *RSC Adv*, vol. 8, no. 49, pp. 28095–28130, 2018, doi: 10.1039/c8ra04164d.
- [18] "National Eczema Society." Accessed: Nov. 10, 2024. [Online]. Available: https://eczema.org/
- [19] "Eczema (Atopic Dermatitis) | Allergy UK | National Charity." Accessed: Nov. 09, 2024.
 [Online]. Available: https://www.allergyuk.org/types-of-allergies/eczema/
- [20] "Eczema: Types, Symptoms, Causes, Diagnosis, and Treatment." Accessed: Nov. 09, 2024. [Online]. Available: https://www.webmd.com/skin-problems-and-treatments/eczema/atopic-dermatitis-eczema
- [21] "Skin cancer | Cancer Research UK." Accessed: Nov. 09, 2024. [Online]. Available: https://www.cancerresearchuk.org/about-cancer/skin-cancer
- [22] H. Sung *et al.*, "Global Cancer Statistics 2020: GLOBOCAN Estimates of Incidence and Mortality Worldwide for 36 Cancers in 185 Countries," *CA Cancer J Clin*, vol. 71, no. 3, pp. 209–249, May 2021, doi: 10.3322/caac.21660.
- [23] P. Åberg, I. Nicander, J. Hansson, P. Geladi, U. Holmgren, and S. Ollmar, "Skin cancer identification using multifrequency electrical impedance A potential screening tool," *IEEE Trans Biomed Eng*, vol. 51, no. 12, pp. 2097–2102, 2004, doi: 10.1109/TBME.2004.836523.
- [24] A. Ezerskaia, S. F. Pereira, H. P. Urbach, and B. Varghese, "Infrared spectroscopic measurement of skin hydration and sebum levels and comparison to corneometer and sebumeter," J. Popp, V. V. Tuchin, D. L. Matthews, and F. S. Pavone, Eds., May 2016, p. 98872G. doi: 10.1117/12.2225434.
- [25] F. Lu *et al.*, "Review of stratum corneum impedance measurement in non-invasive penetration application," Mar. 26, 2018, *MDPI*. doi: 10.3390/bios8020031.
- [26] I. M. Gidado, M. Qassem, I. F. Triantis, and P. A. Kyriacou, "Review of Advances in the Measurement of Skin Hydration Based on Sensing of Optical and Electrical Tissue Properties," Oct. 01, 2022, MDPI. doi: 10.3390/s22197151.

- [27] P. Clarys, R. Clijsen, and A. O. Barel, "Influence of probe application pressure on in vitro and in vivo capacitance (Corneometer CM 825 ®) and conductance (Skicon 200 EX ®) measurements," *Skin Research and Technology*, vol. 17, no. 4, pp. 445–450, Nov. 2011, doi: 10.1111/j.1600-0846.2011.00516.x.
- [28] E. Alanen, J. Nuutinen, K. Nicklén, T. Lahtinen, and J. Mönkkönen, "Measurement of hydration in the stratum corneum with the MoistureMeter and comparison with the Corneometer," *Skin Research and Technology*, vol. 10, no. 1, pp. 32–37, Feb. 2004, doi: 10.1111/j.1600-0846.2004.00050.x.
- [29] S. Astner, S. Dietterle, N. Otberg, H.-J. Röwert-Huber, E. Stockfleth, and J. Lademann, "Clinical applicability of in vivo fluorescence confocal microscopy for noninvasive diagnosis and therapeutic monitoring of nonmelanoma skin cancer," *J Biomed Opt*, vol. 13, no. 1, p. 014003, 2008, doi: 10.1117/1.2837411.
- [30] C. Vinciullo *et al.*, "Photodynamic therapy with topical methyl aminolaevulinate for 'difficult-to-treat' basal cell carcinoma," *British Journal of Dermatology*, 2005, doi: 10.1111/j.1365-2133.2005.06484.x.
- [31] J. De Leeuw, N. Van der Beek, W. D. Neugebauer, P. Bjerring, and H. A. M. Neumann, "Fluorescence detection and diagnosis of non-Melanoma skin cancer at an early stage," *Lasers Surg Med*, vol. 41, no. 2, pp. 96–103, 2009, doi: 10.1002/lsm.20739.
- [32] L. Serrone, F. M. Solivetti, M. F. Thorel, L. Eibenschutz, P. Donati, and C. Catricalà, "High frequency ultrasound in the preoperative staging of primary melanoma: A statistical analysis," *Melanoma Res*, vol. 12, no. 3, pp. 287–290, 2002, doi: 10.1097/00008390-200206000-00013.
- [33] P. Guitera *et al.*, "Melanoma histological Breslow thickness predicted by 75-MHz ultrasonography," *British Journal of Dermatology*, vol. 159, no. 2, pp. 364–369, 2008, doi: 10.1111/j.1365-2133.2008.08681.x.
- [34] J. Vonk *et al.*, "Multispectral optoacoustic tomography for in vivo detection of lymph node metastases in oral cancer patients using an EGFR-targeted contrast agent and intrinsic tissue contrast: A proof-of-concept study," *Photoacoustics*, vol. 26, Jun. 2022, doi: 10.1016/j.pacs.2022.100362.
- [35] S. Laufer, A. Ivorra, V. E. Reuter, B. Rubinsky, and S. B. Solomon, "Electrical impedance characterization of normal and cancerous human hepatic tissue," *Physiol Meas*, vol. 31, no. 7, pp. 995–1009, 2010, doi: 10.1088/0967-3334/31/7/009.
- [36] N. Nishida, H. Yano, T. Nishida, T. Kamura, and M. Kojiro, "Angiogenesis in cancer," *Vasc Health Risk Manag*, vol. 2, no. 3, pp. 213–219, 2006, doi: 10.2147/vhrm.2006.2.3.213.
- [37] M. A. L. Ahmad and F. Mustafa, "Electrical Characterization of Normal and Cancer Cells," *IEEE Access*, vol. 6, pp. 25979–25986, 2018, doi: 10.1109/ACCESS.2018.2830883.
- [38] S. J. Kweon, S. Shin, J. H. Park, J. H. Suh, and H. J. Yoo, "A CMOS low-power polar demodulator for electrical bioimpedance spectroscopy using adaptive self-sampling schemes," in *Proceedings 2016 IEEE Biomedical Circuits and Systems Conference*,

- *BioCAS 2016*, Institute of Electrical and Electronics Engineers Inc., 2016, pp. 284–287. doi: 10.1109/BioCAS.2016.7833787.
- [39] M. P. Bolton *et al.*, "Sources of error in bioimpedance spectroscopy," 1998. [Online]. Available: http://iopscience.iop.org/0967-3334/19/2/011
- [40] S. Grimnes and Ø. G. Martinsen, "Sources of error in tetrapolar impedance measurements on biomaterials and other ionic conductors," in *Journal of Physics D:*Applied Physics, Jan. 2007, pp. 9–14. doi: 10.1088/0022-3727/40/1/S02.
- [41] C. Wang, X. Xin, B. Liang, Z. Li, and J. Miao, "Quadrature errors and DC offsets calibration of analog complex cross-correlator for interferometric passive millimeter-wave imaging applications," *Sensors (Switzerland)*, vol. 18, no. 2, Feb. 2018, doi: 10.3390/s18020677.
- [42] S. Abasi, J. R. Aggas, G. G. Garayar-Leyva, B. K. Walther, and A. Guiseppi-Elie, "Bioelectrical Impedance Spectroscopy for Monitoring Mammalian Cells and Tissues under Different Frequency Domains: A Review," Dec. 21, 2022, *American Chemical Society*. doi: 10.1021/acsmeasuresciau.2c00033.
- [43] Panagiotis Kassanos and Guang-Zhong Yang, "A CMOS programmable phase shifter for compensating synchronous detection bioimpedance systems," *EEE International Conference on Electronics, Circuits and Systems (ICECS)*, 2017, doi: 10.1109/ICECS.2017.8292091.
- [44] M. R. Baidillah *et al.*, "Electrical impedance spectroscopy for skin layer assessment: A scoping review of electrode design, measurement methods, and post-processing techniques," Feb. 28, 2024, *Elsevier B.V.* doi: 10.1016/j.measurement.2023.114111.
- [45] M. R. Baidillah *et al.*, "Electrical impedance spectroscopy for skin layer assessment: A scoping review of electrode design, measurement methods, and post-processing techniques," Feb. 28, 2024, *Elsevier B.V.* doi: 10.1016/j.measurement.2023.114111.
- [46] R. Pradhan, A. Mitra, and S. Das, "Characterization of electrode/electrolyte interface for bioimpedance study," *TechSym 2011 Proceedings of the 2011 IEEE Students' Technology Symposium*, pp. 275–280, 2011, doi: 10.1109/TECHSYM.2011.5783829.
- [47] R. Pradhan, A. Mitra, and S. Das, "Characterization of electrode/electrolyte interface for bioimpedance study," *TechSym 2011 Proceedings of the 2011 IEEE Students' Technology Symposium*, pp. 275–280, 2011, doi: 10.1109/TECHSYM.2011.5783829.
- [48] WHO guidelines on hand hygiene in health care: first global patient safety challenge: clean care is safer care. WHO, 2010.
- [49] M. R. Baidillah, M. Sifuna, D. Kawashima, and M. Takei, "distribution in lower leg fat tissue using Electrical Impedance Tomography Investigation of the effect of varying water content on conductivity distribution in lower leg fat tissue using Electrical Impedance Tomography," no. July, 2019.
- [50] D. Naranjo-Hernández, J. Reina-Tosina, and M. Min, "Fundamentals, Recent Advances, and Future Challenges inBioimpedance Devices for Healthcare Applications," *J Sens*, vol. 2019, 2019, doi: 10.1155/2019/9210258.

- [51] O. G. martinsen Sverre Grimmes, *Bioimpedance & Bioelectricity Basics*, 3rd ed. London UK: Elsevier Inc, 2015.
- [52] M. Ibrani, L. Ahma, and E. Hamiti, "The Age-Dependence of Microwave Dielectric Parameters of Biological Tissues," in *Microwave Materials Characterization*, InTech, 2012. doi: 10.5772/51400.
- [53] U. Pliquett, "Bioimpedance: A review for food processing," *Food Engineering Reviews*, vol. 2, no. 2, pp. 74–94, Jun. 2010, doi: 10.1007/s12393-010-9019-z.
- [54] O. G. M. Sverre Grimnes, *Bioimpedance and Bioelectricity Basics*, United Kin. London: Elsevier Inc, 2015.
- [55] T. K. Bera, J. Nagaraju, and G. Lubineau, "Electrical impedance spectroscopy (EIS)-based evaluation of biological tissue phantoms to study multifrequency electrical impedance tomography (Mf-EIT) systems," *J Vis (Tokyo)*, vol. 19, no. 4, pp. 691–713, 2016, doi: 10.1007/s12650-016-0351-0.
- [56] X. Bai *et al.*, "Electrical impedance analysis of pork tissues during storage," *Journal of Food Measurement and Characterization*, vol. 12, no. 1, pp. 164–172, Mar. 2018, doi: 10.1007/s11694-017-9627-x.
- [57] J. L. Damez, S. Clerjon, S. Abouelkaram, and J. Lepetit, "Dielectric behavior of beef meat in the 1-1500 kHz range: Simulation with the Fricke/Cole-Cole model," *Meat Sci*, vol. 77, no. 4, pp. 512–519, Dec. 2007, doi: 10.1016/j.meatsci.2007.04.028.
- [58] Panagiotis Kassanos, Iasonas F. Triantis, and Andreas Demosthenous, "A CMOS Magnitude / Phase Measurement Chip for Impedance Spectroscopy," *Institute of Electrical and Electronics Engineers (IEEE) Sensor*, vol. 13, no. 6, pp. 2229–2236, 2013, doi: 10.1109/JSEN.2013.2251628.
- [59] L. Constantinou, I. F. Triantis, R. Bayford, and A. Demosthenous, "High-power CMOS current driver with accurate transconductance for electrical impedance tomography," *IEEE Trans Biomed Circuits Syst*, vol. 8, no. 4, pp. 575–583, 2014, doi: 10.1109/TBCAS.2013.2285481.
- [60] C. Conference, "Classical Models of the Interface between an Electrode and Electrolyte M.Sc. Ekaterina Gongadze," *Biomaterials*, 2009.
- [61] K. B. Oldham, "A Gouy-Chapman-Stern model of the double layer at a (metal)/(ionic liquid) interface," *Journal of Electroanalytical Chemistry*, vol. 613, no. 2, pp. 131–138, Feb. 2008, doi: 10.1016/j.jelechem.2007.10.017.
- [62] K. Dudzinski, M. Dawgul, K. D. Pluta, B. Wawro, W. Torbicz, and D. G. Pijanowska, "Spiral Concentric Two Electrode Sensor Fabricated by Direct Writing for Skin Impedance Measurements," *IEEE Sens J*, vol. 17, no. 16, pp. 5306–5314, Aug. 2017, doi: 10.1109/JSEN.2017.2719001.
- [63] P. Kassanos, "Bioimpedance Sensors: A Tutorial," *IEEE Sens J*, vol. 21, no. 20, pp. 22190–22219, Oct. 2021, doi: 10.1109/JSEN.2021.3110283.
- [64] I. M. Gidado, I. I. Nwokoye, I. F. Triantis, M. Qassem, and P. A. Kyriacou, "Multi-Modal Spectroscopic Assessment of Skin Hydration," *Sensors*, vol. 24, no. 5, p. 1419, Feb. 2024, doi: 10.3390/s24051419.

- [65] Y. M. Chi, T. P. Jung, and G. Cauwenberghs, "Dry-contact and noncontact biopotential electrodes: Methodological review," *IEEE Rev Biomed Eng*, vol. 3, pp. 106–119, 2010, doi: 10.1109/RBME.2010.2084078.
- [66] R. R. Khan and S. W. Kang, "Highly sensitive multi-channel IDC sensor array for low concentration taste detection," *Sensors (Switzerland)*, vol. 15, no. 6, pp. 13201–13221, Jun. 2015, doi: 10.3390/s150613201.
- [67] A. R. Todorov, R. Torah, M. Ardern-Jones, and S. Beeby, "Fabrication of a Screen-Printed E-Textile Interdigitated Capacitive Sensor for Measuring Stratum Corneum Hydration †," *Engineering Proceedings*, vol. 52, no. 1, 2024, doi: 10.3390/engproc2023052001.
- [68] "Fig 2 Electrical equivalent model for the total impedance in a two electrode system B) Calculation of Skin-to-Electrode Impedance Fig 4 Agarose Skin Analog Bilayer Model, with CRE resting on top layer."
- [69] T. Songkakul, S. Wu, P. Ahmmed, W. D. Reynolds, Y. Zhu, and A. Bozkurt, "Wearable Bioimpedance Hydration Monitoring System using Conformable AgNW Electrodes," in *Proceedings of IEEE Sensors*, Institute of Electrical and Electronics Engineers Inc., 2021. doi: 10.1109/SENSORS47087.2021.9639469.
- [70] S. D. Campbell, K. K. Kraning, E. G. Schibli, and S. T. Momi, "Hydration characteristics and electrical resistivity of stratum corneum using a noninvasive four-point microelectrode method," J. Invest. Dermatol., vol. 69, no. 3, pp. 290–295, 1977, doi: 10.1111/1523-1747.ep12498927.
- [71] Seward B, "Electrical Impedance Myography: Background, Current State, and Future Directions," *Muscle Nerve*, vol. 40, no. 6, pp. 936–946, 2009, doi: 10.1002/mus.21362.Electrical.
- [72] S. B. Rutkove, R. A. Partida, G. J. Esper, R. Aaron, and C. A. Shiffman, "Electrode position and size in electrical impedance myography," *Clinical Neurophysiology*, vol. 116, no. 2, pp. 290–299, 2005, doi: 10.1016/j.clinph.2004.09.002.
- [73] G. J. Esper, C. A. Shiffman, R. Aaron, K. S. Lee, and S. B. Rutkove, "Assessing neuromuscular disease with multifrequency electrical impedance myography," *Muscle Nerve*, vol. 34, no. 5, pp. 595–602, 2006, doi: 10.1002/mus.20626.
- [74] R. H. Bayford, "Bioimpedance Tomography (Electrical Impedance Tomography)," *Annu Rev Biomed Eng*, vol. 8, no. 1, pp. 63–91, 2006, doi: 10.1146/annurev.bioeng.8.061505.095716.
- [75] M. Amini, J. Hisdal, and H. Kalvøy, "Applications of bioimpedance measurement techniques in tissue engineering," *J Electr Bioimpedance*, vol. 9, no. 1, pp. 142–158, Dec. 2018, doi: 10.2478/joeb-2018-0019.
- [76] A. Albulbul and A. D. C. Chan, "Electrode-skin impedance changes due to an externally applied force," in 2012 IEEE International Symposium on Medical Measurements and Applications Proceedings, IEEE, May 2012, pp. 1–4. doi: 10.1109/MeMeA.2012.6226628.

- [77] E. Priidel *et al.*, "Methods for Detection of Bioimpedance Variations in Resource Constrained Environments," *Sensors*, vol. 20, no. 5, p. 1363, Mar. 2020, doi: 10.3390/s20051363.
- [78] M. Hantschke and I. F. Triantis, "Modeling the Impact of Sensitivity Distribution Variations of Tetrapolar Impedance Configurations in Microfluidic Analytical Devices," *IEEE Sens J*, vol. 21, no. 2, pp. 1655–1664, Jan. 2021, doi: 10.1109/JSEN.2020.3019170.
- [79] Ali Imam Sunny *et al.*, "Feasibility Experiments to Detect Skin Hydration Using a BioImpedance Sensor," 2019, pp. 1–4.
- [80] F. Bibi, M. Villain, C. Guillaume, B. Sorli, and N. Gontard, "A Review: Origins of the Dielectric Properties of Proteins and Potential Development as Bio-Sensors," *Sensors*, vol. 16, no. 8, p. 1232, Aug. 2016, doi: 10.3390/s16081232.
- [81] "Conductivity Sensor For various conductivity measurement applications." [Online]. Available: www.ist-ag.com
- [82] P. Oltulu, B. Ince, N. Kokbudak, S. Findik, and F. Kilinc, "Measurement of epidermis, dermis, and total skin thicknesses from six different body regions with a new ethical histometric technique," *Turkish Journal of Plastic Surgery*, vol. 26, no. 2, p. 56, 2018, doi: 10.4103/tjps.TJPS_2_17.
- [83] K. Chopra *et al.*, "A Comprehensive Examination of Topographic Thickness of Skin in the Human Face," *Aesthet Surg J*, vol. 35, no. 8, pp. 1007–1013, Nov. 2015, doi: 10.1093/asj/sjv079.
- [84] S. Jain, K. Pandey, A. Lahoti, and Pk. Rao, "Evaluation of skin and subcutaneous tissue thickness at insulin injection sites in Indian, insulin naïve, type-2 diabetic adult population," *Indian J Endocrinol Metab*, vol. 17, no. 5, p. 864, 2013, doi: 10.4103/2230-8210.117249.
- [85] I. Medina, S. Scholl, and M. Rädle, "Film Thickness and Glycerol Concentration Mapping of Falling Films Based on Fluorescence and Near-Infrared Technique," Micromachines (Basel), vol. 13, no. 12, p. 2184, Dec. 2022, doi: 10.3390/mi13122184.
- [86] Thorlabs, "Calcium Fluoride Windows," *Thorlabs*, [Online]. Available: https://www.thorlabs.com/newgrouppage9.cfm?objectgroup_id=3978. [Accessed: Sep. 6, 2024].
- [87] K. Budidha, V. Rybynok, and P. A. Kyriacou, "Design and Development of a Modular, Multichannel Photoplethysmography System," *IEEE Trans Instrum Meas*, vol. 67, no. 8, pp. 1954–1965, Aug. 2018, doi: 10.1109/TIM.2018.2810643.
- [88] R. Kong and R. Bhargava, "Characterization of porcine skin as a model for human skin studies using infrared spectroscopic imaging," *Analyst*, vol. 136, no. 11, p. 2359, 2011, doi: 10.1039/c1an15111h.
- [89] S. Yao *et al.*, "A Wearable Hydration Sensor with Conformal Nanowire Electrodes," *Adv Healthc Mater*, vol. 6, no. 6, Mar. 2017, doi: 10.1002/adhm.201601159.
- [90] M. Morin et al., "Skin hydration dynamics investigated by electrical impedance techniques in vivo and in vitro," Sci Rep, vol. 10, no. 1, Dec. 2020, doi: 10.1038/s41598-020-73684-y.

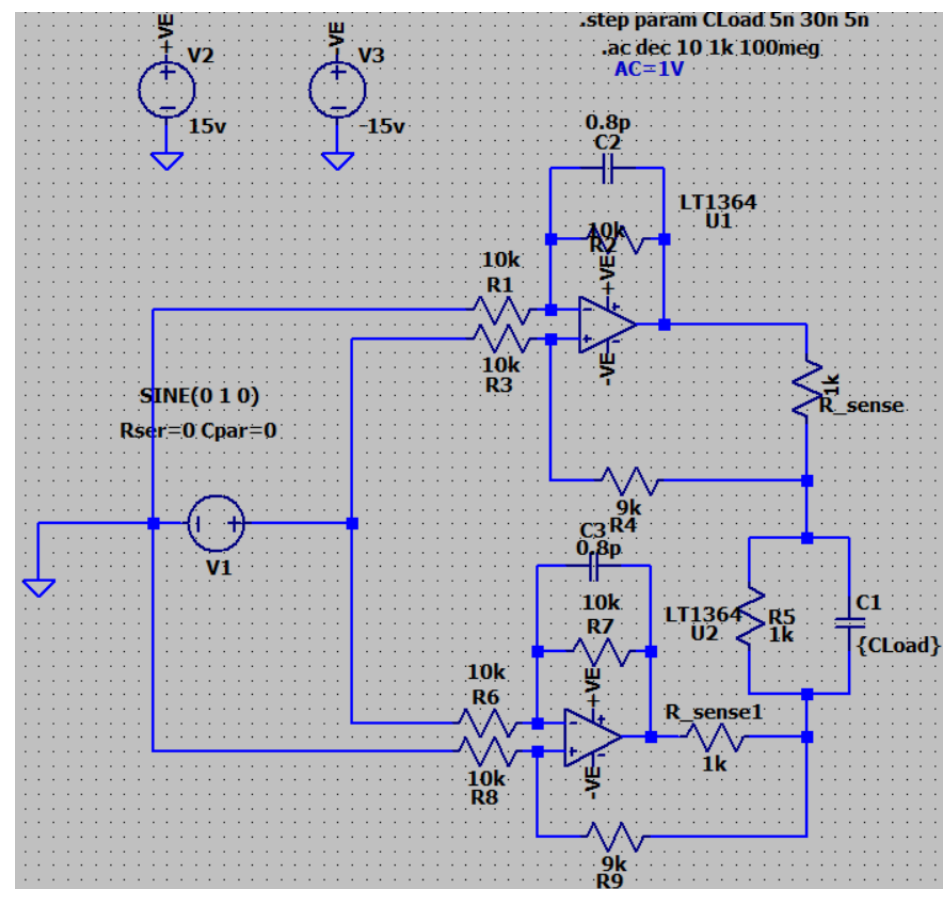
- [91] J. Wang, R. Xu, and S. Yang, "Estimation of plant water content by spectral absorption features centered at 1,450 nm and 1,940 nm regions," *Environ Monit Assess*, vol. 157, no. 1–4, pp. 459–469, Oct. 2009, doi: 10.1007/s10661-008-0548-3.
- [92] Texas Instruments, "AN-1515 A Comprehensive Study of the Howland Current Pump," *Application Note*, vol. SMPA474A, no. April, pp. 1–17, 2013, doi: 10.1212/WNL.55.12.1921.
- [93] A. Mahnam, H. Yazdanian, and M. Mosayebi Samani, "Comprehensive study of Howland circuit with non-ideal components to design high performance current pumps," *Measurement (Lond)*, vol. 82, pp. 94–104, Mar. 2016, doi: 10.1016/j.measurement.2015.12.044.
- [94] K. F. Morcelles, V. G. Sirtoli, P. Bertemes-Filho, and V. C. Vincence, "Howland current source for high impedance load applications," *Review of Scientific Instruments*, vol. 88, no. 11, Nov. 2017, doi: 10.1063/1.5005330.
- [95] I. I. Nwokoye and I. F. Triantis, "A 3 MHz Low-Error Adaptive Howland Current Source for High-Frequency Bioimpedance Applications," *Sensors*, vol. 24, no. 13, Jul. 2024, doi: 10.3390/s24134357.
- [96] P. Bertemes-Filho, A. Felipe, and V. C. Vincence, "High Accurate Howland Current Source: Output Constraints Analysis," *Circuits and Systems*, vol. 04, no. 07, pp. 451–458, 2013, doi: 10.4236/cs.2013.47059.
- [97] V. Grando Sirtoli, V. Coelho Vincence, and P. Bertemes-Filho, "Mirrored enhanced Howland current source with feedback control," *Review of Scientific Instruments*, vol. 90, no. 2, Feb. 2019, doi: 10.1063/1.5079872.
- [98] T. R. Qureshi, C. R. Chatwin, N. Huber, A. Zarafshani, B. Tunstall, and W. Wang, "Comparison of Howland and General Impedance Converter (GIC) circuit based current sources for bio-impedance measurements," in *Journal of Physics: Conference Series*, Institute of Physics Publishing, 2010. doi: 10.1088/1742-6596/224/1/012167.
- [99] D. Bouchaala, O. Kanoun, and N. Derbel, "MINIMIZATION OF STRAY CAPACITANCES IN HOWLAND CURRENT SOURCE."
- [100] M. A. Kadir, A. J. Wilson, and K. Siddique-e Rabbani, "A Multi-Frequency Focused Impedance Measurement System Based on Analogue Synchronous Peak Detection," *Frontiers in Electronics*, vol. 2, Dec. 2021, doi: 10.3389/felec.2021.791016.
- [101] P. Kassanos, I. F. Triantis, A. Demosthenous, and S. Member, "A CMOS Magnitude / Phase Measurement Chip for Impedance Spectroscopy," vol. 13, no. 6, pp. 2229–2236, 2013.
- [102] M. Chen, D. Anzai, J. Wang, and G. Fischer, "Circuit Design for Common-mode Noise Rejection in Biosignal Acquisition based on Imbalance Cancellation of Electrode Contact Resistance," 2019.
- [103] C. H. Y. Ling *et al.*, "Accuracy of direct segmental multi-frequency bioimpedance analysis in the assessment of total body and segmental body composition in middle-aged adult population," *Clinical Nutrition*, vol. 30, no. 5, pp. 610–615, 2011, doi: 10.1016/j.clnu.2011.04.001.

- [104] M. Elia, "Body composition by whole-body bioelectrical impedance and prediction of clinically relevant outcomes: Overvalued or underused?," *Eur J Clin Nutr*, vol. 67, pp. S60–S70, 2013, doi: 10.1038/ejcn.2012.166.
- [105] S. H. Liu, D. C. Cheng, and C. H. Su, "A Cuffless Blood Pressure Measurement Based on the Impedance Plethysmography Technique," *Sensors (Basel)*, vol. 17, no. 5, pp. 1–13, 2017, doi: 10.3390/s17051176.
- [106] A. Hafid, S. Benouar, M. Kedir-Talha, F. Abtahi, M. Attari, and F. Seoane, "Full Impedance Cardiography Measurement Device Using Raspberry PI3 and System-on-Chip Biomedical Instrumentation Solutions," *IEEE J Biomed Health Inform*, vol. 22, no. 6, pp. 1883–1894, 2018, doi: 10.1109/JBHI.2017.2783949.
- [107] V. P. Seppä, J. Viik, and J. Hyttinen, "Assessment of pulmonary flow using impedance pneumography," *IEEE Trans Biomed Eng*, vol. 57, no. 9, pp. 2277–2285, Sep. 2010, doi: 10.1109/TBME.2010.2051668.
- [108] V. Chitturi and N. Farrukh, "Spatial resolution in electrical impedance tomography: A topical review," *J Electr Bioimpedance*, vol. 8, no. 1, pp. 66–78, 2017, doi: 10.5617/jeb.3350.
- [109] N. Goren *et al.*, "Data Descriptor: Multi-frequency electrical impedance tomography and neuroimaging data in stroke patients," *Sci Data*, vol. 5, pp. 1–10, 2018, doi: 10.1038/sdata.2018.112.
- [110] Texas Instruments, "LF298, LF398-N LF198A-N, LF398A-N LFx98x Monolithic Sample-and-Hold Circuits," 2000. Accessed: Sep. 17, 2024. [Online]. Available: https://www.ti.com/product/LF198-N
- [111] I. I. Nwokoye and I. F. Triantis, "A Phase Error Correction System for Bioimpedance Measurement Circuits," *Applied Sciences (Switzerland)*, vol. 14, no. 12, Jun. 2024, doi: 10.3390/app14125202.
- [112] M. Min, T. Parve, A. Ronk, P. Annus, and T. Paavle, "Synchronous sampling and demodulation in an instrument for multifrequency bioimpedance measurement," *IEEE Trans Instrum Meas*, vol. 56, no. 4, pp. 1365–1372, 2007, doi: 10.1109/TIM.2007.900163.
- [113] A. Adler and A. Boyle, "Electrical impedance tomography: Tissue properties to image measures," *IEEE Trans Biomed Eng*, vol. 64, no. 11, pp. 2494–2504, Nov. 2017, doi: 10.1109/TBME.2017.2728323.
- [114] B. H. Brown, "Electrical impedance tomography (EIT): A review," *J Med Eng Technol*, vol. 27, no. 3, pp. 97–108, 2003, doi: 10.1080/0309190021000059687.
- [115] M. S. Mialich, J. Maria, F. Sicchieri, A. Afonso, and J. Junior, "Analysis of Body Composition: A Critical Review of the Use of Bioelectrical Impedance Analysis," *International Journal of Clinical Nutrition, 2014, Vol. 2, No. 1, 1-10,* vol. 2, no. 1, pp. 1–10, 2014, doi: 10.12691/ijcn-2-1-1.
- [116] D. M. Ferreira and M. N. Souza, "Body volumes of neonates assessed by," 2004.
- [117] K. Dheman, P. Mayer, M. Eggimann, M. Magno, and S. Schuerle, "Towards Artefact-Free Bio-Impedance Measurements: Evaluation, Identification and Suppression of

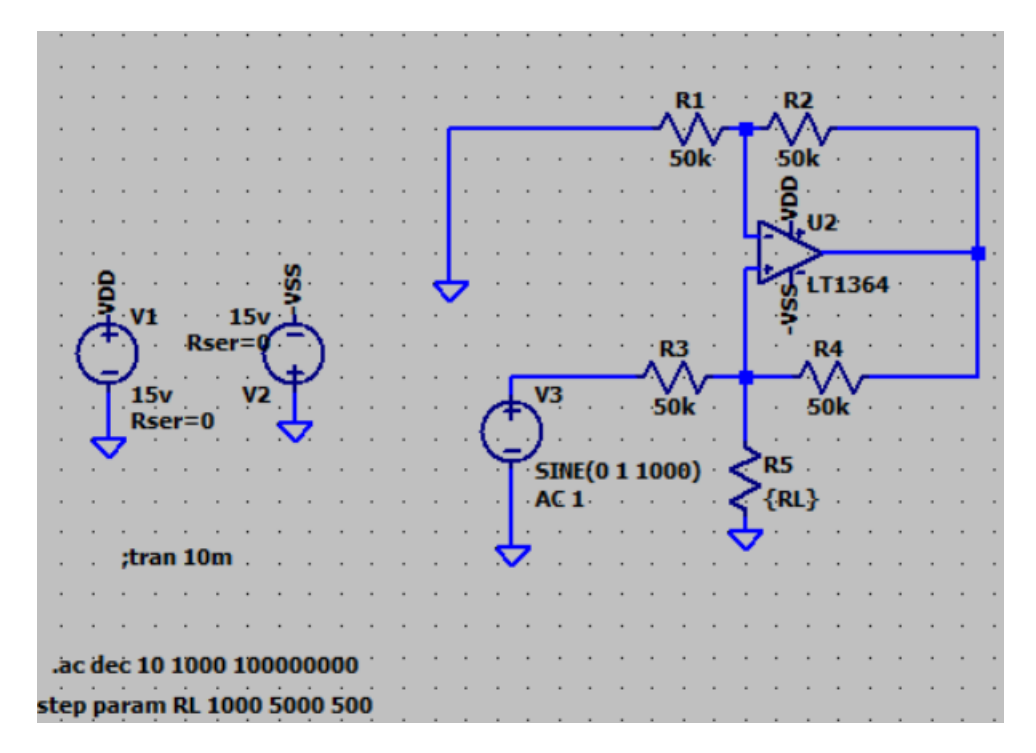
- Artefacts at Multiple Frequencies," *IEEE Sens J*, vol. 22, no. 1, pp. 589–600, Jan. 2022, doi: 10.1109/JSEN.2021.3128555.
- [118] R. P. Braun, J. Mangana, S. Goldinger, L. French, R. Dummer, and A. A. Marghoob, "Electrical Impedance Spectroscopy in Skin Cancer Diagnosis," *Dermatol Clin*, vol. 35, no. 4, pp. 489–493, 2017, doi: 10.1016/j.det.2017.06.009.
- [119] P. Kassanos, L. Constantinou, I. F. Triantis, and A. Demosthenous, "An integrated analog readout for multi-frequency bioimpedance measurements," *IEEE Sens J*, vol. 14, no. 8, pp. 2792–2800, 2014, doi: 10.1109/JSEN.2014.2315963.
- [120] B. Sanchez and S. B. Rutkove, "Electrical Impedance Myography and Its Applications in Neuromuscular Disorders," Jan. 01, 2017, *Springer New York LLC*. doi: 10.1007/s13311-016-0491-x.
- [121] G. Steinbaugh, "Shift registers and resistors deliver multiphase sine waves," EDN Network, Apr. 13, 2006. [Online]. Available: https://www.edn.com/shift-registers-and-resistors-deliver-multiphase-sine-waves/.
- [122] "High Precision Foil Resistor with TCR of \pm 2.0 ppm/°C, Tolerance of \pm 0.005 % and Load Life Stability of \pm 0.005 % RCK Series Vishay Foil Resistors." [Online]. Available: www.vishayfoilresistors.com
- [123] J. M. Algueta-Miguel, J. J. Beato-López, and A. J. López-Martín, "Analog Lock-In Amplifier Design Using Subsampling for Accuracy Enhancement in GMI Sensor Applications," *Sensors*, vol. 23, no. 1, Jan. 2023, doi: 10.3390/s23010057.
- [124] T. Yamaji, H. Tanimoto, and H. Kokatsu, "An I/Q Active Balanced Harmonic Mixer with IM2 Cancelers and a 45 Phase Shifter," 1998.
- [125] Analog Devices, Multiplication Application Guide, D. H. Sheingold, Ed. Norwood, MA, USA: Analog Devices, Inc., 1978, pp. 1–10.
- [126] A. Behrouzirad, P. Sugrue, M. Todorovic, K. G. McCarthy, and P. Galvin, "Analysis and Application of a Buffered Feedback Path Improved Howland Current Source in BioImpedance Measurements," in 2021 32nd Irish Signals and Systems Conference, ISSC 2021, Institute of Electrical and Electronics Engineers Inc., Jun. 2021. doi: 10.1109/ISSC52156.2021.9467881.
- [127] A. Mahnam, H. Yazdanian, and M. Mosayebi Samani, "Comprehensive study of Howland circuit with non-ideal components to design high performance current pumps," *Measurement (Lond)*, vol. 82, pp. 94–104, 2016, doi: 10.1016/j.measurement.2015.12.044.
- [128] R. Ghorbani and M. Nahvi, "Analysis of Performance of Howland AC Current Source for Electrical Impedance Spectro-Tomography," *Sens Imaging*, vol. 20, no. 1, Dec. 2019, doi: 10.1007/s11220-019-0251-1.
- [129] A. S. Tucker, R. M. Fox, and R. J. Sadleir, "Biocompatible, high precision, wideband, improved howland current source with lead-lag compensation," *IEEE Trans Biomed Circuits Syst*, vol. 7, no. 1, pp. 63–70, 2013, doi: 10.1109/TBCAS.2012.2199114.
- [130] D. Bouchaala, Q. Shi, X. Chen, O. Kanoun, and N. Derbel, "A high accuracy voltage controlled current source for handheld bioimpedance measurement," in 2013 10th

- *International Multi-Conference on Systems, Signals and Devices, SSD 2013*, 2013. doi: 10.1109/SSD.2013.6564162.
- [131] R. J. Halter, A. Hartov, and K. D. Paulsen, "A broadband high-frequency electrical impedance tomography system for breast imaging," *IEEE Trans Biomed Eng*, vol. 55, no. 2, pp. 650–659, Feb. 2008, doi: 10.1109/TBME.2007.903516.
- [132] G. S. Sarode, S. C. Sarode, M. Kulkarni, S. Karmarkar, and S. Patil, "Role of bioimpedance in cancer detection: A brief review," *International Journal of Dental Science and Research*, vol. 3, no. 1, Jan. 2016, doi: 10.1016/j.ijdsr.2015.11.003.
- [133] E. Tisserand and Y. Berviller, "Design and implementation of a new digital automatic gain control," in *Electronics Letters*, 2016th ed., vol. 52, IET, 2016. doi: 10.1049/el.2016.1398.
- [134] P. B. Petrović, "A New Precision Peak Detector/Full-Wave Rectifier," *Journal of Signal and Information Processing*, vol. 04, no. 01, pp. 72–81, 2013, doi: 10.4236/jsip.2013.41009.
- [135] H. Guo, X. Sun, S. Li, and Y. Liu, "Design and Experiment of Negative Impedance Converter for Impedance Cancellation of Electromagnetic Moving Coil Geophone," in *Journal of Physics: Conference Series*, Institute of Physics Publishing, Feb. 2020. doi: 10.1088/1742-6596/1449/1/012019.
- [136] V. G. Sirtoli, K. F. Morcelles, and V. C. Vincence, "Design of current sources for load common mode optimization," *J Electr Bioimpedance*, vol. 9, no. 1, pp. 59–71, Nov. 2018, doi: 10.2478/joeb-2018-0011.
- [137] M. Al Ahmad, Z. Al Natour, F. Mustafa, and T. A. Rizvi, "Electrical Characterization of Normal and Cancer Cells," *IEEE Access*, vol. 6, pp. 25979–25986, 2018, doi: 10.1109/ACCESS.2018.2830883.
- [138] E. Pittella, S. Pisa, E. Piuzzi, E. Rizzuto, and Z. Del Prete, "Combined impedance plethysmography and spectroscopy for the diagnosis of diseases of peripheral vascular system," 2017 IEEE International Symposium on Medical Measurements and Applications, MeMeA 2017 Proceedings, pp. 367–372, 2017, doi: 10.1109/MeMeA.2017.7985904.
- [139] D. S. Batista, G. B. Silva, F. Granziera, M. C. Tosin, D. L. Gazzoni Filho, and L. F. Melo, "Howland Current Source Applied to Magnetic Field Generation in a Tri-Axial Helmholtz Coil," *IEEE Access*, vol. 7, pp. 125649–125661, 2019, doi: 10.1109/ACCESS.2019.2939117.
- [140] L. Yan, J. Bae, S. Lee, T. Roh, K. Song, and H. J. Yoo, "A 3.9 mW 25-electrode reconfigured sensor for wearable cardiac monitoring system," in *IEEE Journal of Solid-State Circuits*, Jan. 2011, pp. 353–364. doi: 10.1109/JSSC.2010.2074350.
- [141] M. Rabbani, E. Rahman, A. Al Aishan, M. B. Powner, and I. F. Triantis, "A Low-Cost, Scalable, and Configurable Multi-Electrode System for Electrical Bio-Interfacing with In-Vitro Cell Cultures," *Applied Sciences (Switzerland)*, vol. 14, no. 1, Jan. 2024, doi: 10.3390/app14010162.

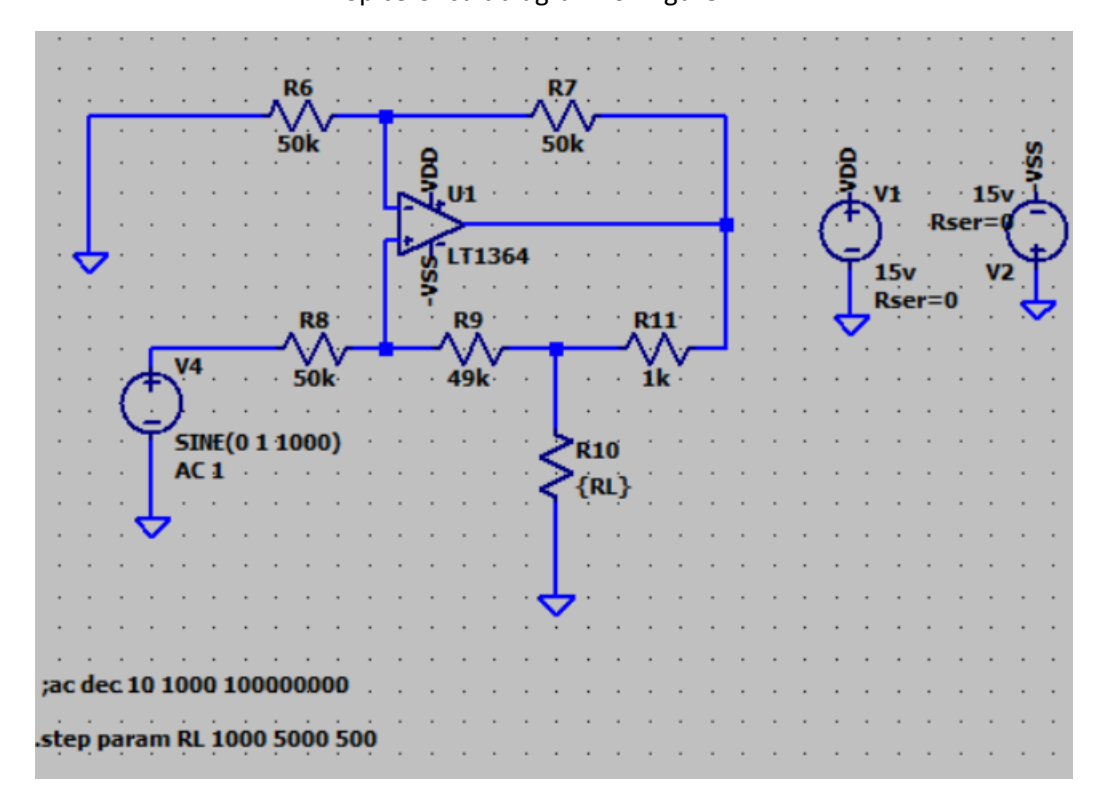
Appendix: Circuit Simulation and PCB Schematics and code



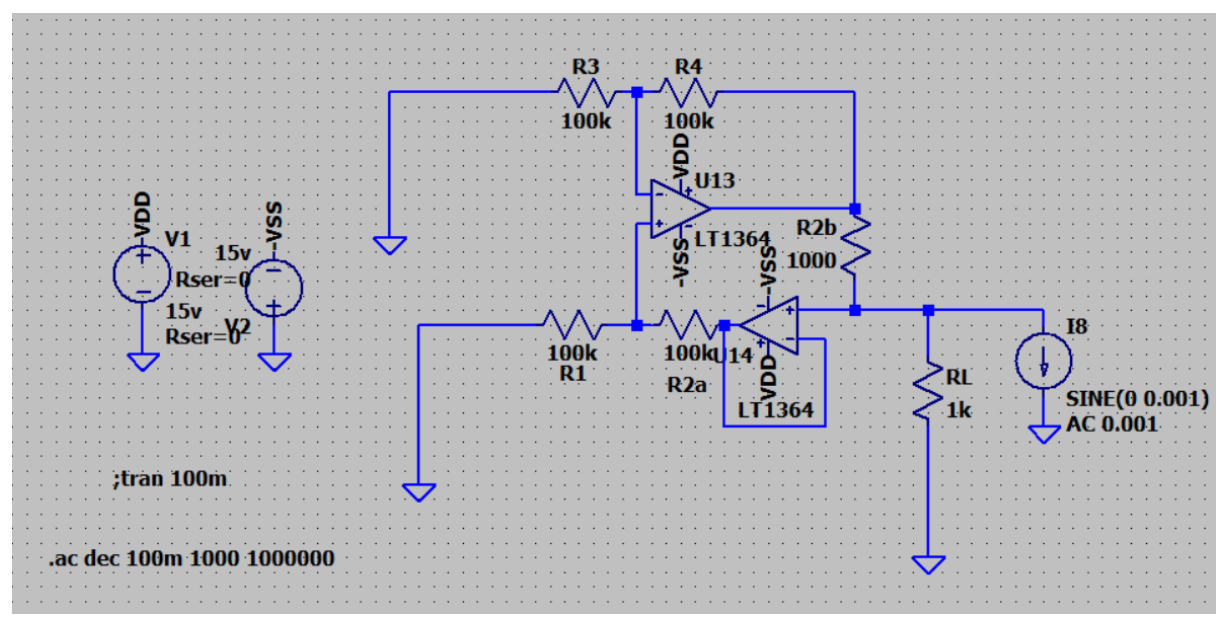
Spice Circuit diagram for Figure 2.14



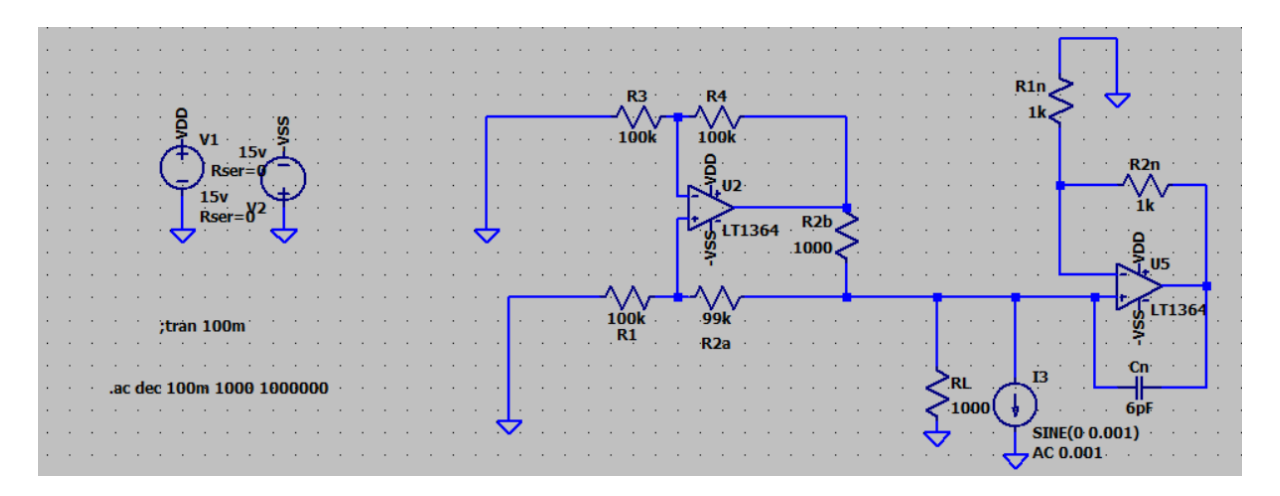
Spice Circuit diagram for Figure 4.4



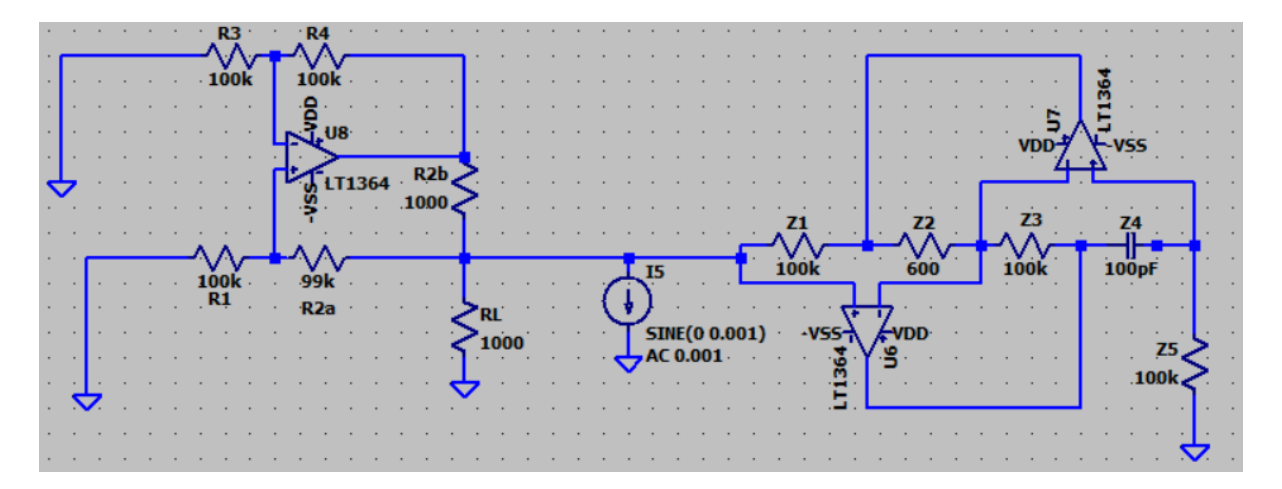
Spice Circuit diagram for Figure 4.5



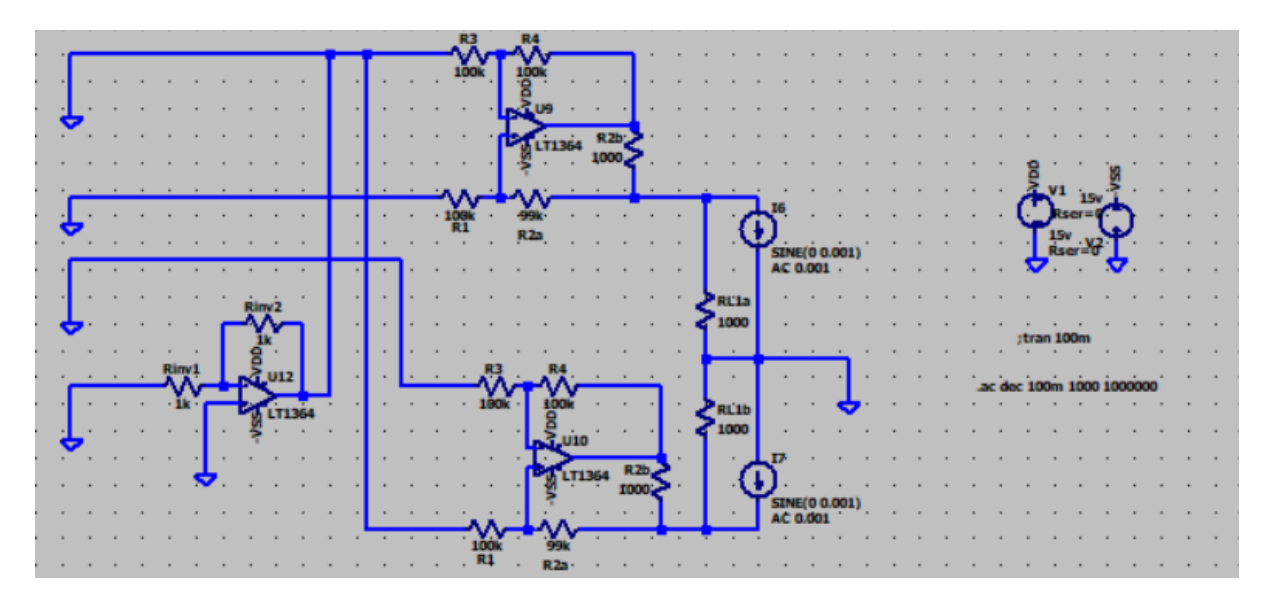
Spice Circuit diagram for the HCS with buffered feedback used for the output impedance graph of buffered feedback topology and shown in Figure 11



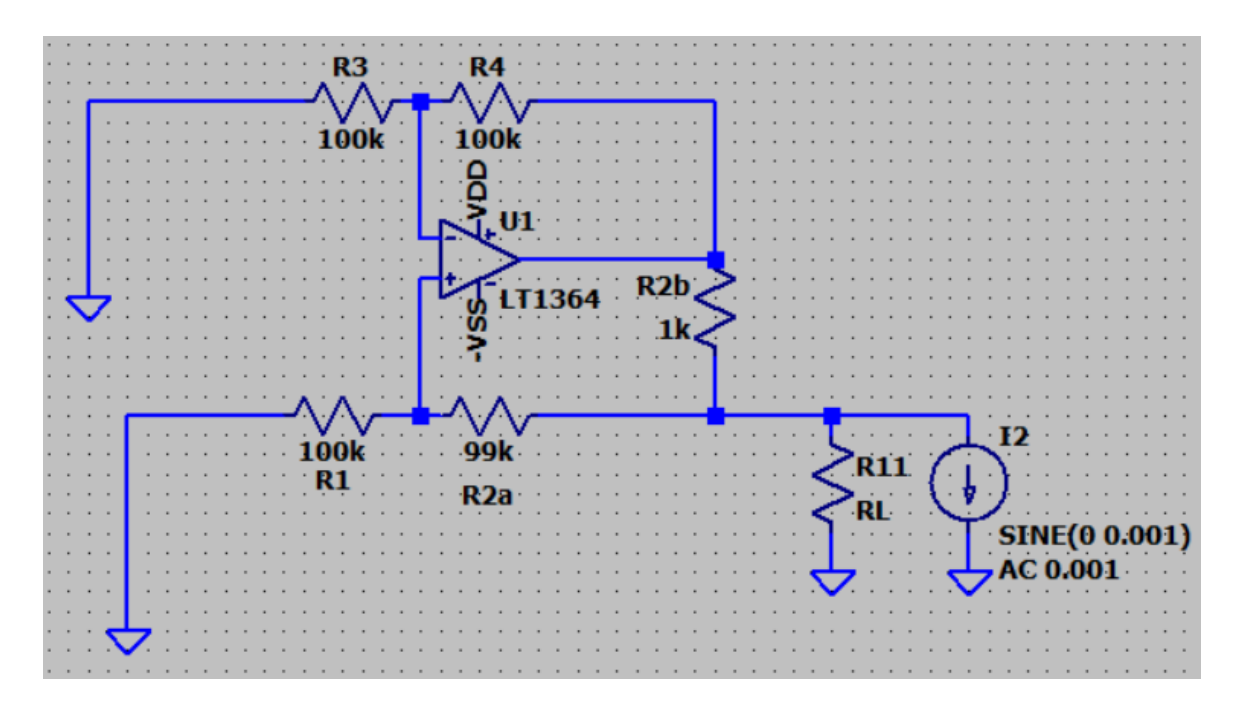
Spice Circuit diagram for the NIC circuit used for the output impedance graph of NIC shown in Fig.11



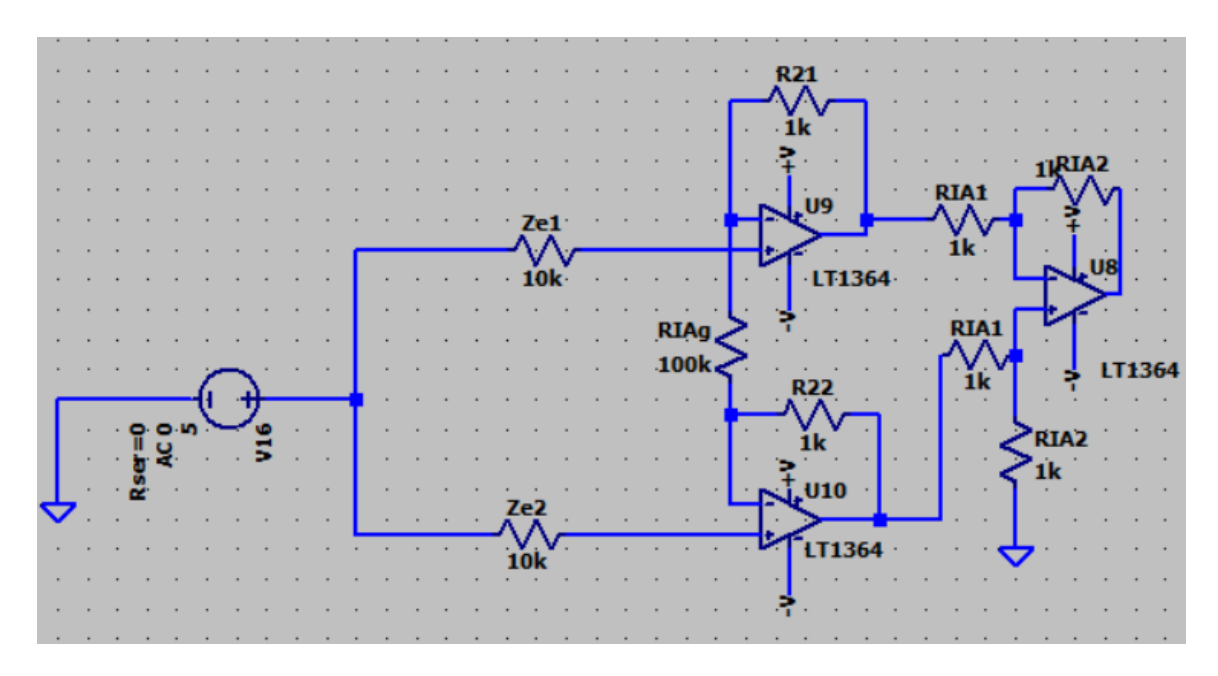
Spice Circuit diagram for the GIC circuit used for the output impedance graph of GIC shown in Fig.11.



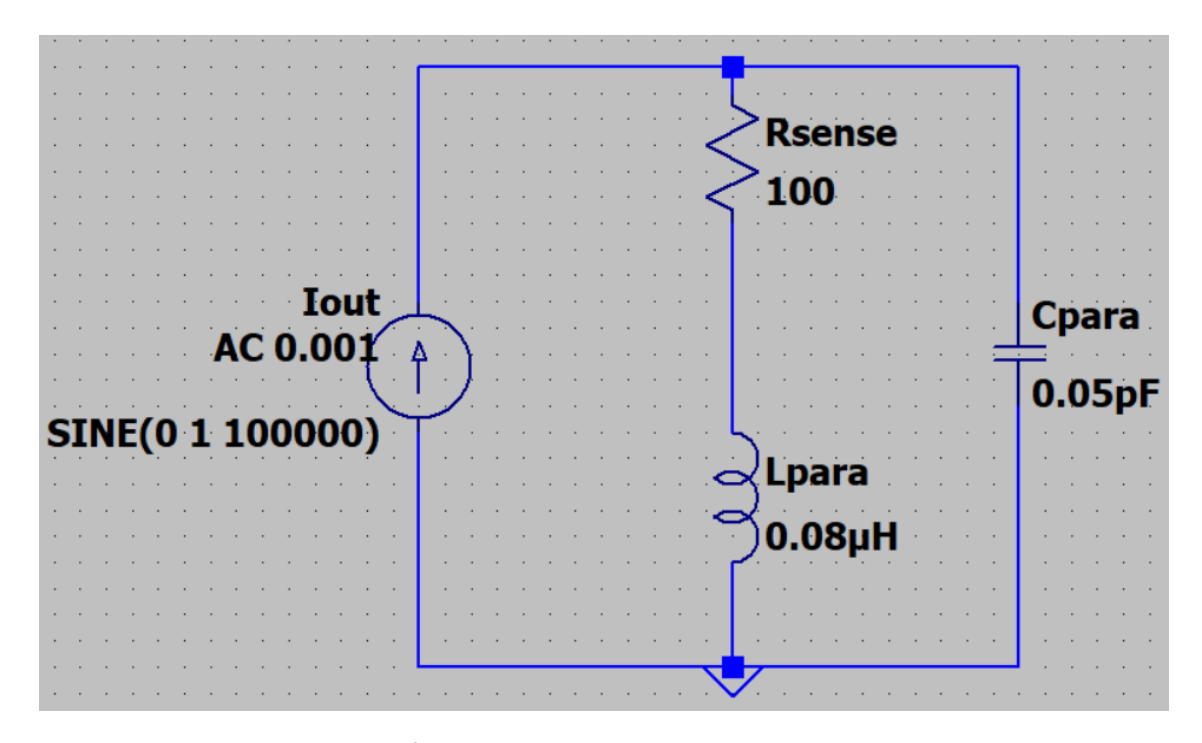
Spice Circuit diagram for MEHCS used for the output impedance graph of MEHCS shown in Fig.11



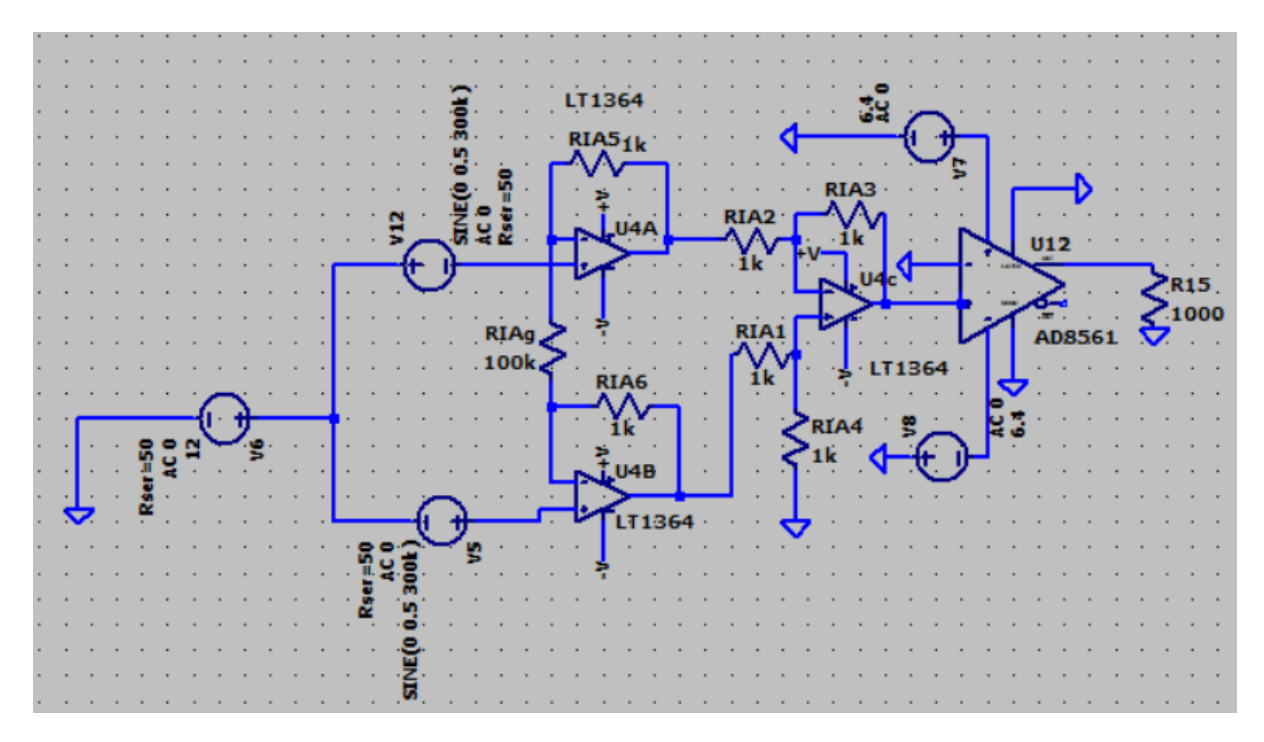
Spice Circuit diagram for EHCS used for the output impedance graph of EHCS shown in Fig.11



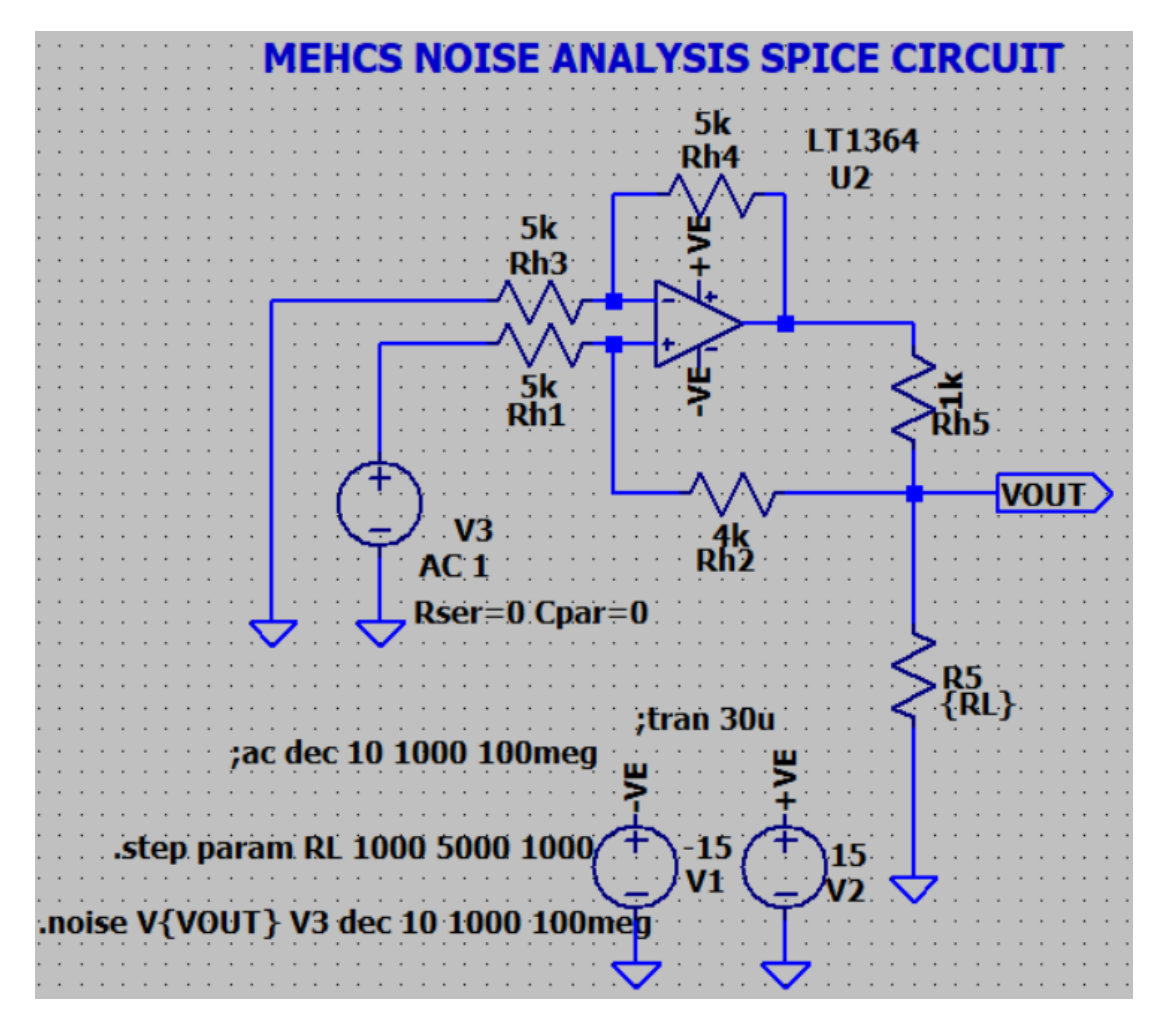
Spice Circuit diagram for instrumentation amplifier used in Fig 4.13



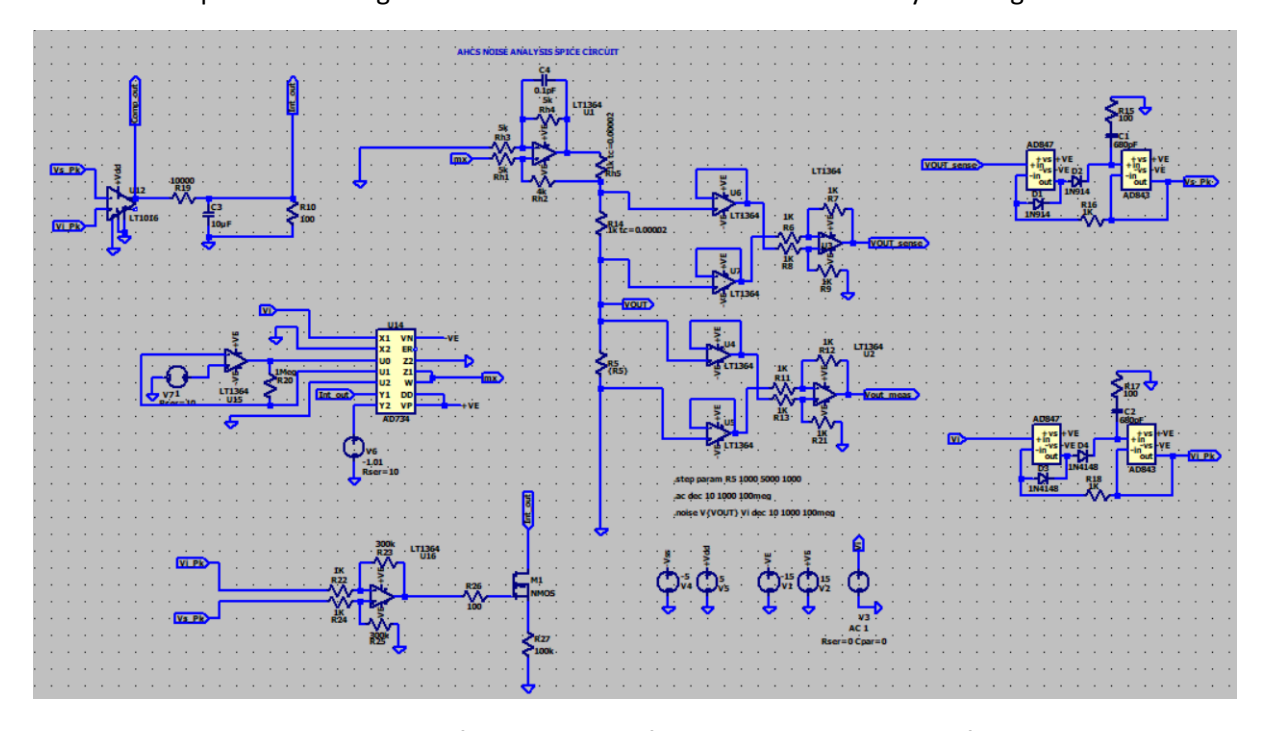
Spice Circuit diagram for Rsense Lumped Impedance model shown in Fig.6.9



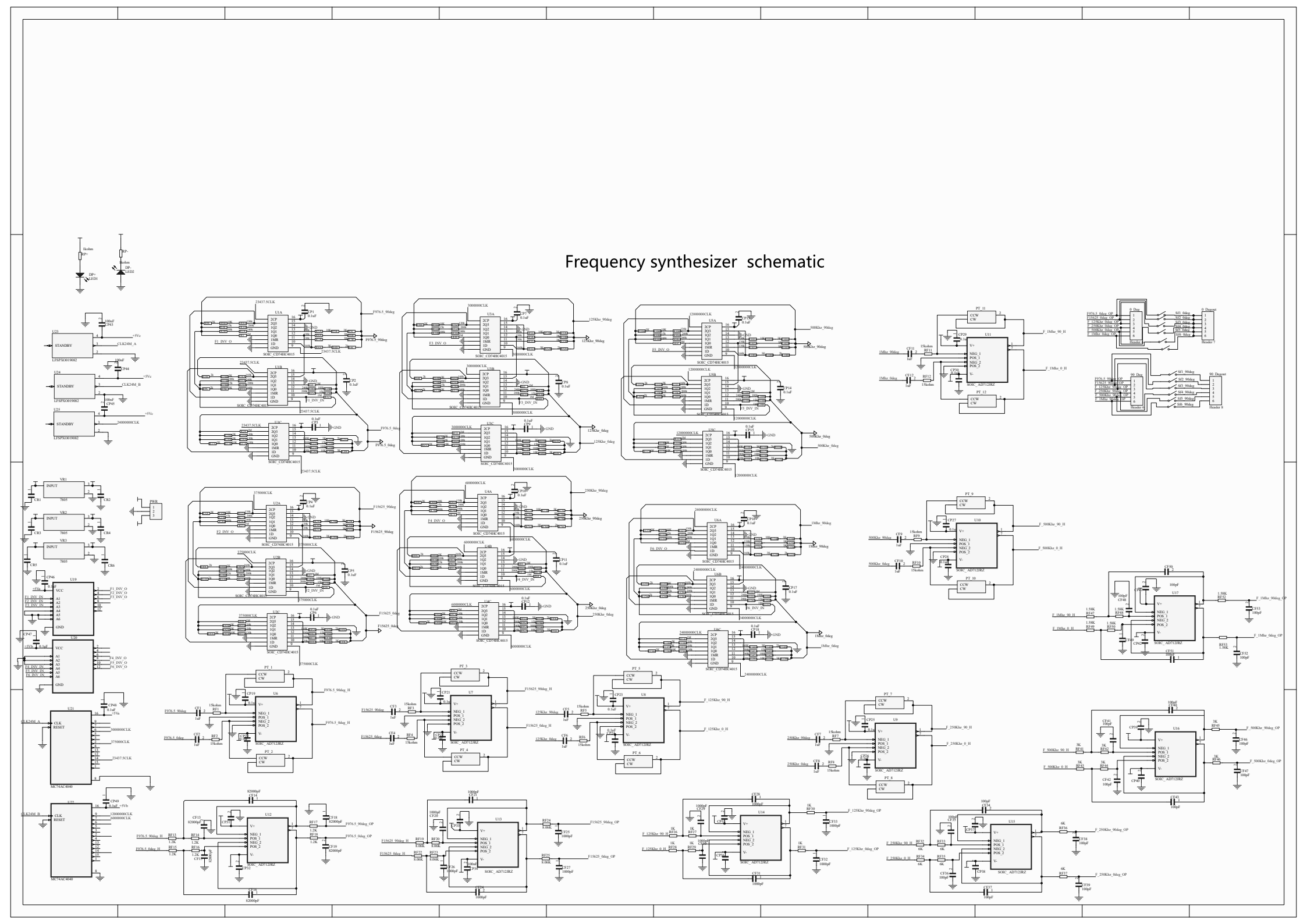
Spice Circuit diagram for simulation of the common mode offset voltage of the instrumentation amplifier of Fig.6.11

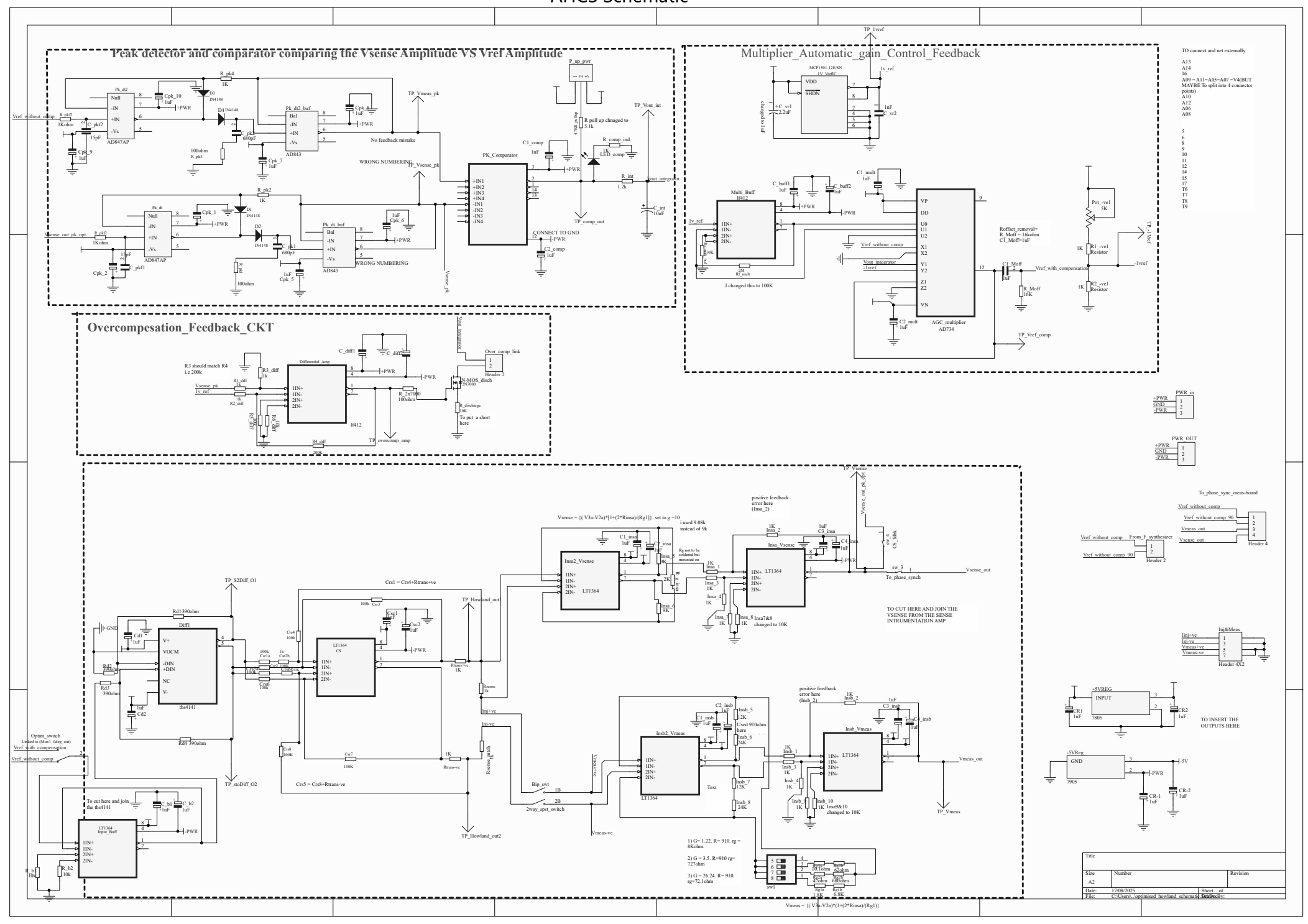


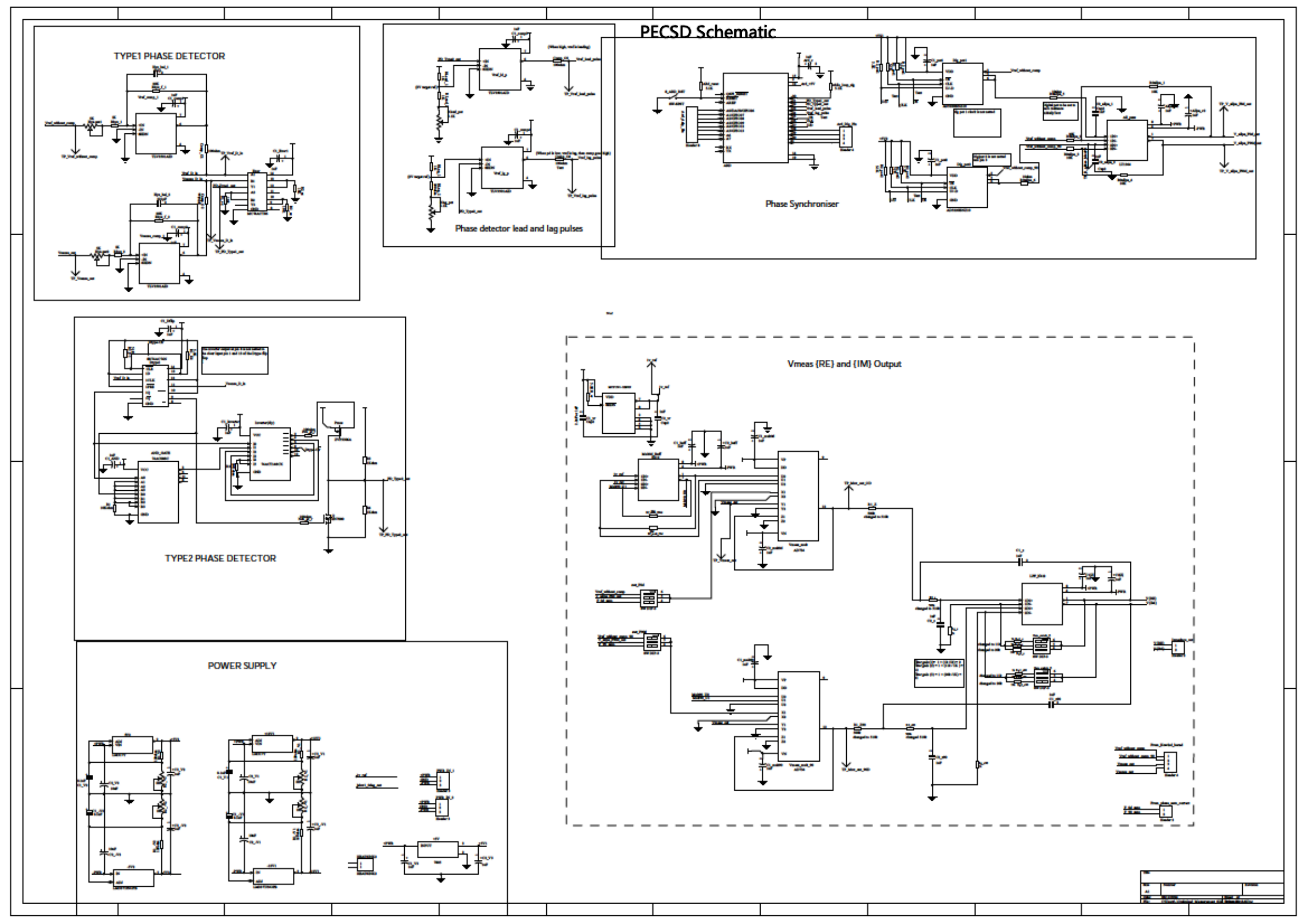
Spice Circuit diagram for simulation of the MEHCS noise analysis of Fig 7.15



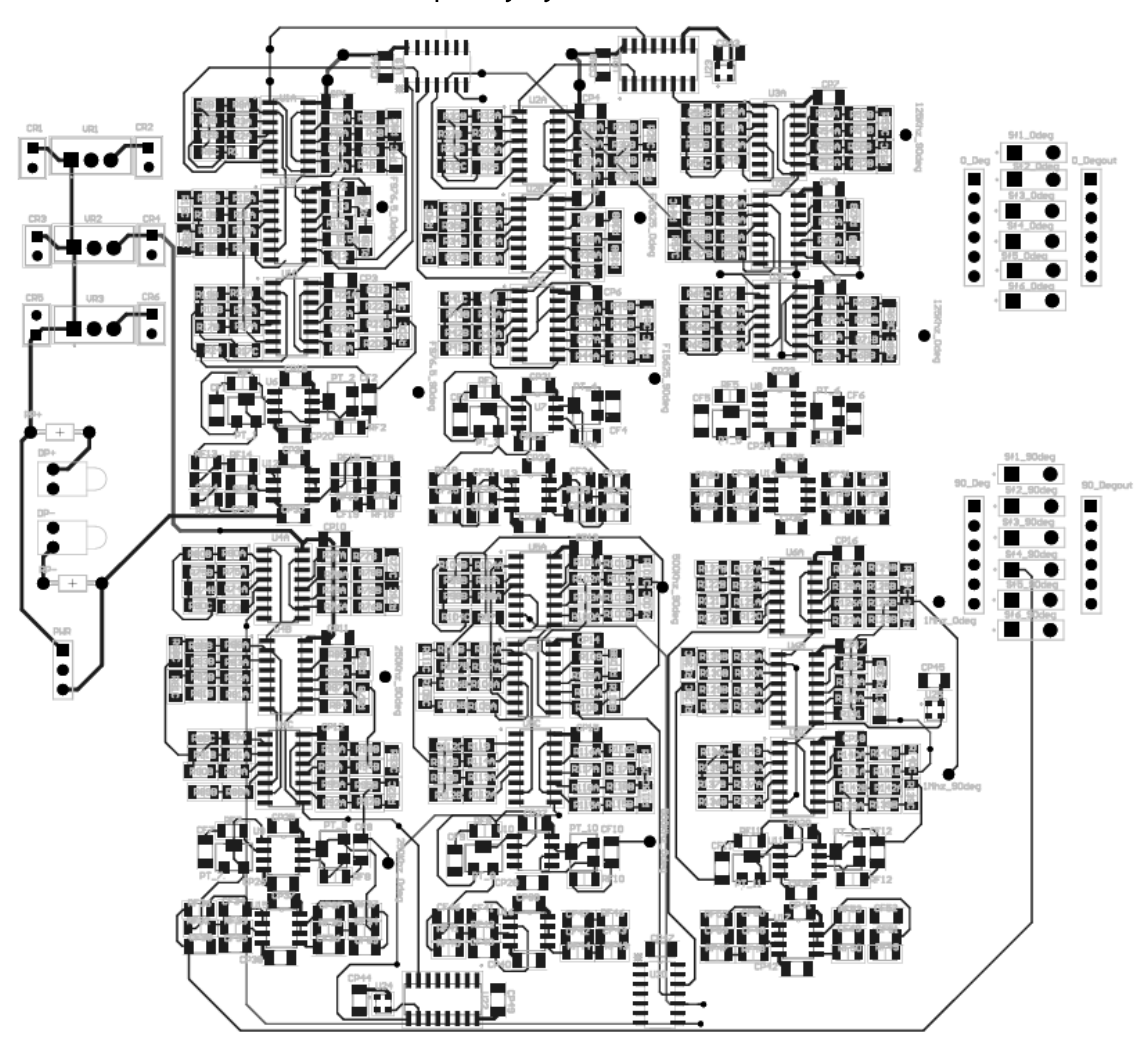
Spice Circuit diagram for simulation of the AHCS noise analysis of Fig 7.15

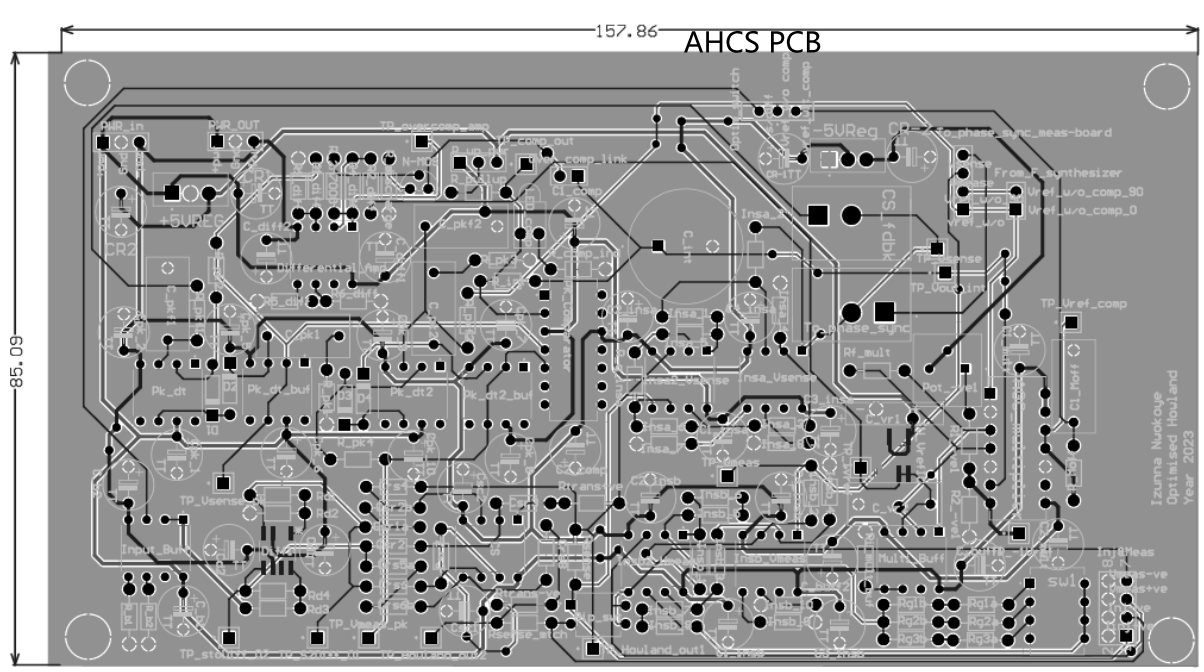


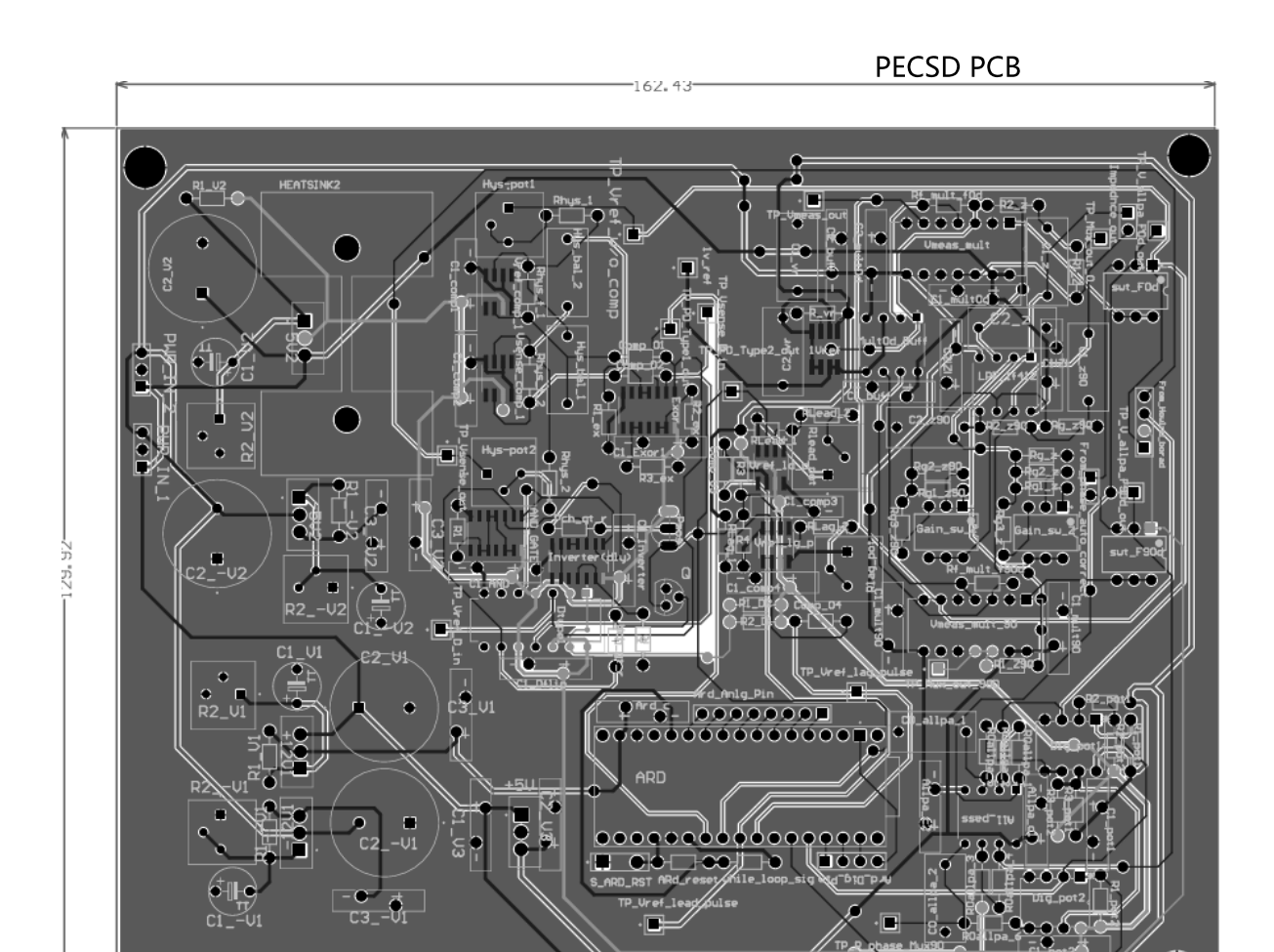




Frequency Syntesizer PCB







// Code to control the Ad5220 Digital potentiometer

```
int CS = 7;  // Chip Select (CS) pin for digital potentiometer, connected to Arduino pin D7
int CLK = 8;  // Clock (CLK) pin for digital potentiometer, connected to Arduino pin D8
int UD = 9;  // Up/Down (U/D) pin for digital potentiometer, connected to Arduino pin D9
int TP1 = 3;  // Phase detector signal, connected to Arduino pin D3
int Relay = 4;  // Relay control, connected to a transistor drive connected to Arduino pin D4

// Initializing the address to store phase detector reading
int storeType1 = 0;

void setup() {
```

pinMode(UD, OUTPUT); // Set U/D pin (D9) as OUTPUT to control phase adjustment

pinMode(CLK, OUTPUT); // Set CLK pin (D8) as OUTPUT to send clock pulses to potentiometer

```
pinMode(CS, OUTPUT); // Set CS pin (D7) as OUTPUT to enable/disable the potentiometer
 pinMode(TP1, INPUT); // Set TP1 pin (D3) as INPUT to read Type 1 phase detector signal
 digitalWrite(CS, HIGH); // Set CS high to disable the potentiometer initially
 digitalWrite(Relay,LOW); // Make sure the relay is not switched on intially
}
void loop() {
 digitalWrite(CS, LOW); // Enable potentiometer by pulling CS low
 digitalWrite(UD, HIGH); // Set U/D high to decrease resistance, reducing phase
 for (int i = 0; i < 128; i++) {
  SendPulse();
                     // Send 128 pulses to adjust resistance to zero initially
}
 digitalWrite(CS, HIGH); // Disable potentiometer by setting CS high
 delay(10);
                    // Short delay
 while (1) {
                    // Infinite loop to monitor phase and adjust resistance
  storeType1 = digitalRead(TP1); // Read phase detector signal is detected)
  delay(10);
  if (storeType1 == HIGH) {
   digitalWrite(Relay,HIGH); // Switch on the transistor drive the relay
   digitalWrite(UD, LOW);
                             // Set U/D low to increase resistance, adding phase
   digitalWrite(CS, LOW);
                             // Enable potentiometer
   delay(1);
   SendPulse();
                        // call the function Send pulse to adjust resistance
   digitalWrite(CS, HIGH); // Store new resistance value by disabling potentiometer
  }
  else {
   delay(1);
                       // Short delay if no adjustment is needed
```

```
}

}

void SendPulse() {  // Function to send a single clock pulse

digitalWrite(CLK, HIGH); // Set AD522 CLK high to start pulse

delay(10);  // Delay for pulse width (can be shortened with delayMicroseconds)

digitalWrite(CLK, LOW); // Set AD522 CLK low to end pulse

delay(10);  // Delay between pulses

}
```